Cranfield
UNIVERSITY

W-A. MARU

Modelling Two-Phase Flow and Transport Effects of Multicomponent Fuels

School of Engineering

Ph.D

Cranfield
UNIVERSITY

School of Engineering

Ph.D. THESIS

Academic Year: 2004-2005

Wessenu-Abegaz MARU

Modelling Two-Phase Flow and Transport Effects of Multicomponent Fuels

Supervisor: Professor J. B. Moss

July 2005

Thesis submitted in fulfilment of the requirements for the degree of
Doctor of Philosophy

ABSTRACT

Three novel multicomponent fuel spray droplet evaporation models are developed by employing the theory of continuous thermodynamics (CT) with the aim of applying them in the design and analysis of various energy conversion devices such as, aircraft jet engines, liquid-fuel rocket engines, diesel engines, and industrial furnaces. The CT methodology seeks to represent complex mixtures – for example, aviation kerosene or JP8 that typically comprise blends of a large number of chemical compounds by using probability distribution functions (PDFs). The components of JP8, which is constituted by the homologous series of paraffin, naphthene, and aromatic hydrocarbons; are each represented by the Pearson-Shultz type three-parameter gamma PDF, where the three (shape, scale, and origin) parameters characterise changes in the mixture composition. The phase transition of the liquid droplet due to evaporation is modelled using both low-pressure (LP) and high-pressure (HP) vapour-liquid equilibrium (VLE) models employing various mixing and combining rules by applying a general cubic equation of state (CEOS). Interestingly enough, the phase transition of the liquid fuel into vapour mixture is characterised by a change in the PDF scale parameter alone. Once the description of the fuel mixture is complete, the traditional species and energy transport equations both for the liquid and vapour phases, respectively, are re-written using the composition PDF moments under Lagrangian and Eulerian frameworks. In order to solve the governing equations for the three droplet evaporation models, which characteristically involve phase change and a moving interface, a novel fully Adaptive Method Of Lines using B-Spline Collocation (AMOLBSC) is developed. The models are tested at various pressures, temperatures, and convective conditions, including at a lean, premixed, prevaporised (LPP) combustor operating condition. In general, the computational results at an ambient pressure close to atmospheric showed good to excellent agreement against available experimental data in the literature. However, for ambient conditions with elevated-high pressures and temperatures, only models that employ the HP formulation gave reliable results. In particular, when the liquid is at or near its critical pressure and temperature, it is characterised by faster vaporisation and shorter droplet lifetime, including some evidence of liquid mass diffusion. The liquid model that incorporates the effects of liquid core circulation using semi-empirical approximation and adaptive mesh refinement (AMR) technique is the most accurate and computationally efficient, although further work is required to establish its ranges of applicability.

ACKNOWLEDGEMENT

I would like to thank my supervisor Prof. J B Moss for giving me the opportunity to work on such an interesting and multi-disciplinary research area. I am also very grateful for his guidance, encouragement, and patience during the majority of the last very difficult few years of this research. His overly enthusiasm and integral view on research and his mission for providing *'only high-quality work and not less'*, has made a deep impression on me.

There are many people to thank for their support and encouragement. I would like to thank all my friends and colleagues in Cranfield for making life both interesting and enjoyable. But, my special gratitude goes to Prof. Dr. E. F. Toro OBE, University of Trento-Italy, my former supervisor, who exposed me to the art of mathematical and numerical modelling for analysing scientific and engineering problems; Prof. W. A. Sirignano, University of California -Irvine, who gave me invaluable comments and advice at the beginning of this research both on crucial model investigations and model validation issues, including areas of current research importance; and Prof. C.E. Polymeropoulos, Rutgers University-New Jersey, for providing the experimental data of JP8, with out it the majority of the model validations would have been very difficult.

I am particularly indebted to my fiancé, Aster Mekonnen, who not only have been a constant inspiration but also who sacrificed on every aspect of her life, including sharing her precious time between her own Ph.D. research and caring for me when I was going through a very difficult time. Babe, I wouldn't have done it if it was not for you.

The chain of my gratitude would be definitely incomplete if I would forget to thank the first cause of this chain, "the prime movers since my childhood", my parents - for their love and inspiration.

TABLE OF CONTENTS

NOMENCLATURE

General Variables

$\Omega^{p}_{J(n)}$	any variable representing the J^{th} homologue of the n^{th} distribution moment of the multicomponent mixture of the p^{th} (liquid or vapour) thermodynamic phase.
$\Omega^{p}_{\bar{J}(n)}$	any variable representing the homologue mole fraction weighted sum of the p^{th} thermodynamic phase of the n^{th} distribution moment.
$\Omega^{\infty}_{J(n)}$	any variable representing the presence of the J^{th} homologue of the n^{th} distribution moment of the multicomponent mixture in the ambient region
$\Omega^{R\infty}_{\bar{J}(n)}$	any variable representing the average vapour mixture of a quantity (in the region between the droplet surface and the ambient), corresponding to the n^{th} distribution moment determined using the one-third rule.
Ω^{p}_{J} -	variable representing the J^{th} homologue of a quantity in the p^{th} thermodynamic phase.

a	parameters of the cubic equation of state; correlation coefficients for thermotransport properties
$\bar{a}$	correlation coefficient for the mixing and combining rules
b	parameters of the cubic equation of state; correlation coefficients for thermotransport properties
$\bar{b}$	correlation coefficients for the mixing and combining rules
c	total molar density of the mixture (kmole/m^3), correlation coefficients for thermotransport properties
h	enthalpy (kJ/kmole)
m	molar mass (kmole)
$\dot{m}$	molar mass flow rate (kmole/s)
r	radial coordinate

t	time (s)
$\boldsymbol{u}$	Instantaneous dispersion velocity of the liquid droplet (m/s
v	mole fraction weighted velocity of the mixture (m/s)
C_D	droplet drag coefficient
Cp	molar specific heat capacity (kJ/kmole-K)
D	droplet diameter (m), mixture molar diffusion coefficient (m^2/s)
$\boldsymbol{F}$	external forces acting on droplet (N)
$G^p(M)$	probability density function representing semi-continuous mixtures
M	molecular weight (kg/kmole)
$N_{T(n)}$	total vapour molar flux for the n^{th} distribution moment (kmole/m^2-s)
P	Pressure (N/m^2)
$\dot{Q}$	rate of heat energy transfer (kW/s)
R	droplet radius (m), gas constant (kJ/kmole-K)
S	source term due to evaporation and combustion
T	temperature (K)
$\boldsymbol{U}$	Instantaneous turbulent velocity of the ambient gas (m/s)
$W_J^p(M_J)$	probability distribution function representing continuous mixtures
X_J^p	mole fraction of the J^{th} homologue of the p^{th} thermodynamic phase.
Y_i	species mass fraction
Z	compressibility factor

Greek Letters

α	shape parameter for the gamma probability distribution function
β	scale parameter for the gamma probability distribution function (kg/kmole)
χ	thermal or mass diffusivity enhancement factor
δ	film thickness for the mass or thermal diffusion (m)

ε	fractional rate of mass vaporisation; parameters of equation of state
ϕ	transported scalar in the mass based Reynolds average Navier-Stokes equation
φ	third moment of the probability distribution function $(kg/kmole)^3$
γ	origin parameter for the gamma probability distribution function (kg/kmole)
λ	thermal conductivity (kJ/m-s-K)
μ	dynamic viscosity (kmole/m-s)
ϖ	activity coefficient
θ	mean or first moment of the probability distribution function (kg/kmole)
ρ	mass density (kg/m^3)
σ^2	variance of the probability distribution function about the mean $(kg/kmole)^2$
τ	droplet relaxation time (s)
ω	accentric factor
ψ	second moment of the probability distribution function $(kg/kmole)^2$
Φ	transported scalar of the Navier-Stokes equation in continuous thermodynamics
Γ	gamma function
Π	moment of the probability distribution function
Θ	fugacity coefficient

Superscripts

∞	far field or ambient gas condition
$\infty 0$	initial condition in the far field or ambient gas region
l	liquid phase
$l0$	initial condition in the liquid phase region
lR	value at the liquid side of the droplet surface
p	thermodynamic phase (liquid or vapour)
v	vapour phase
vR	value at the vapour side of the droplet surface
$R\infty$	vapour mixture value between the region of droplet surface and the ambient gas.

$\overline{\beta}$	alternative co-ordinate system (with $\overline{\beta}=0$ for Cartesian polar, $\overline{\beta}=1$ for Cylindrical, and $\overline{\beta}=2$ Spherical).

Subscripts

b	coefficient for boiling points
cp	coefficient for specific heat capacity
cr	coefficient for critical thermotransport property
d	droplet
f	fine grid
g	gas
i	species, temporal node point
j	spatial node point
kC	coefficients for the thermal conductivity
kT	coefficients for the thermal conductivity
mcr	coefficients for critical molar volume
n	degree of probability distribution function moments $(n=0,1,2,3)$
pcr	coefficients for critical pressure
r	radial discretisation
s	discrete species
J	homologue
M	quantity related to mass diffusion
T	total, quantity related to thermal diffusion
τ	temporal discretisation
ω	coefficients for the acentric factor
Φ	property related to the transported scalar

Dimensionless Groups

B	Spalding transfer number
Le	Lewis number
Nu	Nusselt number
Pe	Peclet Number
Re	Reynolds number
Sc	Schmidt number
Sh	Sherwood number

ABBREVIATIONS

AMR	Adaptive Mesh Refinement
ASTM	American Society for of Testing and
BBO	Basset, Boussinesq, and Oseen
CFD	Computational Fluid Dynamics
CT	Continuous Thermodynamics
EOS	Equation Of State
FCDM	Fractional Composition Distribution Moments
DAE	Differential Algebraic Equation
HP	High Pressure
LP	Low Pressure
LPP	Lean, Premixed, Prevaporised
ODE	Ordinary Differential Equation
PDE	Partial Differential Equation
PDF	Probability Distribution Function
MDLM	Multicomponent Diffusion Limited Model
MEDM	Multicomponent Effective Diffusivity Model
MLE	Maximum Likelihood Estimation
MME	Modified Moment Method
MMLE	Modified Maximum Likelihood Estimation
MOL	Method Of Lines
MWMM	Multicomponent Well Mixed Model
RANS	Reynolds Averaged Navier-Stokes
VLE	Vapour-Liquid Equilibrium
0D	zero-dimensional
1D	one-dimensional
2D	two-dimensional
3D	three-dimensional

PART I: BACKGROUND THEORY AND MODELLING

1. INTRODUCTION

1.1 Motivation

Liquid fuel gas turbine combustor technology has developed gradually and continuously over the last half-century. In recent years, significant efforts have been made in developing advanced combustor concepts in order to meet both present and future needs of improved performance and stringent pollution regulations. Among the various advanced concepts actively studied by the combustor research community is the Lean Premixed Pre-vaporised (LPP) combustor. Figure 1.1 shows an experimental LPP combustor (Prommersberger et al, 1998), with its three main zones.

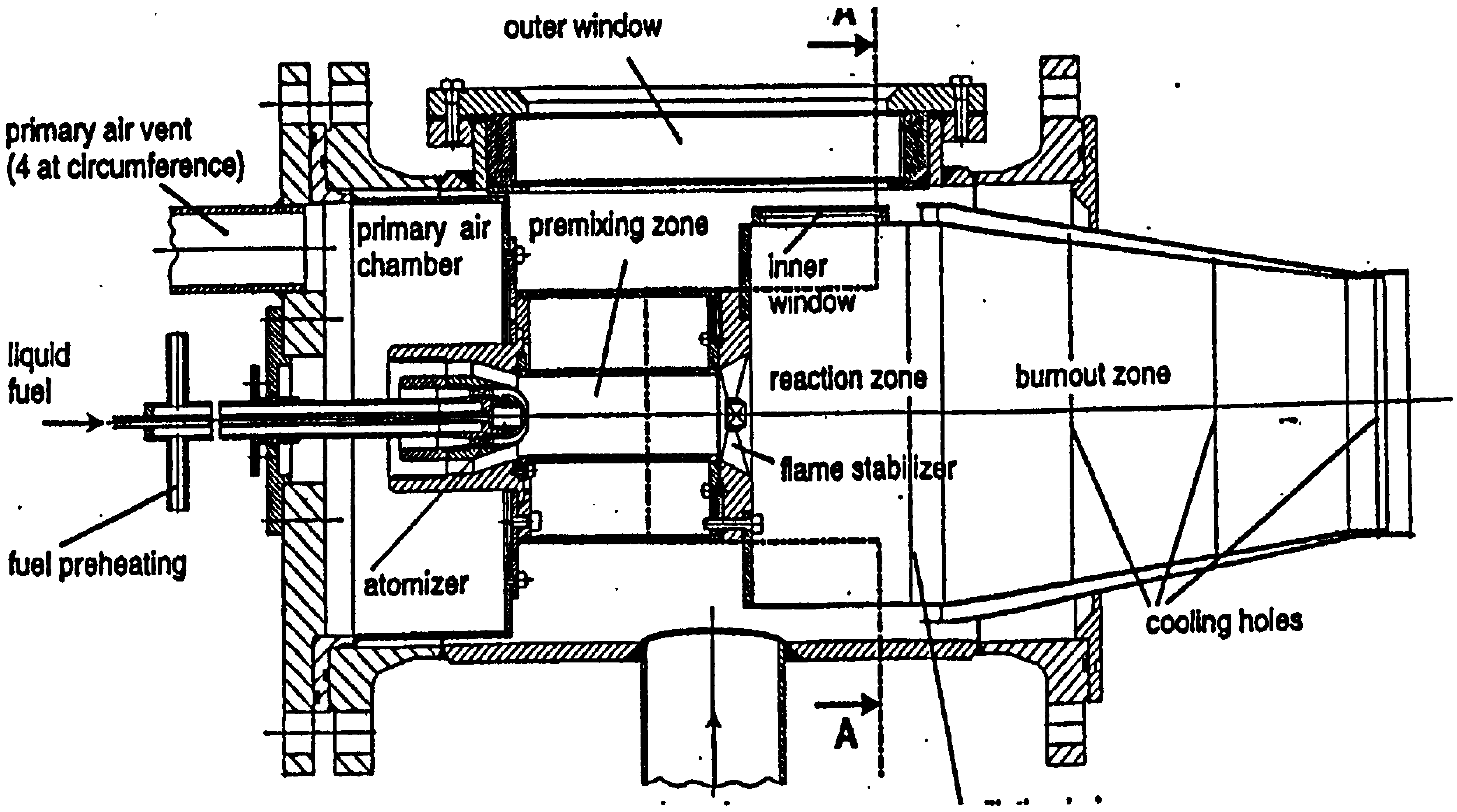

Figure 1.1. Experimental LPP Combustor.

The first section (or the premixing zone) is for fuel injection, fuel-air mixing, and fuel vaporisation. The aim here is to achieve a homogeneous mixture of low equivalence ratio that enables combustion to take place at low temperature and with low NOx production. In the second section (reaction zone), the flame is stabilised by the creation of recirculation zones. Combustion is completed here before the products flow into the third section (burnout zone) of the combustor, which comprises a conventional dilution.

However, while the technology of burning gaseous fuels in a premixed flame is well established, the premixed combustion of liquid fuels is much more difficult to achieve, and posses various problems (Roffe and Ferri, 1976; Schetter et al, 1994). Figure 1.2 depicts the two-phase flow and transport phenomena in a LPP duct (Schmehl et al, 1999). First, the fuel is atomised into clouds of droplets, which further break-up into fine droplets due to aerodynamic shearing. These droplets are dispersed through the (turbulent) hot gas stream and vaporise to provide the required fuel vapour that enables combustion and heat generation. At the same time, the atomised liquid interacts with the wall and could create a film flow.

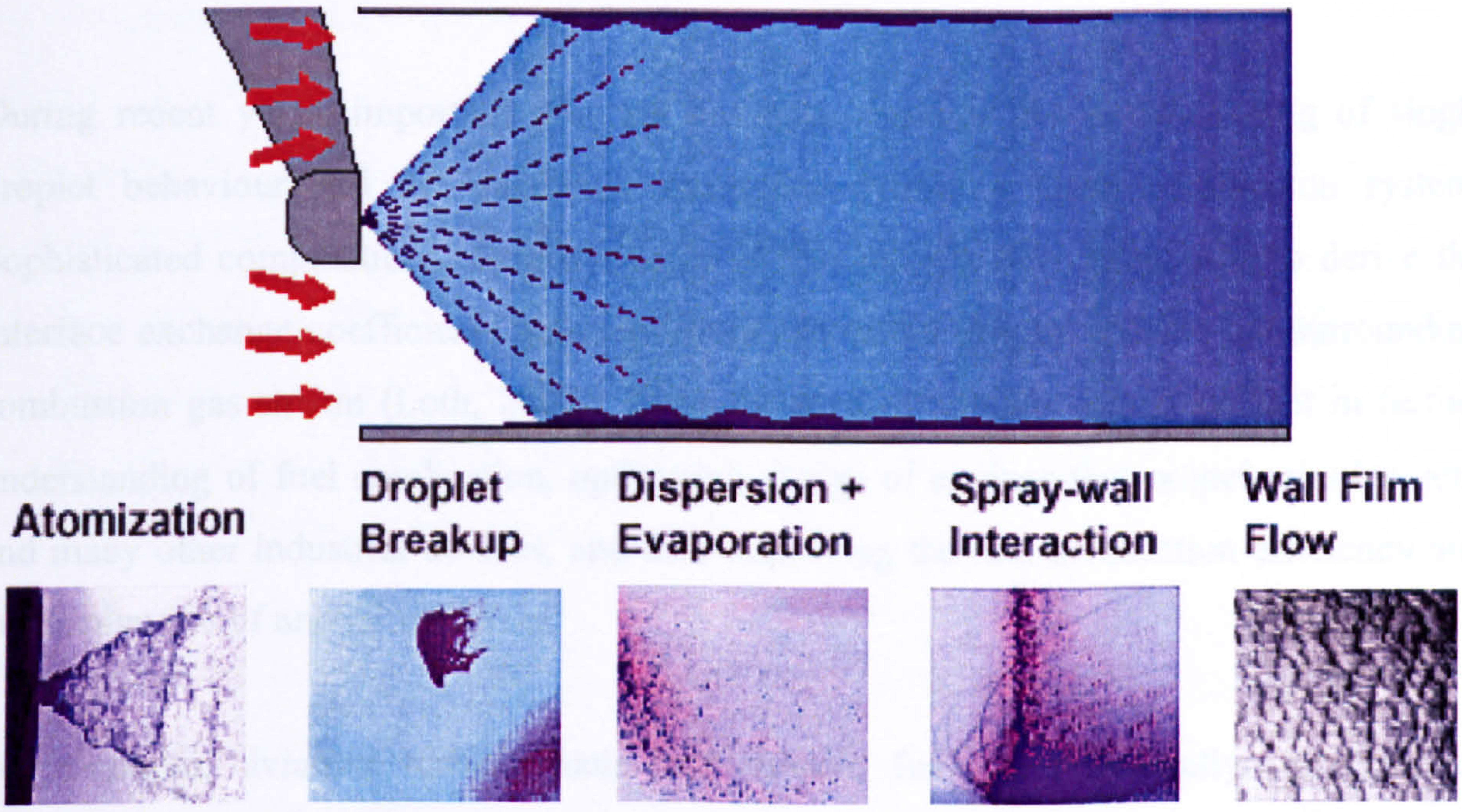

Figure 1.2. The two-phase flow and transport of liquid fuel in a premix duct.

In a LPP combustor, the liquid fuel (droplet or film) is required to vaporise completely and mixed homogeneously with air so that fuel-rich regions arising from non-homogeneous mixing would not lead to hot spots and hence, to locally high rates of NOx formation. It is essential to avoid or minimise the spraying of fuel against the wall so that the formation of carbon-residues and the auto-ignition of liquid films will not happen on the heated wall. In particular, for modern gas turbines operating at high pressures and temperatures, the time available for mixing is limited and the ignition delay of the mixture is very short. Hence, auto-ignition of the mixture and the flash-back of the flame into the premixing duct section should be avoided. Therefore, the vaporisation of fuels is a very important process in combustion devices, simply, liquid fuels do not burn, only the vapour of fuels do. However, fuel evaporation is part of a larger and complex problem – achieving a better physical understanding and a more accurate treatment of the phenomena of spray combustion. A good way to understand spray combustion is to study a single droplet that provides details of the fine scales of the relevant phenomena, such as droplet dynamics and the effect of aerodynamic drag, heat and mass transfer rates, droplet (spray) penetration distance, droplet life time, and vaporisation rate.

During recent years, important progress has been made in the understanding of single droplet behaviour and the gas-liquid interaction within a spray combustion system. Sophisticated computational fluid dynamics (CFD) models have been used to derive the interface exchange coefficients between liquid propellant droplet and the hot surrounding combustion gas stream (Loth, 2000). These research results are very important in further understanding of fuel combustion, optimising design of engines that propel missiles, jets, and many other industrial devices, and thus improving the fuel combustion efficiency and productive use of natural resources.

For example, aviation turbine fuels and missile fuels are, generally, mixtures of hydrocarbons derived from the distillation of petroleum crude oil, except for the presence of trace additives, which are used to enhance specific aspects of operational performance. These fuels are extremely complex, exhibiting most of the possible structural isomers for any possible hydrocarbon composition, which falls within the physical property range of the product mixture. A better understanding of the thermotransport characteristics of these fuels during evaporation and combustion is becoming increasingly important in the design of stable and efficient combustion systems. It is generally recognised that combustion efficiency and emissions performance is dependent on fuel preparation, including the mode of atomisation, the spray break-up, droplet dispersion through the (turbulent) hot gas stream, and its subsequent evaporation. In modelling the detail processes in spray combustion, whilst single or binary component fuel droplet evaporation have attracted considerable research attention, genuine multicomponent droplet evaporation models - constrained by quite tightly drawn fuel specifications and the considerably high computational resources required - have featured less prominently.

1.2 Objective of the Research

The general objective of this investigation is to develop a generic framework for modelling the two-phase flow and transport phenomena, as depicted by Figure 1.2, with the aim of gaining insight into the mechanisms and importance of multicomponent droplet evaporation in combustion devices operating at various temperatures and pressures. As such, the research is geared towards developing:

- New modelling approach for genuine multicomponent liquid-fuel droplet evaporation that can provide much more detailed information on the composition evolution as well as the flow and transport processes inside combustion devices, and that requires comparatively low computational resources,
- Both low and high pressure droplet evaporation models with wide ranges of applications and that account for variable thermotransport properties and non-unity Lewis number,
- Computationally efficient and highly informative model, which can handle various types of fuels, consisting of large numbers of components or whose composition may not be fully specified.

1.3 Research Methodology

To review the whole field of spray dynamics, evaporation and/or combustion is simply far too large a task, and the literature review part of this investigation mainly concentrates on the most salient features of droplet dynamics and evaporation models that have direct relevance in furtherance the research objective outlined earlier. As such, based on a survey on traditional droplet evaporation models and identifying their shortcomings, a new approach for modelling genuine multicomponent fuel droplet evaporation is proposed.

The proposed method is based on the theory of continuous thermodynamic (CT), which has been applied for multicomponent mixtures flash calculations and in modelling polymer solutions in the petroleum and chemical industries (Gal-Or et al, 1975; Cotterman et al, 1985). The CT theory seeks to describe the fluid mixture composition (both liquid and vapour) in terms of distribution functions for the molecular weight. By applying this composition representation in the traditional vapour mixture flow and transport equations, new CT based flow and transport equations are derived for the gas phase. Similarly, new liquid droplet evaporation models that account for droplet heating, internal circulation and multicomponent vapour liquid equilibrium (MVLE) are derived. The liquid models are solved using a modified general purpose package (Madson and Sincovec, 1979), by introducing a novel fully adaptive mesh refinement technique with posterior error control capabilities.To validate the developed models, various numerical tests at various ambient temperatures, pressures, and convective conditions are carried out and compared with the very limited available experimental data for multicomponent droplet evaporation.

1.4 Objective and Outline of Thesis

The objective of the thesis is to demonstrate both the knowledge gap in multicomponent droplet evaporation modelling as well as the importance and validity of the newly developed models together with the task that lie ahead in furtherance the work to a mature CFD modelling tool for practical applications.

To this end, the rest of the thesis is organised as follows. In §2 the classical droplet dynamics and evaporation models are reviewed in detail. First, droplet dynamics models are treated, including their brief historical development. Indeed, the objective here to provide a foundation on the subject and to emphasise on the current state of the art in view of the research framework that aim to develop a generic liquid model solver. The droplet evaporation models, however, both single component and multicomponent fuels, are reviewed in detail. In particular, as the central theme of this research is to develop a genuine multicomponent droplet evaporation model that is also computationally efficient, effort is made to classify models both on their accuracy and the subsequent computational resources requirement, namely - liquid model dimensionality. Once the existing models are assessed, and their shortcomings identified, steps are taken to develop new models for multicomponent droplet evaporation, as stipulated in the objectives of the research.

The vapour phase flow and transport for the new CT based multicomponent models are treated in §3. First, the theoretical background of the CT theory is introduced, and its successful applications in the petroleum and chemical industries are noted. Subsequently, the representation for the composition of the vapour fuel mixtures are applied in the traditional species and energy equations, and new equations in terms of the distribution moments and an energy equation that accounts inter-diffusion are derived. The vapour mixture flow and transport equations, in view of a dispersed liquid phase, are approximated following the well-mixed assumption and film theory. This was followed by the development of three novel liquid models in §4. In particular, multicomponent vapour-liquid equilibrium (MVLE) models both at low-pressures (LP) and high-pressures (HP) are derived. In addition, to account for the effect of variable thermotransport properties and non-unity Lewis number, thermotransport properties correlation based on the composition distribution moments are developed. In view of the huge computational resources requirements in modelling spray evaporation and/or combustion, a generic and efficient numerical and computational framework for the liquid model in general and for droplet evaporation in particular is developed in §5. Various numerical tests are conducted in §6 and §7 and compared with available experimental data to validate the models at various temperatures, pressures, and convective conditions. The numerical results are further discussed in §8 both to identify the performance of the new models and the range of their practical applicability. In particular, the salient ambient conditions that affect the evaporation process, the effect of the numerical treatment both on model accuracy and efficiency, and other related issues are discussed. This is followed by conclusions and recommendations.

2. CLASSICAL DROPLET DYNAMICS AND EVAPORATION MODELS

2.1 *Introduction*

Modelling of droplet dynamics in a turbulent gas stream as two-phase flow and transport phenomena is a challenging problem both from fundamental scientific interests and engineering applications viewpoint. Usually, the problem is studied in a variety of sub-models, and it involves various specialist fields of study. Important considerations include the description of the instantaneous turbulent velocity field for the carrier fluid, effects of flow non-uniformity and droplet relative acceleration, curvilinear trajectory, shear-generated lift forces, and turbulent modulation through momentum exchange.

Droplet evaporation adds another complexity due to energy and mass transfer during droplet heating and evaporation by changing the thermotransport properties of the two-phase system. The problem is even further complicated when the dispersed phase is dense and droplet-droplet interaction is dominant, the pressure exceeds the critical values and the dispersed phase has a large number of components. An excellent reference in this regard is the book by Sirignano (1999), and references therein.

Owing to its vast area of applications, extensive researches have been conducted on droplet dynamics, evaporation and combustion in the last few decades. This review is not intended to be a comprehensive study of the vast literature that already exists on the subject; rather it is intended to focus on the droplet dynamics and evaporation models that have relevant practical applications.

There are various classifications as to how droplet dynamics and evaporation are treated (Crowe et al, 1996, Gouesbet and Berlemont, 1999; Loth, 2000). It is, however, instructive to discuss the salient features in a concise manner. To this end, the droplet dynamics and vaporisation reviews are presented separately, although, they are coupled processes in the stricter sense.

2.2 *Droplet Dynamics Models*

The study of droplet motion has developed in many directions due to the various contexts and applications in which they are used. In particular, since understanding spray and droplet behaviours has a strong impact on vital economic and military issues, accurate predictions are required. For example, dispersion of particles in a turbulent flow field occurs inside most power generation systems, like gas turbine combustors and rocket motors. In addition, the phenomenon of particle dispersion occurs in many other areas of engineering application. These include diesel engines, spray coating, painting, pesticides, aerosols and transport in the natural environment. The study of particle dispersion is an old one, starting with Stoke's seminal attempt to determine the resistive drag force on a rigid sphere in a creeping flow. To that end, the methods of solution for the particle momentum equation in a turbulent flow field have undergone many corrections (Aggarwal and Peng, 1995). For practical applications, the particle motion is simulated using the Basset-Boussinesq-Oseen (BBO) equation (Maxey and Riley, 1983).

Maxey and Riley (1983) pointed out some of the inconsistencies of previous investigations and obtained the modified BBO equation. The authors analysed in detail the forces experienced by a small rigid sphere in an unsteady Stokes flow. The modified BBO equation contains the Stokes drag, the Basset force, the Saffman lift force, the force due to fluid pressure gradient, the inertial force of added mass, and gravity.

However, the results of several studies, e.g. Elghobashi and Truesdell (1992), indicate that if the ratio of the density of the particle to the density of the carrier fluid is large, only the Stokes' drag and the gravity forces are dominant and the other forces can be neglected. Therefore, under the assumption of high liquid to gas density ratio, negligible particle inter-collusion, a particle size smaller than the smallest turbulent length scale and negligible shear force on the particle, the BBO equation can be reduced into a much simplified form. The high value of liquid to gas density ratio implies that the Basset force and the added mass terms are small and are therefore can be neglected (Elghobashi and Truesdell, 1992). For particles with small diameter and low inertia, the

Saffman lift force, which is generated due to the effect of shear on the particle, can be neglected in comparison to the drag force (Crowe et al., 1998). After analysing the liquid to gas density ratio, $\left(\rho^{l}/\rho^{\infty}\right)\geq 100$, Faeth (1983) recommended the equation of motion for a droplet or parcel of droplets to be of the form:

$$\frac{d\boldsymbol{u}_{d}}{dt}=\frac{1}{\tau_{d}}\left(\boldsymbol{U}-\boldsymbol{u}_{d}\right)+\boldsymbol{F}_{d} \qquad (2-1)$$

In equation $(2-1)$, $\boldsymbol{U}$, $\boldsymbol{u}_{d}$, and $\boldsymbol{F}_{d}$ represent the instantaneous gas-phase velocity, the droplet dispersion velocity, and the external forces acting on the droplet (for example – gravity, centrifugal or Coriolis forces), respectively. On the other hand, the droplet relaxation time τ_{d}, is a measure of the ability of the droplet to follow the velocity fluctuation of the gaseous phase, which is given by:

$$\tau_{d}=\frac{4}{3C_{D}\left(Re_{d},B_{M}\right)}\frac{\rho^{l}}{\rho^{R\infty}}\frac{D_{d}^{2}}{Re_{d}\,\upsilon^{R\infty}} \qquad (2-2)$$

In equation $(2-2)$, C_{D} is the drag coefficient, which is a strong function of the droplet Reynolds number Re_{d}, and the Spalding transfer number B_{M}, whereas $\rho^{R\infty}$ and $\upsilon^{R\infty}$ represent the density and kinematic viscosity, respectively; evaluated using the one-third rule of Yuen and Chen (1976) to quantify the average values of the vapour-gas film condition. The droplet density is represented by ρ^{l}, while its diameter is represented by D_{d}. As such, the particle addresses in the computational flow domain can be determined by integrating the particle velocity as:

$$\frac{d\boldsymbol{x}_{d}}{dt}=\boldsymbol{u}_{d} \qquad (2-3)$$

In equations $(2-1)$-$(2-3)$, $\boldsymbol{U}=\overline{\boldsymbol{u}}+\tilde{\boldsymbol{u}}$ is the instantaneous gas-phase velocity with a mean and fluctuation component, while the droplet Reynolds number is defined as:

$$Re_d = D_d \frac{V_{rel}}{\upsilon^{R\infty}} \tag{2-4}$$

In equation $(2-4)$, the relative gas-droplet velocity $V_{rel} = \sqrt{(U - u_{di})^2}$. The functional dependence of the drag coefficient both on the Reynolds number and the Spalding transfer number is of significant importance to understand both droplet dynamics and evaporation. For example, the experimental results of Renksizbulut and Yuen (1983) indicates that evaporation reduces the drag coefficient by a factor of $(1 + B_M)$ compared to the non-evaporating case of $Re_d < 30$. However, typical gas turbines employing JP8 fuel, where the ambient-vapour mixture pressure, temperature, and initial relative gas-droplet velocity are in the order of $P^{\infty 0} = 30\,atm$, $T^{\infty 0} = 1000K$, $\sqrt{(U - u_d)^2} = 30\,m/s$, respectively; attain $Re_d \sim 100$ corresponding to a droplet initial diameter $D_d \sim 50 - 70\,\mu m$. Obviously, for atmospheric combustors, the density and therefore the Reynolds number are expected to be much smaller. To that end, Chiang et al (1992) conducted an exact analysis of the Navier-Stokes equation and recommended a numerical correlation for the drag coefficient for droplet Reynolds number $30 \le Re_d < 200$ as:

$$C_D = \frac{1}{(1 + B_M)^{0.27}} \frac{24.432}{Re_d^{0.721}} \tag{2-5}$$

Unfortunately, most of the droplet evaporation models in the literature applied to gas turbines ignored the effect of vaporisation on drag (Chiang et al, 1992; Sirignano, 1999). For example, for mass transfer number $0.2 < B_M < 6.5$, the drag coefficient could be reduced by about 60 %.

The determination of the interaction between the droplet and the gaseous phase turbulent fluctuation is vital importance to reflect the effect on the droplet movement. However, the gaseous phase turbulent fluctuation $\tilde{u}$ is not available from most turbulence models. Therefore, it is required to provide a procedure for regeneration of the fluctuations, which generally depend on the turbulent quantities. Such treatment is beyond the scope of this research, and excellent reviews on the subject and relevant computational issues can be found in the works of Gouesbet and Berlemont (1999) and Loth (2000).

2.3 Droplet Evaporation Models

2.3.1 Background

In the previous section, the dynamics of droplets and its coupling with the continuous phase is briefly discussed. The situation is further complicated due to the evaporation process. Extensive research has been conducted to understand the processes of droplet heating, evaporation and combustion in the past century. However, there were neither plausible theoretical models nor consistent experimental results until the independent work of two British scientists (Spalding, 1953, Godsave, 1953).

The combined process of droplet heating, evaporation and combustion within a hot (turbulent) gas stream is multidisciplinary in nature, involving heat and mass transport, fluid dynamics, and chemical kinetics (Sirignano, 1999). Modelling such processes has been a challenge, and the quest to develop comprehensive models for practical combustion application is still an ongoing research.

The evaporation of liquid fuels is believed to occur only at the interface between the liquid and the carrier phases. Therefore, the liquid mass deep inside the droplet may not reach the droplet surface quickly enough due to mass-diffusional resistances. Particularly in multicomponent fuels, the mass fraction of the more volatile species decreases at the droplet surface while that of the less volatile species increases with time. The resulting phenomenological description is the unsteady and non-uniform distribution of mass fraction inside the droplet due to preferential evaporation. The vaporised fuel then creates a mixing layer with the ambient gas. The evolution of a liquid drop undergoing phase transition, under chemical and mechanical equilibrium, to form a mixing layer of usable fuel-air vapour mixture is the most complex and interesting aspect of the model development process.

In general, the fundamental problem of droplet heating and evaporation can be viewed as seeking the solution of the unsteady Navier-Stokes, species and energy equations in three dimensions. To this end, various models have been developed, albeit with varying degree of accuracy and computational resource requirements. The reviews by Williams (1973, 1976), Faeth (1977, 1983, 1987), Law (1982), Sirignano (1983; 1993), Aggarwal et al (1984), Aggarwal and Peng (1995), and Sirignano (1999) indicate the complexity of the problem and the plethora of investigations over the years. Nevertheless, models that account for the effects of real (or commercial) fuels and that can be used in practical applications have yet to be developed.

In real fuels, which are essentially multicomponent in nature, the species and energy transport inside the droplet is due to a combination of molecular diffusion, convective motion, internal circulation, and thermal gradient. If a relative velocity between the droplet and the ambient gas is low, molecular diffusion is the primary mode of species transport. In high relative velocity environments, however, internal circulation generated by the shear stress at the drop-interface promotes the convective transport significantly (Sirignano, 1978). In general, the energy transfer from the ambient gas to the liquid is the driving potential that facilitates vaporisation, causing volatility differentials between species with different boiling points. To that end, various computational models have been developed that successfully capture the fluid dynamic characteristics, and to a very limited degree, the multicomponent nature of the fuel.

In this study, droplet evaporation models are categorised into four groups, ranging from zero-dimensional to three-dimensional, where the dimensional group of a model is associated with the spatial treatment of the liquid phase. Models that do not account for the spatial variation in the liquid phase fall under the zero-dimensional model category. In all these four groups, however, only models that are developed based on the isolated droplet assumption are admitted. Although the isolated droplet model is a good assumption to reduce the complexity of both the physical and computational representation, it does not capture the many droplet interactions, which are evident in sprays. As a rule, low dimensional models are thought of as less accurate and less computationally expensive than their high dimensional counterparts. Depending on the thermodynamic and flow variable intensities, however, the performance of low dimensional models may show superiority over high dimensional models both in terms of accuracy and efficiency. As such, the effort to develop a model for practical applications is mostly dictated by striking a balance between computational accuracy and computational resource requirements.

Recently, Dwyer et al (2000) studied the unsteady vaporisation and ignition of six arrays of droplets. The authors solve the three-dimensional low-Mach number NS-equations with variable liquid and gas properties at various Reynolds numbers. Their results show the dependence of droplet interaction with Reynolds number including, droplet drag, heat and mass transfer, and array configuration. In particular, the analysis showed distinctive features between predictions using single droplet models and that of the droplets within the array configuration. Such detailed analysis, if developed further, could be used for validation purposes against simple models. However, unless to appreciate the complexity involved in spray evaporation and combustion problems, complete 3D-spray simulation for practical applications is not possible in the immediate future. Therefore, low dimensional droplet evaporation models remain the most realistic prospect.

To that end, the general two-dimensional (axi-symmetric) model proposed by Sirignano and co-workers (Law and Sirignano, 1977; Prakash and Sirignano, 1975; Law, Prakash and Sirignano, 1977) has been a subject of intense investigation for the last few decades. In these 2D models, the authors consider the motion and evaporation of a droplet in a strong convective field, consisting of an exterior potential flow, interior Hill's vortex and boundary layer near the interfaces. The problem is assumed inherently transient in nature due to the droplet heating, and the temporal variation in the droplet composition and temperature. In particular, the authors argued for the importance of the proper liquid and gas phase description of the heat, mass, and momentum transport processes, and the thermodynamic and mechanical equilibrium at the interface of the two phases. These investigations culminate in the identification of the essential physics for single component (Prakash and Sirignano; 1978, 1980) and multicomponent (Lara-Urbaneja and Sirignano, 1981) convective droplet evaporation models. However, these 2D models proved too complex and computationally expensive to be included in practical spray computations. Therefore, the axi-symmetric models (Prakash and Sirignano; 1978, 1980; Lara-Urbaneja and Sirignano, 1981), appear to have never been used in spray analysis.

Therefore, the need for models of reduced dimensionality (0D or 1D) with reasonable accuracy to mimic the physical processes becomes apparent due to the increasing importance of CFD based methodologies in the design and testing of combustion devices (Tolpadi et al, 2000). In particular, the art of coupling low dimensional droplet evaporation models with experimental data through empirical correlation might pave the way for the required compromise. In addition, effort is being made in the refinement of theoretical models and acquiring of quality experimental data in furtherance of computational accuracy and efficiency.

For example, previously developed 0D (Law, 1976a,b), and 1D (Law and Sirignano, 1977) models, which used the Ranz-Marshall correlation (Ranz and Marshall, 1952) to account for the correction of the spherically symmetric assumption due to the carrier gas convective effects, were shown to be erroneous (Sirignano, 1978). In particular, for highly convective flows that are typical of gas turbine combustors, Sirignano (1978) argued on the need to seek more quality experimental data, like that of Clift et al (1978), or for the development of a more radical approach to correct the spherically symmetric assumption.

But, most of the progress in droplet vaporisation modelling stems from the refinement of high dimensional models and/or the improvement of low dimensional models. The high dimensional models that have been under continuous refinement include the axi-symmetric models of Sirignano and co-workers (Prakash and Sirignano, 1978, 1980; and Lara-Urbaneja and Sirignano, 1981). The refinement of high dimensional models and the improvements in the low dimensional models (Law, 1977; Law and Sirignano,

1977) lead to the film models (Tong and Sirignano, 1982a, 1982b, 1986b; Abramzon and Sirignano, 1989). These models incorporate both the liquid circulation and the effect of Stefan flow on the laminar boundary thickness, and have been used successfully in practical spray computations (Aggarwal et al, 1984; Raju and Sirignano, 1989, 1990, Rangel and Sirignano, 1988; Delplanque and Sirignano, 1995). The film models are generally 1D and assume spherical symmetry as the 0D models.

Such developments indicate that the 0D and 1D isolated droplet evaporation models are the way forward for practical applications. In each group, however, there are distinctive variations, based on the treatment of the liquid phase, gas phase and in particular the manner by which the thermotransport properties are computed. An exhaustive review of every model is beyond the scope of this work. Rather, emphasis here is given on the development of the most popular 0D and 1D models, irrespective of their applicability to either single component or multicomponent fuels. Most single component droplet evaporation models have their multicomponent equivalent, although they are generally tested only for simple binary fuels.

Before proceeding any further, it is instructive to start with a general 1D equations that can serve as a basis to describe the most widely used low dimensional models and as a framework for a new modelling approach. The governing equations for the gas-phase region can be found elsewhere (Zhu et al 2001; Sirignano, 1999). The mass continuity, conservation of species mass, and energy equations in the interior of the spherically symmetric vaporising droplet in an alternate coordinate system, $\bar{\beta}$, are, respectively (Kuo, 1986; Williams, 1965, 1985):

$$\frac{\partial \rho^l}{\partial t} + \frac{1}{r^{\bar{\beta}}}\frac{\partial}{\partial r}(r^{\bar{\beta}} \rho^l v^l) = 0 \tag{2-6}$$

$$\frac{\partial(\rho^l Y_i^l)}{\partial t} + \frac{1}{r^{\bar{\beta}}}\frac{\partial}{\partial r}(r^{\bar{\beta}} \rho^l v^l Y_i^l) = \frac{1}{r^{\bar{\beta}}}\frac{\partial}{\partial r}(r^{\bar{\beta}} \rho^l D_{im}^l \frac{\partial Y_i^l}{\partial r}); \quad i = 1,\dots,N \tag{2-7}$$

$$\frac{\partial(\rho^l T^l)}{\partial t} + \frac{1}{r^{\bar{\beta}}}\frac{\partial}{\partial r}(r^{\bar{\beta}} \rho^l v^l T^l) = \frac{1}{Cp^l\, r^{\bar{\beta}}}\frac{\partial}{\partial r}(r^{\bar{\beta}} \lambda^l \frac{\partial Y_i^l}{\partial r}) \tag{2-8}$$

Equations $(2-6)$-$(2-8)$ describe $(N+2)$ equations of the unknown dependent variables v^l, $Y_i^l = \left(Y_1^l, \dots, Y_N^l\right)$, and T^l, where the mixture thermotransport properties D_{im}^l, Cp^l, and λ^l are determined through correlation and the density , ρ^l, could be determined using an equation of state. Therefore, equation $(2-6)$-$(2-8)$ can be solved subject to the corresponding $(N+2)$ initial (v^{l0} , $Y_i^{l0} = \left(Y_1^{l0}, \dots, Y_N^{l0}\right)$, and T^{l0}) and interface (v^{vR}, $Y_i^{vR} = \left(Y_1^{vR}, \dots, Y_N^{vR}\right)$, and T^{vR}) conditions or their gradients. The process of droplet vaporisation that accounts for the mass, species, and energy conservation at the droplet surface is depicted in Figure 2.1.

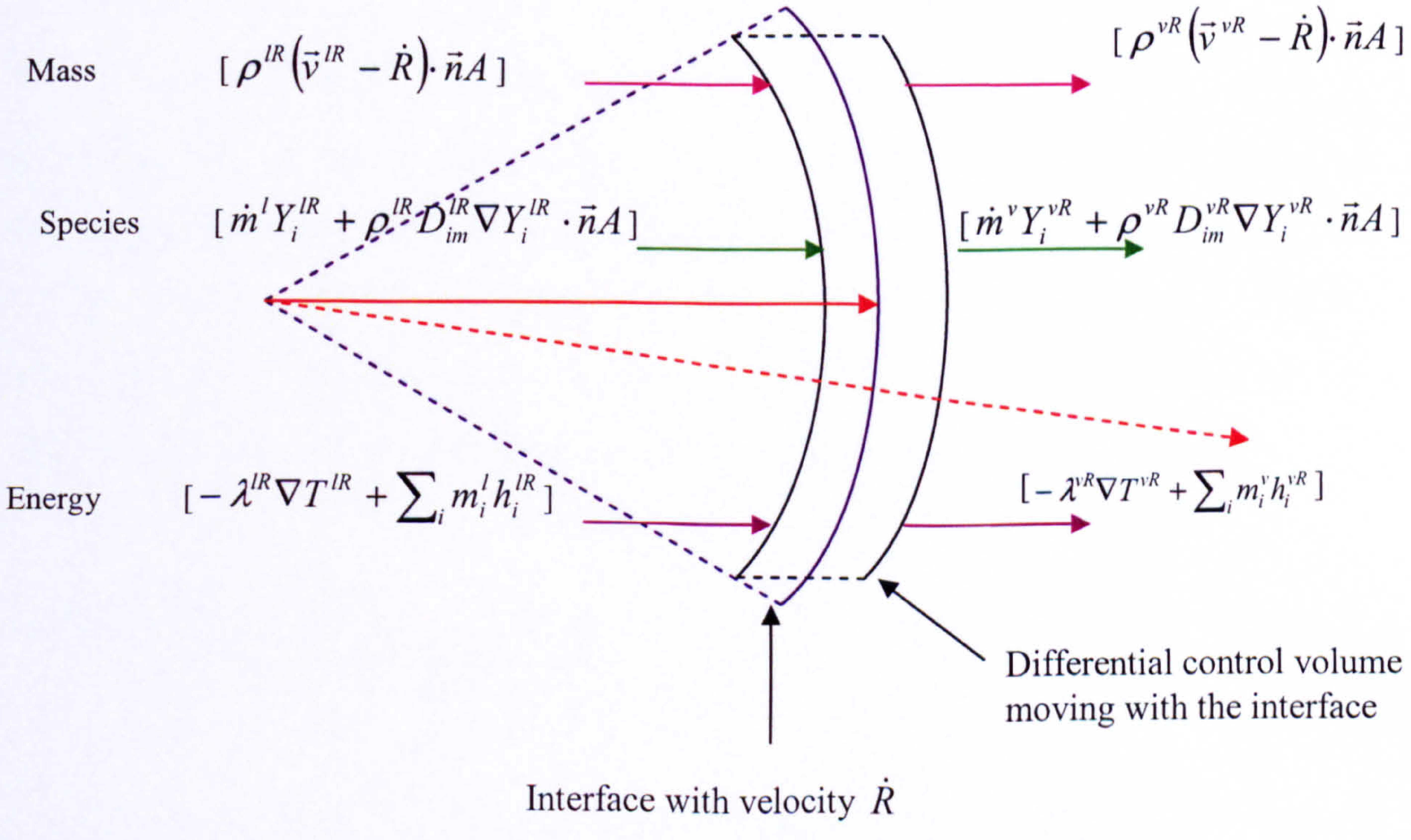

Figure 2.1 Boundary conditions at the droplet surface for mass continuity, species conservation and energy conservation.

Using the mass continuity relation, $r^2\rho^{lR}(v^{lR}-\dot{R})\big|_{R^-} = r^2\rho^{vR}(v^{vR}-\dot{R})\big|_{R^+} = \dot{m}/4\pi$, and assuming no gas penetrates into the droplet surface $(v^{vR}=0)$, the conservation of fuel mass fraction and energy yields the required $(N+1)$ nonlinear interface equations as (Williams, 1965; Torres et al, 2003):

$$\rho^{lR}(v^{lR}-\dot{R})(Y_i^{vR}-Y_i^{lR})+\rho^{lR}D_{im}^{l}\frac{\partial Y_i^l}{\partial r}\Big|_{r=R^-}-\rho^{vR}D_{ia}^{v}\frac{\partial Y_i^v}{\partial r}\Big|_{r=R^+}=0 \qquad (2-9)$$

$$\sum_i L_i^{lR}\rho^{lR}\left[\left(\dot{R}-v^{lR}\right)Y_i^{lR}+D_{im}^{l}\frac{\partial Y_i^l}{\partial r}\Big|_{r=R^-}\right]-\lambda^{lR}\frac{\partial T^l}{\partial r}\Big|_{r=R^-}+\lambda^{vR}\frac{\partial T^v}{\partial r}\Big|_{r=R^+}=0 \qquad (2-10)$$

In addition to the interface conservation conditions, thermodynamic and (material) phase equilibrium is assumed. This means that the temperatures, pressures, and chemical potentials (or fugacities) of each species both at the vapour side and the liquid side of the droplet must be equal, in symbols, these are respectively, $T^{vR}=T^{lR}$, $P^{vR}=P^{lR}$, and $\bar{\mu}_i^{vR}=\bar{\mu}_i^{lR}$. The equality of the chemical potentials, as will be shown in future chapters, is one central aspect of (multicomponent) droplet evaporation modelling, which through the use of equation of state yields the species mass fraction at the droplet surface. An extra interface condition can be formulated by solving for the surface regression rate through summing up equation $(2-9)$ for all fuel species and noting that the convective velocity of the ambient is zero at the droplet surface as:

$$\dot{R}=v^{lR}+\frac{\rho^{vR}}{\rho^{lR}}\left(\sum_i D_{ia}^{v}\frac{\partial Y_i^v}{\partial r}\Big|_{r=R^-}\Big/\varepsilon_i-Y_i^{lR}\right) \qquad (2-11)$$

where, $\varepsilon_i=\dot{m}_i/\dot{m}$ is the fractional mass flux. In addition to the boundary conditions at the interface, the spherical symmetric boundary conditions for the energy and species conservation at the droplet centre can be stated as $(\partial T/\partial r)\big|_{r=0}=0$ and $(\partial Y_i/\partial r)\big|_{r=0}=0$. The prescribed initial conditions inside the droplet $(t=0; r<R)$ for the liquid temperature, liquid fuel species mass fraction, and dissolved gas mass fraction, respectively, are T^{l0}, Y_i^{l0}, and Y_g^{l0}. If no dissolved gas in the liquid phase, $Y_g^{l0}=0$, it

is required $\sum_{l} Y_l^{l0} = 1$. For $t > 0$, depending on the model used (uniform or non-uniform temperature and composition assumption), the liquid temperature, liquid fuel mass fraction, and dissolved gas mass fraction, respectively, are designated by T^l, Y_l^l, and Y_g^l. All the above descriptions are standard ones, but such notations are limited to this section only to elucidate the background material. For the completeness of the discussion in this section however, description of variables is given after each equation. The thermotransport properties appearing in all equations are assumed to follow the methods described by Polling et al (2000). Therefore, assuming the thermotransport properties are determined, the unknown scalars in equations $(2-6)$-$(2-8)$ now can be solved subject to the initial and boundary conditions stated above.

The rest of this section is organised as follows. In §2.3.2, zero-dimensional models are reviewed, followed by 1D models in §2.3.3. For completeness, convection and distortion effects are discussed in §2.3.4. The distinction between isolated droplet models and models involving large numbers of droplets (like sprays, which are of practical importance) are described in §2.3.5. In order to elucidate the essential consideration of accurate thermotransport properties of the liquid and vapour phase modelling, the effects of variable mixture properties are discussed in §2.3.6. In relation to 0D and 1D models, effort is made to identify the most accurate and efficient numerical methods in §2.3.7. This is followed by general remarks in §2.4 that identify the shortcomings in the present models and pave the way for a new modelling strategy.

2.3.2 Zero-Dimensional (0D) Models

The 0D models, in general, assume a quasi-steady and spherically symmetric gas phase, while the temporal variation of the residual temperature and composition at the surface of the liquid drop is permitted. As such, all 0D models ignore the spatial treatment of the liquid phase. However, there are variants in these models. For example, the d^2-law, in effect, is a gas model, totally ignoring the temporal variations of the liquid phase, except its rate of surface regression (Spalding, 1953). As in most of the 0D models, the

d^2-law assumes fast gas-phase heat and mass transfer compared to the droplet surface regression, effectively reducing the gas phase as a steady state process in comparison. In a steady state condition, the vapour fuel mass conservation equation in a spherically symmetric condition takes the form $r^2 \rho^v v^v = \dot{m}/4\pi = const$, where the unknown $\dot{m}$ is the fuel vapour mass flow rate (evaporation rate). Similarly, the vapour fuel species equation $(2-9)$ together with the simplified form of the mass conservation equation yields:

$$\dot{m} = 4\pi \left(\int_R^{\infty} \frac{dr}{\rho^v D_{im}^v r^2} \right)^{-1} \left(\int_{Y_i^R}^{Y_i^{\infty}} \frac{dY_i^v}{\varepsilon_i - Y_i^v} \right) = 4\pi \left(\int_R^{\infty} \frac{dr}{\rho^v D_{im}^v r^2} \right)^{-1} \ell n(1 + B_M) \qquad (2-12)$$

In equation (2.12), the limit of integration ranges between values at the vapour side of the droplet surface to the far field values of the ambient condition. In the event there is fuel vapour at the far field, then $Y_i^{\infty} \neq 0$. Otherwise, $Y_i^{\infty} = 0$ although $Y_{gas}^v \neq 0$. Integration of equation $(2-12)$ yields the molar flux N (or the mass flux depending on the unit used to define ρ) of vaporisation. However, since most of the mathematical expressions in this chapter are used to recapitulate the standard formulations, the amount of matter will be only quantified in mass as opposed to in moles, and the mass flux is:

$$N = \frac{\rho^{R\infty} D_{im}^{R\infty}}{R} \ell n(1 + B_M) \qquad (2-13)$$

The reference thermotransport properties, which represent the average values between the integration limits are defined using the one-third rule of Yuen and Chen (1976) as $A^{R\infty} = A^R + (A^{\infty} - A^R)/3$, where A is either the temperature or species mass fraction. In $(2-12)$, the substitution $N = \dot{m}/4\pi R^2$ is used, while B_M takes the form:

$$B_M = \frac{Y_i^{vR} - Y_i^{v\infty}}{\varepsilon_i - Y_i^{vR}} \qquad (2-14)$$

In equation $(2-14)$, $Y_l^{vR} = Y_l^{vR}(T^{vR})$ is the vapour mass fraction at the vapour side of the droplet surface (^{vR}), which is a function of the droplet surface temperature. The value of Y_l^{vR} is computed by imposing (material) phase equilibrium condition. The fractional mass flux $\varepsilon_l = 1$ and $0 < \varepsilon_l < 1$ correspond to single component and multicomponent fuel conditions, respectively. Assuming equilibrium evaporation, where $\dot{m}^v = \dot{m}^l = 4\pi R^2 \dot{R} \rho^l$, which implies that the rate of liquid supply at the droplet surface is equal to the liquid to vapour conversion rate, equation $(2-11)$ along with equation $(2-13)$ takes the form:

$$\dot{R} = \frac{1}{\rho^l}\left(\frac{\rho^{R\infty} D_{im}^{R\infty}}{R} \ell n\left(1 + B_M\right)\right) = \frac{N}{\rho^l} \qquad (2-15)$$

The traditional form of the droplet regression rate described by equation (2.15) implies that the rate of liquid to mass conversion during evaporation is dependent on the amount of liquid fuel present alone. Godsave (1953) predicted that the plot of the square of the droplet diameter against time as $\left(dD_d^2/dt\right) = -\lambda_{evap} \rightarrow \dot{R} = \lambda_{evap}/8R$. In fact, the author relates the liquid mass loss to the evaporation constant , λ_{evap}, to compute the droplet life time as $\dot{m} = -\left(\rho^l \pi R/2\right)\lambda_{evap} \rightarrow N/\rho^l = \lambda_{evap}/8R$, where ρ^l is the average density of the liquid being converted to vapour. Since the model (Spalding, 1953; Godsave, 1953) predicts the square of the droplet diameter decreasing with time in a linear fashion, it is widely known as the d^2-Law. But, as will be shown in §4, equation $(2-15)$ is insufficient to describe both the composition evolution and the non-steady nature of the liquid mixture density for real fuels.

Similarly, the solution for the steady form of the energy equation $(2-8)$, where the effect of mass and heat diffusion are taking place independently and in a non-uniform manner, which is described by the non-unity Lewis number defined as $Le = \lambda/\rho D C p$, takes the form:

$$\dot{m}=4\pi\left(\int_{R}^{\infty}\frac{dr}{Le\rho^{v}D_{im}^{v}r^{2}}\right)^{-1}\left(\int_{T^{R}}^{T^{\infty}}\frac{CpdT}{CpT+\sum_{l}L_{l}}\right)=4\pi\left(\int_{R}^{\infty}\frac{dr}{Le\rho^{v}D_{im}^{v}r^{2}}\right)^{-1}\ell n(1+B_{T}) \quad (2-16)$$

In equation $(2-16)$, $\sum_{l}L_{l}=\sum_{l}m_{l}(h_{l}^{v}-h_{l}^{l})=L$ represents the latent heat of vaporisation, and the Spalding heat transfer number B_T, is defined as:

$$B_{T}=\frac{Cp^{R\infty}\left(T^{v\infty}-T^{vR}\right)}{L} \quad (2-17)$$

In equation $(2-17)$, $Cp^{R\infty}$ is the reference vapour specific heat capacity, $T^{v\infty}$ is the far field gas temperature and T^{vR} is the droplet surface temperature, which is essentially non-uniform for fuels with multiple boiling points.

The d^2-law had been a subject of extensive research, both experimentally and theoretically. For example, Kumagi and co-workers (Kumagai and Isoda, 1957; Kumagai et al, 1971; Okajima and Kumagai, 1974), removed buoyancy effects for the first time by conducting their experiment in a free falling chamber. In their seminal experiment, an unsteady combustion was observed, and the effect was attributed to unsteady gas-phase transport. These studies progressively relaxed the assumptions and conditions in the classical model and extended the situation for a wider range of applications.

Law (1976a) examined Kumagi and co-workers' experimental data, and suggested that the unsteady combustion phenomena could also be due to additional transient process in the liquid phase. The author stipulates that the exceptionally slow initial burning rate that was observed in previous experiments (Waldman, 1974) is due to a large amount of sensible heat required to heat the droplet. This sensible heat accounts for the heating of the droplet to bring its temperature from the initial value to the final steady-state vaporisation.

Law (1976b) generalised the observation in droplet heating by proposing two droplet evaporation models with distinctive assumptions. The droplet considered was a binary fuel composed of heptanes and octane, to observe the effects of composition in the mode of vaporisation and combustion. In the first, rapid-mixing model, the author assumed the mixture to behave ideally in its phase change characteristics, and the liquid composition and temperature to be spatially uniform, but vary temporally. The rapid-mixing model is a relaxation of the d^2 - law model. Its basic assumption being that the heat transfer rate within the droplet is much faster than the rate at which the average droplet temperature increases, but much slower than the gas phase transport rate. The first assumption is equivalent to saying that the droplet temperature is spatially uniform but temporally varying. The second assumption implies the gas phase process to be quasi-steady, provided the process is in a sub-critical condition.

The results of the rapid mixing model revealed two distinct slopes on the D_d^2 versus time plot. The two slopes, corresponding to each of the binary fuels, indicated the vaporisation to follow the relative volatility of the fuel mixtures considered. In the shell-model, however, the fuel components respond to temperature and diffusion effects to arrange themselves in a shell, so that a quasi-steady type single component vaporisation prevails within each shell. However, evaporation data that involve compositional variation were not available to validate their model. Nevertheless, both models (the rapid mixing and shell models) predict closely the same bulk evaporated mass and vaporisation time, while the rapid-mixing model compares favourably with the experimental droplet temperature profile of El Wakil et al (1956). Although the droplet regression rate resembles the experimental data, there were significant variations between the measured and predicted temperature profiles at the droplet centre, at the droplet surface, and the residual surface temperature. This was attributed by the author as the manifestation of the uniform temperature limit assumption in the rapid-mixing model, which is solely based on the stipulation that the rapid internal liquid circulation is a consequence of the shear stresses on the liquid phase due to convection. However, Sirignano (1978) showed that even in the limit of high vortex strength, the internal liquid circulation can only reduce the characteristic length scale for diffusion by an order of magnitude. As such, the rapid mixing limit can never exist. Rather, the uniform temperature assumption is associated with the infinite conductivity limit, and hence the model is called the infinite conductivity model. Interestingly enough, at low Reynolds number, the infinite conductivity (0D) model was found superior to the conduction limit (1D) model (Law and Sirignano, 1977). This is, of course, contrary to the common belief that higher dimensional models are more accurate than their low dimensional counterparts. The superiority of the infinite conductivity model is due to the absence of liquid mixing at low Reynolds number, which is highly influenced by the turbulent intensity of the carrier phase. At high Reynolds number, however, the internal circulation in the form of a spherical-vortical core motion is responsible for much of the mixing and liquid heating and subsequent vaporisation. In the infinite conductivity model, most of the d^2- law relations remains the same, except the latent heat of vaporisation L, where its value in equations $(2-10)$, $(2-16)$, and $(2-17)$ must be modified (Aggarwal et al, 1984) as:

$$L_{eff} = L + Cp^l\left(T^{vR} - T^{l0}\right) = \sum_l \dot{m}_l(h_l^v - h_l^l) + \left(\frac{\rho^{vR} R Cp^l}{3N}\right)\frac{dT^l}{dt} \qquad (2-18)$$

In many practical situations, droplets vaporise in a convective gas field, where the gas phase convection influences the heat and mass transfer process in at least two ways. First, it increases the gasification rate as well as the heat transfer rate between the phases. Second, it generates liquid circulation inside the droplet, which increases the liquid heat and mass transfer rate. In fact, the effect of convection in droplet heating and vaporisation was well known, even before the development of the classical model itself (Ranz and Marshall, 1952).

The Ranz-Marshall semi-empirical correlation accounts for gas phase convection by expressing the vaporisation and inter-phase heat-transfer rates as modifications to the spherically symmetric assumption. Although this semi-empirical correlation is in a very simple form, there is little theoretical justification about its empiricism, and the correlation is based on experiments conducted on porous spheres under quasi-steady conditions. The accuracy of the correlation is therefore far from correcting the spherical symmetry assumption that reduces the complication arising due to the convective effects of the ambient gas on the droplet surface at the stagnation, shoulder, and wake regions. In addition, the range of applicability of the Ranz-Marshall correlation is limited to low Reynolds numbers (Sirignano, 1999). To this end, the Clift et al (1978) correlation has proved useful for practical spray applications (Abramzon and Sirignano, 1989), where the high Reynolds number flow creates convective and distortion effects. Such convective and distortion effects during droplet evaporation are discussed in § 2.3.4.

2.3.3 One-Dimensional (1D) Models

The majority of 1D droplet evaporation models widely in use today are either developed, or further refined by Sirignano and co-workers (Law and Sirignano, 1977; Abramzon and Sirignano, 1989; Sirignano, 1983, 1993, 1999). The models serve as compromises between the more accurate but computationally complex higher dimensional (2D and 3D) models, and the simple but less accurate 0D models, for their computational accuracy and efficiency.

The earliest documented 1D-models were carried out for hypergolic fuels (Saad and Antonides, 1975), and for fossil fuels (Hubbard et al, 1975). Saad and Antonides (1975) studied the behaviour of temperature distribution and internal heating for a small hypergolic spherical droplet composed of an exothermically reacting liquid, with uniform heat of reaction and no internal circulation. The problem was treated as a 1D transient conduction equation, but with heat generated inside the droplet. The heat generated inside the droplet was therefore responsible for the liquid vaporisation process at its surface.

For fossil fuels, however, evaporation occurs due to an external heat source (like a hot gas stream) exceeding the fuel wet-bulb temperature. To that end, Hubbard et al (1975) developed a 1D single component droplet evaporation model, with gas phase transients and variable mixture properties. The authors describe the liquid phase evolution by the

1D transient species and heat conduction equations $(2-7)$ and $(2-8)$, respectively. The gas-vapour mixture thermotransport properties are estimated using the 1/3–rule (Sparrow and Gregg, 1957). The radial pressure drop is shown to have negligible effect, both in the vapour phase and liquid phase. The model prediction was encouraging. In particular, the model was one step ahead of its time as it employs transient liquid phase modelling and variable thermotransport properties.

Independently, Law and Sirignano (1977) developed a similar model to that of Hubbard et al (1975), but with constant thermotransport properties and including combustion. The Law and Sirignano model, widely known as the conduction limit model, is one of the most accurate 1D-models for fuel evaporation and combustion simulation. However, its extension to multicomponent fuels is limited, at most, to binary fuels. To that end, Kneer et al (1993) considered a hexane/tetradecane mixture at gas turbine operating conditions, and showed the effects of variable mixture property, liquid temperature and concentration profiles on the evaporation process. These findings, although considering only binary fuels, can serve as a testament that real fuels have to be treated using a suitable multicomponent droplet evaporation model.

Motivated by the works of Hubbard et al (1975), a comprehensive and robust model was developed by Abramzon and Sirignano (1989). The effective conductivity model of Abramzon and Sirignano (1989), however, was a significant improvement from all known 1D models. The treatment of the liquid phase is based on a spherically symmetric pseudo-temperature field that was solved using the heat diffusion equation, by introducing an effective conductivity coefficient. The effective conductivity coefficients are determined by fitting values from the numerical results of Johns and Beckman (1966) for mass transfer between a droplet with internal circulation and a moving immiscible liquid. In the vapour phase, it employs the film theory (Bird et al, 1960). The film theory approximates the resistance of heat or mass exchange between a surface and a gas flow as a gas film of constant thickness. The thermal and diffusional film thickness values, however, can be affected by the presence of Stefan flow (blowing). The effective conductivity model incorporates many physical effects as in the detailed axi-symmetric models and it is computationally efficient. These effects include variable physical property, non-unity Lewis number in the gas phase, the influence of Stefan flow on the heat and mass transport, and the effect of the transient liquid heating inside the circulating liquid core. The model treats the evaporating droplet dynamics by introducing a drag correction coefficient, which is a strong function of the Spalding transfer number. The model also determines the mixture thermotransport properties by employing the one-third rule of Yuen and Chen (1976).

As in most 1D models, the effective conductivity model assumes uniform temperature and uniform fuel vapour distribution along the droplet surface. Using film theory analysis, knowledge of the instantaneous heat transferred into the liquid-phase will allow prediction of the temperature inside the droplet as a function of time. The difference between the first type (Hubbard et al, 1975) and the second type (Law and Sirignano, 1977) 1D models is very minor, conceptually. However, the main difference lies in the treatment of the gas-vapour mixture in the mixing layer. The third type of model (Abramzon and Sirignano, 1989), however, was conceptually different from the other two. In particular, the liquid circulation, which is the rate controlling process in highly convective and relatively high temperature ambient conditions, is accounted for by employing an empirical correlation of the effective conductivity/diffusivity coefficient. As such, the effective conductivity model is widely used for practical applications as the treatment of the droplet heating and evaporation in the dispersed phase is the rate controlling mechanism in the prediction of the mixing and combustion processes. However, although highly convective flows directly influence the evaporation through the liquid internal circulation and blowing effect, it might also lead to the distortion of droplets, which could affect the evaporation process significantly. To that end, a brief review on the combined effect of convection and distoration is discussed in the section to follow.

2.3.4 Convection and Distortion Effects

For a spherically symmetric evaporating droplet in a stagnant ambient condition, which includes both the 0D and 1D models described earlier, the non-dimensional heat and mass transfer rates can be described using the Nusselt, Nu, and Sherwood, Sh, numbers by using the heat transfer coefficient h_T, and the mass transfer coefficients h_M, respectively as:

$$Nu = 2\frac{h_T R}{\lambda} = 2\frac{\ell n(1+B_T)}{B_T} \qquad ; \qquad Sh = 2\frac{h_M R}{\rho D} = 2\frac{\ell n\,(1+B_M)}{B_M} \qquad (2-19)$$

Note that in equation $(2-19)$, the heat and mass transfer coefficients are calculated based on the diameter $D_d = 2R$ of the gas film, while the term that accounts for the dependence on the Spalding transfer number is traditionally expressed in the form $(1+B_M)$ instead of the $\ell n\,(1+B_M)/B_M$ presented in $(2-19)$, and will be explained in subsequent sections. Nevertheless, it is important to point out that when all the binary diffusion coefficients are identical, the Sherwood numbers for each species takes the same value, and hence, $Nu = Sh \rightarrow Le = 1$, with constant thermotransport properties.

It is interesting to observe that equation $(2-19)$ provides the classical heated-sphere result, $Nu = Sh = 2$, for the non-vaporising limit in which $B_M = B_T \rightarrow 0$. However, for a droplet vaporising in non-stagnant flow, the Nusselt and Sherwood numbers require corrections to account for the loss in spherical symmetry due to the convective ambient condition. Traditionally, although very similar, two forms of empirical correlations are used to correct these departures. The Frossling (1938), as well as the Ranz and Marshall (1952) correlations are commonly used to account for droplet evaporation in convective environments, which takes the form:

$$(Nu \quad or \quad Sh) = 2 + a.\mathrm{Re}^{1/2}(\mathrm{Pr} \quad or \quad Sc)^{1/3} \qquad (2-20)$$

In equation $(2-20)$, the ambient Reynolds number is in the range $10 < \mathrm{Re} < 1800$, and $a = 0.555$ for Frossling while $a = 0.6$ for Ranz and Marshall correlations. However, motivated by the works of Acrivos and Taylor (1962) that identified the strong coupling between the non-dimensional mass transfer rate and the ranges of the Reynolds number to be used, Faeth (1977) proposed a correlation of the form:

$$(Nu \quad or \quad Sh) = (2 + f(Re, (Pr \quad or \quad Sc)))\frac{\ell n\,(1+B_M)}{B_M} \qquad (2-21)$$

The functional form $f(Re, (Pr \cdot Sc))$ is determined by fitting experimental data, and takes the form:

$$(Nu \quad or \quad Sh) = \left[2 + \frac{0.555\,\mathrm{Re}^{1/2}\,(\mathrm{Pr} \quad or \quad Sc)^{1/3}}{\sqrt{1+(1.232/\mathrm{Re}(\mathrm{Pr} \quad or \quad Sc)^{4/3})}}\right]\frac{\ln\,(1+B_M)}{B_M} \qquad (2-22)$$

However, there is an ambiguity regarding which form, weather the traditional $(1+B_M)$ or the $\ell n\,(1+B_M)/B_M$, of the term that accounts for the Spalding transfer number is suitable to achieve the correct asymptotic behaviour both at very low and very high rate of vaporisation, with a range of Reynolds numbers. At moderate Reynolds numbers, it is easy to observe that the $\ell n\,(1+B_M)/B_M$ expression yield the correct asymptotic behaviour. At very high vaporisation and in particular a very high Reynolds number, such analysis is not very obvious. The direct consequence from equations $(2-20)$-$(2-22)$, just ignoring terms with the mass transfer number B_M, suggests that an increase in the droplet Reynolds number will lead to increased rate of heat and mass transfer, thereby increasing the vaporisation and reducing the droplet life time. But, In the event the mass transfer number is very large (without considering the effect of the Reynolds number), the use of the $(1+B_M)$ term implies unbounded mass or heat flux while the use of the $\ell n\,(1+B_M)/B_M$ term implies no mass or heat flux, which are not realisable due to the supply of mass due to the limit of the boiling point at the droplet surface. In order to understand the issue in detail, it is imperative to see the historical developments of the above correlations.

Although the empirical correlations (Frossling, 1938; Ranz and Marshal, 1952) are widely used in the literature, these experiments were conducted on a wetted-porous sphere, which is highly distinctive and different from a vaporising droplet, particularly at high Reynolds number. The heat and mass transfer of a vaporising droplet at higher Reynolds number is affected by the internal circulation of the liquid core that controls the mixing and evaporation process. But, this is absent in the wetted-porous sphere case. Of course, for a slowly moving droplet, the internal circulation is not dominant, and the droplet lifetime assumes a larger value compared to the characteristic time of the liquid phase transport. Hence, the liquid diffusivity can be assumed to approach infinity as the gradients of the liquid phase scalars (temperature, species concentration) vanish. Therefore, care should be taken in using these old empirical correlations (Frossling, 1938; Ranz and Marshal, 1952). It is not recommended, for example - to use the experimental results of wetted-porous spheres or droplets vaporising at low temperature and low Reynolds number for gas turbine applications. In addition, the correlation proposed by Faeth (1977) becomes questionable when applied for the case of a droplet immersed in a hot and low convective environment experiencing very high evaporation, where the asymptotics yields $\ell n\,(1+B_M)/B_M \rightarrow 0$. But, for highly evaporative droplet in very high convective ambient condition, the asymptotic behaviour of equations $(2-21)$ or $(2-22)$ will be influenced by the relative strength of the Reynolds number as $(Nu \quad or \quad Sh) \rightarrow \sqrt{Re}/(1+B_M)$.

It is interesting to note that the $\ell n(1+B_M)$ term in equation $(2-13)$ results from the spherically symmetric, quiescent vaporising droplet, where the value of B_M does not vary greatly for single component hydrocarbons. However, this dependence has never been tested for highly convective evaporation. In addition, Sirignano (1978) has shown that the natural logarithm functional dependence on the transfer number B_M to be incorrect and can, especially in highly convective unsteady situation, produce serious errors. The $\ell n(1+B_M)$ dependence simply cannot apply when a convective boundary layer exists over the droplet. For this reason, droplet vaporisation with slip in high-temperature convective environments became necessary, when at best the droplet assumes an axi-symmetric situation. However, such models proved computationally expensive, and the uncertainty on the natural logarithm functional dependence remains at large, with far reaching consequences. For example, the contribution of the Spalding transfer number either as $\ell n(1+B_M)$ or $\ell n\,(1+B_M)/B_M$ term is not limited only to heat and mass transfer alone, affecting directly the dynamics and size of the droplet through the drag coefficient. To that end, Yuen and Chen (1976) showed that particle drag is affected by droplet evaporation in two different ways. First, the temperature and concentration gradients, between the droplet surface and the ambient, causes substantial reduction in the absolute viscosity of the gas, which decreases friction drag. Second, evaporation affects the boundary layer surrounding the droplet. This blowing effect reduces friction-drag and increases form-drag. At low Reynolds number, the droplet drag coefficient is close to that for a solid sphere of the same diameter. However, at high convective flows the heat, mass and momentum transfer of a vaporising droplet manifests much more complex phenomena than its solid counterpart. For example, a decrease in viscous drag (due to blowing) is accompanied by an increase in pressure drag of similar magnitude. In order to account for both variable properties and blowing effects, large numbers of steady-state correlations for drag as well as heat and mass transfer have been proposed (Yuen and Chen, 1976; Renksizbulut and Yuen, 1983; Chiang et al, 1992). The appropriate Reynolds number that is used to compute the drag coefficient from the standard curve for a sphere is then based on the one-third rule for viscosity. The drag coefficient is responsible for the relative motion of the droplet, causing distortion.

Unfortunately, most of the vaporisation models in the literature, including those that account for liquid core circulation do not include the effects of distortion. It is evident to observe that droplet distortion increases the effective surface area available for evaporation, and subsequently increases the area-to-volume ratio of the drop. To that end, the only inclusion of the distortion effects on vaporisation on the non-dimensional heat and mass transfer coefficients, to the author's knowledge, is a study by Arcoumanis et al (1997) in diesel spray applications, which takes of the form:

$$(Nu \quad or \quad Sh) = (2 + 0.085\,Re^{0.804}(Pr \quad or \quad Sc)^{1/3})\frac{\ell n\,(1+B_M)}{B_M} \tag{2-23}$$

Note that the modification on the Reynolds number is based on the equivalent diameter of a spheroid corresponding to a diesel spray flow condition, which is reported as highly convective with significantly high pressure. From the results presented, it seems that the inclusion of the distortion in the evaporation model has a far more dramatic effect on vaporisation than, for example, accurate calculation for the internal temperature distribution. On the other hand, previous detailed numerical study of an evaporating and deforming droplet by Haywood et al (1994) suggests that the internal circulation tends to form the drop into a prolate[1] spheroid, and not an oblate spheroid as would be expected. These authors, however, didn't investigate the distortion effect on the Reynolds number, although their numerical study agrees well with the experimental observation of Renksizbulut and Yuen (1983), provided volume equivalent diameter is used. Therefore, models that do not account for distortion effects introduce further error by under-predicting the evaporation rate. The treatment of stability analysis in spray break-up is beyond the scope of this study, and yet, the comment on the limitations described earlier must be an issue to be dealt with.

2.3.5 Multiple Droplets and Sprays

In the majority of droplet evaporation studies, the analysis is focused on an isolated droplet. However, practical sprays contain tens and hundreds of millions of droplets, with the average distance between droplets as low as a few droplet diameters. In such situations, the isolated droplet assumptions will be lost, with considerable influence from neighbouring and/or all droplets in the spray. To this end, Sirignano (1983) classified interactive droplet studies in three categories: droplet arrays, droplet groups, and sprays. The description of the detailed flow and transport process and the associated configuration in each category is beyond the scope of this work. In addition, except for the spray that exists in most practical applications, the other two categories are more or less artefacts that are proved to be very useful for modelling purposes, both theoretical/numerical and physical/experimental. This is due to the fact that certain regimes of flow and transport situations are better explained by employing the modelling assumptions of one or a combination of these categories.

To understand the basis of the distinction, consider a cloud of droplets occupying a certain volume. In this volume, define *the primary ambient-gas conditions* as the

---

[1] A prolate spheroid has the longest axis aligned with the external flow direction, while an oblate spheroid has the shortest axis aligned to the external flow direction.

conditions of the gas surrounding the cloud of droplets, where each droplet in the cloud is in turn surrounded by a gas film. In addition, define the *local ambient-gas condition* as the property of the gas at the edge of the gas film, but within the volume of the cloud. The condition violates the isolated droplet assumption in the event there is an overlap between the gas films of neighbouring droplets in the cloud. During such an overlap, the local ambient condition must assume a different value (like, an average).

As such, Sirignano (1983) identified three distinctive physical phenomena that are associated with the three categories, namely droplet arrays, droplet groups, and sprays. The first possible phenomenon refers to the effect of the droplets on the primary ambient-gas condition. As opposed to the isolated droplet[2] case, the primary ambient-gas shows strong coupling with the local ambient-gas and the liquid phase properties. The second phenomenon is on the direct influence of individual droplets heat and mass transfer interaction on the local ambient-gas condition, which also influences the vaporisation rate. The third phenomenon refers to the geometry and scale of the diffusion field surrounding each individual droplet. It is conjectured (Sirignano, 1999) that by decreasing the spacing between droplets, an increase in local ambient fuel-vapour concentration and a decrease in local ambient temperature is possible. This by itself implies a tendency to decrease the heat and mass transfer rates. In such a situation, a decrease in droplet spacing should result in a decrease in gas diffusion length-scale. Because, the surface area through which diffusion occurs would be proportional to the square of the characteristic diffusion length in the gas film (r_c), while the diffusion rate per unit surface area is inversely proportional to r_c. It follows that a decrease in droplet spacing results in low transfer and vaporisation rates. Effectively, the second and the third phenomena would yield the same qualitative effect when the spacing between droplets (droplet number density) is varied, except the configuration of droplets (distribution) affects the quantitative response. However, spray theory is highly differentiated from both droplet array theory and droplet group theory in that full coupling of primary ambient-gas, local ambient-gas, and liquid droplet properties is considered. Average gas properties are evaluated using primary and local conditions,

---

[2] In the isolated droplet case, it is assumed that the properties in the liquid phase and the gas film surrounding the droplet do not affect the primary ambient-gas condition.

whereas the droplet cloud and its properties are described using statistical means. The first and second phenomena are treated and analysed. However, the dependence of heat or mass transfer coefficients on droplet spacing, which is typical of the third phenomenon, has never been investigated. In addition, significant radiation heat transfer between droplets separated by as much as ten-diameter or greater is reported (Sirignano, 1999), further complicating the earlier phenomenological descriptions. However, the isolated droplet model remains the basic building block to understand the complex dynamics and evaporation of practical sprays.

2.3.6 Effects of Variable Thermotransport Properties

Accurate prediction of the thermotransport properties is an essential part of modelling droplet evaporation and combustion phenomena, as the evolution of the vapour-gas mixture directly influences the liquid mixture's response to the ambient, and subsequently the evaporation, mixing and combustion process. In particular, for mixtures composed of a large number of components, like real fuels, accurate prediction of the thermotransport properties, which represent all the properties of the constituent species, is vital.

Developing prediction methods for mixture thermotransport properties is a subject of an intensive research by its own right, and multitudes of methods have been proposed and applied successfully over the years (Polling et al, 2000). Most of these methods in general estimate the thermotransport properties by using polynomials as strong functions of temperature and composition, and in some instances with pressure.

However, most of the droplet evaporation models which are in use today assume constant values for the latent heat, specific heat, thermal conductivity, diffusion coefficient, viscosity, and density, both for the liquid and vapour phase. In particular, theSchmidt numbers ($Sc = \mu/\rho D$) and the Prandtl ($\Pr = \mu Cp/\lambda$) numbers are taken as identical constants, resulting in unity Lewis number. But, the assumption of unity Lewis number implies equal mass and heat diffusion in a flow field less dominated by convective effects. But, in most convective conditions, the mass diffusion is most likely two-orders of magnitude slower than the thermal diffusion, and the unity Lewis number assumption may not be justified.

For example, Kneer et al (1993) investigated the importance of variable liquid properties on droplet evaporation. The authors found that vaporisation is highly affected by the dependence of liquid properties on temperature and composition. In particular, variable liquid diffusion coefficient controls the relative thermal and mass diffusion, and in turn, the rate of evaporation. Therefore, in order to rectify such inaccuracies, accurate prediction of the thermotransport properties is essential. To that end, a significant part of this thesis will involve the development and validation of predictive methods for the variable thermotransport properties of real fuels (mixtures) by modifying the most widely used methods in the literature (Polling et al, 2000).

2.3.7 Numerical and Computational Issues

One of the most important aspects of droplet evaporation modelling is the development and implementation of accurate numerical methods with relatively high computational efficiency. In practical applications, where the number of droplets is very large (like in sprays), resolving the dynamics and evaporation process could be complicated, and as a result computationally expensive. The droplet heating and evaporation sub-models are, in most situations, very time consuming due to the stiffness of the heat and mass transport time scales. The numerical issues for the higher dimensional models (2D and 3D) are beyond the scope of this work. Rather, great emphasis is given to the 0D and 1D models, which are the case in point for this thesis.

In general, the governing equations for 0D liquid models are ODEs, while for 1D liquid models are PDEs. There are a number of accurate and efficient open-source ODE solvers with various advanced functionality suitable to solve droplet heat and mass transfer (Hindsmarsh, 1983). For example, ODE solvers with automatic time-stepping and a successive error estimation facility can improve both the accuracy and efficiency of the models. However, while employing 1D droplet evaporation models, due to the addition of the spatial resolution, the computational process can be highly complicated. Especially, with the regressing surface (moving boundary) that also involves phase transition, the problem becomes a convection-diffusion type equation with a sharp phase boundary, which is much more difficult to solve. In most situations, implicit methods with uniform spatial grids are employed, where the convective term, which is always positive for evaporation, is approximated using upwind schemes (Sirignano, 1999). But the mathematical models are too complicated to allow an exact evaluation of the error introduced and to estimate the numerical accuracy. Rather, only a few key points are identified to minimise the inaccuracies. For example, a dynamically self-adjusting time step would improve the numerical efficiency. Although the solution is practically independent of time steps, care should be taken to ensure numerical stability. However, the treatment of the space grid size and its spatial location relative to the evolution of the solution variables affects the numerical accuracy, mainly due to numerical diffusion. For example, Sirignano (2003) pointed out the importance of incorporating adaptive mesh refinement (AMR) like techniques to circumvent the problem in the accuracy and computational efficiency of practical spray evaporation and combustion models, as a matter of current research topic. This is described in §5.

2.4 General Remarks

The review has demonstrated the existence of an extensive body of literature dedicated to the dynamics and evaporation of droplets, droplet arrays, droplet groups, and sprays. It is evident that isolated droplet dynamics and single-component evaporation models are well understood. However, many issues of practical importance that are related to multicomponent systems remain unanswered, and the quest for better understanding is an active area of research.

Most of the effort in recent years is focused in extending the existing and widely tested single component models for real fuels, by incorporating accurate estimation of variable thermotransport properties, turbulence coupling, and unsteady drag considerations (Aggarwal, 1987; Chiang et al, 1992; Kneer et al, 1993; Berlemont et al, 1995; Chang and Yang, 1999). In addition, the systematic identification of the inherent limitations of the most widely used models for further improvement is an ongoing activity.

Dimension Class	**Model Name**	**Single Component**		**Multicomponent**	
		Model	Contributor(s)	Model	Contributor(s)
0D	D^2-Law	**M1**	Spalding (1953)	**M1***	Law & Law (1977)
	Infinite Conductivity	**M2**	Law (1976a)	**M2***	Law (1976b)
1D	Conduction Limit	**M3**	Law & Sirignano (1977)	**M3***	Law & Sirignano (1977)
	Vortex	**M4**	Tong & Sirignano (1982b)	**M4***	Tong & Sirignano (1986b)
	Effective Conductivity	**M5**	Abramzon & Sirignano (1989)	**M5***	Delplanque et al (1991)

Table 2.1. Dimensional classification of the most widely used droplet evaporation models.

For example, Aggarwal et al (1984) evaluated four evaporation models (M1, M2, M3, and M4 in Table 2.1) for stochastic spray simulations. The investigation was carried out using the isolated droplet models both in stagnant and convective high temperature environments. The first three models were used to study the evaporation behaviour in stagnant conditions, and subsequent comparisons show a wide discrepancy between these models. For model M1, droplet surface temperature remains at the wet-bulb temperature of the fuel and serves as an asymptote for models M2 and M3. Since model M1 excludes the droplet heating, vaporisation starts quicker, and faster vaporisation rate is predicted compared to models M2 and M3, which show close resemblance to each other except at the droplet surface temperature. The influence of the uniform liquid temperature assumption of model M2 was evident on the surface temperature, where it increases per unit of energy absorbed, but less than was predicted by model M3. It is important to note that accurate prediction of the surface temperature is essential to determine the correct heat transfer to the liquid and to estimate the species mass fraction at the droplet surface. The prediction by model M1 was very poor, and it was discarded for the rest of the investigation. Therefore, only models M2, M3, and M4 are used for vaporisation in convective conditions. The prediction of model M4 lies between model M2 and Model M3. The percentage variation of the droplet lifetime was found very sensitive to the liquid models used. In particular, the evaporation of heavy fuels in low Reynolds number flow conditions, predicted by model M4 and M2 show high resemblance. As expected, the Ranz-Marshall correlation (Ranz and Marshall, 1952) over predicts the rate of vaporisation and under-predicts the droplet surface temperature, confirming its unsuitability.

Aggarwal et al (1984) applied models M1, M2, M3, and M4 for spray simulation, where stochastic methods are used to capture the overall behaviour of the individual droplets. When the three models (M2, M3, and M4) are used, the choice of the liquid heating model significantly affects the bulk spray (liquid) and gas properties. However, the prediction of the droplet surface temperature, the surface regression rate, and the evaporation rate are qualitatively similar to the predictions of the isolated droplet in convective environment. In general, models M1, M2, and the Ranz-Marshall correlation were found unsuitable for practical applications, although no validation against experimental data was carried out. The study recommends that model M3 be used for situations involving transient heating and very small relative velocity. For practical applications however, where high values for the relative velocity, Reynolds number, and temperatures are considered, the authors recommend the use of model M4.

Nevertheless, the works of Aggarwal et al (1984) did not give any conclusive result due to the fact that the evaporation models were compared between each other, rather than comparing either with experimental data or with more detailed non-equilibrium evaporation models, like those proposed by Bellan and Sommerfeld (1978). In fact, comparing models of increasing complexity, while using the same equilibrium evaporation models, becomes a heuristic means of model performance evaluation, with few exceptions (Chen et al, 1997; Miller et al, 1998). It should be emphasised that comparing different equilibrium vaporisation models cannot distinguish the limitations due to the non-equilibrium evaporation process that happens in real situations. An excellent review on models that utilise equilibrium evaporation was given by Aggarwal and Peng (1995). In fact, such equilibrium models were applied to model an advanced spray model for gas turbine combustion applications with limited success (Tolpadi et al, 2000). Therefore, the need for better (accurate and computationally efficient) models that are tested against realistic situations is very evident. Recently, two exceptions that employ experimental data to verify the validity of theoretical droplet evaporation models were presented by Chen et al (1997) and Miller et al (1998), and yet no real fuel was employed in these validations.

While investigating the evaporation behaviour of fuels under relatively low temperatures experimentally, Chen et al (1997) also compared the performance of different (single and multicomponent) models against their experiment. Models M1, M2, M3, M1*, M2*, and M3* were compared against experimental data. At low temperature, the droplet gasification rate is slow and the droplet heat up time could be comparable with the droplet lifetime, emphasising the importance of the liquid transient process. Both single component (hexane or decane) and multicomponent (hexane and decane mixture) fuels were employed. Unlike the conclusions made by Aggarwal et al (1984), however, the predictions of models M1, M2, and M3 for a hexane droplet were indistinguishable, all providing good agreement with the experimental data. However, the prediction for decane was sensitive to the model used, where model M2 shows superiority over models M1 and M3. Model M1 under-predicts both the rate of gasification (particularly at the start) and the droplet lifetime.

For the hexane/decane mixture, the predictions of models M2* and M3* were good, while model M1* does not feature favourably. In fact, the prediction by model M2* was quite accurate compared to the experimental data, which shows batch distillation of binary fuels. This implies that at relatively low temperature, where the energy transfer in the liquid phase is not significant, the spatially uniform assumption seem appropriate. In such situations, 0D models could be more accurate than 1D models. However, an interesting observation was made due to a slight change in the droplet diameter ($D_{d0} = 69\mu m \rightarrow 68\mu m$). When the droplet diameter is decreased, significant improvement to the prediction of model M1* was observed, while the predictions by models M2* and M3* deteriorate, although the relative magnitude remains the same. In addition, the component mass fraction at the droplet surface predicted by models M2* and M3* show significant differences. But, there was no composition measurement to quantify the departure between each model. Moreover, the temperature predictions at the droplet surface by models M2* and M3* were affected due to the change in the liquid composition on the droplet surface. In fact, the liquid composition has a more dominant effect on the value of the composition at the droplet surface, and as such the diffusion limit model under-predicts the vaporisation rate compared to the infinite conductivity model. Such behaviour needs further investigation, particularly with temperature and pressure ranges of practical applications.

On the other hand, Miller et al (1998) compared eight evaporation models: two versions of the transient classical model, four heat and mass transfer analogy models, and two non-equilibrium models (Bellan and Sommerfeld; 1978). The model predictions in the works of Miller et al (1998) are in turn compared with experimental results for water, benzene, decane, heptane, and hexane vaporising droplets at low, moderate, and high temperature quiescent and convective air. For gas temperatures at and above the boiling point of the droplets considered, and with an increase in relative velocity, large deviation between model prediction and experimental result is observed (Miller et al, 1998). In particular, when the initial droplet diameter is $< 50\,\mu m$, like that of the droplet size usually encountered in gas turbines, the non-equilibrium models show superiority over the other models. This indicates two interesting situations in the application of multicomponent droplet evaporation for gas turbine applications.

The first one is the detailed process of evaporation. For example, in multicomponent fuels, the fuel is initially heated as it flows inside the combustor until its temperature exceeds the boiling temperature of the lightest component. The flow then changes into continuously increasing vapour / liquid ratio, and yet, with further heating of the remaining heavier fuel components. The change in the chemical composition of the liquid and gaseous-phase is due to the continuous change in fractional gasification and liquid diffusivity. However, when the fuel temperature reaches the boiling temperature of the heaviest component, all the fuel is converted into vapour. This interesting process implies that fuel components lighter than the heaviest component undergo supercritical gasification, which is not governed by the droplet evaporation models discussed earlier.

The observations in the work of Miller et al (1998) suggest that droplet sizes that are used in practical combustion application are one order of magnitude less than those used in laboratory application. Their result confirms that for practical applications, the non-equilibrium droplet evaporation models are more suitable than the equilibrium evaporation models. The requirement to develop comprehensive models that can capture the physical process in real fuels, based on non-equilibrium theory, is hence a valid argument.

Therefore, although droplet evaporation models develop a more or less sophisticated simulation of the vaporising droplet behaviour, there are still outstanding issues in developing genuine (multicomponent) spray evaporation / combustion models that are required for practical applications. In particular, it is important to establish the sensitivity of models to a range of variables as:

- (low, medium, high) Reynolds number,
- (low, elevated, high) temperatures,
- (low, elevated, high) pressures,
- (small, medium, large) droplet diameters,
- (single, binary, multicomponent, complex) mixture compositions,
- (constant, variable) thermotransport properties, and
- (accurate, efficient, low dimensional) computational and numerical methods.

Ideally, a universal model that can circumvent all these shortcomings is required, and yet, the NFL (no-free lunch) theorem (Wolpert and Macready, 1996) states that there cannot exist any algorithm for solving all problems that is generally (on average) superior to any competitor. This implies that one advantage in one model is found to be a drawback in another. Therefore, the objective of this research is to develop a relatively accurate and computationally efficient multicomponent evaporation model for practical applications.

3. MODELLING MULTICOMPONENT VAPOUR FUEL TRANSPORT

3.1 Introduction

Most of the work, on multicomponent fuel vaporisation concentrated on binary mixtures (Law, 1982; Sirignano, 1983, 1993, 1999; Tong and Sirignano, 1986a, 1986b; Aggarwal, 1987), with few exceptions (Newbold and Amundson, 1973; Hallett and Ricard, 1992). The works of Newbold and Amundson (1973) that deal with three component mixtures and those of Hallett and Ricard (1992) for seven component commercial diesel fuels appear to be the only literatures available for more than two-component fuels. However, these models cannot even approximately reproduce the distillation characteristics of real fuels.

The traditional way of representing complex liquid mixtures for evaporation and combustion applications is based on approximation, through representing the mixture as a small number of discrete components, the choice of which is always somewhat arbitrary. This introduces two inherent problems. The first one is that commercial petroleum fuels contain a large number of components that are difficult or impossible to characterise in terms of the whole spectrum of the individual species in the mixture. The second problem in relation to spray evaporation / combustion calculation is that representing all individual species would be computationally expensive, even in the case of binary fuel approximation.

The composition of commercial fuels is ill defined in the sense that the composition is unknown from standard chemical analysis, only identifying a limited number of components in the most qualitative way. Such qualitative understanding on the behaviour of commercial petroleum fuels has been gained through the experimental results of Chen and El-Wakil (1969). However, an attempt to model such fuels remains only empirical, using the ASTM distillation curve to describe the evolution of droplet evaporation (Bardon et al, 1990; Rah et al; 1986). The ASTM distillation curve has been used in CFD applications to simulate the mixture property variation of multicomponent droplet evaporation / combustion (Prommersberger et al, 1998).

However, the distillation curve model assumes a uniform temperature profile inside the droplet and only multicomponent batch distillation is possible. Therefore, there are no general models for the evaporation and combustion of multicomponent or complex liquid mixtures. This thesis aims to develop a new approach to the evaporation and combustion of real fuels using the theory of continuous thermodynamics. To that end, keeping in mind that any refined model to be of use for simulation purposes of practical applications, the general flow and transport equations that are suitable for multidimensional computations are derived. However, more emphasis is given in deriving the detailed approximate analysis of the vapour mixture transport close to the droplet surface. The derivations are based on the basic assumptions and flow physics of standard models, which however, gave rise new expressions due to the application of the continuous thermodynamics theory in representing the fuel mixtures.

Therefore, this chapter is organised as follows. The development of the theory of continuous thermodynamics is described in §3.2. The conservation equations governing reactive flows are described in §3.3, which serves as a starting point to derive new flow and transport equations of multicomponent mixtures in the framework of continuous thermodynamics as described in §3.4. This is followed by an approximate analysis of the new conservation equations in a form suitable to droplet evaporation modelling. Based on the well mixed assumption and film theory, the vapour-phase analysis for equilibrium evaporation models is derived. For completeness, issues related to equilibrium and non-equilibrium evaporation models are also discussed.

3.2 Theory of Continuous Thermodynamics

Continuous thermodynamics (CT) is a method by which the thermodynamics of complex mixtures are described as continuous mixtures and represented by a continuous distribution function as opposed to discrete values (Ratzsch and Kehlen; 1983; Cotterman and Prausnitz, 1985).

The idea of describing complex mixtures using continuous functions is an old one. The works of Aris and Gavalas (1966); Ratzsch and Kehlen (1983); Kehlen et al (1985);

Cotterman and Prausnitz (1985); and Cotterman et al (1985) pave the way for the systematic development of the theory. In particular, Ratzsch and Kehlen (1983) and Kehlen et al (1985) present a formal mathematical analysis of phase equilibrium in continuous mixtures, with approximations for flash calculations. As such, the continuous thermodynamics method is widely accepted for modelling unit operations in the chemical and petroleum industry (Chou and Prausnitz, 1986, Cotterman and Prausnitz, 1985; Hu et al, 1995).

However, with the exception of Gal-Or et al (1975), who suggested new forms of transport equations for multicomponent mixtures, the technique has not been applied to detailed flow and transport processes or combustion applications until recently (Tamim and Hallett, 1995, Hallett, 2000, Harstad et al, 2003). These recent CT based models, however, are restricted to only a single homologue in quiescent conditions, and in general are not suitable for the modelling and simulation of real fuels in multidimensional computations.

This research is based on the seminal work of Gal-Or et al (1975) and the spurring interest in the subject (Gal-Or, 2005), and aim to provide a comprehensive framework in modelling multiphase flow and transport effects of multicomponent fuels for practical applications that are not addressed in any of the previous models.

To that end, the models developed in this investigation are distinctive in at least four major issues. First, unlike all previous CT based models that employ single distribution to represent the whole fuel mixture as one single homologue, realistic multiple distributions are used to represent real (commercial) fuels of practical importance that are composed of a number of homologues. Second, in addition to making significant improvement to the 0D evaporation model of previous investigators, two more accurate and efficient fully resolved 1D evaporation models are developed and applied for real fuels. Third, the range of applicability is highly improved by deriving both low pressure and high pressure phase equilibrium formulations can be used with any general cubic equation of state. Fourth, in order to increase the computational accuracy and efficiency of the modelling process, a novel fully adaptive mesh refinement (AMR) technology in conjunction with the numerical method of lines (MOL) is developed. As such, in the sections to follow, the multi-distribution based CT formulation, for the general vapour-phase mixture flow and transport as well as its approximate analysis close to the droplet surface, in a form suitable for multidimensional computations are presented.

Consider the physical model of a fuel droplet of complex liquid mixtures with large components in a state of vaporisation. The fuel composition in continuous thermodynamics can be represented by molar distribution functions $W_J^v(M)$ and $W_J^l(M)$ for the vapour and liquid phases, respectively. For completeness, the ambient gas (air) is treated as a composition of discrete species of oxygen and nitrogen, so that the new formulation will be used to deal with semi-continuous mixture systems in each of the phases. The first one is the system of liquid phases, which consists of the liquid fuel (continuous) and the dissolved ambient gas (discrete). The second one is the system of gas phases, which consists of the fuel vapour (continuous), and the discrete species of O_2, N_2 as well as vapour H_2O and CO_2 in the case of combustion. Therefore, the general distribution for the composition of each semi-continuous system can be defined as:

$$G^p(M)=\sum_J X_J^p W_J^p(M)+\sum_s X_s^p \delta(M-M_s) \qquad (3-1)$$

In equation $(3-1)$, under normalisation conditions, the following identities both for the continuous and discrete mixtures, take the form:

$$\int_0^\infty G^p(M)dM=1 \quad ; \quad \int_0^\infty W_J^p(M)dM=1 \qquad (3-2)$$

$$\sum_s X_s^p = 1-\sum_J X_J^p = \qquad (3-3)$$

In equations $(3-1)$-$(3-3)$, the superscript p represents the thermodynamic phases (vapour (v) or liquid (l)), the subscripts J and s represent the index of the homologues series of the continuous mixtures and the index of the discrete species, respectively. The independent variable M is some characterising property, usually either the boiling point or the molecular weight. In equation $(3-2)$, the homologue distribution is constructed based on the individual species contained in the homologues series. Similarly, X_J^p is the *total* mole fraction of the species contained in the homologue J, which is different from the mole fraction of the individual species within the homologue.

It is important to note that equation $(3-1)$ assumes solubility of the ambient gas in the liquid phase, a typical situation that happens at supercritical pressure conditions (Yang, 2001). For practical applications of most combustion devices (like an LPP gas turbine combustor), where the pressure is in the order of 50 bar, the ambient gas is assumed insoluble in the liquid phase. Therefore, the liquid phase contains only continuous mixtures, while the vapour phase contains a semi-continuous mixture, although the general probability distribution function of equation $(3-1)$ is to be used.

3.2.1. The Probability Distribution Function (PDF)

In principle, any type of PDF may be used in the CT formulation. However, the compositions of complex hydrocarbon mixtures are best described by the Γ-distribution (gamma distribution), which is widely known as the Schultz or Pearson type III distribution (Cotterman et al, 1985) of the form:

$$W_J^p(M) = \frac{1}{\beta_J^p \Gamma(\alpha_J^p)} \left(\frac{M-\gamma_J^p}{\beta_J^p} \right)^{\alpha_J^p - 1} exp\left[-\left(\frac{M-\gamma_J^p}{\beta_J^p} \right) \right] \qquad (3-4)$$

In equation $(3-4)$, Γ is the gamma function and the parameter γ_J-fixes the origin of the distribution when W_J^p is zero, i.e. if W_J^p is to be zero when $M=0$, then $\gamma_J^p=0$. However, regardless of γ_J^p, $W_J^p(\infty)=0$. α_J^p and β_J^p are the shape and scale parameters, respectively, and determine the shape evolution of the distribution.

For the system of phases that contained continuous fuel mixtures, application of equations $(3-1)$-$(3-4)$ gives the n^{th}- moment of the molar distribution, $\Pi_{J(n)}^{P}$, as:

$$\Phi_{J(n)}^{P} = X_{J}^{P} \Pi_{J(n)}^{P} = \int_{M_0}^{M_\infty} X_{J}^{P} M_{J}^{n} W_{J}^{P}(M) dM \qquad (3-5)$$

In equation $(3-5)$, $\Phi_{J(n)}^{P}$ is a scalar value, which represents the *fractional* moments of the distribution, while the n^{th}-molar distribution moments corresponding to the first four moments ($n=0,1,2,3$) are given by:

$$\begin{cases} \Pi_{J(n=0)}^{P} & = & 1 \\ \Pi_{J(n=1)}^{P} & = & \theta_{J}^{P} \\ \Pi_{J(n=2)}^{P} & = & \psi_{J}^{P} \\ \Pi_{J(n=3)}^{P} & = & \varphi_{J}^{P} \end{cases} \qquad (3-6)$$

The moments in equation $(3-6)$ describe the characteristics of the distribution. The first moment θ_{J}^{P} describes the mean of the distribution; the second moment about the origin ψ_{J}^{P} describes the width of the distribution, while the third moment φ_{J}^{P} describes the asymmetry of the distribution. The moments of the distribution are defined using the parameters of the distribution as in Abramovitz and Stegun (1970) as:

$$\theta_{J}^{P} = \alpha_{J}^{P} \beta_{J}^{P} + \gamma_{J}^{P} \qquad (3-7)$$

$$\psi_{J}^{P} = \alpha_{J}^{P}(\alpha_{J}^{P}+1)(\beta^{2})_{J}^{P} + 2(\alpha\beta\gamma)_{J}^{P} + (\gamma^{2})_{J}^{P} = (\alpha\beta^{2})_{J}^{P} + (\theta^{2})_{J}^{P} \qquad (3-8)$$

$$\begin{aligned} \varphi_{J}^{P} &= \alpha_{J}^{P}(\alpha_{J}^{P}+1)(\alpha_{J}^{P}+2)(\beta^{3})_{J}^{P} + 3\alpha_{J}^{P}(\alpha_{J}^{P}+1)(\beta^{2})_{J}^{P} \gamma_{J}^{P} \\ &+ 3(\alpha\beta\gamma^{2})_{J}^{P} + (\gamma^{3})_{J}^{P} = (\theta\psi)_{J}^{P} + 2(\alpha\beta^{2})_{J}^{P}[\beta+\theta]_{J}^{P} \end{aligned} \qquad (3-9)$$

For multidimensional computation, however, the molar distribution moments must be transformed to the mass distribution moments as (Appendix-A1):

$$\left(\Pi_{J(n)}^{p}\right)_{mass} = \left(\frac{\Pi_{J(n+1)}^{p}}{\theta_{J}^{p}}\right)_{molar} \qquad (3-10)$$

The interesting result in equation $(3-10)$ implies that the n^{th} moment of the mass distribution will always be the next higher moment of the molar distribution divided by the mean of the molar distribution. However, as will be seen in later sections, phase equilibrium calculations and property correlation must be undertaken in molar terms, and the alternative forms described by both the molar and mass distributions are equally essential formulations.

It is also important to observe that equation $(3-4)$ requires the estimation of the three distribution parameters α_J^p, β_J^p, and γ_J^p, given random samples of M of a complex mixture. In representing fuel mixtures using gamma distributions, usually, either distillation or mass chromatography data of the fuel considered is used to determine the lightest and heaviest components that correspond to the minimum and maximum values of the random variable M. The assumption is that the lightest component can be fitted as the origin (left leg) of the distribution while the heaviest component will be fitted with the right leg of the distribution. Nevertheless, the problem of estimating the parameters of the three parameter gamma distribution has always remained a challenging and an interesting one, despite the intensive research on the subject due to its crucial use in many areas of applications, including hydrology and financial risk analysis (Hirose, 1995, Balakrishnan and Wang, 2000). In fact, the parameter estimation of the three-parameter gamma distribution is an active research topic by its own right (Pang et al, 2004). To that end, various methods have been developed to estimate the parameters of the three-parameter gamma distribution involving very large sets of data. Maximum likelihood estimation (MLE) methods for equation $(3-4)$ were described in Johnson and Kotz (1970), and Bowman and Shenton (1988).

Johnson and Kotz (1970) indicated the difficulty in finding the MLEs when $\beta_J^p \to 1$, and suggested the use of MLE for $\beta_J^p \geq 2.5$. Cohen and Norgaard (1977) and Cohen and Whitten (1982, 1986) proposed the modified maximum likelihood estimation

(MMLE) and the modified moment estimation (MME) to avoid these irritating problems when $\beta_j^p \leq 2.5$. Both the MMLE and MME were implemented in this study to test the fuel under consideration – the jet propulsion fuel 8, widely known as JP8.

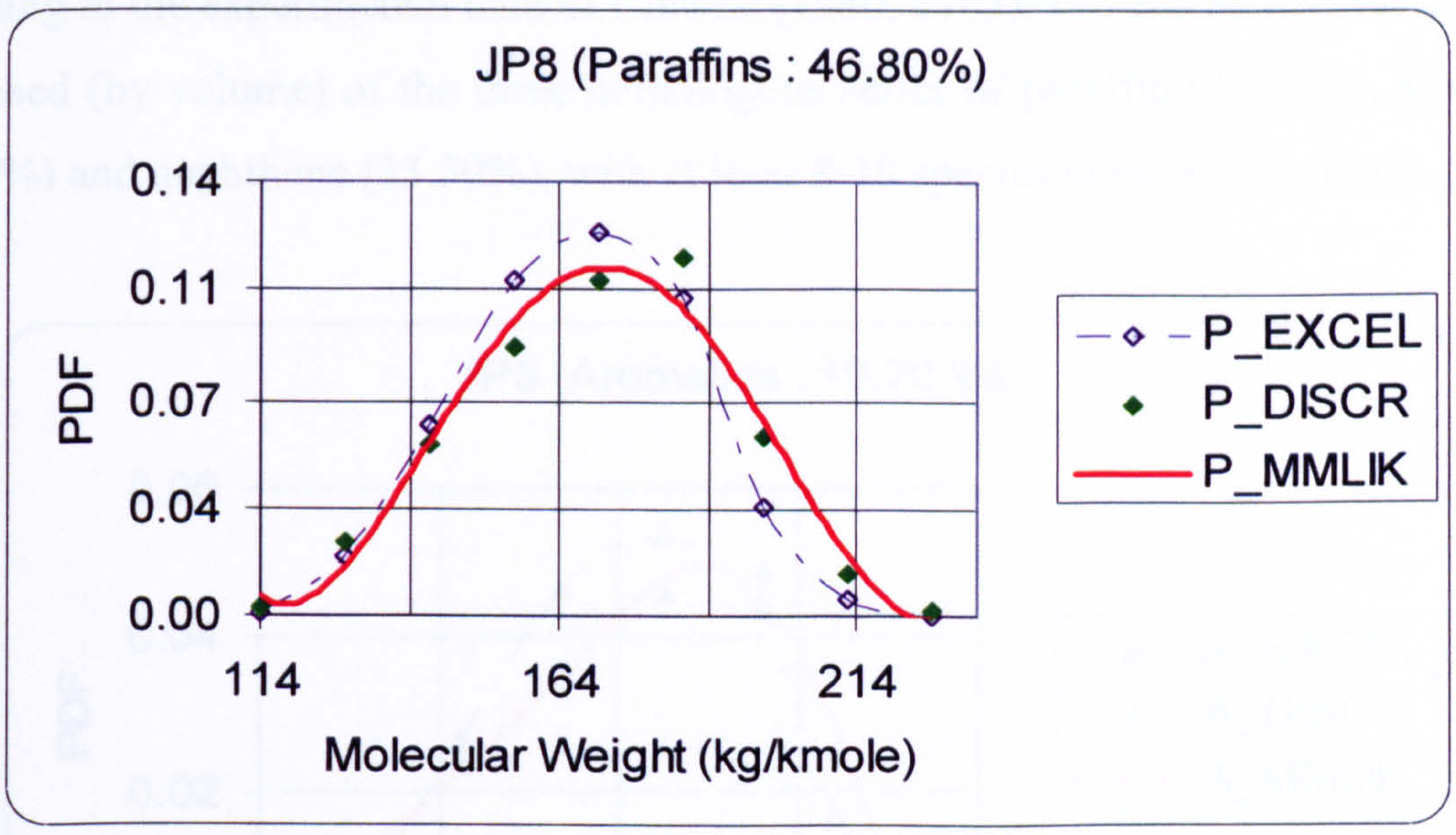

Figure-3.1. Liquid Paraffin composition PDF by volme within JP8 fuel mixture based on predicted distribution parameters (open triangle with broken lines represents the prediction of the inbuilt Microsoft Excell Gamma Distribution Function, solid triangle represents the sample experimental composition data of Clewell, 1983; solid line represents the modified maximum likelihood estimate).

The consideration of JP8 as the fuel of choice in this investigation is justified due to among other things – its importance both from economic, military and environmental view point. In particular, the replacement of the highly volatile fuel JP4 and others by fuel JP8 under the single fuel concept to eliminate current operational and logistical problems across the US and most NATO states defence establishment is the main driver in this study.

JP8 is a kerosene based multipurpose and complex mixture of fuels containing more than 200 aliphatic and aromatic hydrocarbon compounds with 8-20 (or perhaps more) carbon atoms, including thousands of isomeric forms that distil between 412-666K, and with 3-6 non-hydrocarbon performance additives. The precise composition of JP8 varies from batch to batch, with a range of established boiling points and containing (maximal percentage by volume) sulphur (0.3%), olefins (0.5-5.0%), paraffin (33-61%), aromatics (12-22%), and naphthene (10-45%). The aromatics limit is primarily to prevent excessive smoke production, which is generally not desired in jet fuels. However, according to the experimental data of Clewell (1980, 1983), JP8 can be considered to be composed (by volume) of the three homologous series of paraffin (46.80%), aromatics (19.70%) and naphthene (33.50%), with at least 8-10 species in each homologue.

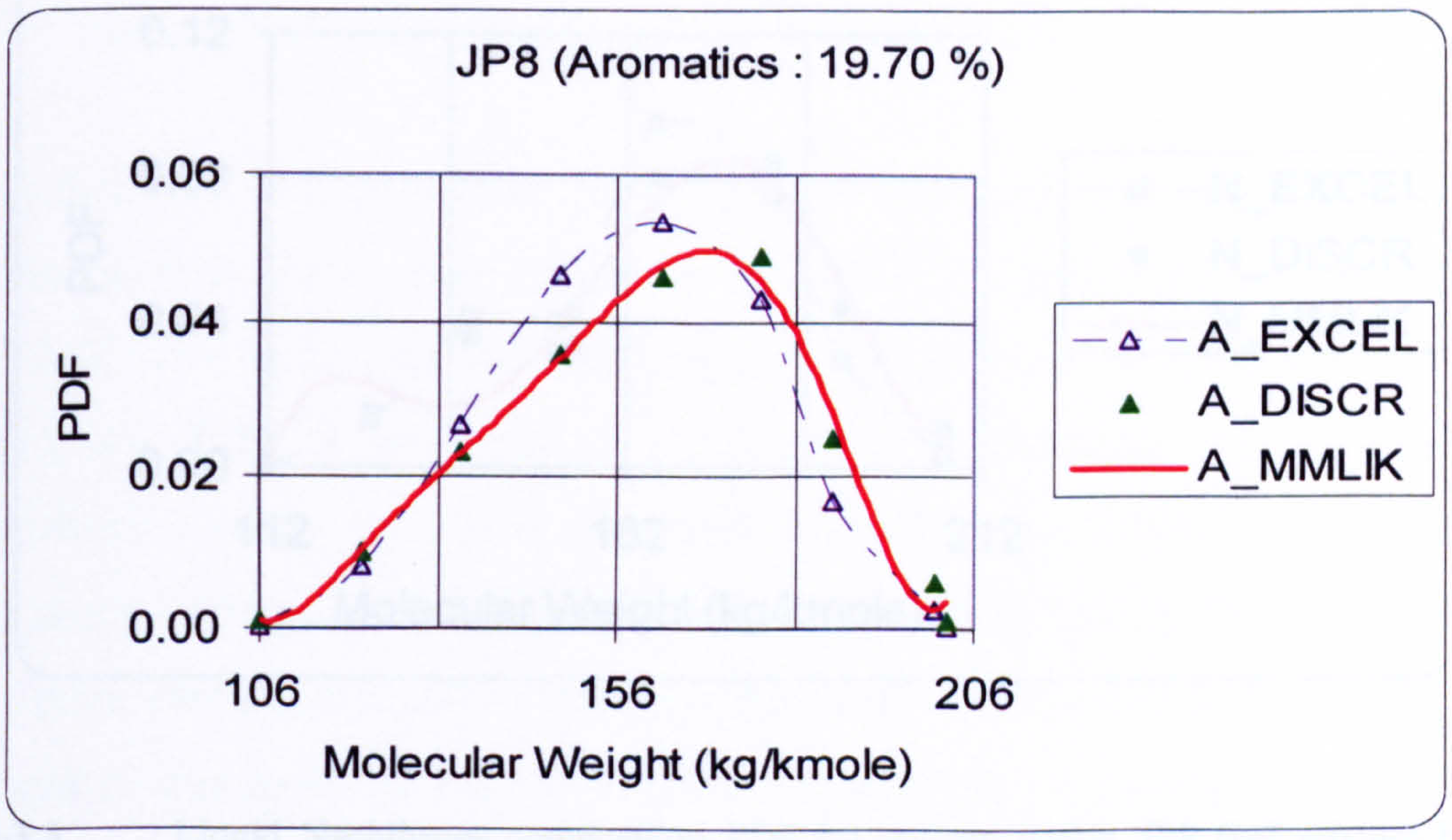

Figure-3.2. Liquid Aromatics composition PDF by volume within JP8 fuel mixture based on predicted distribution parameters (open triangle with broken lines represents the prediction of the inbuilt Microsoft Excell Gamma Distribution Function, solid triangle represents the sample experimental composition data of Clewell, 1983; solid line represents the modified maximum likelihood estimate).

Based on the composition and the range of molecular weights, predictions were made by employing the MMLE and MME methods. However, there appears to be a problem in directly applying the MMLE and MME methods to capture the fuel mixture under consideration This is due to the small number of components considered, while the MMLE and MME methods were developed under the assumption of very large data sets, for example, - the hydrological data of 100-years of rainfall or river flow (Balakrishnan, 2001).

To circumvent this difficulty, the origins of each homologue distributions are set with the corresponding lightest components of the fuel mixtures, which effectively reduced the number of the PDF parameters to solve in each homologue to two, as opposed to the three parameters stipulated by equation $(3-4)$.

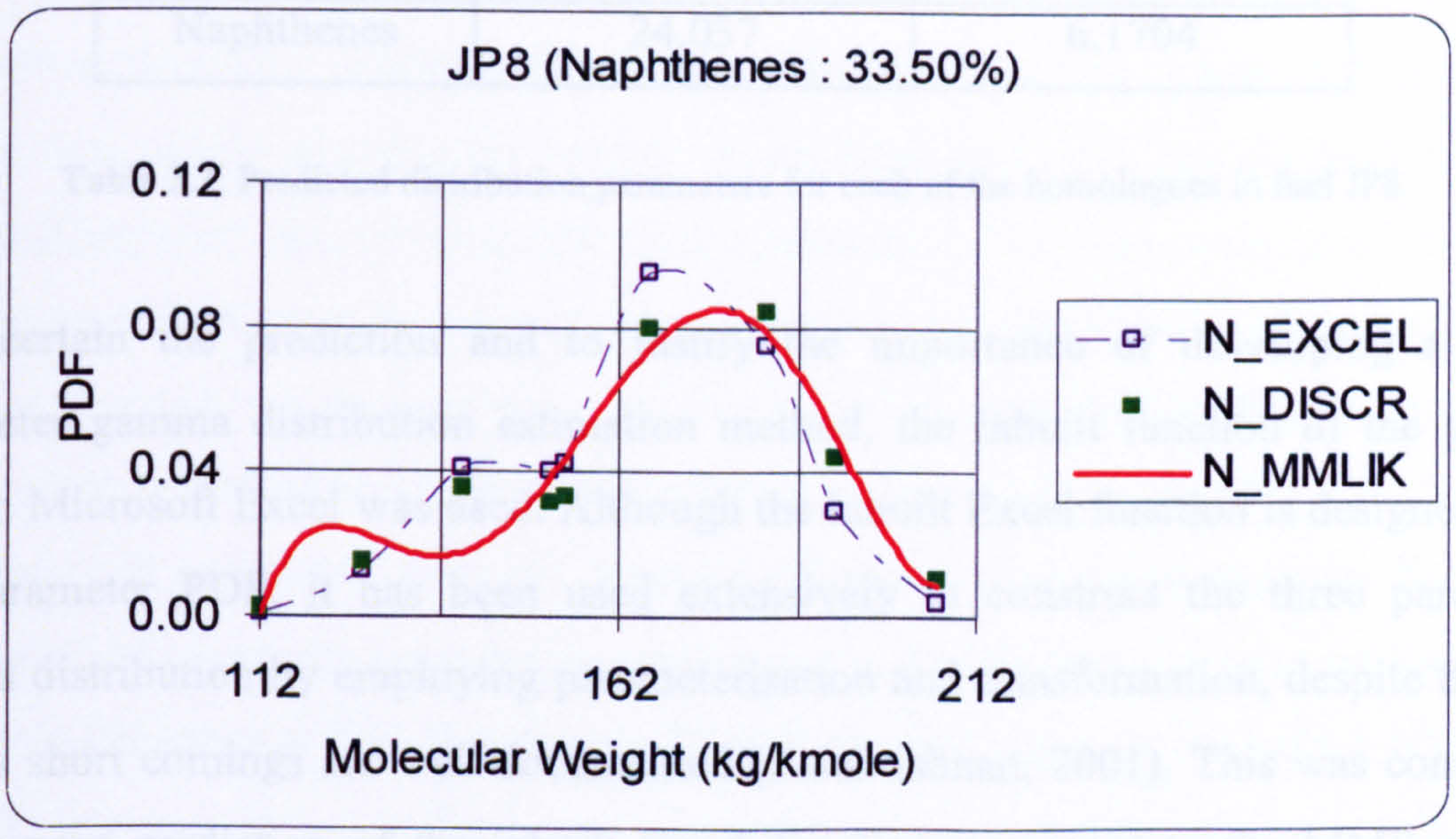

Figure-3.3. Liquid Naphthenes composition PDF by volume within JP8 fuel mixture based on predicted distribution parameters (open triangle with broken lines represents the prediction of the inbuilt Microsoft Excel Gamma Distribution Function, solid triangle represents the sample experimental composition data of Clewell, 1983; solid line represents the modified maximum likelihood estimate).

By using the lightest components as the origin of the liquid mixture distribution, both the MMLE and MME are applied to determine the distribution parameters. Both methods predict similar distribution means θ_J^l. Although the sum of the fractional first moments of the distribution, $\sum_J \Phi^l_{J(n=1)} = \sum_J X^l_J \theta^l_J$, is similar to the mean molar weight of fuel JP8 (Vargaftik, 1975), the MMLE and MME methods predicted very different scale and shape parameters, α_J^l and β_J^l, respectively. The MMLE predictions for the shape parameters were found to be very small, mainly in the range $0.7 \le \beta_J^l \; 2.8$, instigating a narrow distribution width that tends to go to zero before the droplet finishes vaporising.

Homologue	α	β
Paraffins	25.092	6.3239
Aromatics	26.090	5.9289
Naphthenes	24.037	6.1704

Table 3.1. Predicted distribution parameters for each of the homologues in fuel JP8

To ascertain the prediction and to justify the importance of developing a three-parameter gamma distribution estimation method, the inbuilt function of the gamma PDF in Microsoft Excel was used. Although the inbuilt Excel function is designed for a two-parameter PDF, it has been used extensively to construct the three parameter gamma distribution by employing parameterisation and transformation, despite the fact that its short comings are well documented (Balakrishnan, 2001). This was confirmed by the poor prediction of the inbuilt Excel function compared to the MME method developed in this investigation (Figure 3.1-3.3). It must be pointed out that the PDF from the Excel function did employ the two-parameters of the PDF predicted using the MME method (Table 3.1). On the other hand, since the low shape parameter prediction of the MMLE method didn't provide any realistic value in comparison with either the experimental, MME prediction, and the empirical correlation of the excel function, it was discarded from this investigation. Since the prediction of the MME method is the most accurate and provides plausible results both for the distribution mean and stable distribution parameters (non-zero distribution width), it is adopted in this study.

3.3 General Conservation Equations for Reacting Flows

The Reynolds Averaged Navier-Stokes (RANS) equations are the most widely used models as a framework to develop multidimensional reactive flow codes, which for a general flow variable ϕ take the form:

$$(\rho\phi)_t + div(\rho u\phi) = div(\Gamma_\phi \, grad\,\phi) + S_\phi^{ch} + S_\phi^{vap} \qquad (3-11)$$

In equation $(3-11)$, possible substitutions of ϕ are, 1 for the continuity equation, u, v, w for the velocity components in the momentum equations, h for the enthalpy (energy) equation, discrete Y_i for the species mass fraction equations (or X_i for the species mole fractions, depending on how the density is defined), and other scalars representing different models. For example, the standard $k-\varepsilon$ turbulence model is included by solving two additional transport scalars, representing the turbulent kinetic energy k, and its dissipation rate ε (Launder and Spalding, 1974). The systems of transport equations are typically formulated in non-orthogonal curvilinear co-ordinates with different interpolation schemes and pressure correction methods, introducing simple and advanced solvers. The temperature distribution is derived from the enthalpy field and the density is calculated from an equation of state for an ideal mixture. Since the purpose of this research is to develop evaporation models that can later be interfaced with multidimensional RANS codes like SOFIE, the two terms on the right hand side of $(3-11)$, S_ϕ^{vap} and S_ϕ^{ch}, represent source terms that account for the fuel evaporation and combustion, respectively.

However, the general form of the conservation equations described by equation $(3-11)$, in the case of multicomponent fuels, requires as many transport equations as the species present. Hence, in addition to source terms for momentum coupling and energy transfer, it requires as many source terms as the species present. Therefore, in the materials presented in this section, the traditional conservation equations represented by equation $(3-11)$ are modified in such a way that is consistent in form, but completely new in its content and the mode of phase coupling under the framework of the CT theory.

To elucidate the modelling process, consider the species mass fraction equations, and the energy equation described by equation $(3-11)$ applied to real fuels with large number of mixtures.

$$\begin{aligned}(\rho Y_i)_t + div(\rho u Y_i) &= div(\Gamma_{Y_i}\, grad\, Y_i) + S_{Y_i}^{ch} + S_{Y_i}^{vap} \quad ; \; i = 1, \ldots, N \\ (\rho h)_t + div(\rho u h) &= div(\Gamma_h\, grad\, h) + S_h^{ch} + S_h^{vap}\end{aligned} \qquad (3-12)$$

The model equation $(3-12)$ is computationally cumbersome, owing to the large number of N fuel species ($N \sim$ tens of thousands), and the millions of drops in a spray. In addition, the determination of the enthalpy, h, of a mixture involving a large number of fuel species requires – for example, higher order polynomial fit for the specific heat capacity and a large database for the heat of formation. Therefore, to balance physical accuracy against computational complexity, traditional models represented by the general governing equations $(3-11)$ or $(3-12)$ usually employ binary or surrogate fuels. However, such models can not represent the complex thermotransport property evolution and the chemical kinetics that takes place during spray evaporation and combustion (Sirignano, 1999). Therefore, the need for comprehensive and computationally efficient models that can be used in detailed evaporation and combustion modelling of practical applications is transparent.

3.4 New Conservation Equations in Continuous Thermodynamics

Instead of using discrete species mass fractions as in equation $(3-12)$, the CT formulation utilises PDFs of the form in $(3-1)$ or $(3-5)$ to represent the complex fuel composition as a whole. For commercial liquid fuels – for example aviation kerosene or JP8, which typically comprises a large numbers of chemical compounds, it is possible to reduce it into a small number of homologous series as discussed in §3.2.1. Using the PDF for each homologue and employing the relations in equations $(3-5)$ - $(3-10)$ into either the general form equation $(3-11)$ or $(3-12)$, the new vapour-phase species and energy transport moment equations for multicomponent reactive flows take the form (Appendix-A2 and Appendix-A3):

$$\left(\rho_{\bar{J}(n)}^{v} \Phi_{J(n)}^{v}\right)_t + div\left(\rho_{\bar{J}(n)}^{v} v^{v} \Phi_{J(n)}^{v}\right) = div\left(\Gamma_{\Phi_{J(n)}^{p}}\, grad\, \Phi_{J(n)}^{v}\right) + S_{\Phi_{J(n)}^{v}}^{ch} + S_{\Phi_{J(n)}^{v}}^{vap} \quad (3-13_a)$$

In equation $(3-13_a)$, the average mass density, $\rho^v_{\bar{J}(n)}$, of the gas-vapour mixture is determined following the ideal equation of state for mixtures of discrete species, which is of the form $\rho = P/RT\sum_i (Y^v_i/M) = P\sum_i X^v_i M/RT$. Rather than the conversion relation of mole fraction to mass fraction, $Y^v_m = X^v_m M_m / \sum_l X^v_l M_l$, or mass fraction to mole fraction, $X^v_m = (Y^v_m / M_m) / \sum_l (Y^v_l / M_l)$ for discrete species, the continuous equivalent (Appendix-A1) is used as $Y^v_J = X^v_J \theta^v_J / \theta^v_{\bar{J}}$, where $\theta^v_J = \int_M W^p_J(M) M dM$. Therefore, the average vapour mass density, $\rho^v_{\bar{J}(n)}$, which must account for both the continuous homologues and the discrete species that form the gas-vapour mixture, can be expressed by using the more general distribution function given by equation $(3-1)$, and takes the form:

$$\rho^v_{\bar{J}(n)} = \frac{P^v}{RT^v} \int_M X^v_J G^v(M) M dM = \frac{P^v}{RT^v}\left(\sum_J X^v_J \theta^v_J + \sum_s X^v_s M_s \right) \qquad (3-13_b)$$

Note that the average mass density of the mixture given by $(3-13_b)$ is different from the saturation density at the droplet surface, which is computed using the Rackett equation (Polling et al, 2000) employing the corresponding saturation pressure and temperature. The average liquid mixture density, on the other hand, is determined from mass balance based on the distribution mean and the instantaneous droplet radius as discussed in §4.

Although the fractional distribution moments $\Phi^v_{J(n)}$ in equation $(3-13)$ and as defined in equation $(3-5)$, are in theory infinite, only the first two or three moments are sufficient to understand the behaviour of the distribution evolution (Cotterman et al, 1985). As such, only the first three moments are considered in this study. These three moments are, however, complemented by two important derived quantities that further characterise the fuel evolution. The first is the variance about the mean, $\sigma^2 = \alpha\beta^2$, which characterises the central width of the distribution. The second is the skewness, $2/\sqrt{\alpha}$, of the distribution, which characterises the asymmetric evolution of the distribution shape due to the relative changes in the mean and variance of the distribution. As such, it is anticipated that the fuel vapour composition evolution will be captured both in space and time, allowing us to extract detailed information that is not available in traditional methods. Contrary to traditional methods, which in principle require solving tens and thousands of transport equations, the CT theory only requires at most three moment transport equations for each homologous series, and an energy equation, no matter how many species are present.

Note that equation $(3-13)$ is general for all multicomponent fluid mixtures, with appropriate source terms. For a two-phase multicomponent mixture in a Lagrangian framework, however, the flow and transport conditions due to the gas-vapour boundary layer around each droplet must be treated with great care. In fact, the coupling of the general form represented by equation $(3-13)$ and the fluid dynamics and transport behaviour in the liquid phase has been the subject of intense investigation for over fifty years. In particular, for fuels that are composed of a large number of components and that undergo phase change, the analysis or the computation might be intractable. To that end, based on the assumptions made on the property of the gas-vapour boundary layer, various models have been developed (Sirignano, 1999). In the sections to follow, the focus will be on the analysis of the gas-phase that gave rise the 0D and 1D models discussed in §2.3.2 and §2.3.3, respectively.

3.4.1. Approximate Analysis of the Vapour Mixture Transport

The newly derived equations $(3-13)$ describe the general flow and transport of multicomponent gas-vapour mixtures that can be solved with appropriate initial and boundary conditions. Due to the presence of a dispersed phase (like liquid droplets), and the resulting phase coupling in the momentum, energy, and fractional moment transport, there is a complex interaction between the streamlines of the main flow and the droplet. Since in both the 0D and 1D droplet models the flow field around the evaporating droplet is treated as spherically symmetric, equation $(3-13)$ can suitably be described in a spherical coordinate form that is similar to the classical models in equations $(2-6)$-$(2-8)$. As the liquid to gas density ratio is very high, the flow field can be further assumed quasi-steady. This is justified based on the small characteristic time of the (fast) gas phase evolution compared to that of the liquid phase (Hubbard et al, 1975). Therefore, the simplified form of equation $(3-13)$ that can describe the fractional moment and energy transport equations (in an alternate coordinate with $\bar{\beta}=0$ for Cartesian polar, $\bar{\beta}=1$ for Cylindrical, and $\bar{\beta}=2$ Spherical coordinates) can be written as (Appendix A2 and Appendix A3):

$$\frac{1}{r^{\bar{\beta}}}\frac{\partial}{\partial r}\left(r^{\bar{\beta}} v^{v} c^{v}_{\bar{J}(n)} \Phi^{v}_{J(n)}\right) = \frac{1}{r^{\bar{\beta}}}\frac{\partial}{\partial r}\left(c^{v}_{\bar{J}(n)} D^{v}_{Jm(n)}\, r^{\bar{\beta}} \frac{\partial(\Phi^{v}_{J(n)})}{\partial r}\right) + S^{ch}_{\Phi^{v}_{J(n)}} + S^{vap}_{\Phi^{v}_{JJ(n)}} \qquad (3-14)$$

$$\begin{aligned} &\frac{1}{r^{\bar{\beta}}}\frac{\partial}{\partial r}\left(r^{\bar{\beta}} c^{v}_{\bar{J}(n)} v^{v} Cp^{v}_{\bar{J}(n)} T\right) = \frac{1}{r^{\bar{\beta}}}\frac{\partial}{\partial r}\left(r^{\bar{\beta}} \lambda^{v}_{\bar{J}(n)} \frac{\partial T}{\partial r}\right) \\ &+ \frac{c^{v}_{\bar{J}(n)} D^{v}_{\bar{J}m(n)}}{r^{\bar{\beta}}}\left\{\frac{\partial}{\partial r}\left(r^{\bar{\beta}} h^{v}_{\bar{J}(n)} \frac{\partial \Phi^{v}_{J(n=0)}}{\partial r}\right) - h^{v}_{\bar{J}(n)} \frac{\partial}{\partial r}\left(r^{\bar{\beta}} \frac{\partial \Phi^{v}_{J(n=0)}}{\partial r}\right)\right\} + S^{ch}_{h_J} + S^{vap}_{h_J} \end{aligned} \qquad (3-15)$$

In equations $(3-14)$ and $(3-15)$, it is assumed that the steady form of the mass continuity, with $\Phi^{v}_{J(n)}=1$ in equation $(3-13)$, to take the form $r^{\bar{\beta}}\, c^{v}_{\bar{J}(n)} v^{v} = const = \dot{m}_{(n)}/4\pi$, the details of which will be given later. In addition, the average molar density of the vapour mixture, $c^{v}_{\bar{J}(n)}$, is determined using the relation $\rho^{v}_{\bar{J}(n)} = c^{v}_{\bar{J}(n)} \theta^{v}_{\bar{J}}$ and equation $(3-13_b)$, where the mixture is assumed to follow the ideal equation of state. v^{v} is the average molar mixture velocity, and $\Phi^{v}_{J(n)}$ represents the first four fractional molar distribution moments (or transported scalars of fuel composition) corresponding to $n=0,1,2,3$. The thermotransport properties $\lambda^{v}_{\bar{J}(n)}$, $Cp^{v}_{\bar{J}(n)}$, and $D^{v}_{\bar{J}m(n)}$, respectively, are the average fuel vapour mixture thermal conductivity, the average fuel vapour mixture specific heat capacity, and the homologue diffusion coefficient (not binary diffusion coefficient) as described in §4.4. $S^{vap}_{(\Phi^{v}_{J(n)};h_J)}$ and $S^{ch}_{(\Phi^{v}_{J(n)};h_J)}$ represent the source terms due to the liquid evaporation and combustion of the fractional composition distribution moments and the energy transfer, while Cp_A is the specific heat capacity of the ambient gas at the far end. The second term on the RHS of equation $(3-15)$ represents the inter-diffusion, which has never been included in any of the classical droplet evaporations models reviewed in §2.

In order to solve the composition and energy equations described by $(3-14)$ and $(3-15)$, prescribed initial conditions and interface (boundary) conditions are required as discussed in §2.3.1 and depicted by Figure 2.1. In the CT framework, the interface condition at the droplet surface can be described by enforcing similar flow physics as in equations $(2-9)$ and $(2-10)$, but accounting for changes due to the PDF representation of the fuel composition. The conservation condition at the droplet surface dictates that the form of equations $(3-14)$ and $(3-15)$, without the source terms, must equally apply for the liquid side and the vapour side. In addition, the material continuity can be stated in a similar manner to the one discussed in §2.3.1, namely, $r^{\bar{\beta}} c^{l}_{\bar{J}(n)}(v^{l}-\dot{R})\big|_{R^-} = r^{\bar{\beta}} c^{v}_{\bar{J}(n)}(v^{v}-\dot{R})\big|_{R^+} = \dot{m}_{(n)}/4\pi$, where the regression rate of the droplet surface, $\dot{R}$, and the evaporation rate, $\dot{m}_{(n)}$, are yet to be determined. Therefore, the fractional composition distribution moment conservation conditions at the droplet surface can be given as (Williams, 1965; Torres et al, 2003, Maru and Moss, 2003):

$$\left[c^{l}_{\bar{J}(n)}(v^{l}-\dot{R})(\Phi^{v}_{J(n)}-\Phi^{l}_{J(n)}) + c^{l}_{\bar{J}(n)} D^{l}_{Jm(n)} \frac{\partial \Phi^{l}_{J(n)}}{\partial r} \right]_{r=R^-} = \left[c^{v}_{\bar{J}(n)} D^{v}_{Jm(n)} \frac{\partial \Phi^{v}_{J(n)}}{\partial r} \right]_{r=R^+} \qquad (3-16)$$

Note that the form of equation $(3-16)$ is similar to the expression of the classical model discussed in equation $(2-9)$, except the changes in composition representation, where a balance of equation $(3-14)$ is taken between the phases, including the surface regression rate. Similarly, the argument on the energy balance at the droplet surface has its roots in the classical model equation $(2-10)$. Using the continuity equation and imposing the temperature equilibrium condition discussed in §2.3, which is stated as $T^{vR} = T^{lR}$, the interface energy balance that includes the inter-diffusion takes the form:

$$\left[\sum_J \mathrm{L}_J \mathrm{c}^{\mathrm{l}}_{\mathrm{J(n)}} \left\{ \left(\dot{\mathrm{R}} - \mathrm{v}^{\mathrm{l}}\right)\Phi^{\mathrm{l}}_{\mathrm{J(n)}} + \mathrm{D}^{\mathrm{l}}_{\mathrm{Jm(n)}} \frac{\partial \Phi^{\mathrm{l}}_{\mathrm{J(n)}}}{\partial r} \right\} - \lambda^{\mathrm{l}}_{\bar{\mathrm{J}}(\mathrm{n})} \frac{\partial \mathrm{T}}{\partial r}\right]_{\mathrm{r=R^-}} = \left[\lambda^{\mathrm{v}}_{\bar{\mathrm{J}}(\mathrm{n})} \frac{\partial \mathrm{T}}{\partial r}\right]_{\mathrm{r=R^+}} \qquad (3-17)$$

In equation $(3-17)$, the term on the RHS is the heat flux from the gas-vapour mixture to the droplet surface, while on the LHS, the last term is the heat flux to the interface of the droplet from the interior of the droplet, the middle term accounts for the inter-diffusion, which is responsible for an energy transport due to mass diffusion, while the first term accounts for the mass flux due to the heat energy of the liquid core under circulation. In other words, the heat fluxes from the ambient and the droplet interior are balanced by the vaporisation and inter-diffusion heat and mass transfers. The latent heat of vaporisation is of the form $\sum_J \mathrm{L}_J = \sum_J \left(Cp^v_J \nabla T^v - Cp^l_J \nabla T^l\right) = h^v_{\bar{J}(n)} - h^l_{\bar{J}(n)}$, while the homologue mixture specific heat capacity is $CP^p_J = (a_{cJ} - Cp_A) + b_{cJ}\theta^p_J$, and the air specific heat capacity in the liquid is assumed $Cp_A = 0$. The effective enthalpy of vaporisation is $L = \sum_J \mathrm{L}_J \eta_{J(n)} = 1/N_{T(n)} \sum_J L_J N_J$. The molar flux $N_{T(n)}$ or $\dot{m}_{(n)}/4\pi r^2$ will be determined in later sections. In fact, one of the main objectives in droplet evaporation calculation is the determination of the vaporisation rate $\dot{m}_{(n)}$ or the molar flux $N_{T(n)}$, and equally the rate of heat energy intake by the liquid droplet, $Q^l_{J(n)}$.

In this section, two methods are presented for the analysis of the vapour heat and mass transfer processes at the close proximity of the droplet surface, namely, the well mixed assumption and the film theory. Although the vapour-phase analysis of droplet evaporation models based on the well mixed assumption and the film theory are very well known, detailed development is provided both to clarify the new developments and to appreciate some of the significant modifications due to the application of CT.

3.4.1.1. The Well Mixed Assumption

Although the real case for an evaporating droplet is somewhere in between the well-mixed assumption and the diffusion limited case (Law and Sirignano, 1977), for a liquid mixture containing large components, a uniform composition and temperature profile may be valid for the following reasons. First, the effects of departure are most evident for binary fuels with vastly different boiling points, where the mixture is made up of one very volatile and one heavy component, with distinctive diffusion coefficients and specific heat capacities as opposed to the continuous thermotransport property that is expected in a mixture with large number of components. For real fuels considered in this study, the continuous production of vapour mixture at the droplet surface is expected to contribute to the well-mixed nature of the mixture. Second, for practical applications, the effect of droplet injection into a combustion chamber introduces high relative velocity, which causes internal circulation and an increase in the effective diffusion rate for better mixing. In addition, droplet break-up (secondary atomisation) and deformation could further contribute internal mixing (Arcoumanis et al 1997) and would make realistic mixing extremely difficult. Third, although theoretical analysis would point to a mass-diffusion limited case for a quiescent droplet, experimental evidence points to well-mixed droplet vaporisation behaviour in the case of injected droplets (Law, 1982).

In the well-mixed assumption, the gas-vapour mixture field at the close proximity of the droplet is quasi-steady, and the liquid composition and temperature spatially uniform. This implies the liquid internal (circulation) velocity is negligible and the specific heat capacity does not vary appreciably, making the mass transfer due to inter-diffusion negligible. Under these conditions, the vapour mixture fractional composition distribution moment equations in $(3-14)$ can be reduced to evaluate the vapour molar flux of the fuel that contributes the source term as:

$$\frac{\partial}{\partial r}\left(\mathrm{r}^{\bar{\beta}} c^{v}_{\bar{J}(n)} v^{v} \Phi^{v}_{J(n)} - c^{v}_{\bar{J}(n)} D^{v}_{Jm(n)}\, \mathrm{r}^{\bar{\beta}} \frac{\partial \Phi^{v}_{J(n)}}{\partial r} \right) = 0 \qquad (3-18)$$

Note that the total balance at the droplet surface due to the interface condition in equation $(3-16)$ implies that the mass flows of all species, except the fuel vapour, are zero. In addition, the value inside the bracket in equation $(3-18)$ is a constant, $\dot{m}_{(n)}/4\pi$, that accounts for the rate of mass balance due to convection and diffusion. As such, in the gas-vapour mixture, based on mass continuity, where the steady form of equations $(3-13)$, $(3-14)$ or $(3-18)$ takes a value of $\Phi^{v}_{J(n)}=1$, the total molar flux across the droplet surface, $N_{T(n)}$, is defined as:

$$\frac{\dot{m}_{(n)}}{4\pi r^{2}}=c^{v}_{\bar{J}(n)}v^{v}=N_{\bar{J}(n)}=N_{T(n)} \qquad (3-19)$$

Equation $(3-19)$ along with the simplified form of the relation defined by equation $(3-18)$ can be rewritten to give an equation which is unique in $\eta_{J(n)}$ as:

$$N_{T(n)}\Phi^{v}_{J(n)}-c^{v}_{\bar{J}(n)}D^{v}_{Jm(n)}\frac{\partial\Phi^{v}_{J(n)}}{\partial r}=N_{J(n)}=\eta_{J(n)}N_{T(n)} \qquad (3-20_{a})$$

However, it is easy to observe that equation $(3-20_{a})$ is nothing but the Stefan-Maxwell convection-diffusion equation for multicomponent mixtures (Bird et al, 1960). Note that except for the average molar density $c^{v}_{\bar{J}(n)}$, and the total molar flux $N_{T(n)}$, all other terms represent the Jth-homologue value corresponding to the nth-fractional composition distribution moments. It is desirable to express equation $(3-20_{a})$ in a form suitable both to determine the vapour field composition profile and to estimate the material flux across the droplet surface. Such a result is given by equation $(3-25_{a})$. However, in order to determine the material flux across the droplet surface, first, equation $(3-20_{a})$, upon using the relation in $(3-19)$ can be re-written as:

$$\dot{m}_{(n)}=4\pi\left(\int_{R}^{\infty}\frac{dr}{c^{v}_{\bar{J}(n)}D^{v}_{Jm(n)}r^{2}}\right)^{-1}\left[\int_{\Phi^{vR}_{J(n)}}^{\Phi^{\infty}_{J(n)}}\frac{d\Phi^{v}_{J(n)}}{-\left(\eta_{J(n)}-\Phi^{v}_{J(n)}\right)}\right] \qquad (3-20_{b})$$

Note the departure of equation $(3-20_b)$ from the classical expression (Spalding, 1953) and the modified model described by equation $(2-12)$. Taking the case $n=0$, which corresponds to the 0th-distribution moment, and using equations $(3-5)$–$(3-9)$, $(3-16)$ and $(3-19)$, integration of equation $(3-20_b)$ yields the molar flux or the molar material flow across the droplet surface as:

$$N_{T(0)} = \frac{c^{R\infty}_{J(n)} D^{v}_{Jm(n)}}{2R} Sh^{R\infty}_{J(n)} \ell n\left(1 + B_{M_{J(n)}}\right) \qquad (3-21)$$

The CT form of the total molar flux described by equation $(3-21)$ is very similar to that of the classical model described by equation $(2-13)$, except for the form of the thermotransport properties used. In equation $(3-21)$, $D^{v}_{Jm(n)}$ is the vapour homologue diffusion coefficient as determined in §4.4, while $c^{R\infty}_{J(n)}$ and $Sh^{R\infty}_{J(n)}$ are the average gas-vapour mixture molar density and Sherwood number, respectively, computed using reference composition and temperature values based on the one-third rule (Yuen and Chen, 1976) as $A^{R\infty}_{J(n)} = (1-\xi)A^{vR}_{J(n)} + \xi A^{\infty}_{J(n)}$, where A is either temperature or the fractional composition distribution moments and $\xi = 1/3$. Convection effects are accounted through the Sherwood number as discussed in later sections. In equation $(3-21)$, the modified Spalding mass transfer number $B_{M_{J(n)}}$, which describes the distribution moments mass driving potential for each homologue J takes the form:

$$B_{M_{J(n)}} = \frac{\Phi^{vR}_{J(n)} - \Phi^{\infty}_{J(n)}}{\eta_{J(n)} - \Phi^{vR}_{J(n)}} \qquad (3-22)$$

The form of the Spalding transfer number $B_{M_{J(n)}}$ in equation $(3-22)$ is quite different from the original definition given by Spalding (1953). The most obvious difference here is the introduction of the fractional molar flux $\eta_{J(n)}$. In addition, the transfer number is defined for all $n-$distribution moments, where for $n=0$, the transfer number in equation $(3-22)$ reduces to a *similar* form to the modified transfer number for multicomponent fuels described by equation $(2-14)$. As such, for fuels that comprise more than one homologue, which in turn may contain thousands of species, the fractional molar flux $\eta_{J(n)} \neq 1$, and it must satisfy the closure identity as:

$$\eta_{J(n)} = \frac{N_{J(n)}}{N_{T(n)}} \quad ; \quad \sum_{J=1}^{K} \eta_{J(n)} = 1 \qquad (3-23)$$

Note that to determine the total molar flux in equation $(3-21)$, the Spalding mass transfer number $B_{M_{J(n)}}$, the instantaneous droplet radius R, and the thermotransport properties must be determined. The thermotransport properties can be determined following the methods outlined in §4.4 at the reference temperature and compositions. However, to determine $B_{M_{J(n)}}$ using equation $(3-22)$, the two unknowns, the fractional molar flux $\eta_{J(n)}$ and the fractional composition distribution moments at the droplet surface, $\Phi_{J(n)}^{vR}$, must be computed first. The fractional composition distribution moments will be extracted from phase equilibrium conditions that is discussed in §4.3. On the other hand, since both the total and homologue molar fluxes are unknown, it is not possible to compute the fractional molar flux using equation $(3-23)$ at this stage. The method to determine the instantaneous droplet radius is discussed in §4.2.1. Therefore, the relation given by equation $(3-22)$ is cyclic in $B_{M_{J(n)}}$ and $\eta_{J(n)}$, and it requires further development. The obvious step is to quantify the molar flux based on the energy conservation. But, as would be seen in later sections, that avenue too requires knowledge of the vapour phase quantities, including vapour phase thermotransport properties as well as the residual temperature at the droplet surface. Therefore, a method of generating an initial guess based on the information available is developed.

In order to determine an initial guess for $\eta_{J(n)}$, equation $(3-21)$ is rewritten as $RN_{T(0)}/c_{J(n)}^{R\infty} = D_{Jm(n)}^{v} Sh_{J(n)}^{R\infty} \ell n\left(1 + B_{M_{J(n)}}\right)$, where the LHS is independent of what homologue is used, although the Spalding number and the homologue diffusion coefficient on the RHS change with the homologue type. For $J = 1$, the equality becomes $RN_{T(0)}/c^{R\infty}_{J(n)} = D^{v}_{1m(n)} Sh^{R\infty}_{J(n)} \ell n\left(1+B_{M_{1(n)}}\right)$. Since the value $RN_{T(0)}/c^{R\infty}_{J(n)}$ is the same in both expressions, it follows that $\ell n\left(1+B_{M_{1(n)}}\right) = \left(D^{v}_{Jm(n)}/D^{v}_{1m(n)}\right)\ell n\left(1+B_{M_{J(n)}}\right)$. This expression implies that the Spalding mass transfer number is dependent on the ratios of the homologue diffusion coefficients as $B_{M_{J(n)}} = \left[\left(1+\mathrm{B}_{\mathrm{M}_{1(n)}}\right)^{\mathrm{D}^{v}_{1(n)}/\mathrm{D}^{v}_{J(n)}} - 1\right]$. Therefore, an initial guess for the homologue fractional molar fluxes, after rearranging equation $(3-22)$ and using the above relation for $B_{M_{J(n)}}$, takes the form:

$$\eta_{J(n)} = \Phi^{vR}_{J(n)} + \left(\Phi^{vR}_{J(n)} - \Phi^{\infty}_{J(n)}\right) \Big/ \left[\left(1+\mathrm{B}_{\mathrm{M}_{1(n)}}\right)^{\mathrm{D}^{v}_{1(n)}/\mathrm{D}^{v}_{J(n)}} - 1\right] \qquad (3-24)$$

Equation $(3-24)$ requires an approximate knowledge of the composition profile so that the composition gradients are readily determined. In order to understand the composition profile within the radius of the mass transfer limit, $r^{MTL}_{J(n)} = \dot{\mathrm{m}}_{(n)} / 4\pi c^{v}_{J(n)} D^{v}_{Jm(n)}$, equation $(3-20)$ can be rearranged as:

$$\int_{\Phi^{vR}_{J(n)}}^{\Phi^{\infty}_{J(n)}} \frac{d\Phi^{v}_{J(n)}}{\eta_{J(n)} - \Phi^{v}_{J(n)}} = r^{MTL}_{J(n)} \int_{R}^{\infty} \frac{dr}{r^{2}} \qquad (3-25_{a})$$

The mass transfer limit, unlike -for example, the radius of a flame front, is not clearly defined. Therefore, the information in equation $(3-25_{a})$ implies that by integrating between the droplet surface and a quasi-steady far field, where the oxidiser becomes dominant, the vapour homologue composition profile can be approximated as:

$$\Phi^{v}_{J(n)}(r) = \begin{cases} \eta_{J(n)} - \left(\eta_{J(n)} - \Phi^{vR}_{J(n)}\right)\left(1+B_{M_{J(n)}}\right)^{\left(-r^{MTL}_{J(n)}/r\right)} & ;n=0 \\ \Phi^{vR}_{J(n)} - \dfrac{1}{B_{M_{J(n)}}}\left(\Phi^{vR}_{J(n)} - \Phi^{\infty}_{J(n)}\right)\left[\left(1+B_{M_{J(n)}}\right)^{\left(1-r^{MTL}_{J(n)}/r\right)} - 1\right] & ;n=1,2,3 \end{cases} \qquad (3-25_{b})$$

Note that the vapour field profile in the mass transfer limit satisfies the conditions at the droplet surface and at the far end (infinity). However, for most practical situations, the mass transfer limit of integration is finite, mostly in the order of 10-15 times of the droplet radius. Equation $(3-25)$ can be used to approximate terms containing the gradient of the transported scalar or the fractional composition distribution moments $\Phi^{v}_{J(n)}(r)$. However, the determination of $\eta_{J(n)}$ in equation $(3-24)$ requires knowledge of $B_{M_{1(n)}}$, which is still unknown. In order to circumvent this problem, the solution of the energy equation is considered.

The energy equation $(3-15)$, neglecting the inter-diffusion term due to the well-mixed assumption, where the vapour fuel specific heat capacity do not vary appreciably, takes the form:

$$\frac{1}{r^{\beta}}\frac{\partial}{\partial r}\left(r^{\beta} c^{v}_{J(n)} v^{v} Cp^{v}_{J(n)} T\right) = \frac{1}{r^{\beta}}\frac{\partial}{\partial r}\left(r^{\beta} \lambda^{v}_{J(n)} \frac{\partial T}{\partial r}\right) \qquad (3-26_{a})$$

Substituting the continuity of material described by equation $(3-19)$ into the LHS of equation $(3-26_{a})$ and rearranging, it takes the form:

$$\frac{\partial}{\partial r}\left(\frac{\dot{m}_{(n)}}{4\pi} Cp^{v}_{J(n)} T - r^{\beta} \lambda^{v}_{J(n)} \frac{\partial T}{\partial r}\right) = 0 \qquad (3-26_{b})$$

Equation $(3-26_{b})$ implies that the expression inside the bracket is a constant. In general, this accounts for the energy transferred due to convection and conduction from the hot ambient gas to the dispersed phase, which must balance the heat required for heating up the droplet and the heat release due to vaporisation and takes the form:

$$\frac{\dot{m}_{(n)}}{4\pi} Cp^{v}_{J(n)} T - r^{\beta} \lambda^{v}_{J(n)} \frac{\partial T}{\partial r} = \frac{\dot{m}_{(n)}}{4\pi} L^{eff}_{J(n)} = \frac{\dot{Q}^{l}_{J(n)}}{4\pi} + \frac{\dot{m}_{(n)}}{4\pi} L_{J(n)} \qquad (3-27_{a})$$

In equation $(3-27_{a})$, the rate of heat entering the liquid phase is represented by $\dot{Q}^{l}_{J(n)}$, while the effective latent heat of vaporisation, which was described by equation $(2-18)$

in the classical model is now given by $L^{eff}_{\bar{J}(n)} = L_{\bar{J}(n)} + Cp^{v}_{\bar{J}(n)} \int_{T} dT$. In the well mixed assumption, only the residual liquid temperature at the droplet surface is considered. Equation $(3-27_a)$ can be re-written in two different forms to derive both the evaporation rate and the temperature profile of the vapour field. In order to derive the temperature profile of the vapour field, equation $(3-27_a)$ together with the expression for the effective latent heat vaporisation described earlier, can be rearranged to give:

$$\frac{\dot{\mathrm{m}}_{(n)} Cp^{v}_{\bar{J}(n)}}{4\pi\lambda^{v}_{\bar{J}(n)}} \left[\left(T - T^{vR}\right) + \frac{L_{\bar{J}(n)}}{Cp^{v}_{\bar{J}(n)}} \right] = \mathrm{r}^{\bar{\beta}} \frac{\partial T}{\partial \mathrm{r}} \qquad (3-27_b)$$

By using a substitution of $r^{HTL}_{\bar{J}(n)} = \dot{\mathrm{m}}_{(n)} Cp^{v}_{\bar{J}(n)} / 4\pi\lambda^{v}_{\bar{J}(n)}$ as the radius of the heat transfer limit, equation $(3-27_b)$ gives the following integral.

$$\int_{T}^{T^{\infty}} \frac{dT}{\left(T - T^{vR}\right) + L_{\bar{J}(n)} / Cp^{v}_{\bar{J}(n)}} = r^{HTL}_{\bar{J}(n)} \int_{r}^{\infty} \frac{dr}{r^{2}} \qquad (3-27_c)$$

The integral in equation $(3-27_c)$ can be evaluated to yield the vapour field temperature profile as:

$$T(r) = \left(T^{v} - \frac{L_{\bar{J}(n)}}{Cp^{v}_{\bar{J}(n)}} \right) + \left[\left(T^{\infty} - T^{vR}\right) + \frac{L_{\bar{J}(n)}}{Cp^{v}_{\bar{J}(n)}} \right]^{\left(r^{HTL}_{\bar{J}(n)}/r\right)} \qquad (3-27_d)$$

On the other hand, equation $(3-27_a)$ can be rearranged in a form similar to the classical model described by $(2-16)$ as:

$$\frac{\dot{\mathrm{m}}_{(n)}}{4\pi} = \int_{R}^{\infty} \left(\frac{dr}{Le^{v}_{\bar{J}(n)} c^{v}_{\bar{J}(n)} D^{v}_{Jm(n)} r^{2}} \right)^{-1} \int_{T^{vR}}^{T^{\infty}} \left(\frac{Cp^{v}_{\bar{J}(n)} dT}{Cp^{v}_{\bar{J}(n)} T + L^{eff}_{\bar{J}(n)}} \right) \qquad (3-28_a)$$

Equation $(3-28_a)$ can be integrated to give the molar flux of the fuel vapour in terms of the thermal driving potential $B_{T_{(n)}}$ as:

$$N_{T(n)} = \frac{Le_{\bar{J}(n)}^{R\infty} c_{\bar{J}(n)}^{R\infty} D_{Jm(n)}^{v}}{2R} Nu_{\bar{J}(n)}^{R\infty} \ell n\left(1 + B_{T_{(n)}}\right) = \frac{\lambda_{\bar{J}(n)}^{R\infty}}{2RCp_{\bar{J}(n)}^{R\infty}} Nu_{\bar{J}(n)}^{R\infty} \ell n\left(1 + B_{T_{(n)}}\right) \quad (3-28_b)$$

In equation $(3-28_b)$, the thermal driving potential (or the Spalding heat transfer number) is defined as:

$$B_{T(n)} = \frac{Cp_{\bar{J}(n)}^{v}\left(T^{\infty} - T^{vR}\right)}{L_{\bar{J}(n)}^{eff}} \qquad (3-29)$$

For non-unity Lewis number, where mass diffusion and thermal diffusion are different, a close examination of equations $(3-21)$ and $(3-28)$ reveal that the Spalding mass and heat transfer numbers related as:

$$B_{T(n)} = \left[1 + B_{M_{\bar{J}(n)}}\right]^{\Omega_{\bar{J}(n)}} - 1 \qquad (3-30)$$

In equation $(3-30)$, the following relations are used:

$$\Omega_{\bar{J}(n)} = \frac{1}{Le_{\bar{J}(n)}^{R\infty}} \frac{Sh_{\bar{J}(n)}^{R\infty}}{Nu_{\bar{J}(n)}^{R\infty}} \frac{Cp_{\bar{J}(n)}^{R\infty}}{Cp_{\bar{J}(n)}^{l}} \quad ; \quad Le_{\bar{J}(n)}^{R\infty} = \frac{\lambda_{\bar{J}(n)}^{R\infty}}{c_{\bar{J}(n)}^{R\infty} D_{\bar{J}m(n)}^{R\infty} Cp_{\bar{J}(n)}^{R\infty}} \qquad (3-31)$$

Note that, the $1/3^{rd}$ -rule is used to compute values in equation $(3-31)$. The Sherwood and Nusselt numbers, following the standard expression in $(2-19)$ take the form:

$$Sh_{J(n)}^{v} = 2\frac{(\partial\Phi_{\mathrm{J(n)}}^{\mathrm{v}}/\partial\mathrm{r})}{\left[(\Phi_{\mathrm{J(n)}}^{v\infty} - \Phi_{\mathrm{J(n)}}^{\mathrm{vR}})/2\mathrm{r}\right]}; \quad Nu_{\bar{J}(n)}^{v} = 2\frac{(\partial\mathrm{T}^{\mathrm{v}}/\partial\mathrm{r})}{\left[(\mathrm{T}^{\mathrm{v}\infty} - \mathrm{T}^{\mathrm{vR}})/2\mathrm{r}\right]} \qquad (3-32)$$

For an evaporating droplet in a convective (turbulent) gas field, the effect is accounted for by modifying the Sherwood and Nusselt numbers in equation $(3-32)$ through empirical correlation (Ranz and Marshall, 1952; Clift t al, 1978), similar to the one given for the classical models by equations $(2-20)$-$(2-22)$, which is left here to avoid duplication. The general form of equation $(3-32)$ in the CT framework is given in the next section under the film theory treatment. Before concluding the gas phase analysis of the well mixed model of this section however, some standard and new results are stated for completeness. The detailed derivations are described in the liquid phase modelling section of §4.

First, the expression for molar flux will be used to determine the rate of change in the residual liquid phase compositions $d\Phi^l_{J(n)}/dt$, the residual temperature dT^l/dt, and the rate of change in the droplet radius dR/dt, described by equations $(4-5)$, $(4-10)$, and $(4-12)$, respectively. The results of the residual values of the liquid phase together with the vapour phase analysis enables to determine the rate of heat energy entering the liquid phase and the rate of the vapour fuel entering the ambient gas environment as described by the source terms in equations $(3-14)$ and $(3-15)$. The rate of heat flux into the droplet, which is required to complete equation $(3-27_a)$, can be stated based on the classical models (Sirignano, 1999) as:

$$\dot{Q}^l_{\bar{J}(n)} = \dot{\mathrm{m}}_{(\mathrm{n})}\left(L^{eff}_{\bar{J}(n)} - L_{\bar{J}(n)}\right) = \frac{4}{3}\pi \mathrm{R}^3 c^l_{\bar{J}(n)} Cp^l_{\bar{J}(n)} \frac{dT^l}{dt} \qquad (3-33_a)$$

The only change in the form of equation $(3-33_a)$ from the classical model is in the way the average thermotransport properties are calculated, where a fractional composition distribution moment averaging is used as opposed to mass averaging in the classical model. Following the analysis suggested by Delplanque and Sirignano (1995), the fractional composition distribution moments and enthalpy source terms described by equations $(3-14)$ and $(3-15)$ can be stated as:

$$S^{vap}_{\Phi^{v}_{J(n)}} = \frac{4\pi}{R} N_{J(n)} \left(1 - \frac{\Phi^{v}_{J(n)}}{\eta_{J(n)}} \right) \quad ; \quad S^{vap}_{h^{v}_{J(n)}} = \frac{4\pi}{R} N_{T(n)} \left(\frac{h^{v}_{J(n)}(T^{\infty}) - h^{l}_{J(n)}(T^{vR})}{1 + B_{T(n)}} \right) \qquad (3-33_b)$$

In equation $(3-33_b)$, the homologue molar flux is used for the source term of the fractional composition distribution moment equation $S^{vap}_{\Phi^{v}_{J(n)}}$, whereas the total molar flux is used in the energy source term $S^{vap}_{h_J}$. In addition, recalling the form of the fractional vapour composition distribution moments, $\Phi^{v}_{J(n)} = X^{v}_{J} \Pi^{v}_{J(n)}$, the vapour source distribution moment $\Pi^{v}_{J(n)}$ is derived based on the liquid phase analysis (§4 equation $(4-8)$), which can be stated as:

$$\Pi^{v}_{J(n)} = \frac{1}{\eta_{J(n)} B_{M_{J(n)}}} [X^{vR}_{J} \Pi^{vR}_{J(n)} (1 + B_{M_{J(n)}}) - X^{\infty}_{J} \Pi^{\infty}_{J(n)}] \qquad (3-34)$$

All the initial and boundary conditions discussed in §2.3 apply. The liquid phase treatment is presented in §4. What is to follow, however, is a gas phase approximation technique based on film theory.

3.4.1.2. The Film Theory

The film theory (Bird et al, 1960; Frank-Kamenetskii, 1969) assumes that the resistance to the heat and mass exchange between a surface and a bulk gas flow is concentrated within some fictional gas film of constant thickness. To that end, Abramzon and Sirignano (1989) employ the film theory, and extended the Hubbard et al (1975) model by taking into account the effect of convective transport caused by the droplet motion relative to the gas. The effective conductivity model of Abramzon and Sirignano (1989), in fact extended the works of Hubbard et al (1975) significantly. In particular, the authors introduced general values for the Schmidt, Prandtl, and Lewis numbers, thereby relaxing the unity Lewis number condition and allowing for variable properties. They also considered a range of Falkner-Skan solutions (White, 1991) to develop the average transport rates across the gas boundary layer on the droplet surface. The model is also extended for multicomponent fuels (Delplanque et al, 1991). The effective conductivity model (Abramzon-Sirignano; 1989; Delplanque et al, 1991) is proved to be the most robust and accurate 1D model available in the literature, and has been applied for multidimensional applications.

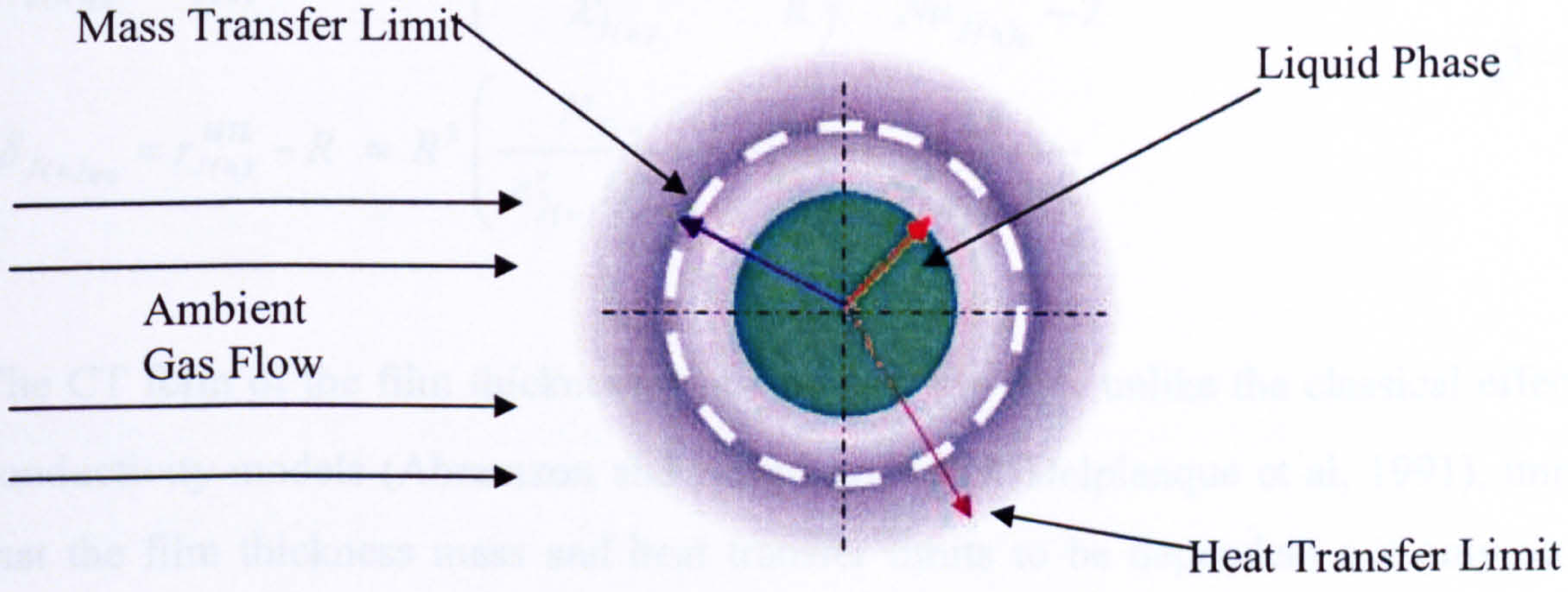

Figure 3.4 Vapour film around an evaporating fuel droplet

However, as in most multicomponent models developed over the years, the effective diffusivity model has been applied only for binary fuels. In the materials to follow, the film theory model (Abramzon and Sirignano; 1989; Delplanque et al, 1991) will be modified in the framework of continuous thermodynamics, and the modified model will be referred to as the multicomponent effective diffusivity model (MEDM), to signify its ability to genuinely model multicomponent fuels.

For multicomponent fuels, with different thermotransport properties, the mass and heat transfer follows the general transport equation $(3-13)$. In such situations, the boundary layers are distributed according to the mass diffusion and thermal diffusion of the fuel components, forming different mass and heat transfer limits. Figure 3.4 depicts an isolated multicomponent droplet that is vaporising in a convective ambient condition, with radii of mass transfer limits corresponding to the J^{th} −homologue of the n^{th} −distribution moments, which can be expressed as $r_{J(n)}^{MTL} = N_{T(n)}R^2 / c_{\bar{J}(n)}^{v} D_{Jm(n)}^{v}$, and a radius of the total mixture heat transfer limit, which can be expressed as

$r_{\bar{J}(n)}^{HTL} = N_{T(n)} R^2 Cp_{\bar{J}(n)}^{v} \big/ \lambda_{\bar{J}(n)}^{v}$. In the CT framework, the mass and heat transfer film thickness that surrounds the vaporising droplet of instantaneous radius R can be approximated as:

$$\begin{aligned} \delta_{\bar{J}(n)_{T0}} &= r_{\bar{J}(n)}^{HTL} - R = R^2 \left(\frac{N_{T(n)} Cp_{\bar{J}(n)}^{v}}{\lambda_{\bar{J}(n)}^{v}} - \frac{1}{R} \right) = \frac{2R}{Nu_{\bar{J}(n)_0} - 2} \\ \delta_{J(n)_{M0}} &= r_{J(n)}^{MTL} - R = R^2 \left(\frac{N_{T(n)}}{c_{\bar{J}(n)}^{v} D_{Jm(n)}^{v}} - \frac{1}{R} \right) = \frac{2R}{Sh_{J(n)_0} - 2} \end{aligned} \qquad (3-35)$$

The CT form of the film thicknesses in equation $(3-35)$, unlike the classical effective conductivity models (Abramzon and Sirignano, 1989, Delplanque et al, 1991), implies that the film thickness mass and heat transfer limits to be dependent not only on the total molar flux but also quadratically on the size of the droplet. In fact, it can be conjectured that for a vapour film to occur, the mass and heat propagation length scales, $c_{\bar{J}(n)}^{v} D_{Jm(n)}^{v} \big/ N_{T(n)}$ and $\lambda_{\bar{J}(n)}^{v} \big/ N_{T(n)} Cp_{\bar{J}(n)}^{v}$ respectively, must not exceed the droplet radius. These propagation length scales quantify the relative strength of heat and mass diffusions, where the ratio is in fact the Lewis number. If the heat and mass propagation length scales are identical, the unity Lewis number applies. Therefore, the heat and mass transfer limits in equation $(3-35)$ become identical, and hence the Sherwood and Nusselt numbers. Therefore, the relation in $(3-35)$ insures the inherent capability of the model to handle both unity and non-unity Lewis numbers. This implies variability of thermotransport properties within the film, contrary to the customary film theory (Bird et al, 1960). In fact, the relations in equation $(3-35)$ is based on the requirement that the rates of purely molecular transport by mass and thermal diffusion through the film must be equal to the actual intensity of the convective heat or mass transfer between the surface and the external flow.

In the film model, it is argued that for a quasi-steady condition in the vapour film, the mass flows of all the fractional composition distribution moments (except the fuel vapours) are all zero. The molar form of the fractional composition distribution moment equations in $(3-14)$ with the flux balance at the droplet surface as described by equation $(3-16)$ simplify to a form similar to the well mixed assumption in equation $(3-20)$. The resulting equation is, in fact, similar to the Stefan-Maxwell convection diffusion equation for multicomponent systems (Bird et al, 1960). Integration of equation $(3-20)$ across the variable film thickness described by equation $(3-35)$ yields the vapour molar flux across the film surface as:

$$N_{T(0)} = \frac{c^{R\infty}_{J(n)} D^{v}_{Jm(n)}}{2R} Sh^{R\infty(*)}_{J(n)} \ell n\left(1+B_{M_{J(n)}}\right) \tag{3-36}$$

Similarly, using the energy equation $(3-15)$ with the interface condition in equation $(3-17)$, the problem reduces to a form similar to equation $(3-27)$, which can be integrated twice to give an equation similar to equation $(3-28)$ as:

$$N_{T(0)} = \frac{\lambda^{R\infty}_{J(n)}}{2RCp^{R\infty}_{J(n)}} Nu^{R\infty(*)}_{J(n)} \ell n\left(1+B_{T_{(n)}}\right) \tag{3-37}$$

Although the form of the molar flux for the well mixed assumption in equation $(3-21)$ and for the film theory in equation $(3-36)$ look identical, there are notable differences in the manner the Sherwood numbers are defined. The same holds true for the Nusselt numbers in equation $(3-28)$ and $(3-37)$.

The Sherwood and Nusselt numbers variation are as a result of the thickening of the laminar boundary layer due to the Stefan flow or blowing effect (Schlichting, 1979). In the original film model, the only variability allowed is the film thickening due to the blowing effect or Stefan flow. Therefore, the film thickness described by equation $(3-35)$ must account for the boundary layer thickening effect. To that end, Abramzon and Sirignano (1989) defined the relative film thickness due to thermal diffusion $F_T = \delta_{J(n)_T} / \delta_{J(n)_{T0}}$, and mass diffusion $F_M = \delta_{J(n)_M} / \delta_{J(n)_{M0}}$, as a means to measure the film thickening due to blowing effect. Interestingly enough, the authors found that the relative film thickness to be insensitive to the flow geometry as well as the Reynolds, Prandtl, and Schmidt numbers, but highly dependent on the Spalding transfer number. Using the relative film thickening effect along with the initial film thickness given by equation $(3-35)$, the modified Sherwood and Nusselt numbers, respectively, are given by $Sh_{J(n)}^{R\infty(*)} = 2 + \left(Sh_{J(n)0}^{R\infty} - 2\right)/F_M$ and $Nu_{\bar{J}(n)}^{R\infty(*)} = 2 + \left(Nu_{\bar{J}(n)0}^{R\infty} - 2\right)/F_M$. It is evident that as the limit for the relative film thickness approaches unity, the modified transfer numbers approach the transfer numbers that correspond to no film thickening, as defined by equation $(3-35)$. It should be noted that the modified transfer numbers, $Sh_{J(n)}^{R\infty(*)}$ and $Nu_{\bar{J}(n)}^{R\infty(*)}$, and those that appear in equation $(3-35)$ as a measure of the heat and mass transfer within the film are different from the actual Sherwood and Nusselt numbers defined in equation $(3-32)$. In fact, for MEDM, the actual Sherwood numbers and Nusselt number are related to the modified Sherwood numbers and Nusselt number as $Sh_{J(n)}^{R\infty} = Sh_{J(n)}^{R\infty(*)} \ell n(1 + B_{M_{J(n)}})/B_{M_{J(n)}}$ and $Nu_{\bar{J}(n)}^{R\infty} = Nu_{\bar{J}(n)}^{R\infty(*)} \ell n(1 + B_{T_{(n)}})/B_{T_{(n)}}$, respectively. Note that the standard Sherwood and Nusselt numbers are defined as the dimensionless gradients of composition and temperature as in equation $(3-32)$. An interesting development from the above argument is that equation $(3-35)$ is applicable to the well mixed assumption considered earlier, provided the film thickness is assumed appreciably thick compared to the droplet diameter and in the event the film thickness remains constant under blowing effect.

On the other hand, a close examination of equations $(3-36)$ and $(3-37)$ reveals that the equality of the molar fluxes due to mass diffusion and thermal diffusion can be used to relate the Spalding transfer numbers as:

$$B_{T(n)} = \left(1 + B_{M_{\bar{J}(n)}}\right)^{\Omega_{\bar{J}(n)}^{(*)}} - 1 \qquad (3-38)$$

As in equation $(3-31)$, the following relations are used in equation $(3-38)$:

$$\Omega^{(*)}_{\bar{J}(n)} = \frac{1}{Le^{v\infty}} \frac{Sh^{R\infty(*)}_{\bar{J}(n)}}{Nu^{R\infty(*)}_{\bar{J}(n)}} \left(\frac{Cp^{vR}_{\bar{J}(n)}}{Cp^{lR}_{\bar{J}(n)}} \right) \qquad ; \qquad Le^{R\infty}_{\bar{J}(n)} = \frac{\lambda^{R\infty}_{\bar{J}(n)}}{c^{R\infty}_{\bar{J}(n)} D^{v}_{Jm(n)} Cp^{R\infty}_{\bar{J}(n)}} \qquad (3-39)$$

In equation $(3-39)$, the term $\left(Cp^{vR}_{\bar{J}(n)} / Cp^{lR}_{\bar{J}(n)}\right)$, is the weighting factor for the energy transfer rate at the droplet surface between the liquid and vapour phases as suggested by Sirignano (1999), where the averaging is taken using the compositions at the droplet surface where as the specific heat capacity correlations in the vapour phase and liquid phase are employed appropriately. In situations where the droplet is superheated, the ratio of the specific heat capacity goes to unity. In addition, if the Lewis number is close to unity, the Spalding transfer numbers can be taken as identical, which implies a balance in the thermal diffusion $\lambda^{R\infty}_{\bar{J}(n)} / c^{R\infty}_{\bar{J}(n)} Cp^{R\infty}_{\bar{J}(n)}$, and the mass diffusion $c^{R\infty}_{\bar{J}(n)} D^{v}_{Jm(n)}$ of the vapour mixture within the film.

It is also important to realise that the expressions for the gas phase approximations, both for the well-mixed assumption and the film theory look similar, except for the expressions of the Sherwood and Nusselt numbers. The Spalding heat and mass transfer numbers in equations $(3-22)$ and $(3-29)$ (or $(3-30)$), respectively are also valid expressions for the film theory, when the latent heat of vaporisation in equation $(3-29)$ can be quantified from $L^{eff}_{\bar{J}(n)} = \left| h^{l}_{J(n)}(T_s) - h^{v}_{J(n)}(T_s) \right|$.

At this stage, it must be pointed out that although the various forms of the Sherwood and Nusselt numbers are related to each other, the relative film thicknesses F_T and F_M must be determined. This requires knowledge of the vapour thermotransport properties across the film as stipulated by equation $(3-35)$ and the momentum boundary layer thickness. The detailed treatment of the classical boundary layer theory of an incompressible fluid with density $\rho^{v}_{\bar{J}(n)}$, dynamic viscosity $\mu^{v}_{\bar{J}(n)} = \upsilon \rho^{v}_{\bar{J}(n)}$ past a spherical particle of nominal radius R with no slip boundary condition is beyond the scope of this work.. However, it suffices to state that the transition from zero velocity at the particle surface to the full magnitude at some distance from it takes place in the boundary layer whose thickness can be related as:

$$\delta \sim \sqrt{\upsilon R / U_{\perp}} \tag{3-40}$$

It is easy to observe from equation $(3-40)$ that the depth of the boundary layer in such situation is inversely proportional to the velocity perpendicular to the particle radius, $U_{\perp}$, and directly proportional the size of the particle. This implies that near the particle surface, the viscosity forces tend to diminish the velocity profile inside the boundary layer, and hence the boundary layer thickness must increase by mass conservation. Therefore, it can be inferred, as in the mass and thermal diffusional boundary layers, the momentum boundary layer thickness is also dependent on the molar flux produced at the droplet surface.

To that end, Abramzon and Sirignano (1989) considered a range of Falkner-Skan solutions (White, 1991) to develop the average transport rates across the gas boundary layer on the droplet surface, which enables them to solve the 2D forms of equation $(3-13)$ with nonzero pressure gradients. The correlation of the numerical results for the Falkner-Skan solutions is in the ranges of $B_{T_{(n)}} \geq 0$; $B_{M_{J(n)}} \leq 20; 1 \leq (Pr, Sc) \leq 3$, and gave the relative film thickening of the form:

$$F(B_{T_{(n)}}) = \delta_{\bar{J}(n)_T} / \delta_{\bar{J}(n)_{T0}} = (1 + B_{T_{(n)}})^{0.7} \frac{\ell n(1 + B_{T_{(n)}})}{B_{T_{(n)}}} \tag{3-41}$$

$$F(B_{M_{J(n)}}) = \delta_{J(n)_M} / \delta_{J(n)_{M0}} = (1 + B_{M_{J(n)}})^{0.7} \frac{\ell n(1 + B_{M_{J(n)}})}{B_{M_{J(n)}}} \tag{3-42}$$

Therefore, the Sherwood numbers and the Nusselt number for the effective diffusivity model take the form:

$$Sh_{J(n)}^{R\infty} = Sh_{J(n)}^{R\infty(*)} \frac{\ell n(1 + B_{M_{J(n)}})}{B_{M_{J(n)}}} = 2 \frac{\ell n(1 + B_{M_{J(n)}})}{B_{M_{J(n)}}} + \frac{Sh_{J(n)_0} - 2}{(1 + B_{M_{J(n)}})^{0.7}} \tag{3-43}$$

$$Nu_{\bar{J}(n)}^{R\infty} = Nu_{\bar{J}(n)}^{R\infty(*)} \frac{\ell n(1+B_{T_{(n)}})}{B_{T_{(n)}}} = 2\frac{\ell n(1+B_{T_{(n)}})}{B_{T_{(n)}}} + \frac{Nu_{\bar{J}(n)_0} - 2}{(1+B_{T_{(n)}})^{0.7}} \qquad (3-44)$$

In equations $(3-43)$ and $(3-44)$, the vaporisation of droplets in convective environments is corrected through empirical correlations of the form given by equations $(2-20)$-$(2-22)$. However, it was clear that those correlations have the behaviour of over estimating the transfer rates at low Reynolds numbers (Crocco and Cheng, 1956; Abramzon and Sirignano, 1989). To that end, the Clift et al (1978) correlation, described by equation $(3-45)$ is used in equation $(3-43)$ and $(3-44)$.

$$\begin{aligned} Nu_{J(n)0} &= 1 + \left(1 + Re\, Pr_{J(n)}^{v}\right)^{1/3} \cdot f(Re) \quad ; \quad Pr_{J(n)}^{v} = \mu_{J(n)}^{v} Cp_{J(n)}^{v} / \lambda_{J(n)}^{v} \\ Sh_{J(n)0} &= 1 + \left(1 + Re\, Sc_{J(n)}^{v}\right)^{1/3} \cdot f(Re) \quad ; \quad Sc_{J(n)}^{v} = \mu_{J(n)}^{v} / c_{J(n)}^{v} D_{J(n)}^{v} \end{aligned} \qquad (3-45)$$

The validity of equation $(3-45)$, in fact, is dependent on the ranges of the Reynolds number, the Prandtl number, and the Schmidt numbers. For the range of heat and mass transfer numbers $(0.25 < (Pr_{J(n)}^{v}, Sc_{J(n)}^{v}) < 100)$ and ranges of Reynolds numbers described by equation $(3-46)$, the correlation accurately approximates the numerical results of many workers with an error less than 3% (Abramzon and Sirignano, 1989).

$$f(Re) = \begin{cases} 1 & ;\ Re \ll 1 \\ Re^{0.077} & ;\ Re < 400 \end{cases} \qquad (3-46)$$

Therefore, the working formula of the molar flux of an evaporating droplet in a convective ambient condition due to the heat driving potential, equation $(3-36)$, and the mass driving potential, equation $(3-37)$, takes the form:

$$N_{T(n)}\begin{cases} = \dfrac{c_{\bar{J}(n)}^{R\infty} D_{Jm(n)}^{v}}{2R}\left[2\ell n(1+B_{M_{J(n)}}) + \dfrac{Sh_{J(n)0}-2}{B_{M_{J(n)}}^{-1}(1+B_{M_{J(n)}})^{0.7}}\right] \\ = \dfrac{\lambda_{\bar{J}(n)}^{R\infty}}{2RCp_{\bar{J}(n)}^{R\infty}}\left[2\ell n(1+B_{T_{(n)}}) + \dfrac{Nu_{J(n)0}-2}{B_{T_{(n)}}^{-1}(1+B_{T_{(n)}})^{0.7}}\right] \end{cases} \qquad (3-47)$$

The implication of equation $(3-47)$ is that the film thickening due to Stefan flow is accounted by a film possessing variable thermotransport properties, where the values of the Sherwood and Nusselt numbers are calculated using equation $(3-45)$. However, in order to solve the equations presented so far, conditions at the droplet surface must be known a priori. This requires the approximation of the liquid phase heat and mass transfer, and the analysis of the phase equilibrium at the droplet surface, assuming equilibrium evaporation.

3.4.2. Equilibrium versus Non-Equilibrium Vaporisation

Droplet evaporation models that are used in the application of energy conversion devices, with few exceptions (Bellan and Sommerfeld, 1978; Harstad and Bellan, 1987), assume equilibrium evaporation, where vapour particles from the liquid phase strike and cross the droplet surface as Stefan flow with no accumulation. In particular at the interface, mechanical and thermodynamic equilibrium is assumed. The mechanical equilibrium stipulates that the liquid surface is impenetrable, implying the species equations from the liquid side are balanced by the diffusion from the gas side, or no accumulation of gas in the liquid phase.

In addition, thermodynamic equilibrium, with the exception of pressure effects, assume that the (liquid) phase change at the droplet surface to occur at the boiling point temperature, although a method to accurately predict the droplet surface temperature (and equally the vapour pressure) is not available. In fact, liquid particles agitated by the ambient heat source release large numbers of fuel vapour, which successively strike the stagnation surface (in the case of droplet vaporising in a convective environment) or accumulate (stagnant case) due to the inertial effect of the regressing surface, hindering further evaporation in a thin layer. Such non-equilibrium evaporation is governed by the Langmuir-Knudsen evaporation law.

Bellan and Sommerfeld (1978) first introduced the non-equilibrium Langmuir-Knudsen evaporation law to model droplet vaporisation for combustion applications. The authors demonstrated that for temperatures not too close to the boiling point, the ratio between the Stefan flow velocity (the normal velocity of the particle striking the droplet surface) and the gas field velocity to be in the order between $O(10)$ and $O(10^2)$, respectively, where the equilibrium assumption is valid. However, for temperatures close to the boiling point, the two velocities become of the same order, and non-equilibrium assumptions must be introduced for evaporative mass flux to occur. Recently, Miller et al (1998) conducted numerical experiments using eight 0D droplet evaporation models, two of which were based on the Langmuir-Knudsen non-equilibrium evaporation law. The authors concluded that for small droplets and ambient gas temperature at or above the boiling point (which are typical conditions of gas turbines or most energy conversion devices), the non-equilibrium models prediction were found superior over the equilibrium evaporation models, confirming the significance of non-equilibrium effects at practical operating conditions. However, these models were not compared to experimental data, owing to the sensitivity of models with droplet size. It is anticipated that the models considered here, although they are all based on equilibrium evaporation, non-equilibrium models might be essential in furtherance the CT based formulation. In addition, departures of model predictions against experimental data must account for the errors introduced due to the lack of non-equilibrium effects.

4. MODELLING MULTICOMPONENT LIQUID FUEL EVAPORATION

4.1 Introduction

The liquid phase treatment in evaporation modelling involves various sub-models, heat and mass transfer, phase transition, and the effect of evaporation on the droplet dynamics through the drag coefficient. The droplet dynamics are modelled based on the discussion in §2.2. This section is focused on the liquid heat and mass transfer as well as the phase change sub-models. The chapter is organised as follows. In §4.2 three-liquid phase evaporation models are treated in the context of continuous thermodynamics. The appropriate phase transition analysis, both for low- and high-pressure conditions are presented in §4.3. In order to increase the accuracy and efficiency of the droplet evaporation modelling, which controls the evaporation process, variable thermotransport property correlations are derived in §4.4 (Appendix A6). The thermotransport properties that are correlated based on the composition distribution moments and some corresponding PDF parameters, in general, vary linearly with composition while their dependence with temperature is non-linear. The correlation is based on known property correlation techniques in the literature, although due to the CT formulation, the composition is accounted based on a PDF rather than a discrete species.

4.2. Vaporisation Sub-Models

The evaporation of droplets in spray combustion is very complex, and affects the entire combustion process. In this section, the liquid phase models (one 0D and two 1D models), introduced in §2.3 are modified in the framework of the CT formulation. The 0D model has its origin from the infinte diffusivity model (Law, 1976a); which employs the well mixedness assumption to accommodate multicomponent fuels. The two 1D models are based on the diffusion limit (Law and Sirignano, 1977), and the effective diffusivity model (Abramzon and Sirignano, 1989), which employ the spatial variation of composition and temperature in the liquid phase. The advantages and disadvantages of these models together with their range of applicability is discussed in §2. However, the models in this research are derived from from basic principles and the deviations from the classical models due to the CT formulation are discussed. In particular, compared to the gas phase analysis described in §3, the form of the governing equations of the liquid phase show much more noticeable departure from the traditional models. Therefore, to indicate the genuine representation of the multicomponent fuel composition and to acknowledge the departure of the resulting governing equation from the equivalent classical models, the models are preceded by *multicomponent*. However, except for the composition representation, the assumptions and the flow physics remains identical to the traditional models.

4.2.1 Multicomponent Well-Mixed Model (MWMM)

The well-mixed model is a simplification of the complex flow and transport processes inside the liquid. Instead of modelling the internal processes inside the liquid core, the well-mixed model utilises the expected effects caused by these internal processes at a very fast rate compared to the gas phase time scale. To that end, the well-mixed model assumes the composition and temperature distribution inside the liquid core to be uniform both spatially and temporally, and yet, the residual liquid phase composition and temperature varying temporally. However, the analysis for the temporal variation of composition and temperature of the liquid phase, in view of the fact that heat conduction is faster than species mass diffusion, requires great care. In fact, the heat diffusion could be orders of magnitude faster than the mass diffusion, resulting in stiff ordinary differential equations (ODEs). The difficulties and remedies in the numerical implementation of such stiff ODEs are discussed in later sections.

Consider an isolated droplet of complex liquid mixture – for example, JP8 evaporating in a stagnant or convective environment. The homologue vapour molar flux out of the liquid core due to evaporation, assuming no gas solubility in the liquid core, is the rate of change of the liquid per unit surface area of the droplet, which can be described by employing the molar density distribution as:

$$N_{J(n)} = -\frac{1}{A}\frac{d}{dt}\left(V_d \int_M X_J^l \, c_{J(n)}^l(M) W_J^l(M) dM\right) \tag{$4-1_a$}$$

The form of the homologue molar flux in equation $(4-1_a)$ is equivalent to the one described by equation $(3-20)$, although the derivation is different. In equation $(4-1_a)$, the mole fractions of the species contained in the liquid homologue J are represented by X_J^l, while V_d and A represent the droplet volume and the droplet surface area, respectively. By defining the average liquid density $c_{\bar{J}(n)}^l = \int_M c_{J(n)}^l(M) W_J^l(M) dM$, equation $(4-1_a)$ can be rewritten as:

$$N_{J(n)} = -\frac{1}{A}\left(\frac{dX_J^l}{dt} c_{\bar{J}(n)}^l V_d + X_J^l \frac{d}{dt}(c_{\bar{J}(n)}^l V_d)\right) \tag{$4-1_b$}$$

In equation $(4-1_b)$, the droplet molar mass is of the form $m_{(n)} = c_{\bar{J}(n)}^l V_d$, and using the relation for the total molar flux in equation $(3-19)$ as well as noting the volume to area ratio for a sphere is $V_d / A = R/3$, equation $(4-1)$ simplifies to:

$$N_{J(n)} = -\frac{R c_{\bar{J}(n)}^l}{3}\frac{dX_J^l}{dt} + X_J^l N_{T(n)} \tag{$4-2$}$$

It is easy to observe either from the classical model equations $(2-6)$-$(2-8)$ or the steady form of equation $(3-13)$ or equations $(3-14)$-$(3-17)$, conservation condition at the droplet surface dictates that the molar flux leaving the liquid core as represented by equation $(4-2)$, must balance the vapour molar flux described by equation $(3-20)$, which can be stated as:

$$-\frac{R c_{\bar{J}(n)}^l}{3}\frac{dX_J^l}{dt} + X_J^l N_{T(n)} = N_{T(n)} \Phi_{J(n=0)}^v - c_{\bar{J}(n)}^v D_{Jm(n)}^v \frac{\partial \Phi_{J(n=0)}^v}{\partial r} \tag{$4-3$}$$

In equation $(4-3)$, the 0^{th}-fractional composition distribution moment $\Phi^{v}_{J(n=0)} = X^{v}_{J}$, is used in order to develop an expression for the transient nature of the fractional composition distribution moments, which after rearranging yields:

$$\frac{dX^{l}_{J}}{dt} = \frac{3N_{T(n=0)}}{Rc^{l}_{J(n)}}\left[\left(X^{l}_{J} - X^{v}_{J}\right) + \frac{c^{v}_{J(n)}D^{v}_{Jm(n)}}{N_{T(n=0)}}\frac{\partial X^{v}_{J}}{\partial r}\bigg|_{R}\right] \qquad (4-4)$$

Weighting equation $(4-4)$ by the distribution variable M $n-$times, the evolution equation for the fractional composition distribution moments of the liquid phase takes the form:

$$\frac{d\Phi^{l}_{J(n)}}{dt} = \frac{3N_{T(n)}}{Rc^{l}_{J(n)}}\left[\left(\Phi^{l}_{J(n)} - \Phi^{v}_{J(n)}\right) + \frac{c^{v}_{J(n)}D^{v}_{Jm(n)}}{N_{T(n)}}\frac{\partial \Phi^{v}_{J(n)}}{\partial r}\bigg|_{R}\right] \qquad (4-5_{a})$$

Note that equation $(4-5_{a})$ is a general form, which reduces to equation $(4-4)$ for $n=0$. In addition, the derivation of equation $(4-5)$, which is solely based on the molar flux balance at the droplet surface, is very distinctive from the classical models. Rather than merely quantifying the bulk liquid lost to evaporation as in the classical models, the CT based model equation $(4-5_{a})$ quantifies the evolution of the composition as the fractional composition distribution moments of the liquid phase. However, in order to understand the distribution evolution the time derivative term on the LHS of equation $(4-5_{a})$ must be expanded as in equation $(3-5)$, which is $\Phi^{p}_{J(n)} = X^{p}_{J}\Pi^{p}_{J(n)}$, so that the composition distribution moments evolution equation take the form:

$$\frac{d\Pi^{l}_{J(n)}}{dt} = \frac{3N_{T(n)}}{Rc^{l}_{J(n)}X^{l}_{J}}\left[\left(\Phi^{l}_{J(n)} - \Phi^{v}_{J(n)}\right) + \frac{c^{v}_{J(n)}D^{v}_{Jm(n)}}{N_{T(n)}}\frac{\partial \Phi^{v}_{J(n)}}{\partial r}\bigg|_{R}\right] - \frac{\Pi^{l}_{J(n)}}{X^{l}_{J}}\frac{dX^{l}_{J}}{dt} \qquad (4-5_{b})$$

One further simplification has to be carried out in order to quantify both the evolution equations in equation $(4-4)$ and $(4-5)$ and the source term (source composition distribution moment) described by equations $(3-33)$ and $(3-34)$. This is achieved by evaluating the gradient term $\left(\partial \Phi^{v}_{J(n)}/\partial r\right)_R$ in equations $(4-4)$ and $(4-5)$ from the fractional vapour composition distribution moments profile given by equation $(3-25)$.

Before proceeding to that stage however, it must be pointed out that the classical droplet evaporation models assume an arbitrary vapour thickness, which is taken as the mixing layer between the droplet surface and the far field, where the ambient gas is very dominant. In this study, the vapour thickness is estimated as the mass transfer limit, $r^{MTL}_{J(n)} = \dot{m}_{(n)}/4\pi c^{v}_{\bar{J}(n)} D^{v}_{Jm(n)}$, which should not be confused with the mass transfer length scale described by equation $(3-35)$. In the classical droplet evaporation models, there is no mechanism to predict the film thickness, except for a burning droplet, where the vapour thickness is taken as the diffusion mixing layer between the droplet surface and the flame front. As such, the vapour thickness in the classical models is always an approximation based on personal judgement that better fits experimental data. In this study, however, depending on the ambient temperature and convective velocity conditions, a range of values $r^{MTL}_{J(n)} \sim 14R$ to $r^{MTL}_{J(n)} \sim 32R$ have been observed, compared to the $r^{MTL}_{J(n)} \leq 20R$ suggested by (Continillo and Sirignano, 1991) for similar values of ambient conditions. But, these authors neither considered the effect of the ambient conditions nor they provided explanation for their estimation. As such, further work is required to establish the exact functional dependencies of ambient condition on the film thickness. This is important as it might increase both the accuracy and efficiency of the models, in particular by reducing the computational burden during the liquid and gas phase mesh generation. From equation $(3-25_b)$, the $\left(\partial \Phi^{v}_{J(n)}/\partial r\right)_R$ term can be approximated by:

$$\begin{cases} \dfrac{\partial}{\partial r}\left(\eta_{J(n)} - \left(\eta_{J(n)} - \Phi^{vR}_{J(n)}\right)\left(1 + B_{M_{J(n)}}\right)^{\left(-r^{MTL}_{J(n)}/r\right)}\right)_R & ;n=0 \\ \dfrac{\partial}{\partial r}\left(\Phi^{vR}_{J(n)} - \dfrac{1}{B_{M_{J(n)}}}\left(\Phi^{vR}_{J(n)} - \Phi^{v\infty}_{J(n)}\right)\left[\left(1 + B_{M_{J(n)}}\right)^{\left(1-r^{MTL}_{J(n)}/r\right)} - 1\right]\right)\Bigg|_R & ;n\geq 1 \end{cases} \qquad (4-6_a)$$

Interestingly enough, the gradient of both the 0^{th} and higher fractional composition distribution moments yield similar expression as:

$$\left.\frac{\partial \Phi^{v}_{J(n)}}{\partial r}\right|_{R}=\begin{Bmatrix}\dfrac{1}{R(1+B_{M_{J(n)}})}\dfrac{(\eta_{J(n)}-\Phi^{v\infty}_{J(n)})}{(1+B_{M_{J(n)}})} & ;\ n=0\\ \dfrac{1}{R(1+B_{M_{J(n)}})}\dfrac{(\Phi^{vR}_{J(n)}-\Phi^{v\infty}_{J(n)})}{B_{M_{J(n)}}} & ;\ n\geq 1\end{Bmatrix}=\frac{(\eta_{J(n)}-\Phi^{vR}_{J(n)})}{R(1+B_{M_{J(n)}})} \qquad (4-6_{b})$$

Note that the last term dX^{l}_{J}/dt in equation $(4-5_{b})$ is nothing but equation $(4-4)$. By utilising the gradient of the fractional composition distribution moments in equation $(4-6_{b})$ together with the relation in equation $(3-20)$ both into equations $(4-4)$ and $(4-5_{b})$, the evolution equauation for the liquid composition distribution moments take the form:

$$\frac{d\Pi^{l}_{J(n)}}{dt}=\frac{3\eta_{J(n)}N_{T(n)}}{Rc^{l}_{J(n)}X^{l}_{J}}\left(\Pi^{l}_{J(n)}-\Pi^{v}_{J(n)}\right)=\left(\Pi^{l}_{J(n)}-\Pi^{v}_{J(n)}\right)/\tau_{DT} \qquad (4-7)$$

Thefore, the evolution of the liquid composition distribution moments are dependent on the amount of vapour being distilled out $\Pi^{v}_{J(n)}$, as a source term to the ambient at a distillation time of $\tau_{DT}=Rc^{l}_{J(n)}X^{l}_{J}/3\eta_{J(n)}N_{T(n)}$, where the vapour source takes the from:

$$\Pi^{v}_{J(n)}=\frac{1}{\eta_{J(n)}B_{M_{J(n)}}}\left[X^{vR}_{J}\Pi^{vR}_{J(n)}(1+B_{M_{J(n)}})-X^{v\infty}_{J}\Pi^{v\infty}_{J(n)}\right] \qquad (4-8)$$

If there is no fuel vapour at the far field, $\Phi^{v\infty}_{J(n)}=0$ because $X^{v\infty}_{J}=0$, then the Spalding mass transfer number takes the value $B_{M_{J(n)}}=X^{vR}_{J}/\eta_{J(n)}-X^{vR}_{J}$, which implies that the fractional vapour composition distribution moment source term in equation $(4-8)$ to take the form $\Pi^{v}_{J(n)}=\Pi^{vR}_{J(n)}$, which is the expected result. Unlike the classical models that relate the liquid mass removal only with an ambient temperature condition in excess of the fuel boiling point, it is interesting to observe from equation $(4-7)$ that the rate of the composition evolution (or the distillation time $\tau_{DT} = Rc^{l}_{\bar{J}(n)}X^{l}_{J}/3\eta_{J(n)}N_{T(n)}$) is mostly dependent on the total molar flux $N_{T(n)}$ described by equation $(3-21)$, which in turn is dependent on the Reynolds number through the Sherwood number and the composition gradient through the Spalding mass transfer number. For a very small $N_{T(n)}$, the distillation time becomes very large as expected, while a higher molar flux due to either high ambient convection or temperature (or a combination of both) increases the rate of the composition evolution.

On the other hand, the liquid form of equation $(3-13)$, where the transport scalar is enthalpy, describes the rate of heat energy transfer through conduction and convection as well as liquid circulation and inter-diffusion takes the form:

$$\begin{aligned}\frac{\partial}{\partial t}\left(c^{l}_{\bar{J}(n)}T\right)+\frac{1}{r^{2}}\frac{\partial}{\partial r}\left(r^{2}c^{l}_{\bar{J}(n)}v^{l}T\right)&=\frac{1}{r^{2}}\frac{\partial}{\partial r}\left(r^{2}\frac{\lambda^{l}_{\bar{J}(n)}}{Cp^{l}_{\bar{J}(n)}}\frac{\partial T}{\partial r}\right)\\&+\frac{1}{r^{2}}\frac{\partial}{\partial r}\left(r^{2}\frac{(a_{c}+b_{c}\theta^{l}_{J(n)})}{Cp^{l}_{\bar{J}(n)}}c^{l}_{\bar{J}(n)}D^{l}_{\bar{J}m(n)}\frac{\partial X^{l}_{J}}{\partial r}\right)\frac{\partial T}{\partial r}\end{aligned} \qquad (4-9)$$

In the 0D and 1D droplet evaporation models, the liquid circulation is, either ignored or approximated as an effective property with the thermal diffusion using empirical correlations. In equation $(4-9)$, the first term on the RHS is the conduction term, while the second is the inter-diffusion. However, the energy transport in the liquid phase due to mass diffusion (interdiffusion) is very small compared to the heat energy transport due to convection and conduction. Therefore, the evolution of the droplet temperature (mostly referred as the droplet heating) follows the classical model (Sirignano, 1999), except that the thermotransport properties are modified to account for the CT formulation as:

$$\frac{dT^l}{dt}=\frac{3}{c^l_{\bar{J}(n)}RCp^l_{\bar{J}(n)}}\left[\frac{\lambda^{R\infty}_{\bar{J}(n)}}{R}\frac{\ell n(1+B_{T(n)})}{B_{T(n)}}(T^{\infty}-T^{vR})-N_{T(n)}L_{\bar{J}(n)}\right] \tag{4-10}$$

The first term in the square bracket on the RHS of equation $(4-10)$ is the rate of the energy flux across the surface area of the droplet by convection, while the second term represents the rate of the energy flux across the droplet surface due to the latent heat of vaporisation. The effect of radiation is ignored. For computational purposes, equation $(4-10)$ can be cast in a similar form to equation $(4-7)$ and take the form:

$$\frac{dT^l}{dt}=\frac{-3\eta_{J(n)}N_{T(n)}}{Rc^l_{\bar{J}(n)}X^l_J}\left[\Xi^{lR}_T-\Xi^{\infty}_T\right] \tag{4-11}$$

In equation $(4-11)$, the following substitution are made, where $\Xi^{lR}_T=A_{qR}/A_{\lambda/R}$ and $\Xi^{\infty}_T=\left(A_{q\infty}-N_{T(n)}L_{\bar{J}(n)}\right)/A_{\lambda/R}$ are expressions with a unit of temperature, while $A_{q\infty}=\lambda^{R\infty}_{\bar{J}(n)}\ell n(1+B_{T(n)})T^{\infty}/RB_{T(n)}$ and $A_{qR}=\lambda^{R\infty}_{\bar{J}(n)}\ell n(1+B_{T(n)})T^{lR}/RB_{T(n)}$ represent the convective heat flux emanating from the ambient and to the convective heat flux entering the liquid droplet, respectively. It is interesting to observe that the expression $1/A_{\lambda/R}=X^l_J/Cp^l_{\bar{J}(n)}\eta_{J(n)}N_{T(n)}$ has a unit of thermal conductivity per unit length, signifying the heat transferred across the droplet radius through condution.

It must be pointed out however that equation $(4-11)$ is not as simple as it looks while solved in conjunction with equation $(4-7)$. First, the time scale for the heat diffusion is significantly different from the time scale of mass diffusion, which introduces numerical stiffness. Therefore, the coupled ODEs represented by equations $(4-7)$ and $(4-11)$ must be treated with great care. Second, there is not yet an exact method to compute the droplet surface temperature in the MWMM. In most situations, the wet-bulb temperature is assigned as the surface temperature below which there will not be any evaporation. In situations when the effective latent heat of vaporisation is considered, it is possible to use the relation $L_{eff}=L_{\bar{J}(n)}+Cp^l_{\bar{J}(n)}(T^{vR}-T^{l0})$, and compute the surface temperature, which due to phase equilibrium during evaporation $T^{lR} = T^{vR}$. For multicomponent fuels, the surface temperature is time dependent, which varies based on the component being vaporised and the amount of heat release due to the latent heat of vaporisation on the liquid surface. Unlike the single component assumptions, where the surface temperature will not exceed the boiling temperature, in multicomponent fuels, the boiling point itself is transient. The variation of boiling point with partial evaporation of components is further complicated due to variations in pressure. To that end, with the exception of the heating period, the saturation temperature or boiling point temperature T^{vR} is correlated with molecular weight as one of the thermotransport properties discussed in later sections, while the evolution equation in $(4-11)$ governs the droplet heating. Once the residual liquid composition and temperature are calculated, the extra equation to be solved to complete the droplet heating and evaporation is the droplet surface (or radius) regression rate, dR/dt.

From equations $(4-1_b)$ and $(4-2)$, it is easy to observe that the total molar flux is of the form $N_{T(n)} = -\frac{1}{A}\frac{d}{dt}(c^l_{\bar{J}(n)} V_d)$, where the liquid average molar density is in turn related to the distribution first moment as $\rho^l_{\bar{J}(n)} = c^l_{\bar{J}(n)} \theta^l_{\bar{J}(n)}$. By replacing the droplet volume and surface area as $V_d = 4\pi R^3/3$ and $A = 4\pi R^2$, respectively, and expanding through the time derivative the total molar flux takes the form:

$$N_{T(n)} = \frac{-1}{3R^2}\left[\frac{R^3}{\theta^l_{\bar{J}}}\frac{d\rho^l_{\bar{J}}}{dt} + \rho^l_{\bar{J}} R^3 \frac{d}{dt}\left(\frac{1}{\theta^l_{\bar{J}}}\right) + \frac{\rho^l_{\bar{J}}}{\theta^l_{\bar{J}}}\frac{dR^3}{dt}\right] \qquad (4-12_a)$$

Solving for the droplet regression rate, equation $(4-12_a)$ yields:

$$\frac{dR}{dt} = \frac{R}{3}\left[\frac{1}{\theta^l_{\bar{J}}}\frac{d\theta^l_{\bar{J}}}{dt} - \frac{1}{\rho^l_{\bar{J}}}\frac{d\rho^l_{\bar{J}}}{dt}\right] - \frac{N_{T(n)}}{c^l_{\bar{J}(n)}} = \frac{R}{3}\Delta_{\theta^l_{\bar{J}}\rho^l_{\bar{J}}} - \frac{N_{T(n)}}{c^l_{\bar{J}(n)}} \qquad (4-12_b)$$

Equation $(4-12)$ is unique from all the classical models in the literature, including equation $(2-15)$, due to the liquid density variability. $\Delta_{\theta_{\bar{J}}^{l}\rho_{\bar{J}}^{l}} = \dot{\theta}_{\bar{J}}^{l}/\theta_{\bar{J}}^{l} - \dot{\rho}_{\bar{J}}^{l}/\rho_{\bar{J}}^{l}$ represents the difference between the frequency of the liquid distribution mean and the liquid density due to both mass and thermal diffusion whereas the $N_{T(n)}/c_{\bar{J}(n)}^{l}$ term represents the rate of liquid volume shrinking due to evaporation per unit area. Now, with the initial conditions discussed in §2.3 and the phase equilibrium conditions discussed in §4.3, the well-mixed model is soluble. The computational implementations of the model is discussed in §5.

4.2.2 Multicomponent Effective Diffusivity Model (MEDM)

The effective diffusivity model (Abramzon and Sirignano, 1989; Delplanque et al, 1991) is a natural extension of the diffusion limit model (Hubbard et al, 1975; Law and Sirignano, 1977), which solves the spherically symmetric species and energy equation of the liquid phase using the component heat conductivity and mass diffusivity coefficients. Instead, the effective diffusivity model solves the same model equation by using the effective (thermal and mass) diffusivity coefficients of Johns and Beckmann (1966) to account for the liquid internal circulation.

In this study, unlike the traditional effective diffusivity model, the effects of different diffusion coefficients and different molecular weights are taken into account due to the inherent advantages gained through the formulation of CT theory. This is due to the fact that thermotransport properties applicable to the entire constituents are determined based on the methods described in §4.4. The conservation equations for the liqud fractional composition distribution moments and energy transport of a 1D spherically symmetric droplet can be extracted from the liquid form of equation $(3-13)$ by ignoring the convection (or the internal circulation) and the associated source terms. However, although the equation that accounts for the liquid core circulation is ignored, the main task of the MEDM is the inclusion of the circulation effect as an effective conductivity of energy transport and as an effective diffusivity of material transport.

Assuming the transported scalar $\Phi^{l}_{J(n)}$ in the liquid form of equation $(3-13)$ represents both the fractional composition distribution moments and the energy (in temperature), the governing equation for the MEDM in spherical coordinate takes the form:

$$\frac{\partial \Phi^{l}_{J(n)}}{\partial t} = \Gamma^{eff}_{\Phi^{l}_{J(n)}} \frac{1}{r^{2}} \frac{\partial}{\partial r}\left(r^{2} \frac{\partial \Phi^{l}_{J(n)}}{\partial r} \right) \qquad (4-13)$$

Equation $(4-13)$ is subject to the initial condition prescribed by equation $(4-14)$, the symmetric boundary condition at the droplet centre prescribed by equation $(4-15)$, and the interface condition at the droplet surface prescribed by equation boundary $(4-16)$, which take the forms:

$$\Phi^{l}_{J(n)}(r, t=0) = \Phi^{l0}_{J(n)} = const \qquad (4-14)$$

$$\frac{\partial \Phi^{l}_{J(n)}}{\partial r}(r=0, t) = 0 \qquad (4-15)$$

$$\frac{\partial \Phi^{l}_{J(n)}}{\partial r}(r=R, t) = \begin{cases} N_{T(n)}\left(\Phi^{l}_{J(n)} - \eta_{J(n)}\right) / c^{l}_{\bar{J}(n)} D^{l}_{Jm(n)} \\ \dot{q}^{l}_{\bar{J}(n)} / \lambda^{l}_{\bar{J}(n)} \end{cases} \qquad (4-16)$$

The boundary condition at the droplet surface described by equation $(4-16)$, both for the fractional composition distribution moments and the heat energy, signifies the spatial variation of the molar and heat fluxes, $\mathrm{N}_{\mathrm{T(n)}}$ and $\dot{q}^{l}_{\bar{J}(n)}$, respectively; across the droplet surface, where $\dot{q}^{l}_{\bar{J}(n)} = \dot{Q}^{l}_{\bar{J}(n)} / 4\pi R^{2} = \dot{Q}^{l}_{\bar{J}(n)} = \mathrm{N}_{\mathrm{T(n)}}\left(L^{eff}_{\bar{J}(n)} - L_{\bar{J}(n)}\right)$. Note that for fuel JP8, $\Phi^{l}_{J(n)}$ in equation $(4-13)$ represents twelve-liquid fractional composition distribution moments corresponding to three-homologues ($J = 1,2,3$) and four-moments ($n = 0,1,2,3$), and one energy equation in temperature. These vectors of values, which are applicable both in the vapour and liquid phases, are given as a transpose:

$$\Phi^{l}_{J(n)} = \left[\Phi^{l}_{J(0)}, \Phi^{l}_{J(1)}, \Phi^{l}_{J(2)}, \Phi^{l}_{J(3)}, T^{l}\right]^{T} \qquad (4-17)$$

In addition, the coefficient $\Gamma^{eff}_{\Phi^{l}_{J(n)}}$ in equation $(4-13)$ represents effective mass diffusivity for the composition equation or effective thermal diffusivity for the energy equation. Before introducing the form of the effective diffusivities however, it should be pointed out that the homologue mass diffusivity is simply given by $D^{l}_{Jm(n)}$, while the thermal diffusivity is of the form:

$$\alpha^{l}_{\bar{J}(n)} = \lambda^{l}_{\bar{J}(n)} / c^{l}_{\bar{J}(n)} Cp^{l}_{\bar{J}(n)} = Le^{l}_{\bar{J}(n)} D^{l}_{\bar{J}(n)} \qquad (4-18)$$

For an evaporating spherical liquid droplet, the effective mass and thermal diffusion coefficnet $\Gamma^{eff}_{\Phi^{l}_{J(n)}}$ is used not only to model the mass and thermal diffusivities due to molecular transport, but also the mass and thermal diffusivities of the viscous convection due to the liquid core circulation based on the correlation of Johns and Beckmann (1966), and Abramzon and Sirignano, 1989) as:

$$\Gamma^{eff}_{\Phi^{l}_{J(n)}} = \begin{cases} \chi_{D} D^{l}_{J(n)} \\ \chi_{\alpha} Le^{l}_{\bar{J}(n)} D^{l}_{\bar{J}(n)} \end{cases} \qquad (4-19)$$

In equation $(4-19)$, $\chi_{(\alpha;D)}$ is the Johns-Beckmann enhancement coefficient for the thermal and mass diffusivities, $Le^{l}_{\bar{J}(n)}$ is the average liquid Lewis number, $D^{l}_{J(n)}$ is the homologue liquid mass diffusion coefficient, and $D^{l}_{\bar{J}(n)}$ is the average mixture liquid mass diffusion coefficient. The correlation coefficients of the thermal and mass diffusivities take the form (Johns and Beckmann, 1966):

$$\chi_{(\alpha;D)} = 1.86 + 0.86\, tanh\left[2.225\ \ell og_{10}\left(\frac{Pe^{l}_{J(n)}\big|_{(\alpha;D)}}{30}\right)\right] \qquad (4-20)$$

The Johns-Beckmann correlation coefficient $\chi_{(a;D)}$ varies from about 1 (corresponding to droplet Peclet number $Pe^{l}_{J(n)}\big|_{(a;D)} < 10$) to 2.72 (corresponding to droplet Peclet number $Pe^{l}_{J(n)}\big|_{(a;D)} > 500$). The Peclet number is a dimensionless mass/energy transport number that characterises the relative importance between convective and mass/thermal diffusion. Abramzon and Sirignano (1989) suggested the evaluation of the liquid Peclet number using a maximum surface velocity as $Pe^{l}_{J(n)} = 2RU_s / Le^{l}_{J(n)} D^{l}_{J(n)}$, where the maximum surface velocity is estimated using an expression of the form $U_s = \left(U_{rel}\mu^{v}_{J(n)} / 32\mu^{l}_{J(n)}\right)\mathrm{Re}_d\, C_F(\mathrm{Re}_d)$, where $C_F = 12.69 / \mathrm{Re}_d^{2/3}\left(1 + B_{M_{J(n)}}\right)$ is the friction drag coefficient estimated using a droplet Reynolds number $\mathrm{Re}_d = 2RU_s\rho^{R\infty}_{J(n)} / \mu^{R\infty}_{J(n)}$.

Although Abramzon and Sirignano (1989) and Sirignano (1999) reported that the above relation is applicable for all ranges of Peclet numbers, it is clear to see that the model breaks down when the relative velocity is $U_{rel} = 0$ or when the droplet and the carrier gas motion cancel each other out, a condition however most likely to happen when a stagnant droplet vaporises in a quiescent ambient environment. In this study, the surface velocity of the droplet is approximated using the droplet surface regression rate $\dot{R}$, and the Reynolds number is calculated according to the relation $\mathrm{Re}_d = 2R\dot{R}c^{l}_{J(n)} / \mu^{l}_{J(n)}$, so that the liquid Prandtl and Schmidt numbers are used to calculate the liquid Peclet number as:

$$Pe^{l}_{J(n)}\big|_{(x)} = \begin{cases} Re_d\ Pr^{l}_{J(n)}\ \big|_{(x=\alpha)} & ;\ Pr^{l}_{J(n)} = \mu^{l}_{J(n)} Cp^{l}_{J(n)} / \lambda^{l}_{J(n)} \\ Re_d\ Sc^{l}_{J(n)}\ \big|_{(x=D)} & ;\ Sc^{l}_{J(n)} = \mu^{l}_{J(n)} / c^{l}_{J(n)} D^{l}_{J(n)} \end{cases} \qquad (4-21)$$

It is clear to observe from equation $(4-20)$ and $(4-21)$ that the MEDM has the capacity to increase the transport coefficient by a factor $\chi_{(a;D)} \cong 2.72$ as opposed to the $\chi_{(a;D)} \cong 1$ corresponding to the purely diffusive condition as shown in equation $(4-19)$.

Since equations $(4-13)$-$(4-17)$ represent a moving boundary problem for an evaporating droplet, such problems are customarily solved by first transforming the moving boundary vaporising droplet problem into a fixed boundary problem by means of variable transformation.

However, the transformed equation will generate a pseudo-convection term in the equation, where the parabolic equation in equation $(4-13)$ changes to a parabolic-hyperbolic nature. The numerical solution of such transient convection-diffusion equation is quite complex, in particular because of the abrupt changes due to the presence of the phase boundaries and the presence of high vaporisation (or the presence of high droplet surface regression rate and hence high convection) flow field. To that end, the transformations and a novel numerical method and computational procedure for solving equation $(4-13)$ are discussed in §5.

4.2.3 Multicomponent Diffusion Limit Model (MDLM)

The diffusion limit model of Law and Sirignano (1977) is a special case of the effective conductivity model. Therefore, all the model equations $(4-13)$-$(4-21)$ apply, except the effective diffusivity coefficient in equation $(4-20)$ takes the form:

$$\chi_{\alpha_i} = \chi_D = 1.0 \qquad (4-22)$$

For the gas phase analysis, in theory, either the well-mixed model or the film theory may be used in conjunction with the liquid model discussed above. However, the well mixed gas phase analysis is computationally efficient, and it is a natural choice for practical applications.

4.3. *Multicomponent Vapour - Liquid Equilibrium (MVLE)*

4.3.1 Introduction

One of the most essential aspects of droplet evaporation modelling is the determination of the mixture composition during (vapour-liquid) phase equilibrium. In particular, the percentage composition at the droplet surface, among other things, is the main determining factor on the overall behaviour of vaporisation.

The scientific literature that accounts for the research activities in fluid phase equilibria spans over 150 years (Polling et al, 2000). However, for all the thousands of articles and hundreds of monographs and books produced, reflecting the importance of the subject in the chemical and petrochemical industry separation processes, the understanding of fluid phase equilibria of mixtures containing large number of components is still at its infancy (Prausnitz, 2000; Toikka and Jenkins, 2002). For example, in order to know the partial composition of the vapour which is in equilibrium with the liquid mixture, it is no longer sufficient to know the thermotransport properties of the liquid phase at that particular composition, but in addition, it is required to know how these properties depend on composition. To know the partial properties, current methods typically differentiate experimental data with respect to composition, which inherently introduce loss of accuracy, making phase equilibria calculations more difficult and less accurate. It is impossible, and neither is it the purpose of this section to provide a review on such a large subject. However, since the most important contribution of the continuous thermodynamics framework stems in the treatment of the vapour-liquid equilibrium, a brief related background description is presented.

It is well know that the criteria for multicomponent (vapour-liquid) phase equilibrium requires (as discussed in § 2.3) that the temperature, pressure, and chemical potential of each component in the liquid phase must equal those in the vapour phase. To that end, the phase equilibrium calculations of multicomponent fuels for single homologue in the framework of CT based on the equality of chemical potentials is described by Cotterman et al (1986). However, the fundamental engineering equation for material equilibrium is the fugacity f_J^p, which is related to its departure function chemical potential $\bar{\mu}_J^p$ (Cotterman et al, 1986; Polling et al, 2000) as:

$$f_J^p = X_J^p P \, exp\left(\frac{\bar{\mu}_J^p(P,T,X_J^p) - \bar{\mu}_J^0(T,P)}{R_u T}\right) \qquad (4-23)$$

The aim here is to evaluate the fractional composition distribution moments of the vapour phase $\Phi_{J(n)}^v = X_J^v \Pi_{J(n)}^v = X_J^v$ while the liquid phase is given. In phase equilibria calculation, it is customary to seek for the K-value, where $K_J = X_J^v / X_J^l$. Although, from the view point of information, the K-value does not improve the description of phase equilibrium, it serves as a measure of the quantitative volatility distribution of the mixture. In particular, the K-values posses the advantage of direct measurement from experiments. The question of quantitative description lies wholly in the expression of the dependencies of the K-values on pressure, temperature and composition of the phases. To that end, the starting point for the determination of these dependencies is the equilibrium criterion itself, where it is required that the fugacity in each of the phases must be equal, where for each fractional composition distribution moment it takes the form:

$$f_J^v = f_J^l \qquad (4-24)$$

The simple looking equation $(4-24)$ is a very special one, so much so that in the last 80 years, the subject of phase equilibria is largely devoted to find computationally efficient and accurate correlation methods to it. As it stands, the form of equation $(4-24)$ is little practical value unless it signifies a measurable quantity. To that end, relating the fugacities to measurable values is achieved through the use of auxiliary functions; such as fugacity coefficients Θ_J^p, and activity coefficients ϖ_J^p, which are described by Muhlbaur and Raal (1995) as:

$$\Theta_J^p = f_J^p / X_J^p P \qquad (4-25)$$

$$\varpi_j^p = f_j^p / X_j^p f_j^{p0} \qquad (4-26)$$

There are essentially four possibilities when equations $(4-25)$ and $(4-26)$ are applied between the two phases, but only two of the combinations yield the modern practical methods required to develop the two main concepts of modern correlation approaches. In one of the methods, referred to afterwards as the direct VLE (DVLE) method, the fugacity is evaluated from equation $(4-25)$ applied to both phases as:

$$\Theta_j^v X_j^v P_j^v = \Theta_j^l X_j^l P_j^l \qquad (4-27)$$

However, the second method, referred to afterwards as the combined (CVLE) method applies equation $(4-25)$ to determine the fugacity of the vapour phase while the liquid phase fugacity is determined by using equation $(4-26)$ as:

$$\Theta_j^v X_j^v P_j^v = \varpi_j^l X_j^l f_j^{l0} \qquad (4-28)$$

The DVLE methods, described by equation $(4-27)$, employs suitable EOS $P = P(V, T, a, b, g^p(M))$ applicable to all components over the entire density range of both phases. By using the exact thermodynamic relation for the Helmholtz energy and the chemical potential, the fugacity coefficients are given (Appendix-A4 : A4.1) as:

$$R_u T \,\ell n \Theta_j^p(M) = \int_V^\infty \left\{ \left[\frac{\delta P}{\delta g^p(M)} \right] - \frac{R_u T}{V'} \right\} dV' - R_u T \ln Z \qquad (4-29)$$

Equation $(4-29)$ is a general form for semi-continuous mixtures, although the essence of fugacity is based on a component wise description, and $g^p(M)$ is an extensive (composition dependent) distribution that describes the mixture. The application of equation $(4-29)$ into equation $(4-27)$ is not straightforward, as the selected EOS (literally among hundreds) is required to be flexible enough to fully describe the system (P,T,V) behaviour for both phases in the (P,T,X_j^p) ranges under study.

The CVLE method on the otherhand describes the fugacity coefficient for the vapour phase by employing equation $(4-29)$ as in the DVLE method. However, to determine the liquid fugacity, the activity coefficient is related to the molar Gibb free energy $G_j^{l,E}$, using the Gibbs-Duhem equation (Muhlbauer and Raal, 1995; Polling et al, 2000), which is given here for completeness as:

$$\sum X_j^l d\, ln\varpi_j^l = \sum X_j^l d\left(\frac{G_j^{l,E}}{R_u T}\right) \qquad (4-30)$$

It is evident, from equations $(4-29)$ and $(4-30)$ that the CVLE method appears computationally expensive as it requires the development of algorithms both for the EOS and activity coefficient models. Nevertheless, the CVLE methods are proved to permit excellent representation of the liquid and vapour phases of complex systems in low to medium pressure ranges (Orbey and Sandler, 1995). Such pressure ranges could be of practical importance in modelling combustion devices. To that end, a simplified form of the combined VLE method is used to model low pressure droplet evaporation, whereas the direct VLE method is used to model high pressure droplet evaporation.

4.3.2 Low Pressure Formulation

At low pressure, the CVLE method of equation $(4-28)$ is employed. The adjustment restrictions for the low pressure case are looser compared to its high pressure counterpart, which requires suitable EOS. In fact, for the dependence of the vapour phase fugacity coefficient, any arbitrary EOS can be used. For this reason, the number of investigated and verified correlations in the literature is much greater than those for the DVLE methods. However, the disadvantage arises due to the standard state fugacity, which strongly influences the numerical value of the activity coefficient, as shown by equation $(4-26)$. The standard state fugacity f_J^{l0}, in the CT framework, is the fugacity of the fractional composition distribution moments at arbitrarily chosen pressure and temperature. The choice of the standard-state pressure and composition is dictated by convenience. To that end, two primary thermodynamic properties, namely the saturation vapour pressure P_J^{sat} and the liquid density $\rho_{J(n)}^{l}$ are used to determine the standard-state fugacity. The saturation vapour pressure depends only on temperature, composition, and to a lesser extent on pressure. The liquid density primarily depends on temperature, composition, and to a lesser extent on pressure. At low pressure, the vapour pressure is by far the most important. Therefore, the standard-state fugacity takes the form (Polling et al, 2000):

$$f_J^{l0}(T,M,P) = P_J^{sat}(T,M,P)\Theta_J^{sat}(T,M,P) \quad exp \int_{P_J^{sat}}^{P} \underbrace{\frac{V_J^{l0}(T,P)}{R_u T} dP}_{d\rho_{J(n)}^{l}} \tag{4-31}$$

Therefore, the CVLE based method for phase equilibrium described by equation $(4-28)$ together with the relations in equations $(4-25)$, $(4-26)$ and $(4-31)$ yield:

$$X_J^v P = X_J^v P_J^{sat}(T,M)\Im_J \tag{$4-32_a$}$$

In equation $(4-32_a)$, $\Im_J = \left(\Theta_J^{sat}/\Theta_J^v\right)\varpi_J^v \exp \int_{P_J^{sat}}^{P} \left(V_J^{l0}/R_u T\right) dP$ is substituted for the correction factor $\Im_J$. It is instructive to note that the CT formulation, although seeming to lump each homologous series into a bin while making its properties evolve with the distribution, the system (mixture) temperature and pressure that apply for equations $(4-31)$ and $(4-32)$ introduce some concern. For example, in situations where the system temperature and pressure exceed the critical values that constitute the distribution range, it implies that the liquid state described by the loci of the distribution does not exist, which requires the standard liquid state to take a hypothetical quantity. For subcritical (moderate pressure) values, however, the correction factor $\Im_J$ is often near unity. In particular, for sufficiently low pressures, a correction factor value of

$\Im_J = 1$ is justified. In such conditions, the activity coefficient can be set to unity, resulting in equation $(4-32)$ reducing to the familiar Raoult's law. Therefore, the low pressure (material) phase equilibrium takes the form (Maru and Moss, 2003):

$$\int_{M^+}^{M^\infty} \Phi^v_{J(n)} G^v(M) dM = \int_{M^+}^{M^\infty} \Phi^l_{J(n)} \frac{P^{sat}_{J(n)}(T,M)}{P^\infty} G^l(M) dM \qquad (4-32_b)$$

Note that equation $(4-32_b)$ represents the semi-continuous distribution function $G^p(M)$, although systems of semi-continuous vapour mixtures and continuous liquid mixtures are assumed in the modelling process. Using the classical Clausius-Clapeyron relation for the saturation vapour pressure and integrating over all the components in each distribution, the homologue molar fraction at the droplet surface yields (Appendix-A4.2):

$$\mathrm{X}^{vR}_J = K_J \mathrm{X}^l_J \qquad (4-33)$$

$$\gamma^{vR}_J = \gamma^l_J \quad ; \quad \alpha^{vR}_J = \alpha^l_J \quad ; \quad \beta^{vR}_J = \beta^l_J / \left(1 + \mathrm{A}_J \mathrm{B}_J \beta^l_J\right) \qquad (4-34)$$

In equation $(4-33)$, K_J is the K-value of the homologue, while in equation $(4-34)$, A_J and B_J are defined by correlating the saturation temperature in the Clausius-Clapeyron relation through Trouton's rule as a linear correlation with the molecular weight (as described in Appendix A4.2), which are of the form:

$$K_J = \frac{\mathrm{P}^{sat}_J}{P} \frac{\mathrm{Exp}\left[\mathrm{A}_J\left(1 - \gamma^l_J \mathrm{B}_J\right)\right]}{\left(1 + \mathrm{A}_J \mathrm{B}_J \beta^l_J\right)^{\alpha^l_J}}; \quad \mathrm{A}_J = \frac{\mathrm{L}_J}{\mathrm{R}_u}\left(1 - \frac{\mathrm{a}_{bJ}}{\mathrm{T}^{vR}}\right); \quad \mathrm{B}_J = \left(\frac{\mathrm{b}_{bJ}}{\mathrm{T}^{vR} - \mathrm{a}_{bJ}}\right) \qquad (4-35)$$

It is interesting to observe from equation $(4-34)$ that during phase equilibrium, two of the distribution parameters are identical in both the liquid and vapour phases, with the exception for the scale parameter β^p_J . On the other hand, a_{bJ} and b_{bJ} in equation $(4-35)$ represent the correlation coefficients for the homologue boiling temperatures, which are described in §4.4.

4.3.3 High Pressure Formulation

As shown by many investigators (Cotterman et al, 1985; Delplanque and Sirignano, 1993; Givler and Abraham, 1996; Zhu and Aggarwal, 2000), the (material) phase equilibrium at high pressures must be treated using an equation of the form in equation $(4-29)$ along with a suitable equation of state (EOS). In this study the general two-parameter EOS (Holderbaum and Gmehling, 1991) is used.

$$P=\frac{R_uT}{V_m-b}-\frac{a}{(V_m+\varepsilon_1 b)(V_m+\varepsilon_2 b)} \tag{4-36}$$

In equation $(4-36)$, well-known equations of state are obtained by specifying the values of ε_1 and ε_2. For example – using $\varepsilon_1=1+\sqrt{2}$ and $\varepsilon_2=1-\sqrt{2}$ recovers the Peng-Robinson equation of state (PR-EOS), while the Soave-Redlich-Kwong equation of state (SRK-EOS) is recovered for values $\varepsilon_1=1$ and $\varepsilon_2=0$. Parameters a and b are functions of temperature and composition, obtained via mixing rules and combining rules as described in Polling et al (2000), which are here modified to handle wide ranges of semi-continuous hydrocarbon mixtures as:

$$b=\sum_{s=1}^{q} X_s^p b_s^p(s)+\sum_{J=1}^{K}\int_M \Phi_{J(n=0)}^p b_J^p(M) W_J^p(M)\,dM \tag{4-37}$$

$$\begin{aligned} a=&\sum_{s=1}^{q}\sum_{s'=1}^{q} X_s^p X_{s'}^p a_s^p(s,s')+2\sum_{s=1}^{q}\sum_{J=1}^{K} X_s^p \int_M \Phi_{J(n=0)}^p a_{Js}^p(s,M) W_J^p(M)\,dM \\ &+\sum_{J^+=1}^{K'}\sum_{J=1}^{K}\int_{M^+}\int_M \Phi_{J(n=0)}^p \Phi_{J^+(n=0)}^p a_J^p(M,M^+) W_{J^+}^p(M^+) W_J^p(M)\,dM^+ dM \end{aligned} \tag{4-38$_a$}$$

In equation $(4-38_a)$, the cross-terms in the mixing rule are calculated using geometric mean average as:

$$\begin{aligned} a_s^p(s,s') &= \sqrt{a_s^p(s,s)}\sqrt{a_{s'}^p(s',s')}(1-\kappa_{ss'}) \\ a_{Js}^p(s,M) &= \sqrt{a_s^p(s,s)}\sqrt{a_J^p(M,M)}(1-\kappa_{sM}) \\ a_J^p(M,M^+) &= \sqrt{a_J^p(M,M)}\sqrt{a_J^p(M^+,M^+)}(1-\kappa_{MM^+}) \end{aligned} \qquad (4-38_b)$$

In equation $(4-38_b)$, the binary interaction parameter κ_{ij} is assumed to be constant over the range of the molecular weight in each distribution. The parameters a_J^p and b_J^p for the continuous mixtures are approximated by linear correlation with the molecular weight as:

$$\begin{aligned} a_J^p(M,M) &= a_0(T) + a_1(T)M \\ b_J^p(M) &= b_0 + b_1 M \end{aligned} \qquad (4-39_a)$$

For the discrete species, the parameters that best fit the EOS in equation $(4-36)$ are given by:

$$a_s^p(s,s) = ad_{EOS}\frac{R_u^2 T_{cr}^2}{P_{cr}}\left[1+f_w\left(1-T_r^{0.5}\right)\right]^2 \quad ; \quad b_s^p(s,s) = bd_{EOS}\frac{R_u T_{cr}}{P_{cr}} \qquad (4-39_b)$$

In equation $(4-39)$, the parameters are correlated to yield a best fit for the SRK equations of state as:

$$\begin{aligned} &a_0(T) = a_{00} + a_{01}T + a_{02}T^2 \quad ; \quad a_1(T) = a_{10} + a_{11}T + a_{12}T^2 \\ &ad_{EOS} = 0.08664 \quad ; \quad bd_{EOS} = 0.42748 \\ &f_\omega = 0.480 + 1.574\omega - 0.176\omega^2 \end{aligned} \qquad (4-40)$$

In equations $(4-39)$ and $(4-40)$, ω is the acentric factor, and the coefficients for the mixing and combining rules are given in Table A7.1.

Equation $(4-36)$ is applicable both for the liquid and vapour phases. This requires the determination of the molar volume. To that end, the parameters of the equation of state

a and b are determined according to equations $(4-37)$ and $(4-38)$, and through parameterisation, equation $(4-36)$ takes the form:

$$Z^3 + Q_1 Z^2 + Q_2 Z + Q_3 = 0 \qquad (4-41)$$

In equation $(4-41)$, the substitutions $Z = V_m P/R_u T$; $Q_1 = (\varepsilon_1 + \varepsilon_2 - 1)B^* - 1$; $B^* = bP/R_u T$, $Q_2 = (\varepsilon_1\varepsilon_2 - \varepsilon_1 - \varepsilon_2)B^{*2} - (\varepsilon_1 + \varepsilon_2)B^* + A^*$; $A^* = aP/R_u^2 T^2$; and $Q_3 = -A^* B^* - \varepsilon_1\varepsilon_2 B^{*2} - \varepsilon_1\varepsilon_2\, B^{*3}$ are used in equation $(4-36)$. The solution of equation $(4-41)$ is computed iteratively, only accepting real solutions. The possible solutions must be selected carefully according to the physics of the problem. In general, the highest root among the three real roots (or if only one root exists) represents the compressibility factor for the vapour phase, while the smallest root represents the compressibility factor for the liquid phase. The values of $\bar{a}$ and $\bar{b}$ from the mixing rules described by equations $(4-37)$ and $(4-38)$, and the solution of equation $(4-41)$ completes equation $(4-36)$ to be used in equation $(4-29)$ to calculate the phase equilibrium.

Using equation $(4-36)$ in equation $(4-29)$ the fugacity coefficient takes the form (Appendix –A4.3):

$$\begin{aligned} \ell n\Theta_j^p(M) = & \left[\frac{\bar{a}(M)}{a} - \frac{\bar{b}(M)}{b}\right]\frac{A^*}{B^*(\varepsilon_2 - \varepsilon_1)} ln\left(\frac{Z + \varepsilon_1 B^*}{Z + \varepsilon_2 B^*}\right) - ln(Z - B^*) \\ & + \frac{\bar{b}(M)}{b}\left[\frac{B^*}{(Z - B^*)} - \frac{ZA^*)}{(Z + \varepsilon_1 B^*)(Z + \varepsilon_2 B^*)}\right] \end{aligned} \qquad (4-42)$$

Note that equation $(4-42)$ is a generalised formulation applicable for any two-parameter equation of state to describe the VLE of multicomponent mixtures, in particular those containing multiple homologues. For values ε_1 and ε_2 corresponding to the PR-EOS and for parameters $\bar{a}(M)$ and $\bar{b}(M)$ representing a single homologue, equation $(4-42)$ is identical to the expression derived by Cotterman et al (1986) for paraffin. In addition, equation $(4-42)$ is applicable both for the vapour and liquid phases, provided with the exception of ε_1 and ε_2, all other variables in equation $(4-42)$ take different values for the different phases. The phase-label here is dropped to eliminate confusion.

Using equation $(4-39)$ into equation $(4-42)$ and rearranging, an equation that relates the fugacity coefficient as a linear function with the molecular weight is derived as:

$$\ell n\Theta_J^p(M) = C_{1J}^p + C_{2J}^p M \qquad (4-43)$$

In equation $(4-43)$, the following substitutions are used.

$$C_{1J}^p = \aleph_1^p \frac{a_0}{a^p} - \aleph_1^p \frac{b_0}{b^p} + \aleph_2^p \frac{b_0}{b^p} - \ell n(Z^p - B^{*p}) \qquad (4-44)$$

$$C_{2J}^p = \aleph_1^p \frac{a_1}{a^p} - \aleph_1^p \frac{b_1}{b^p} + \aleph_2^p \frac{b_1}{b^p} \qquad (4-45)$$

$$\aleph_1^p = \frac{A^{*p}}{B^{*p}(\varepsilon_2 - \varepsilon_1)} \ell n\left(\frac{Z^p + \varepsilon_1 B^{*p}}{Z^p + \varepsilon_2 B^{*p}}\right) \qquad (4-46)$$

$$\aleph_2^p = \frac{B^{*p}}{(Z^p - B^{*p})} - \frac{Z^p A^{*p})}{(Z^p + \varepsilon_1 B^{*p})(Z^p + \varepsilon_2 B^{*p})} \qquad (4-47)$$

Rewriting equation $(4-43)$ both for the vapour phase and liquid phase, and taking the difference between the fugacity coefficients, the following equation is derived as:

$$\ell n\left(\frac{\Theta_J^l(T,P,M)}{\Theta_J^v(T,P,M)}\right) = \Delta C_{1J} + \Delta C_{2J} M \qquad (4-48_a)$$

In equation $(4-48)$, $\Delta C_{1J} = C_{1J}^l - C_{1J}^v$ and $\Delta C_{2J} = C_{2J}^l - C_{2J}^v$, and the values of $C_{1J}^{(l,v)}$ and $C_{2J}^{(l,v)}$ are calculated based on equations $(4-44)$ and $(4-45)$, respectively.

Equation $(4-48)$ is nothing but an equation that gives the ratio of the fugacity coefficients as an exponential form, whose power is a linear function of the molecular weight – the essential independent variable at the heart of the CT based modelling. Note that equation $(4-27)$ can be expressed as $X_J^v = (\Theta_J^l / \Theta_J^v) X_J^l$. Similarly, equation $(4-48_a)$ can be expressed in a form containing the ratio $(\Theta_J^l / \Theta_J^v)$ as:

$$\frac{\Theta_J^l(T,P,M)}{\Theta_J^v(T,P,M)} = Exp(\Delta C_{1J} + \Delta C_{2J} M) \qquad (4-48_b)$$

Applying equation $(4-48_b)$ into equation $(4-27)$, the CT form of (material) phase equilibrium takes the form:

$$\int_{M^+}^{M^\infty} X_J^v G^v(M) dM = \int_{M^+}^{M^\infty} X_J^l \frac{\Theta_J^l(T,P,M)}{\Theta_J^V(T,P,M)} G^l(M) dM \qquad (4-49_a)$$

Using equations $(3-1)$, $(3-4)$, and $(4-48)$, equation $(4-49_a)$ can be rewritten as:

$$X_J^{vR} = \int_{M^+}^{M^\infty} X_J^l \frac{Exp\left[\Delta C_{1J} + \gamma_J^l \Delta C_{2J}\right]}{\beta_J^l \Gamma(\alpha_J^l)} \left(\frac{M-\gamma_J^l}{\beta_J^l}\right) Exp\left[-\left(\frac{M-\gamma_J^l}{\beta_J^l}\right)\left(1-\beta_J^l \Delta C_{2J}\right)\right] dM \qquad (4-49_b)$$

Using Euler's definition for the gamma function, and integrating $(4-49_b)$ yields:

$$X_J^{vR} = K_J X_J^l \left(Exp\left[\Delta C_{1J} + \gamma_J^l \Delta C_{2J}\right] / \left(1-\beta_J^l \Delta C_{2J}\right)^{\alpha_J^l} \right) \qquad (4-49_c)$$

Similarly, the high pressure counterpart of the K-value in equation $(4-35)$ becomes:

$$K_J = Exp\left[\Delta C_{1J} + \gamma_J^l \Delta C_{2J}\right] / \left(1-\beta_J^l \Delta C_{2J}\right)^{\alpha_J^l} \qquad (4-49_d)$$

Weighting equation $(4-49_b)$ n-times yields the moment of the fuel distribution, whose parameter in the liquid and vapour phase can be related as:

$$\gamma_J^{vR} = \gamma_J^l \quad ; \quad \alpha_J^{vR} = \alpha_J^l \quad ; \quad \beta_J^{vR} = \beta_J^l \Big/ \left(1 - \beta_J^l \Delta C_{2J}\right)^{\alpha_J^l} \tag{4-50}$$

Similar to the low pressure case described by equation $(4-34)$, only the distribution scale parameter characterises the phase change at the droplet surface as shown in equation $(4-50)$.

4.4 Fuel Mixture Thermotransport Properties

Computational modelling techniques that are employed to simulate the flow and transport characteristics of fuels in combustion devices are heavily reliant on the presence of highly accurate data for the mixtures and materials thermotransport properties. But, in most situations, highly accurate thermotransport properties are often tedious, expensive and dangerous to gather experimentally or very complex to predict computationally. Therefore, most computational or correlation techniques for the predictions of mixtures thermotransport properties are based on a largely sparse experimental data set of limited ranges of temperatures and pressures or based on empirically determined data sets for the pure components that constitute the mixture.

In general, the thermotransport properties are assumed to vary with temperature, pressure, and composition. To understand their variability and to design empirical correlations with the fractional composition distribution moments, detailed investigation is carried out for fuel JP8, which is also applicable for most liquid hydrocarbons. To save space and keep the continuity of the discussion on the liquid phase modelling, the complete procedure for thermotransport properties correlations is presented in Appendix A6, and the interested reader is advised to refer to that section of the thesis.

5. NUMERICAL AND COMPUTATIONAL MODELLING

5.1. *Introduction*

In recent years, much effort is devoted to the development of massive, generally parallel computer codes for predicting realistic spray combustion applications. The development of such codes requires implementation of stable and accurate numerical models in a modular manner to be integrated with the main flow solver.

In hybrid (Eulerian-Lagrangian) two phase flow computations, the gas phase and the liquid phase are analysed in separate modular codes, where the coupling of the two phases is accounted by source or sink terms as described by equation $(3-13)$. The incorporation of models that include the complex turbulent gas phase flow laden with millions of liquid droplets or sprays, which in turn constitute sub-models of the liquid break-up, droplet collusion, droplet coalesce, film flow and wall-film interaction, liquid heating and evaporation, and chemical kinetics certainly prove to be computationally intensive. In fact, each computations are performed in a time slice manner in a sense that the source terms provided by the droplet calculations for the n^{th} time level are used in the $(n+1)^{th}$ time level of the gas phase calculations. This is achieved after proper interpolation of the interactions (coupling) between the gas phase and liquid phase models. The objective of this work is to develop a comprehensive droplet evaporation model in a suitable form to be integrated with gas phase flow solvers as prescribed by equation $(3-13)$. However, this section is only concerned on the numerical issue of the liquid phase, while the gas-phase flow and transport is beyond the scope of this work.

The spray or liquid phase modelling employs various models, which fall under the droplet dynamics or evaporation sub-models. The numerical issues associated with the droplet dynamics are described in § 2.3.7. For completeness, however, this section recapitulates the salient features of those droplet dynamics models while concentrating on the evaporation (heat and mass transfer) sub-models, described in § 3 and §4. The system of liquid phase dynamics and evaporation sub-models to be solved are:

- The liquid droplet momentum described by equation $(2-1)$, and the droplet trajectory described by equation $(2-3)$,
- The liquid fractional composition distribution moments evolution described by equations $(4-4)$ and $(4-5)$ for the MWMM, equation $(4-13)$ for the MEDM, and $(4-13)$ with condition in equation $(4-22)$ for the MDLM,
- The droplet regression rate (or liquid mass balance) described by equation $(4-12)$, and
- The liquid energy equation described by equation $(4-11)$ for the case of the MWMM, equation $(4-13)$ for the case of the MEDM, and equation $(4-13)$ with condition in equation $(4-22)$ for the case of MDLM.

In general, the governing equations describing the droplet momentum/trajectory, the droplet surface regression rate, the MWMM composition and energy transport equations are ODEs, which can be solved by using accurate ODE-solvers, like SVODE (Hindsmarsh, 1983). SVODE solves the initial value problem of stiff or non-stiff systems of ODEs with variable coefficients. The solution procedure for SVODE is described elsewhere (Wang et al, 2002).

On the other hand, the fractional composition distribution moments and energy equations of the MEDM and MDLM described, respectively, by equation $(4-13)$ and $(4-13)$ with conditions in equation $(4-22)$, subject to the initial and boundary condition given by equations $(4-14)$-$(4-18)$ are parabolic PDEs. Due to the complexity of the boundary conditions arising from the non-linear phase transition of multicomponent systems and the presence of an intrinsic moving interface due to evaporation, however, these simple looking PDEs are proved very difficult to solve (Sirignano, 1999). Therefore, the development of stable, accurate, and most importantly, efficient numerical integration schemes are essential. Considering the thousands and millions of droplets present in practical sprays, the importance of efficient numerical schemes can not be understated. It is important to emphasise that the parabolic PDEs in equation $(4-13)$ that describes the fractional composition distribution moments and the energy transport of the liquid phase, in view of the moving boundary relative to a fixed reference frame, generates a pseudo-convective interface velocity, resulting in hyperbolic-parabolic PDEs that are very complicated to solve.

To that end, the numerical method of lines (MOL), which is one of the most popular techniques in solving low dimensional PDEs in an attempt to take advantage of the robust and accurate open source ODE solvers, is employed in this investigation. In particular, the MOL framework has the distinct advantage to develop very general purpose computer software for solving broad classes of problems. In addition, the MOL has the capability to be interfaced with other software and it can also be integrated with new and efficient developments. For example – to improve computational accuracy and efficiency, the MOL is being exploited in conjunction with adaptive mesh refinement (AMR) technology for various applications (Vande Wouwer et al, 2001).

5.2. Adaptive Method of Lines (AMOL)

The numerical method of lines (MOL) is a comprehensive approach to the solution of time dependent PDEs by reducing the PDEs to systems of ODEs or DAEs (Vande Wouwer et al, 2001). The standard MOL involves two steps. The first step is the spatial discretisation, where terms in the governing PDEs involving spatial derivatives are approximated by using, for example - finite difference method (Mitchell, 1980), finite element method (Fairweather, 1973), or collocation method (Madsen and Sincovec, 1979; Keast and Muir, 1991). Such discretisation results in semi-discrete ODEs (discrete in space and continuous in time) or commonly known as differential-algebraic equations (DAEs). Therefore, the first step reduces the initial and boundary value problem (IBVP) of the governing PDEs into ODEs. The second step is the time integration. The resulting systems of ODEs are integrated using standard DAE solvers, such as DASSL (Petzold, 1982), GEARIB (Hindmarsh, 1976); SVODE (Hindsmarsh, 1983). Most of the ODE/DAE solvers developed in the last couple of decades have the capability to automatically adapt the time step size (and possibly the order of the integration formula) while providing stability and better accuracy.

Symptomatic to the success in the time adaptation, discretisation of the spatial domain of a system of PDEs using adaptive methods have drawn considerable attention in recent years (Vande Wouwer et al, 2001). The use of AMR techniques provides a far more efficient way to treat problems with solutions exhibiting rapid spatial variations, for example – phase boundaries, shock waves, and contact discontinuities. However, to this author's knowledge, there are only few fully adaptive MOL packages that have the capability to control both temporal and spatial errors. These (experimental) fully adaptive MOL codes include PDEXPACK due to Nowak et al (1996); HPSIRK and HPDASSL due to Moore (1995), BACOL due to Wang (1999) and HPNEW due to Moore (2001). However, despite the extensive investigations and ongoing developments in adaptive MOL, there are relatively few robust, accurate, efficient, and general purpose software packages for the solution of PDEs, like the one encountered in droplet evaporation.

Therefore, the purpose of this numerical and computational modelling is to design a framework package that is robust, accurate, and efficient with the aim of simulating spray dynamics, evaporation, and combustion. However, in this study, the practical application is restricted to only droplet evaporation. To that end, in the following section, the droplet evaporation models developed in §4 will be further refined in a form more suitable to the development of a fully adaptive MOL.

5.2.1 Droplet Evaporation with Moving Interface

For an evaporating droplet, equations $(4-13)$-$(4-16)$ represent a moving boundary with an interface velocity described by equation $(4-12)$. In order to solve the problem in a fixed coordinate system, a transformation to a frame of reference moving with the interface must be carried out. Ideally, referring to Figure 5.1, the liquid phase and the vapour phase can be described in a non-dimensional liquid-space and vapour-space as:

$$\begin{aligned}
\zeta^{l} &= \frac{r-R_L}{R_C-R_L} = \frac{r}{R(t)} \qquad ; \qquad r < R(t) \\
\zeta^{v} &= \frac{r-R_C}{R_R-R_C} = \frac{r'}{R'(t)} \qquad ; \qquad r > R(t)
\end{aligned} \qquad (5-1_a)$$

In equation $(5-1_a)$, the liquid-space ζ^{l}, and the vapour space ζ^{v} are treated separately. It further implies that the liquid-space with boundaries at $\zeta^{l}|_{r=R_L}=0$ and $\zeta^{l}|_{r=R_C}=1$ always fall in the range $0 \le \zeta^{l} \le 1$, which is the region between the droplet centre and the droplet surface. Similarly, the vapour-space with boundaries at $\zeta^{v}|_{r=R_C}=0$ and $\zeta^{v}|_{r=R_R}=1$ always fall in the range $0 \le \zeta^{v} \le 1$, which corresponds to the region between the droplet surface and the far field ambient condition.

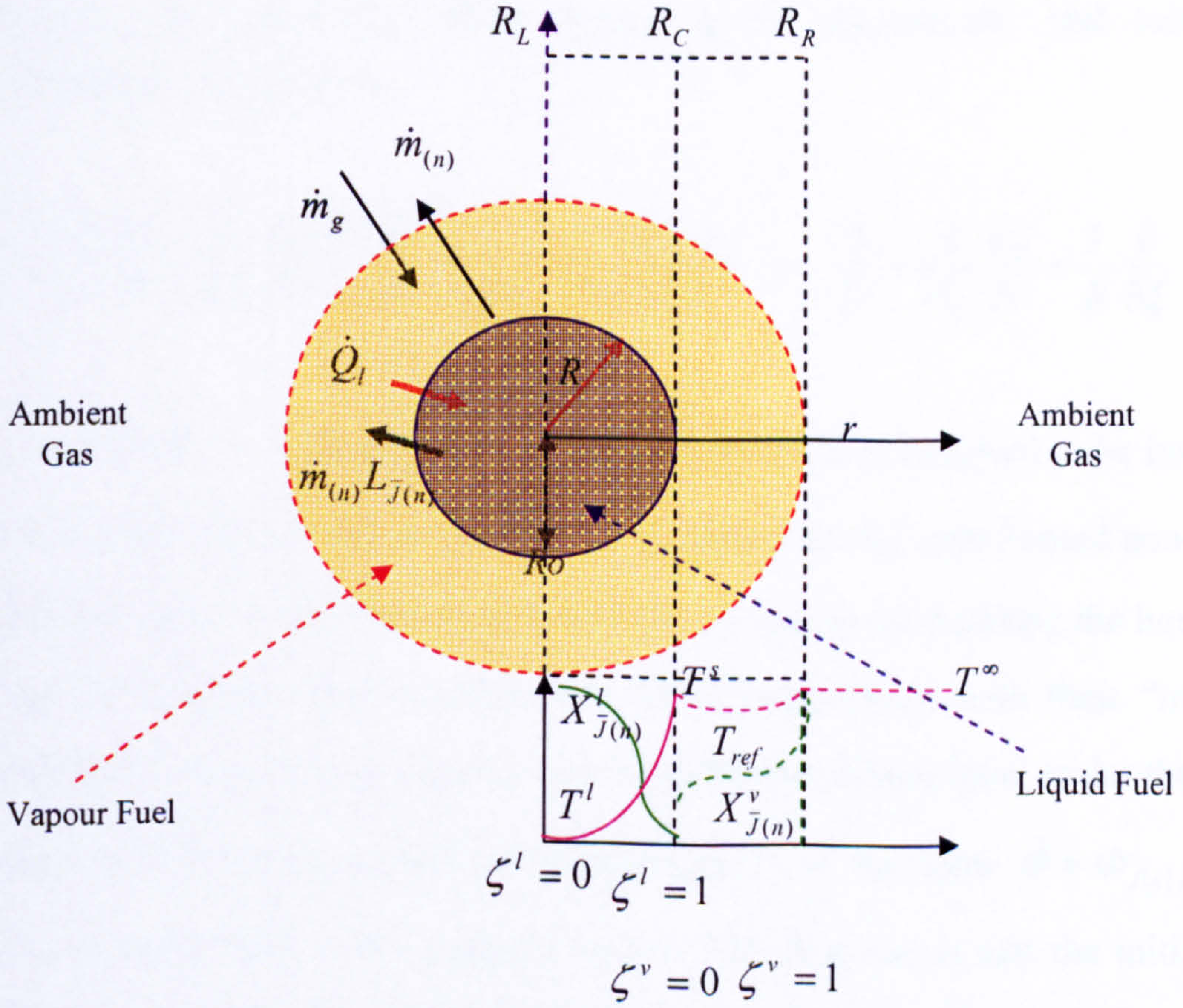

Figure 5.1 Droplet evaporation with a coordinate system incorporating a moving boundary

However, in the current low dimensional droplet evaporation modelling, the vapour phase approximation follows the formulation discussed in §3. Therefore, in this study, the focus will be on the fractional composition distribution moments and temperature evolution of the liquid phase, and the temporal variation of the vapour composition and temperature field at the droplet surface. Hence, in accordance with the liquid-space and vapour-space transformations, a non-dimensional time $\tau_{\bar{\Phi}^l_{J(n)}}$, which is normalised by the mass and thermal diffusion time $t^{diff}_{\bar{\Phi}^l_{J(n)}}$ can be defined as:

$$\tau_{\bar{\Phi}^l_{J(n)}} = \int_0^t \frac{dt'}{t^{diff}_{\bar{\Phi}^l_{J(n)}}} \qquad ; \qquad t^{diff}_{\bar{\Phi}^l_{J(n)}} = \frac{R^2(t')}{\Gamma^{eff}_{\Phi^l_{J(n)}}} \qquad (5-1_b)$$

With the variable transformation in equations $(5-1)$ and employing the chain rule for the time and space derivatives (dropping the superscripts and subscripts), the differentials take the form:

$$\frac{\partial}{\partial t} = \frac{\partial}{\partial \tau}\frac{\partial \tau}{\partial t} + \frac{\partial}{\partial \zeta}\frac{\partial \zeta}{\partial r}\frac{\partial r}{\partial \tau}\frac{\partial \tau}{\partial t} = \left[\frac{\partial}{\partial \tau} + \frac{\zeta}{R}\frac{\partial R}{\partial \tau}\right]\frac{\Gamma}{R^2} \quad ; \quad \frac{\partial}{\partial r} = \frac{\partial}{\partial \zeta}\frac{\partial \zeta}{\partial r} = \frac{1}{R}\frac{\partial}{\partial \zeta} \qquad (5-1_c)$$

In equation $(5-1_c)$, the non-dimensional liquid-space is assumed to be invariant in the non-dimensional time-space as $\partial\zeta/\partial\tau = 0$. Based on the transformed non-dimensional coordinate system described by equation $(5-1)$, and by normalising the liquid fractional composition distribution moments and liquid temperature with their "initial values" counterparts, described by equation $(4-14)$, the non-dimensional scalar that defines the evolution of the composition and temperature is of the form $\hat{\Phi} = \Phi^l_{J(n)}/\Phi^{l0}_{J(n)}$. Two issues must be clear at this stage, however. The first one is that the initial values are updated every time step during numerical computations. The second one is that the scalar $\hat{\Phi}$, while considering fuel JP8, has in fact 13-entries corresponding to the 12-normalised fractional composition distribution moments ($J = 1,2,3$ and $n = 0,1,2,3$) and the normalised liquid temperatures. Therefore, the required non-dimensional governing equation in the transformed coordinate system takes the form:

$$\frac{\partial\hat{\Phi}}{\partial\tau}=-\frac{\zeta}{R}\frac{\partial R}{\partial\tau}\frac{\partial\hat{\Phi}}{\partial\zeta}+\frac{1}{\zeta^2}\frac{\partial}{\partial\zeta}\left(\zeta^2\frac{\partial\hat{\Phi}}{\partial\zeta}\right) \tag{5-2$_a$}$$

In equation $(5-2_a)$, it is easy to observe that the droplet regression rate described by equation $(4-12)$ in the actual coordinate system can be used to determine the value of the term $\partial R/\partial\tau=\left(R^2/\Gamma\right)\frac{dR}{dt}$. As such, equation $(5-2_a)$ can further be simplified as:

$$\frac{\partial\hat{\Phi}}{\partial\tau}=\left(\frac{2}{\zeta}-\frac{\zeta}{R}\frac{\partial R}{\partial\tau}\right)\frac{\partial\hat{\Phi}}{\partial\zeta}+\frac{\partial^2\hat{\Phi}}{\partial\zeta^2} \tag{5-2$_b$}$$

Similarly, the initial and boundary conditions described by equations $(4-14)$-$(4-16)$, when used in the transformed coordinate take the form:

$$\hat{\Phi}(\zeta,\tau=0)=1 \tag{5-3}$$

$$\left(\frac{\partial\hat{\Phi}}{\partial\zeta}\right)_{\zeta=0}=0 \tag{5-4}$$

$$\left(\frac{\partial\hat{\Phi}}{\partial\zeta}\right)_{\zeta=1}=\begin{cases}\hat{\dot{m}}\left(\hat{\Phi}-\hat{\eta}\right)/3\hat{R}\\ \hat{Q}/3\hat{R}\end{cases} \tag{5-5}$$

The initial condition for the normalised composition and the normalised liquid temperature are given by equation $(5-3)$. The normalised radius $\hat{R}=R/R_0$, where R_0 is the initial (original) droplet radius, and the normalised fractional molar flux $\hat{\eta}$ is computed based on the fractional molar flux of each homologue at successive time levels. The dimensionless rates of the molar mass leaving the droplet and heat entering the droplet, $\hat{\dot{m}}$ and $\hat{Q}$, respectively, are of the form:

$$\hat{\dot{m}} = \frac{\dot{m}_{(n)}}{\frac{4}{3}\pi R_0^3 c^{l}_{\bar{J}(n)}} \frac{\Pi^{l}_{J(n)}}{\Pi^{l0}_{J(n)}} \frac{R_0^2}{\Gamma_{\Phi^{l}_{J(n)}}} \qquad (5-6_a)$$

$$\hat{Q} = \frac{\dot{Q}_{\bar{J}(n)}}{\frac{4}{3}\pi R_0^3 c^{l}_{\bar{J}(n)} Cp^{l}_{\bar{J}(n)} T^{l0}} \frac{R_0^2}{\Gamma_{\Phi^{l}_{J(n)}}} \qquad (5-6_b)$$

In equation $(5-6)$, the appropriate effective diffusivities described by equation $(4-19)$ are used. The actual rate of molar mass flowing out of the liquid is determined by using the relation for the total molar flux given by equation $(5-7)$.Similarly, the actual rate of heat entering the droplet is determined by simplifying the gas phase analysis in equations $(3-27)$-$(3-29)$, which is of the form described by equation $(5-7)$.

$$\dot{m}_{(n)} = 4\pi R^2 N_{T(n)} \quad ; \qquad \dot{Q}_{\bar{J}(n)} = \dot{m}_{(n)} \left[\frac{Cp^{R\infty}_{\bar{J}(n)} \left(T^{\infty} - T^{vR} \right)}{B_{T_{(n)}}} - L^{eff}_{\bar{J}(n)} (T^{vR}) \right] \qquad (5-7)$$

Note that in equation $(5-2_b)$, a substitution as in equation $(5-8)$ gives a dimensionless pseudo-convective velocity vector, which represents the relative movement between the interface and the grid as:

$$V_R = \left(\frac{2}{\zeta} - \frac{\zeta}{R} \frac{\partial R}{\partial \tau} \right) = \left(\frac{2}{\zeta} - \frac{\zeta}{R} \frac{dR}{dt} t \right) \qquad (5-8)$$

Note that equation $(5-8)$ is in general non-linear owing to the presence of a non-linear droplet regression rate dR/dt. To that end, the final form of the liquid phase heat and mass transfer sub-model for an evaporating droplet with internal circulation (reinstating the subscripts and superscripts) takes the form:

$$\left(\hat{\Phi}^{l}_{J(n)} \right)_{\tau_{\bar{\Phi}^{l}_{J(n)}}} = V_R \left(\hat{\Phi}^{l}_{J(n)} \right)_{\zeta^{l}} + \left(\hat{\Phi}^{l}_{J(n)} \right)_{\zeta^{l}\zeta^{l}} \qquad (5-9)$$

Equation $(5-9)$ is a transient hyperbolic-parabolic (convection-diffusion) equation that involves a sharp density and velocity gradient at the phase interface, and hence very difficult to solve. Although, various sophisticated and accurate methods are developed to solve this type of problems (Boden 1997, Toro, 1997; Sirignano, 1999), the computational resources requirement is very high. Therefore, it is difficult to include such computationally expensive approaches in the simulation of practical combustion devices to numerically simulate the dynamics, evaporation and chemical kinetics of multicomponent sprays that consist of thousands and millions of droplets.

In this study, the most popular and freely available, but standard, MOL solver PDECOL (Madsen and Sincovec, 1979; Keast and Muir, 1991) is considered for further improvement so that it will be used to simulate the complex processes in sprays. The effort in the extension and development of PDECOL resulted in a new code called AMOLBSC. The details of the new fully Adaptive Method of Lines using Basis Spline Collocation (AMOLBSC) is described in Appendix A5. In the section to follow, only the most salient numerical and computational issues related to AMOLBSC are discussed.

5.3. *Computational Issues*

5.3.1. Background

In AMOLBSC, equation $(5-9)$ along with the prescribed initial and boundary conditions in equations $(5-3)$-$(5-5)$ are discretised using collocation scheme based on basis spline (B-spline) interpolation (de Boor, 1978; Madsen and Sincovec, 1979; Keast and Muir, 1991). As such the interval $\Lambda=[\zeta_C,\zeta_R]=[0,1]$ is divided into $N+1$ subintervals or meshes by using a set of distinct breakpoints (knots). In each subinterval, the unknown vector valued function $\hat{\Phi}^l_{J(n)}$ in equation $(5-9)$ is approximated by a polynomial of order p by requiring both $\hat{\Phi}^l_{J(n)}$ and its highest derivatives are continuous across the breakpoints so that the approximate solution

$\tilde{\Phi}(\tau,\zeta)=\sum_{j=0}^{N}\tilde{\sigma}_j(\tau)\tilde{B}_j^p(\zeta)$ satisfies the PDEs in $(5-9)$ along with the prescribed initial and boundary conditions in equations $(5-3)$-$(5-5)$. The approximate solution $\tilde{\Phi}$ is now decoupled into the time-dependent coefficients $\tilde{\sigma}_j$ and the space dependent B-splines $\tilde{B}_j^p$ of maximum continuity. When $\tilde{\Phi}$ is used in equations $(5-9)$ and $(5-3)$-$(5-5)$ at $p-1$ designated collocation points, it resulted in semi-discrete systems of equations (see equation $(A5-10)$ in Appendix 5) of the form:

$$\tilde{P}(\tau,\tilde{\sigma},\dot{\tilde{\sigma}})=\tilde{F}(\tau,\tilde{\sigma})\ \dot{\tilde{\sigma}}(\tau)\ -\ \tilde{H}(\tau,\tilde{\sigma})=0 \qquad (5-10)$$

In equation $(5-10)$, for $N+1$ number of meshes and B-spline representation of order p with $p-1$ collocation points in each interval, there are $N_C=N(p-1)+2$ gaussian collocation points in the computational domain $\Lambda=[0,1]$. Obviously, N_C equations are required to determine the vector of the B-spline coefficients (see equation $(A5-14)$ in Appendix 5) in a form:

$$\tilde{\sigma}_{n+1}^{j+1}=\tilde{\sigma}_{n+1}^{j}-\tilde{M}\tilde{P}(\tau_{n+1},\tilde{\sigma}_{n+1}^{j},\frac{\tilde{\alpha}}{\Delta\tau_{n+1}}\tilde{\sigma}_{n+1}^{j}+\tilde{\beta}) \qquad (5-11)$$

One of the most important features of the B-spline functions is that only p of them have non-zero values at any point $\zeta\in[0,1]$. This is equivalent to saying that the value of the N_C approximate equations for the PDEs in $(5-9)$ or its spatial derivatives at some interior point depends only on p B-spline coefficients $\tilde{\sigma}_j$. Such compact support of B-splines, for PDEs of the form in $(5-9)$ along with either of the commonly used types of boundary conditions (Drichlet, Neuman or Robbin) yield an almost block diagonal (ABD) matrices, which highly improves the efficiency of the method in comparison to most other discretisation techniques (Keast and Muir, 1991).

Note that equation $(5-11)$ corresponds to the approximation computed in a piecewise polynomial subspace of degree p. A posterior error estimate, both globally and locally, can be established by generating a similar equation as in $(5-11)$ but for a piecewise polynomial subspace of degree $p+1$ (see equation $(A5-18)$ in Appendix 5), where both the global and local posterior spatial error estimates, respectively, $\|e\|$ and $\|e_i\|$, are calculated at each *successful* time step. In the following section, the global error along with the distribution of the local errors across the mesh is used to design an adaptive mesh refinement strategy.

5.3.2. Strategy for Adaptive Mesh Refinement (AMR)

Any adaptive strategy has to answer the three basic questions of *when*, *where*, and *how* to refine the mesh. In general, mesh refinement is necessary *when* the solution obtained is not satisfactory. The accuracy of the solution may be assessed by use of (posterior) error estimates and in some cases by employing heuristic considerations so that the reliability of the methods may be tested. Therefore, once it has been judged necessary to refine, the posterior error estimates can be used *where* the refinement should occur. However, before the posterior error estimates are employed to decide where the position of mesh refinement is, it is essential to choose the suitable refinement scheme or a combination of refinement schemes to use, and *how* to proceed. In this investigation, an h-type refinement scheme is adopted mainly due to the need to resolve the behaviour of evaporation close to the droplet surface by refining any coarse meshes present. Although h-refinement techniques are based on a simple procedure of subdivision of meshes, the prerequisite for refinement is very complex, and it requires the analysis of the resulting spatial errors at each mesh interval (or globally) along with the time integration scheme adopted.

For a fixed and uniform mesh using a collocation method with B-splines, computational evidence (Adjerid et al, 1992) shows that the spatial L^2-norm error to be

$O(\overset{N}{\underset{i}{max}}\,\Delta\zeta_i^{p+1})$, where $\Delta\zeta_i = [\zeta_i - \zeta_{i-1}]_{i=1}^{N}$. This is equivalent to saying that in each interval $\Delta\zeta_i$, the L^2-norm error estimate converges to the exact error as:

$$\lim_{\Delta\zeta_i \to 0}\left\|\tilde{\Phi} - \bar{\tilde{\Phi}}\right\|_2 = \lim_{\Delta\zeta_i \to 0}\left\{\int_{\zeta_{i-1}}^{\zeta_i}\left(\tilde{\Phi} - \bar{\tilde{\Phi}}\right)^2 d\zeta\right\}^{1/2} \to \left\|\tilde{\Phi} - \Phi\right\|_2 = \left\{\int_{\zeta_{i-1}}^{\zeta_i}\left(\tilde{\Phi} - \Phi\right)^2 d\zeta\right\}^{1/2} \qquad (5-12)$$

In equation $(5-12)$, the vector valued function $\Phi(\tau,\zeta)$ is the exact solution. Therefore, the order of convergence in L^2-norm for the error estimates can be taken as:

$$\|e_i\| \propto \Delta\zeta_i^{p+1} \qquad ; \qquad \|e\| \propto \Delta\zeta^{p+1} \qquad (5-13)$$

In addition, using a quasi-uniform mesh for a boundary value problem for ODEs, Ascher et al (1995) have shown that as $N \to \infty$ (for all meshes satisfying $\Delta\zeta_i \le K_{constant}\,\overset{N}{\underset{i}{min}}\,\Delta\zeta_i$), a numerical scheme of order $p+1$ to yield an error of order $O(1/N^{p+1})$. It is assumed that the same property holds for PDEs, where the global error estimate is $\|e\| \propto 1/N^{p+1}$. Once the approximate error and its order are computed at each successful time step, some parameters that can characterise the error distribution can be defined in order to make decisions on the mesh refinement procedure.

To that end, let $\varepsilon_e^m = \overset{N}{\underset{i=1}{max}}\sqrt[p+1]{\|e_i\|}$ and $\varepsilon_e^a = \sum_{i=1}^{N}\sqrt[p+1]{\|e_i\|}\;/N$, respectively, represent a measure of the maximum and the average subinterval error estimates. Therefore, the ratio $\varepsilon_R = \varepsilon_e^m / \varepsilon_e^a$ can be used as an indicator for the error distribution over the mesh subinterval. For example, Ascher et al (1995) defined meshes with $\varepsilon_R \le 2$ to be asymptotically distributed and used it as a test to invoke refinement. Therefore, in theory, the first test to invoke refinement, if it is the initial time step or if $\|e\| > 1$, is when the condition $\varepsilon_R \le 2$ is not satisfied.

However, there are additional practical issues to be satisfied. For example – the frequency of remeshing and the order of the BDF time-integration ($q < 7$) must be taken into consideration to avoid interpolation of solutions from a different mesh structure and to avoid computational inefficiency. Therefore, the minimum or maximum number of meshing frequencies must be established. In order to determine the number of meshing frequencies, a measure of an *ad hoc* error propagation technique is employed on the assumption, in most situations, the normalised error estimate increases gradually. This is valid due to the fact that after the first time step or first remeshing, the normalised error estimate must be in the range $0 < h_1 < \|e\| < h_2 < 1$, while after repeated remeshing, numerical experimentation suggests the normalised error to be stable in the range $0.23 < \|e\| < 0.47$, and it is used here as a second test for remeshing.

Another important issue is the number of nodes to be deleted or inserted after the first test (and possibly the second test) is satisfied. In this case, it is assumed that both the time step size and the normalised spatial error estimate are known. In addition, if the first test ($\varepsilon_R \leq 2$ and $\|e\| > 1$) fails in the first time step, the same number of mesh is used on the assumption that such failure is due to the current mesh being not well distributed rather than requiring mesh deletion or insertion. The number of remeshing attempts is selected judiciously ($r < q+1$) based on the order of the BDF time-integration ($q < 7$). It must be pointed out that the approximate solution with the new mesh number (N^*) might fail one of the spatial error tests described earlier. Since the mesh is asymptotically distributed in most situations, the first test $\varepsilon_R \leq 2$ plays a minimal role in predicting N^*. Instead, from $\|e\| \propto 1/N^{p+1}$ and $0.23 < \|e\| < 0.47$, a normalised error estimate of the new mesh can be established at a priori as $\|e^*\| \propto (N^*)^{-(p+1)}$. But, the second test requires that the new normalised error to be bounded as $0.23 < \|e^*\| < 0.47$, where $0.23 = \|e^*_{min}\|$ and $\|e^*_{max}\| = 0.47$. Therefore, dividing $\|e\| \propto 1/N^{p+1}$ by $\|e^*_{min}\| < (N^*)^{-(p+1)}$ or $\|e^*_{max}\| > (N^*)^{-(p+1)}$, the new mesh number can be quantified as $N^* = N \sqrt[p+1]{\|e\| / \|e^*_{min}\|}$ or $N^* = N \sqrt[p+1]{\|e\| / \|e^*_{max}\|}$.

Depending on the posterior normalised error of the current time step, $\|e\| > \|e^{*}_{max}\|$ implies mesh insertion ($N^{*} > N$) while $\|e\| < \|e^{*}_{min}\|$ implies mesh deletion ($N^{*} < N$), while no refinement is necessary when the second test, $\|e^{*}_{min}\| < \|e\| < \|e^{*}_{max}\|$, is satisfied. Therefore, if the first test ($\varepsilon_R \le 2$ and $\|e\| > 1$) and the second test ($0.23 < \|e\| < 0.47$) failed, AMOLBSC then generates a new mesh by predicting N^{*} in the computational domain with interval $\{\zeta^{*}_{j}\}_{j=0}^{N^{*}} \in \Lambda = [0,1]$ such that the new normalised error estimate of the PDEs in $(5-9)$ applied on the new mesh satisfies the relation:

$$\sqrt[p+1]{\|e^{*}_{i}\|} = \sqrt[p+1]{\sum_{d=1}^{N_{PDE}} \int_{\zeta^{*}_{i-1}}^{\zeta^{*}_{i}} \left\{\left(\tilde{\Phi} - \bar{\tilde{\Phi}}\right) \Big/ \left(\in_A + \in_R \left|\tilde{\Phi}\right|\right)\right\}^2 d\zeta} = Const = \sum_{i=1}^{N} \sqrt[p+1]{\|e_i\|} \quad / N^{*} \qquad (5-14)$$

Equation $(5-14)$ is a direct consequence of the L^2-norm described by equation $(5-13)$ as a measure of the normalised error estimate for the global mesh refinement similar to that described by Ascher et al (1995). It signifies that the normalised error estimate for each new subinterval is the same. In §5.3.3, the derivations and developments of the preceding sections are used to build a computational algorithm for mesh refinement.

5.3.3. Computational Algorithm

Based on the strategy for the adaptive mesh refinement (AMR) technique described in the previous section, a computational algorithm or a logical step-by-step procedure for mesh adaptation is developed. At the start of the computation, it is assumed that the mesh is well distributed, and hence only the second test is required. If the second test ($\|e^{*}_{min}\| < \|e\| < \|e^{*}_{max}\|$) fails, then N^{*} predicted from $N^{*} = N \sqrt[p+1]{\|e\| / \|e^{*}_{(min,\, max)}\|}$ and r-number of remeshing attempts ($r < q+1$) for q-order of BDF time-integration ($q < 7$) is carried out to go to the next time step. Otherwise, the following algorithm is repeated until satisfactory solution is found.

1. For the BDF time integration interval $\lfloor \tau_n, \tau_{n+q} \rfloor$, if an attempt is made r-times, set $N^* = N$; otherwise predict $N^* = N \sqrt[p+1]{\|e\| / \|e^*_{(min,\, max)}\|}$.
2. Use N^* from step 1, and generate a new mesh that satisfies the global mesh redistribution described by equation $(5-14)$.
3. Use the solutions at current times steps (and possibly the previous q time steps of the previous mesh) and interpolate it as a solution for the new mesh.
4. If this is one of the first r-remeshing attempts, perform a continuation integration from τ_n using the DAE solver that uses a BDF.
5. After calculating the normalised spatial error estimates, apply the second test $\|e^*_{min}\| < \|e\| < \|e^*_{max}\|$.
6. If step 5 is satisfied, then continue with the DAE solver, otherwise go to step 1.

The above algorithm is primarily for the adaptive mesh refinement strategy. In the following, however, the general structure of the software package AMOLBSC is described in detail.

5.3.4. Structure and Implementation of AMOLBSC

AMOLBSC is designed as a framework for solving the general spray dynamics, evaporation, and combustion models that arise in various power generation applications, such as gas turbine combustors, diesel engines and rocket motors. The code is rooted on well established algorithms that have been under constant improvement and that have been tested for various applications in the last two to three decades (Madsen and Sincovec; 1979; Petzold, 1982; Keast and Muir, 1991; Ascher et al, 1995; Moore, 1995). AMOLBSC employs only h-refinement (Adjerid et al, 1992) for the spatial discretisation while, like in HPDASSL (Moore, 1995), it uses DASSL (Petzold, 1982) to carry out the time integration.

Although AMOLBSC is based on PDECOL (Madsen and Sincovec; 1979), various improvements have been made. The multi-step method DAE solver STIFIB in PDECOL, which is a modification of GEARIB due to Hindmarsh (1976), is replaced by DASSL (Petzold, 1982) to take advantage of its capability to control both the spatial and temporal errors by employing an efficient approach to integrate the DAE systems with a given temporal tolerance such that the temporal error is roughly the same as the spatial error described in Appendix 5. To ensure that the temporal error estimate will not distort the spatial error estimate, the control mechanism in DASSL that requires the temporal error estimate to be less that one-third of the temporal tolerance given to the code is employed. Therefore, the absolute and relative tolerances for the spatial error control are set to be equal to those of the temporal error controls. However, DASSL only offers two options, a full matrix or a banded matrix, for the solution of DAEs. In most situations, the banded matrix solver is employed for computational efficiency. But, Keast and Muir (1991) have shown that the matrix $\tilde{M}$ in equation $(5-11)$ is an almost block diagonal (ABD) matrix, which proved to be 70% more efficient compared to employing banded matrix solvers. Therefore, the ADB solver COLROW (Diaz et al, 1983) is incorporated in DASSL as a third option to solve DAEs.

Note that due to the spatial discretisation employed in AMOLBSC to estimate the spatial errors (see appendix §A5.2.5), the resulting set of DAEs of the piecewise polynomial subspace of degree p and $p+1$ are combined into a large set of DAEs. But, the Jacobian associated with these equations consists of two decoupled ABDs, where the linear system is solved by calling COLROW twice. However, remeshing results in a new DAE system and the time integration must continue based on the current time step as its starting point. In most of the fully adaptive MOL codes, it is customary to interpolate the solution from the old mesh to the new mesh at the current time step and then to restart the integration as though solving a new problem, for example - with a low order method and smaller time step. However, such approaches have been shown to be inefficient (Berzins et al, 1998). As such, AMOLBSC interpolates the solution information from the old mesh to the new mesh for as many previous steps as necessary as suggested by (Berzins et al, 1998). Since the interpolation of all the integration history vectors that are required by DASSL are computation intensive, at most, only the current time step and the last five time steps (corresponding a 5th order BDF) are employed for the restart.

The advantage of DASSL, however, is offset by its instability and inefficiency due to the slightest inconsistencies in the initial values used (Leimkuhler et al, 1991). This prompts a special treatment of the boundary condition (see appendix §A5.2.2) so that problems whose boundary conditions are inconsistent with their initial condition can be handled. Because, in order to be consistent, the initial conditions of an index[3]-m DAE must satisfy not only the algebraic constraints, but also the m^{th}-derivative of the algebraic constrains, and Newton iterations are employed to solve the systems (see equations $(A5-12)$ in appendix 5), unless only Dirichlet boundary conditions are applied. The initial guess for the Newton method is obtained by requiring that the piecewise polynomial agrees with the initial condition of the PDEs on both boundaries so that the initial value , $\tilde{\sigma}(0)$, will be known. Once, $\tilde{\sigma}(0)$ is known, $\dot{\tilde{\sigma}}(0)$ is obtained by differentiating equation $(A5-9)$ in time, which is of the form described by equation $(A5-12)$. Therefore, the capability of treating non-Dirichlet boundary conditions with inconsistent initial conditions removes one of the famous weaknesses in PDECO/EPDCOL as pointed out by Keast and Muir (1991). At present, AMOLBSC is implemented to solve the 0D and 1D evaporation models, which are either ODEs or PDEs.

---

[3] The index plays an important role in the classification and numerical solution strategy of DAEs. It signifies the minimum number of times, m, that all or part of $\tilde{P}(\tau,\tilde{\sigma},\dot{\tilde{\sigma}})=0$, described by equation $(5-10)$, must be differentiated with respect to τ in order to determine $\dot{\tilde{\sigma}}$ as a continuous function of $\tilde{\sigma}$, where for a B-spline of maximum continuity $C^m(A)$, the index number is $m-1$, where for $m=2$, the usual index-1 DAE results.

PART II: VALIDATION AND NUMERICAL EXPERIMENTS

6. JP8 DROPLET EVAPORATION AT LOW PRESSURE

6.1 *Introduction*

In the following chapters, numerical experiments are carried out to assess and validate the models developed earlier. Since the experimental data of droplet evaporation for real fuels at gas turbine operating conditions, in particular involving composition measurements, is scarce, the model assessment and validation is mainly focused on comparing the performance of the different models developed earlier. However, before examining the performance of all the models developed in earlier chapters by comparing the models with each other, as is usually done in most combustion research (Sirignano, 1999), it is essential first to establish which parameters of the PDF in the CT formulation are useful in extracting the necessary information required to characterise the evaporation process comprehensively.

Therefore, it must be borne in mind from the outset that the purpose of this section is to understand the evolution of the parameters and the moments of the PDF as well as the heat and mass transfer behaviour without giving much emphasis on the liquid model used itself. However, once the model is compared with the available experimental data, and the most salient features that characterise the evaporation processes are identified, all the three liquid models will be compared with each other at various ambient conditions in Chapter 7, including with experimental data of kerosene type fuel. To that end, in this section, one model will be chosen so that it will be first assessed against two sets of experimental data, one set of data corresponding to low temperature and low pressure conditions and the other corresponding to distillation temperature conditions.

In order to validate the new models developed in the framework of CT, the vaporisation behaviour of an isolated droplet of six complex mixture model fuels (J1-J6) and one real fuel (J7) are considered. J7 is a military kerosene similar to Jet-A, which is commonly known as jet propulsion fuel-8 (JP8). J7 and JP8 are used interchangeably except for the fact that J7 mainly refers to the numerically simulated results while JP8 refers to the real fuel properties and the experimental data used. Each group of the model fuels (J1-J7) are composed of either single or multiple homologous series, which in turn are composed of large number of complex hydrocarbons. The homologous series considered are paraffin (C_nH_{2n+2}), naphthene (C_nH_{2n}), and aromatic (C_nH_{2n-6}). The hydrocarbons in each homologue are in the range of carbon numbers $C_8 - C_{16}$. The group of the model fuel mixtures are shown with their respective percentage composition in Table 6.1.

	Paraffin	**Naphthene**	**Aromatic**
BP (K) range	*311.15-560.15*	*397.15-573.15*	*412.15-597.15*
W (kg/kmole) range	*114.20-226.40*	*112.20-206.40*	*106.20-202.30*
Model Fuel Groups	**Composition in% Volume**		
J1	100.0000	-	-
J2	-	100.0000	-
J3	-	-	100.0000
J4	60.2015	39.7985	-
J5	69.8830	-	30.1170
J6	-	60.5364	39.4639
J7 (JP8)	47.8000	31.6000	20.6000

Table 6.1 Composition of model fuel groups and the ranges of boiling points and molecular weights of the mixture components in each homologous group.

Since the numerical tests are designed to validate the various evaporation models under wide ranges of ambient thermodynamic and flow conditions, both for the model fuels and real fuel shown in Table 6.1, it must be pointed out that in the sections to follow, some descriptors are used to categorise the numerical test conditions.

Accordingly, the ambient pressure, temperature, velocity, and droplet diameter are collectively referred to as *Model Parameters*, while their qualitative description is designated as (low, medium and elevated or high) *Model Parameter Intensity.* With the exception of the droplet diameter, the qualitative descriptions are based on the quantitative values of the model parameters. Similarly, the fuel groups J1 to J7 are designated as *Model Fuels*. The evaporation models, namely MWMM, MEDM, and MDLM are collectively referred to as *Liquid Models*. However, to avoid confusion in the abbreviation of the liquid models, extra dimensional descriptors are used to immediately signify the spatially resolved models (1D-MEDM and 1D-MDLM) from the spatially non-resolved models (0D-MMMM).

Considering three liquid models, seven model fuels, and four model parameters (pressure, temperature, velocity and droplet size) with at least three parameter intensities (low, moderate or elevated/high), the possible number of combinations of numerical experiments could be large. Such a large matrix of tests may not provide revealing information about the accuracy and efficiency of the models to be tested. In addition, the comparison of such a large data base could prove intractable.

Therefore, a systematic approach is required to generate a reasonable comparison set with the limited experimental data available so that it will be possible to assess and reveal the essential features of the models and their range of practical applicability. For example, past investigations (Sirignano, 1978; Aggarwal et al, 1984) showed that at a relatively low ambient temperature and low convective velocity conditions, the heat transfer and internal circulation are not significant in the liquid phase, and hence these model parameters are less important in affecting the evaporation process. Therefore, application of the 1D-MEDM and/or 1D-MDLM models may not provide important information other than that extracted using the 0D-MWMM, where the later model is preferred for its computational efficiency. In fact, for such low model parameter intensity, results from the counterpart classical models of the 0D-MWMM were shown to be superior to the 1D-MDLM (Aggarwal et al, 1984). On the other hand, the operating conditions of most combustion devices in practical applications have model parameters in the range of medium to high parameter intensity, but droplet sizes much smaller than those used for experimental purposes. In such situations, the counterpart classical models of the 1D-MEDM and/or 1D-MDLM were shown to be superior to the 0D-MWMM as expected (Aggarwal et al, 1984; Sirignano, 1999). Therefore, in this investigation, the 0D-MWMM is used in the low-medium range of model parameter intensities, where the droplet size is much bigger than those used in practical applications. However, the 1D-MEDM and 1D-MDLM will be used in the elevated-high model parameter intensities (§7). This strategy will reduce the number of numerical experiments to be done without compromising the objective of the model validation for practical applications. In addition, since all models are used to investigate the vaporisation behaviour at elevated conditions, the model comparison between the 0D and 1D models will be an interesting one.

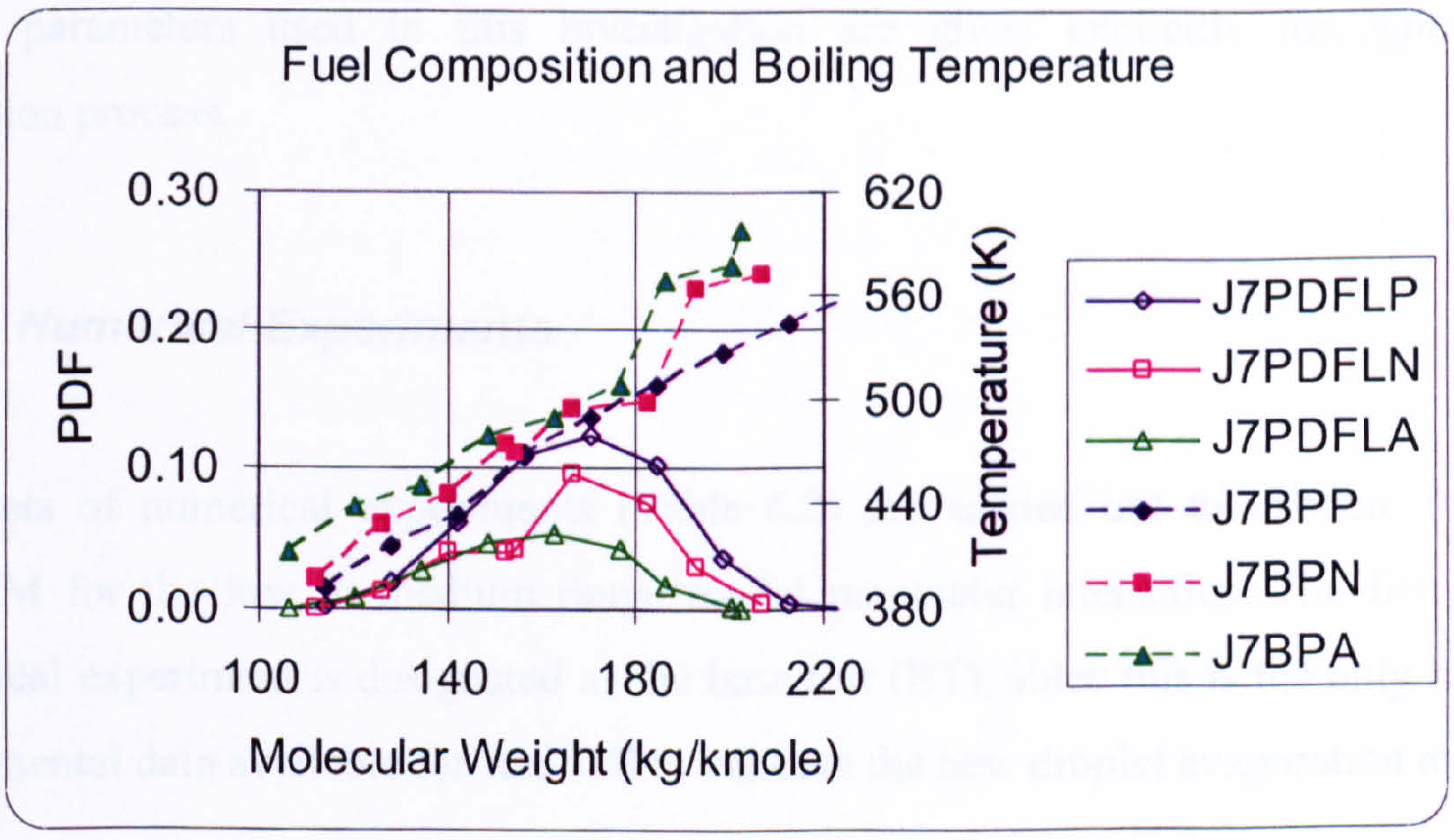

Figure 6.1 A re-plot of the initial liquid composition PDFs (Figures 3.1-3.3) of paraffin (J7PDFLP-open diamond with solid line), naphthene (J7PDFLN-open rectangle with solid line) and aromatic (J7PDFLA-open triangle with solid line), and their boiling point temperatures for paraffin (J7BPP-solid diamond with dashed lines), naphthene (J7BPN-solid diamond with dashed lines), and aromatic (J7BPA-solid triangle with dashed lines) based on data taken from Vargafftik (1975).

It must be pointed out however, the classifications of the model parameter intensities (as low, medium and elevated or high) are loosely defined in a sense that the classifications do not necessarily conform to related scientific terms or to those used by other investigators, except the qualitative descriptors (low, medium, elevated or high) follow the quantitative values of the ambient pressure or temperature fields or both. For example, the ranges of temperatures within the boiling point of selected paraffin, naphthene, and aromatic homologue components (Figure 6.1), can be partitioned and used as a guide to describe the corresponding model parameter intensities. As such, the ambient temperature values that are below the boiling points of any of the components can be taken to fall in the region of the low (temperature) model parameter intensity.

If the ambient temperature is significantly higher than the boiling point of the heaviest component, then the situation falls in the region of the high (temperature) model parameter intensity. If the ambient temperature falls between these ranges, it most likely represents the medium model parameter intensity. The descriptor elevated is used to indicate (mostly in conjunction with pressure) values that fall in the medium to high ranges, when the ambient temperature condition is high enough to vaporise all the components in the mixture. To avoid confusion, however, the numerical values of the model parameters used in this investigation are given explicitly throughout the validation process.

6.2 Numerical Experiments

Two sets of numerical experiments (Table 6.2) are carried out to validate the 0D-MWMM for the low to medium range model parameter intensities. The first set of numerical experiment is designated as the base test (BT), since this is the only realistic experimental data available for fuel JP8 to validate the new droplet evaporation models.

Type of Experiment	*Model Parameters*			
	$V^{v\infty}\,(m/s)$	$T^{v\infty}(K)$	$P^{v\infty}\,(bar)$	$D_p^l(\mu m)$
BT	3.00	294.15	1.00	639.0
DT	30.0	600.15	1.00	639.0

Table 6.2 Model Parameters for BT and DT Numerical Experiments.

The second set is designated as the distillation test (DT), where the droplet is numerically simulated to undergo distillation. The numerically simulated droplet distillation is then compared with the distillation data of various kerosene type fuels in the literature. The comparisons between the two sets of numerical experiments and the experimental data of Runge et al (1998) and the distillation data of kerosene type fuels serves as a basis to validate the MWMM.

The governing equations for the MWMM describe the evolution of the liquid fractional composition distribution moments (in the form of equation $(4-4)$ and $(4-5)$or equation $(4-7)$), the evolution of the droplet residual temperature (equation $(4-11)$) and the evolution of the droplet size (equation $(4-12_b)$). Using the gas-phase analysis results from §3 in conjunction with the numerical solution of the liquid phase equations in §4 provide the complete solution required by the model. Traditionally, the droplet area or volume regression (normalised by its initial area or volume, respectively) and the droplet residual temperature have been used as the main parameters to characterise droplet evaporation, both for single and/or binary fuels. This is mainly due to the fact that the two parameters are relatively easier to measure, while composition measurements for complex fuels have been plagued by lack of technological progress in the area. In this investigation, the behaviour of the composition evolution will be given special attention so that better understanding on multicomponent evaporation models that can be used for practical application can be established. As such, the discussion will focus on two issues. The first is the fractional composition distribution evolution while the second is the evolution of droplet size and its residual temperature.

6.2.1 Base Test (BT) against the Experiments of Runge et al (1998)

The experimental investigation of Runge et al (1998) was conducted for an isolated multicomponent droplet suspended in an air stream moving at various relative velocities. The use of suspended droplet was necessary because of the very long vaporisation times, depending on the ambient temperature and flow conditions used and only considering vaporisation of the droplet until 20% of the volume of fuel remaining, which is reported to have taken 5-30 minutes for JP4 while it took 30 minutes to more than 15 hours for the less volatile JP8.

The work was motivated by the lack of low temperature experimental data to quantify the vaporisation behaviour of fuel jettisoning during military aircraft refuelling of JP4 and JP8 so that some mechanism could be in place to reduce the substantial increase in ground contamination by jettisoned liquid, and more importantly, to reduce the permissible toxicity exposure levels of JP8 vapours and aerosols to refuelling crews. The experimental work is of current interest due to the importance of fuel JP8 both from economic, military and environmental view points. Its importance is attributed to the replacement of the more volatile fuel JP4 by the less volatile fuel JP8 across the US defence establishment and NATO states, in particular the Air Force.

The experimental parameters, which are used as model parameters for the MWMM are shown in Table 6.2, and designated as BT. The droplet initial temperature is 10^0C and the ambient gas is pure air, with no fuel vapour present prior to vaporisation. In order to extract the essential features of the CT based multicomponent droplet evaporation models, the evolution patterns of both the liquid and vapour PDF parameters and its moments are studied in detail. In addition, like in any other droplet evaporation model investigations, the behaviour of the droplet volume or area regression rate, the droplet temperature and the liquid and vapour 0^{th}-fractional distribution moments are studied. In this section, only the low pressure (LP) vapour-liquid equilibrium (VLE) formulation discussed in §4 is used.

6.2.1.1. Evolution of Fractional Composition Distribution Moments

In Figures 6.2-6.11, the time evolution of the composition PDFs, their mean, variances, skewness as well as their shape and scale parameters, both for the liquid phase and the vapour phase at the droplet surface are presented. Except for the naphthene homologue, which decreases nearly linearly, the evolution of the liquid composition PDFs are characterised by sharp drops in the variance (or width) of the PDFs (Figures 6.2 and 6.6) while progressively loosing its asymmetry (skewness) to the left (Figure 6.2 and 6.8). The decrease in the liquid PDF width is symptomatic with the depletion of the most volatile components of the mixture. The effect of this progressive removal of the volatile components is reflected on the increasing PDF height while it is loosing its width (Figure 6.2), in particular, for about the first five minutes or so. This is depicted by the relatively rapid growth in height of the from the initial PDFs (Figure 6.1) until the 316 second time-section plot of the PDF (Figure 6.2). However, due to the low ambient temperature and due to the remaining high molar weight components, it is not possible to prompt enough mass diffusion and/or strong convective weathering in order to sustain the initial growth of the PDF mean or rapid decrease in the variance of the distribution. Instead, the mean starts to grow very slowly towards the maximum homologue molecular weight range ($C_8 - C_{16}$) as its horizontal asymptote (Figure 6.4). However, it is clear to see that all the components are not removed from the liquid as the computation is halted once the droplet shrinks to 20% of its original volume. The nearly linear decrease in the naphthene PDF variance (Figure 6.6) can be attributed to the initial composition PDF (Figures 3.3 or 6.1) that is skewed to the left, where the percentage of the lighter components enveloped in the PDF tail are very small. Therefore, once those volatile components are depleted, the remaining components, which have relatively higher molecular weights force the shrinking rate of the variance (PDF width) to slow down.

The vapour composition PDF time evolutions show similar trends (Figures 6.3, 6.5, 6.7, and 6.9), although they represent significantly different thermodynamic state and their numerical values differ appreciably. First, it is well established that for compounds of the same carbon number, the order of increasing boiling point by homologue is iso-paraffin, n-paraffin, naphthene, and aromatic (Kuo, 1986). For example, the components that boil near 225 C (the middle of the distillation curve for kerosene type fuels) are likely to be C_{12}-paraffin, C_{11}-naphthene, and C_{10}-aromatic. Similarly, density increases with carbon numbers in the same homologous series. As such, for compounds with the same carbon number, the order of increasing density by homologue is paraffin, naphthene and aromatic – which will be referred as the paraffin-naphthene-aromatic or PNA sequence in the sections to follow.

Although the thermal driving potential, due to the low ambient condition, is not contributing significantly for the accumulation of vapour at the droplet surface through mass diffusion, the ambient convection is responsible for the progressive stripping of the comparatively low density components. Therefore, mass transfer is mainly through slow molecular diffusion in the liquid and convection at the droplet surface as described by the molar flux relation equation $(3-21)$, where the convective effect on the spherical symmetry assumption is accounted for through the Clift et al (1978) correlation described by equation $(3-45)$. Since further supply of light species is limited by the slow rate of diffusion, the vapour PDF mean at the droplet surface (Figure 6.5) remains consistently lower than the liquid PDF mean (Figure 6.4). This lower PDF mean will tend to reduce the surface vapour pressure (equation $(A4-7_b)$ in Appendix 4), which is characterised by the liquid PDF origin γ_j^l and scale β_j^l parameters, and the boiling point temperature of the homologues, although it would have been compensated due to the possibility of heating the droplet to a relatively higher temperature had the ambient temperature been high itself.

The width of the distribution at a first glance, however, shows somewhat unexpected result (Figures 6.3 and 6.7), where due to the accumulation of vapour at the droplet surface, the variance of the distribution is expected to grow. In fact, although not dropping sharply compared to the liquid distribution variance (Figure 6.6), the vapour distribution variance at the droplet surface is decreasing nearly linearly. This could be attributed to the very slow molecular diffusion in the liquid and the comparatively fast convective weathering at the droplet surface, where the accumulation of vapour is very small. The evolution of the PDF loss of symmetry for the liquid phase (Figure 6.8) and the vapour phase (Figure 6.9) are relatively identical. This is not unexpected, as it is predicted by the theory (equation $(4-34)$) that the change from liquid to vapour is only characterised by the scale parameter β_j^v.

Except for the PDF mean θ_j^v (Figures 6.4 and 6.5) and the PDF scale parameter β_j^v (Figures 6.10 and 6.11), however, neither the PDF variance $(\sigma^2)_j^v$ (Figures 6.6 and 6.7), nor the PDF skewness $2.0/\sqrt{\alpha_j^v}$ (Figures 6.8 and 6.9) or equally the PDF shape parameter α_j^v (Figures 6.10 and 6.11) highlight the PNA sequence as would be expected. Two possible explanations are envisaged in this regard. The first one is related to the low ambient temperature and its effect on the vapour pressure, while the second is related to the use of the diffusion coefficients. Due to the low ambient temperature, the depletion of mass from the liquid is mainly controlled by convective weathering, while the contribution due to boiling evaporation is, in fact, non existent in this case. Since the vapour pressure $P_j^{sat}(M,T) \sim Exp\left[1-\left(T_b/T^R\right)\right]$ is intimately linked to the droplet surface temperature T^R and controls the behaviour of the PDF scale parameter β_j^p (but not directly the shape parameter α_j^p), the low temperature environment reduces the vapour pressure value and hence the scale parameter β_j^p. This is in turn used to update the PDF shape parameter using the relation $\alpha_j^p = (\sigma^2)_j^p / \beta_j^p$, where a slight fall in β_j^p could increase the value of α_j^p. On the other hand, since the variance is calculated from $(\sigma^2)_j^p = \psi_j^p - (\theta^2)_j^p$ as a fairly small difference between the large values of ψ_j^p and $(\theta^2)_j^p$, it is sensitive to small variation in these quantities. Such variation could be introduced, albeit for small differences, by using the same diffusion coefficients $D_{Jm(n)}^p = \overline{D}_{Jm(1)}^p = \overline{D}_{Jm(2)}^p$ (Appendix 2) both for the first moment θ_j^p and the second moment ψ_j^p. Therefore, while updating α_j^p using the relation $\alpha_j^p = (\sigma^2)_j^p / \beta_j^p$, a small drop in $(\sigma^2)_j^p$ can overestimate the values of α_j^p. These arguments will be assessed in the DT-numerical experiment, which is performed under a higher ambient temperature condition. On the other hand, the relative growth of the distribution mean is depicted by the ratio of the liquid and vapour PDF scale parameters, which indicates the rapid convective weathering of the vapour mixture compared to the rate of accumulation due to liquid mass diffusion (Figure 6.12). The liquid thermal diffusion time is $o(10^2)$ higher than the mass diffusion time, and as the droplet diameter decreases, so are the time scales, which is expected.

Figures 6.14 and 6.15 depict the 0th mass fractional composition distribution moments for each homologue, respectively, of the liquid and the vapour at the droplet surface. The relatively rapid depletion of the liquid paraffin is marked by the relative increase in the other competing homologues (Figure 6.14), indicating clear preferential mass diffusion. The accumulation of vapour at the droplet surface also reflects the observation in the liquid process, where the paraffin that was depleted from the liquid at a greater proportion appears as the homologue that accumulates at a higher proportion at the droplet surface. In about the first three minutes, the paraffin, naphthene, and aromatic corresponding to PDF mean, respectively of C_{12}, C_{11}, and C_{10} are depleted (Figures 6.4 and 6.14). But, as the carbon numbers, and correspondingly the densities, of the homologues increase, the rate of liquid depletion decreases proportionally. In fact, the naphthene and aromatic reach at inflection points to mark the resistance to mass diffusion more clearly (Figure 6.14). While the more volatile paraffin and naphthene are removed, the proportion of the aromatic content increases linearly. The vapour profile at the droplet surface (Figure 6.15) also indicates the same preferential diffusion, where at the beginning of the vapour accumulation, the proportion of paraffin is higher than the naphthene, which in turn is higher than the aromatic, showing the expected PNA sequence.

However, once the volatile naphthene components (mostly contained within the left tail of the PDF – Figure 3.3) are depleted from the liquid and stripped from the droplet surface, the supply of naphthene through liquid mass diffusion could not keep pace with the convective weathering and the proportion of naphthene vapour drops rapidly as a result. Since the paraffin and the aromatic have a more or less symmetric PDF, the proportion of the vapour accumulation at the droplet surface shows an increasing trend in the first three minutes. Like in the liquid phase, the accumulation of vapour through liquid mass diffusion at the droplet surface, which is stripped by the convective environment reaches inflection point, where the proportions of the paraffin and the aromatic are relatively decreasing while the naphthene start to increase. However, the proportional values remain to follow the PNA sequence, where paraffin constitutes the highest proportion of the vapour followed by the naphthene and aromatic.

The vapour molar fluxes (the total and for each homologue) is depicted by Figure 6.16, where it also included the instantaneous droplet area as the liquid mass is depleted. The fractional molar flux is also depicted by Figure 6.17. As in all the previous cases, the molar fluxes show predominantly the PNA sequence to support the argument of preferential diffusion of components of the same carbon numbers of different homologues. The slow liquid mass diffusion and the comparatively very low thermal input are marked by the large Lewis and Peclet numbers as expected (Figure 6.18). This implies that the contribution of the ambient temperature on the liquid thermal diffusion is insignificant, which supports the condition to be in convective weathering rather than evaporation. For the vapour at the droplet surface, the plots of the Reynolds number and the relatively low Lewis number show the expected PNA sequence.

6.2.1.2. Evolution of Droplet Size and Residual Temperature

The time history of the droplet size and its residual temperature are the most frequently used quantities both in theoretical, numerical and experimental investigations of droplet evaporation. Since comparisons of genuine multicomponent droplet evaporation models and detail measurements of composition at any resolutions are scarce (or non-existent to this author's knowledge), droplet size and residual temperature time histories are better understood than , for example – composition evolutions. Therefore, it is instructive to gauge the prediction of any new model with respect to the transient behaviours of the droplet size and its residual temperature.

Figures 6.20 and 6.21, respectively, depict the droplet normalised volume regression and the droplet residual temperatures for all the model fuels shown in Table 6.1. The numerical solutions, based on equation $(4-12_b)$ for the droplet radius and based on equation $(4-11)$ for the droplet residual temperature reveals some interesting results. Since model fuel J1 is 100% paraffin, which is the most volatile homologue in the mixtures considered, the recession is very rapid until the PDF mean reaches around 185 kg/kmole, which corresponds to n-tridecane (C_{13}-paraffin). However, the relative change becomes nearly linear for the remaining of the droplet life time. This is also reflected in the droplet residual temperature time history (Figure 6.21), where the droplet is heating up at a relatively faster rate until it reaches a temperature of 292K that corresponds to a PDF mean of 182 kg/kmole, and with an increment of 5kg/kmole, the droplet thermally stabilise with the ambient. The second model fuel to diffuse fast is J4 followed by model fuel J2. It is interesting to observe from the volume regression and temperature plots of both J4 and J2 that a clear preferential diffusion is taking place. In the beginning of the vaporisation process (Figure 6.20), the composition of J4 (which is 60% paraffin and 40 % naphthene) depletes faster than J2 (which is 100% naphthene), and yet, J4 is slower than J1 (100% paraffin). Once most, but not all, of the paraffin is depleted and the majority of the fuel remaining is naphthene, the J4-curve resembles the 100% naphthene curve (J2). Similarly, the heating time is faster for J4 than for J2, although it is believed that the contribution of the thermal energy to motivate liquid diffusion is insignificant.

Similar behaviours are observed for rest of the model fuels, where the percentage composition and the PNA sequence intimately dictate the diffusion behaviour and hence the droplet life time. Although Figures 6.20 and 6.21 depict the numerical simulation for all the model fuels, Figure 6.22 is intended to further elucidate the numerical simulation of model fuel J7, which is in fact JP8, against the experimental data of Runge et al (1998). It is clear to see that at the beginning of the evaporation process, the MWMM prediction for the droplet volume regression is excellent.

However, between two-three minutes through the evaporation process (which are the inflection points for the 0th fractional moments depicted by Figure 6.14 and 6.15 and Figure 6.23 corresponding to a liquid PDF mean of 166 kg/kmole and a vapour PDF mean of 139 kg/kmole), the model over-predicts the rate of evaporation. This is due to the fact that the MWMM instantaneously transfers the most volatile liquid components from the centre to make the droplet composition uniform, unlike for example – the MDLM, in which the diffusion limits such a transfer. The fractional composition and PDF mean plots (Figure 6.23) and the initial composition PDF (Figure 3.3) indicate that it is the relatively rapid depletion of both the liquid paraffin and naphthene, in particular the naphthene at a higher rate corresponding to the most volatile components enveloped by the PDF tail that accounted for the over-prediction.

However, just on the transition (Figures 3.3 and 6.23), the model shows component resistance for further convective weathering. The rest of the prediction is excellent to good. At the end of the vaporisation process where the high molecular weight components remain, the model under-predicts the process. Extended computations to asses the tendency of the prediction also show that liquid mass depletion becomes practically very slow. Although there was no reason given by Runge et al (1998) as to why the measurement was carried out until 20% of the droplet volume remains, one reason could be due to the long time which was taken once the heavier molecular weight components remain.

6.2.2 Distillation Test (DT) against various Kerosene type fuels

The numerical distillation test (DT) is carried out to verify the performance of the model at temperatures within the envelope of the components boiling points that constitute fuel JP8, and to appreciate the effect of moderate forced convective environment in the droplet life time. The model parameters are given in Table 6.1, and the droplet initial temperature is $21\ {}^{0}C$. For the BT in the previous section, it was tried to establish the salient features in the time evolution of the PDF moments and other quantities. However, there were issues that seem in conflict with the developed theory – for example, the decreasing nature of the width of the distribution while it is expected to increase due to the addition of more heavy components with time. Due to the low ambient temperature condition in the BT, it was difficult to establish the contribution of the thermal energy in the evolution of the PDF and the subsequent evaporation.

This section gives a concise description of the MWMM results at the specified temperature and convective conditions. Rather than to present the time-wise description of the PDF moments, some quantities are depicted against the percentage distillates of the fuel (which is designated as volume % evaporated). The aim is to understand the evolution of the initial PDF corresponding to the depletion and accumulation of the distillates along with the PDF moments so that the PDF moments can be well understood in relation to the vapour produced at the droplet surface or the liquid mass depleted.

Figures 6.24 and 6.25 describe both the liquid and vapour PDFs mean and variance against the volume percent of fuel evaporated. Unlike in the BT plots (Figures 6.4-6.7), the DT results show a relatively linear increasing trend both in the liquid and vapour PDFs mean (Figure 6.24), while the liquid PDF width (variance) decreases with liquid depletion and increases with vapour accumulation at the droplet surface (Figure 6.25). These results indicate that with an increasing droplet temperature corresponding to increasing liquid mass depletion, the portion of heavy components in fuel vapour increases and the heavy end of the vapour distribution is extended while that of the liquid is shrinking. A close observation on the liquid PDF mean (Figure 6.24) shows that the PNA sequence is still maintained, although the aromatic PDF mean grows faster than the naphthene PDF mean at the end of the evaporation. The vapour PDF mean show a more complex evolution, where the aromatic homologue is the first to vaporise followed by the paraffin and naphthene, and the PNA sequence is obvious only after quarter of the droplet life time (~8ms) is elapsed. This is also reflected in the vapour PDF variance (Figure 6.25). To elucidate this inconsistency further, the PDF parameters both for the liquid and the vapour at the droplet surface are plotted, respectively, in Figure 6.26 and Figure 6.27. As expected the shape parameters for the liquid and the vapour PDFs are identical, while the PDF scale parameters of the vapour at the droplet surface are scaled down versions of the liquid PDF scale parameters. Such ratios in the scale parameters are shown both time wise (Figure 6.28) and composition wise (Figure 6.29).

The time-wise scale parameter ratio plots needs a closer inspection, however. Through the first droplet evaporation time of 4.44 ms for the paraffin, naphthene, and 3.57 ms for the aromatic homologues, the ratio of the scale parameters, respectively, are nearly constants with PNA sequence of 1.155, 1.137, and 1.117. These values are all very close to unity. Referring to the theory developed in §4.3 (equation $(4-34)$ or $(4-50)$ and Appendix 4), it is easy to observe that rapid phase transition or vapour accumulation is characterised by a value $\beta_j^l/\beta_j^g >> 1$. This evidence is further supported by the volume percent of fuel evaporated (Figure 6.30), which shows only a very slight vaporisation at the beginning of the droplet life time. In fact, the normalised droplet area time history shows that at the beginning of the evaporation process, the droplet is inflated by up to 20% in volume due to thermal expansion (Figures 6.32 and 6.33). Referring to the molar flux relation described by equation $(3-21)$, where $N_{T(0)} \propto 1/2R$, the swelling of the droplet is expected to slightly decrease the evaporation rate by lengthening the droplet life time.

The numerical distillation result (Figures 6.30 and 6.31) is compared with various kerosene type fuels. All the kerosene data falls under the envelope of the most volatile (JP8_MIN) and the heaviest (JP8_MAX) type JP8 fuels. It must be pointed out that JP8 fuel additives, which constitute less than 0.3 % of the total fuel composition, are not included in the model development of this investigation. Interestingly, the simulated distillation of model fuel J7 (J7MV) is in good agreement with most of the kerosene type data.

The result also reveals many features that can not be explained using traditional droplet evaporation models. The fractional vaporisation and its rate of mixing, both in the vapour and liquid phase, reveal more complex process than those described by binary diffusion assumptions. The vaporisation rate of each homologous series is significantly different. The paraffin and the naphthalene vaporise equally at the beginning of the droplet life time, the paraffin setting the pace afterwards. When the droplet temperature is 450 K, 17% of the paraffin, 15% of the naphthene, and 5% of the aromatics (or 12 % of the total JP-8 fuel) has vaporised. However, the aromatic vaporisation rate increases dramatically by the time the droplet temperature reaches 515 K. At this stage, 58.69% of the paraffin, 57.48% of the naphthalene, and 59.18% the aromatics (54.67 % of the total JP8 fuel) has vaporised. But, the paraffin and naphthalene evaporation rate increases further while the droplet temperature reaches a temperature of 557 K, while the increase in the evaporation rate of the aromatics becomes insignificant although it continued to vaporise until the droplet temperature reaches 590K.

The fractional vaporisation behaviour will enable mapping of the volatility differentials of each component, and may have significant implications in locating auto-ignition points in some advanced combustion devices, like the LPP combustor. Similar distillation prediction has been reported at different temperature and pressure conditions (Maru and Moss, 2003). In general, the comparison between the simple multicomponent well-mixed model against both the experimental data of Runge et al (1998) and the distillation curves of kerosene type fuels show good to excellent agreements. However, the vaporisation behaviour of the aromatic fuel is not always consistent with the PNA sequence. This could be due to the complexity of the benzene ring that is difficult to account for its complex thermotransport properties by using linear correlation as implemented in this investigation. However, the evolution of the fuel mixture is depicted with better clarity, in particular, the PDF scale parameter as a means to characterise vaporisation is a new understanding, and further investigation is required.

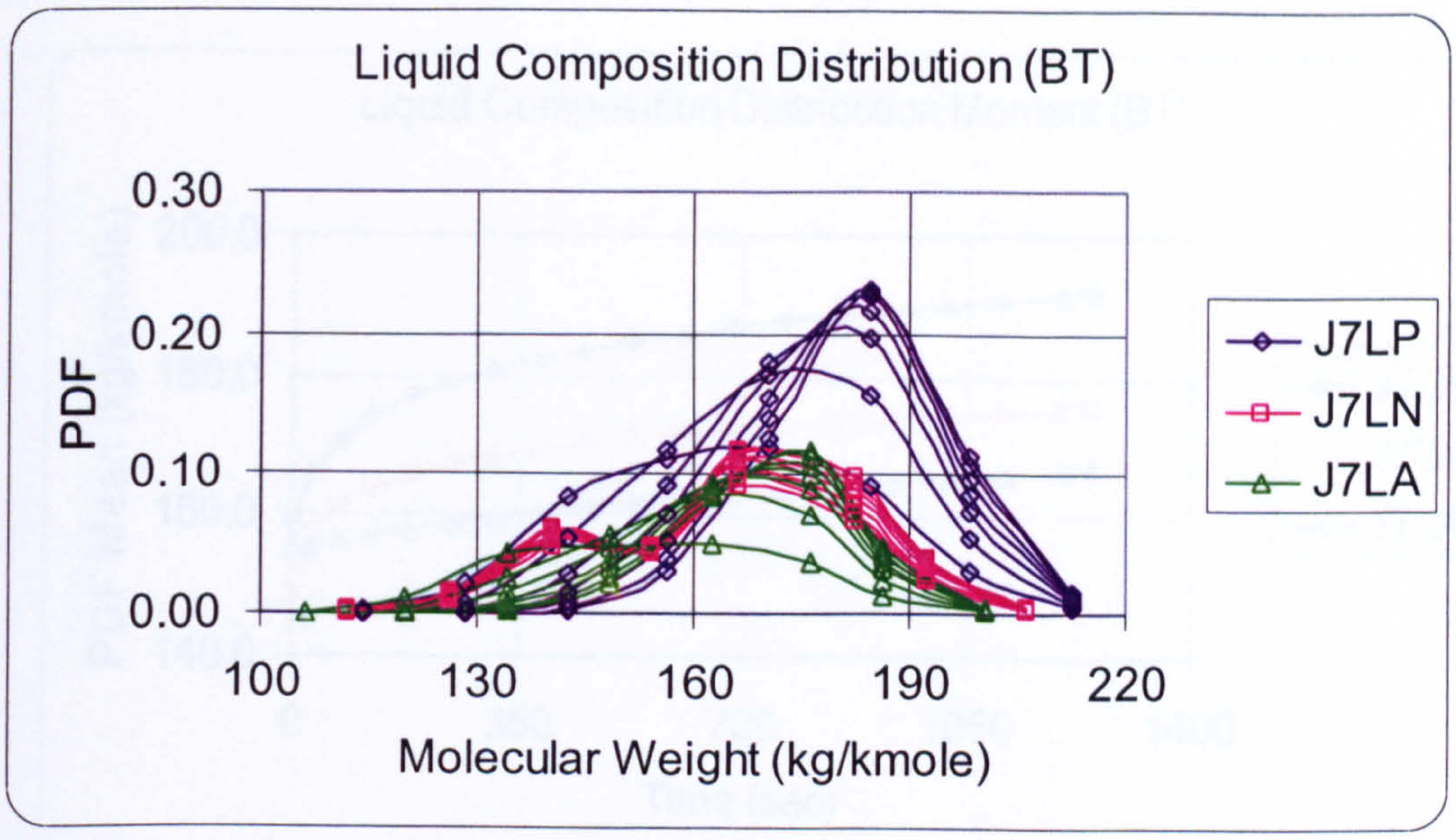

Figure 6.2. Liquid mixture composition distribution against molecular weight for model fuel J7 with homologues paraffin (J7LP-open diamond with solid line), naphthene (J7LN-open rectangle with solid line) and aromatic (J7LA-open triangle with solid line) at selected evaporation times of 0, 126, 316, 531, 768, 1021, and 1291 seconds: initial droplet diameter 639 μm, temperature $10\,^0c$, ambient convective velocity 3m/s at atmospheric conditions.

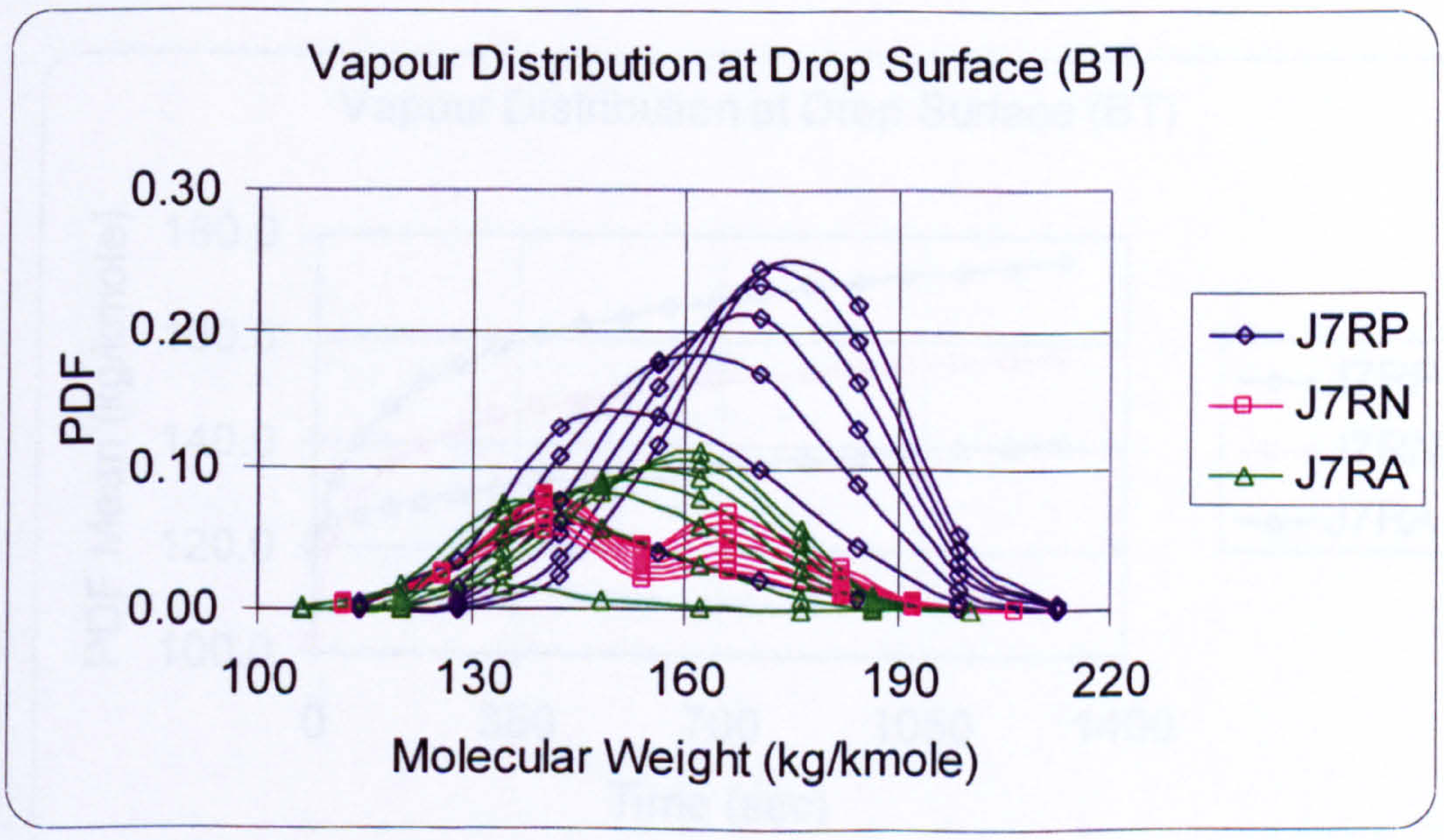

Figure-6.3. Vapour mixture composition distribution at the droplet surface against molecular weight for model fuel J7 with homologues paraffin (J7RP-open diamond with solid line), naphthene (J7RN-open rectangle with solid line) and aromatic (J7RA-open triangle with solid line) at selected evaporation times of 0, 126, 316, 531, 768, 1021, and 1291 seconds: initial droplet diameter 639 μm, temperature $10\,^0c$, ambient convective velocity 3m/s at atmospheric conditions.

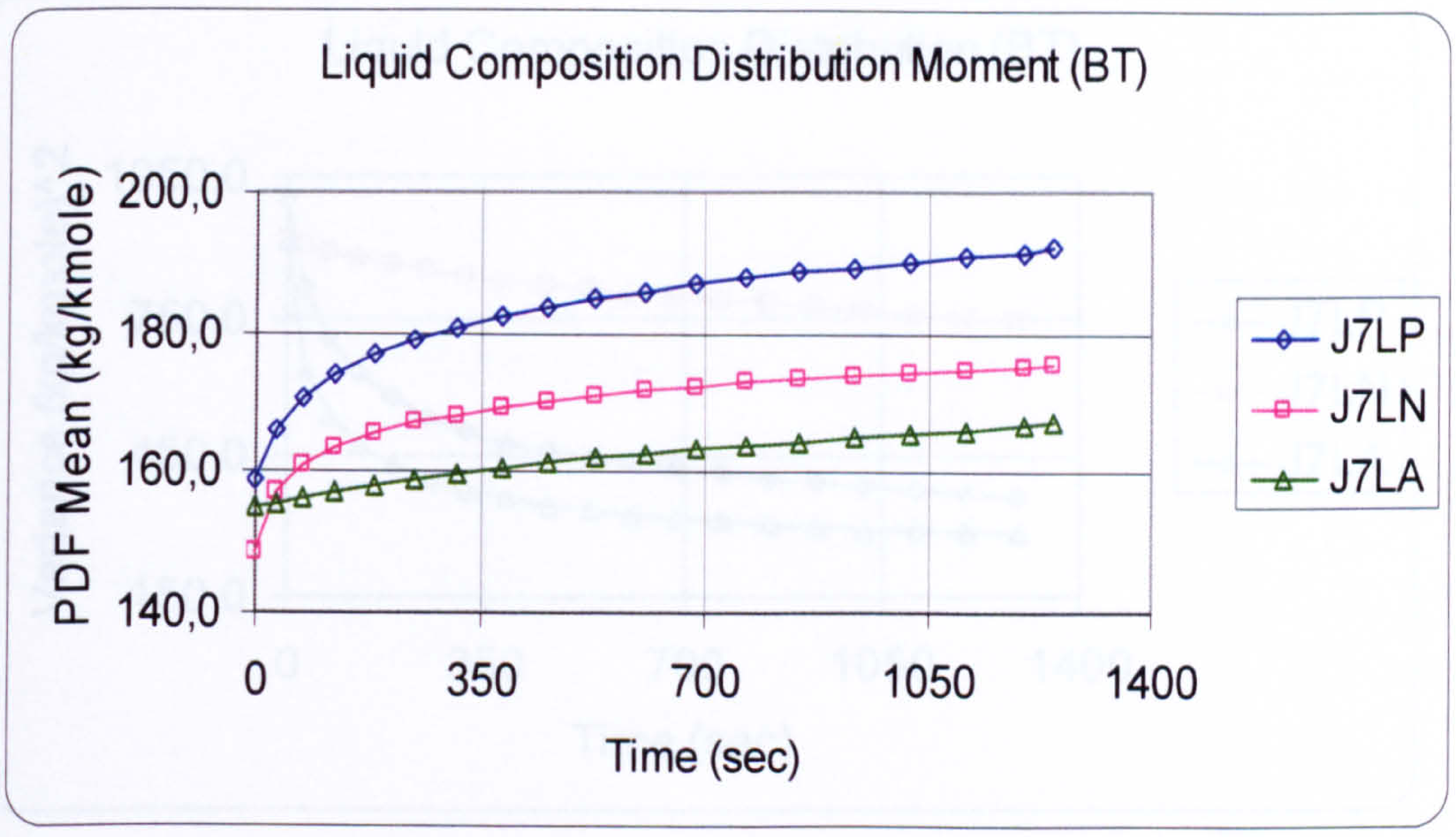

Figure-6.4. Liquid mixture composition distribution mean against evaporation time for model fuel J7 with homologues paraffin (J7LP-open diamond with solid line), naphthene (J7LN-open rectangle with solid line) and aromatic (J7LA-open triangle with solid line)- initial droplet diameter 639 μm, temperature $10^{0}c$, ambient convective velocity 3m/s at atmospheric conditions.

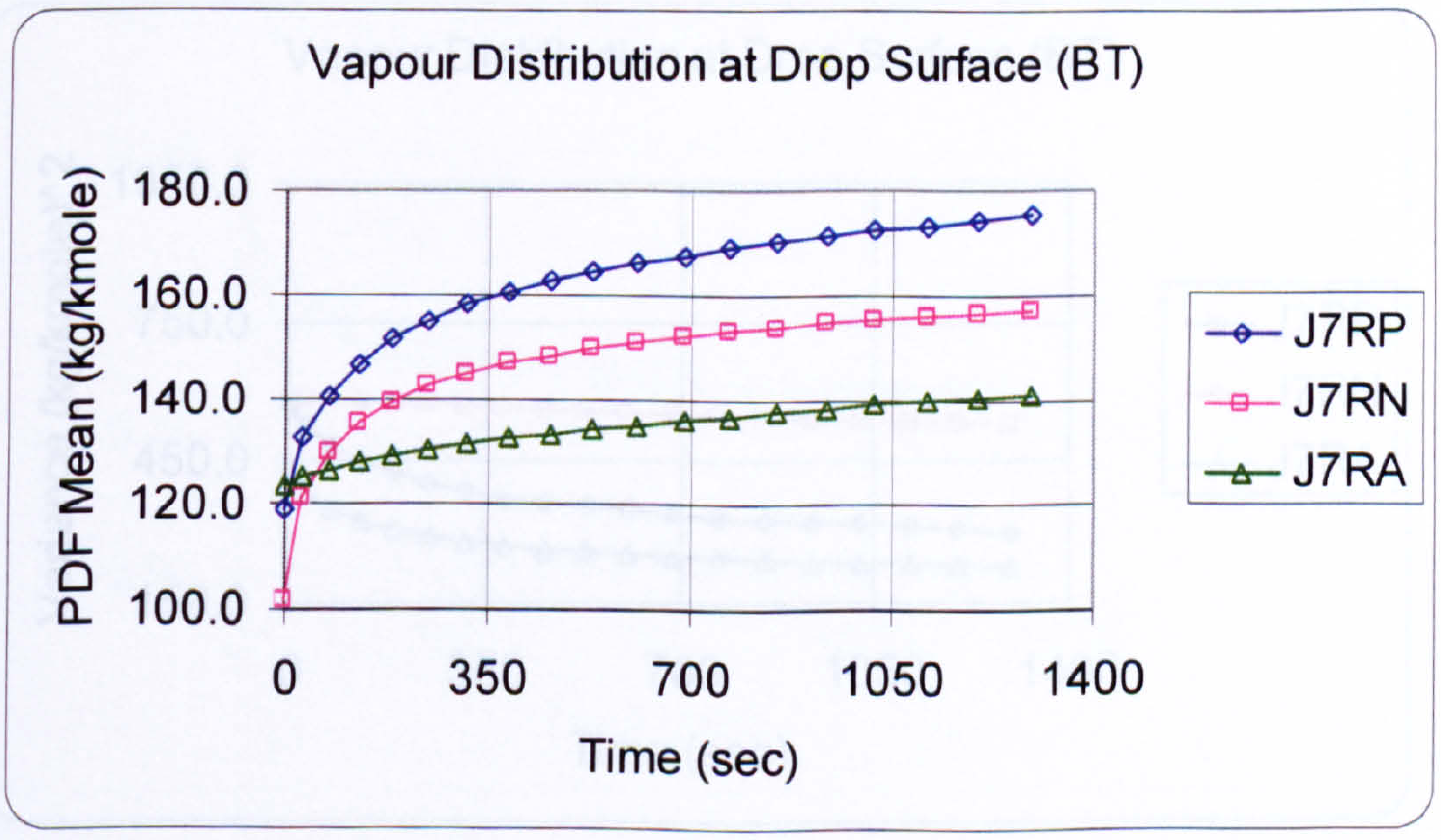

Figure-6.5. Vapour fuel mixture composition distribution at the droplet surface against evaporation time for model fuel J7 with homologues paraffin (J7RP-open diamond with solid line), naphthene (J7RN-open rectangle with solid line) and aromatic (J7RA-open triangle with solid line)- initial droplet diameter 639 μm, temperature $10^{0}c$, ambient convective velocity 3m/s at atmospheric conditions.

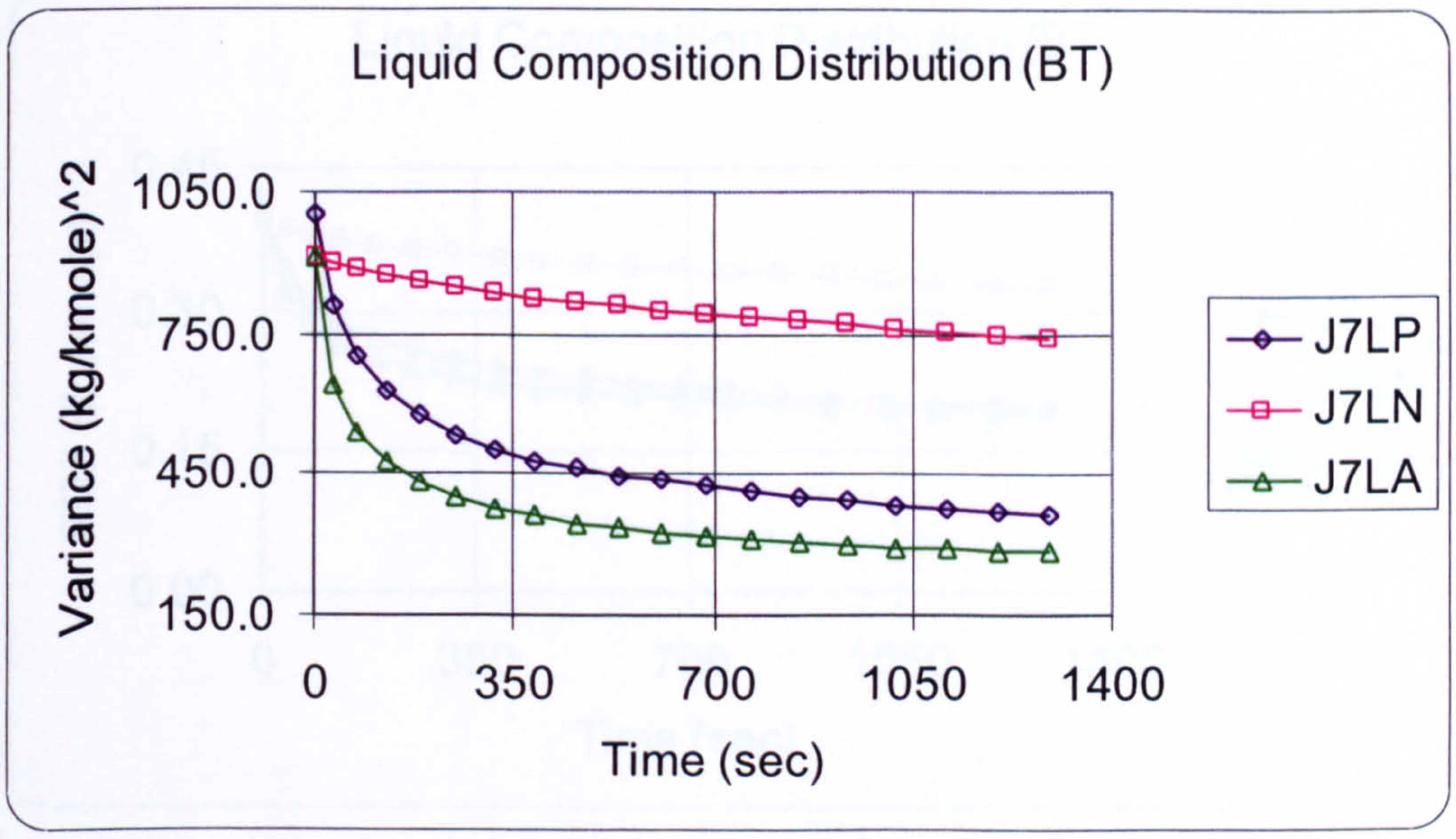

Figure-6.6. Liquid mixture composition distribution variance against evaporation time for model fuel J7 with homologues paraffin (J7LP-solid diamond with solid line), naphthene (J7LN-solid rectangle with solid line), and aromatic (J7LA-solid triangle with solid line)- initial droplet diameter 639 μm, temperature $10\,^0c$, ambient convective velocity 3m/s at atmospheric conditions.

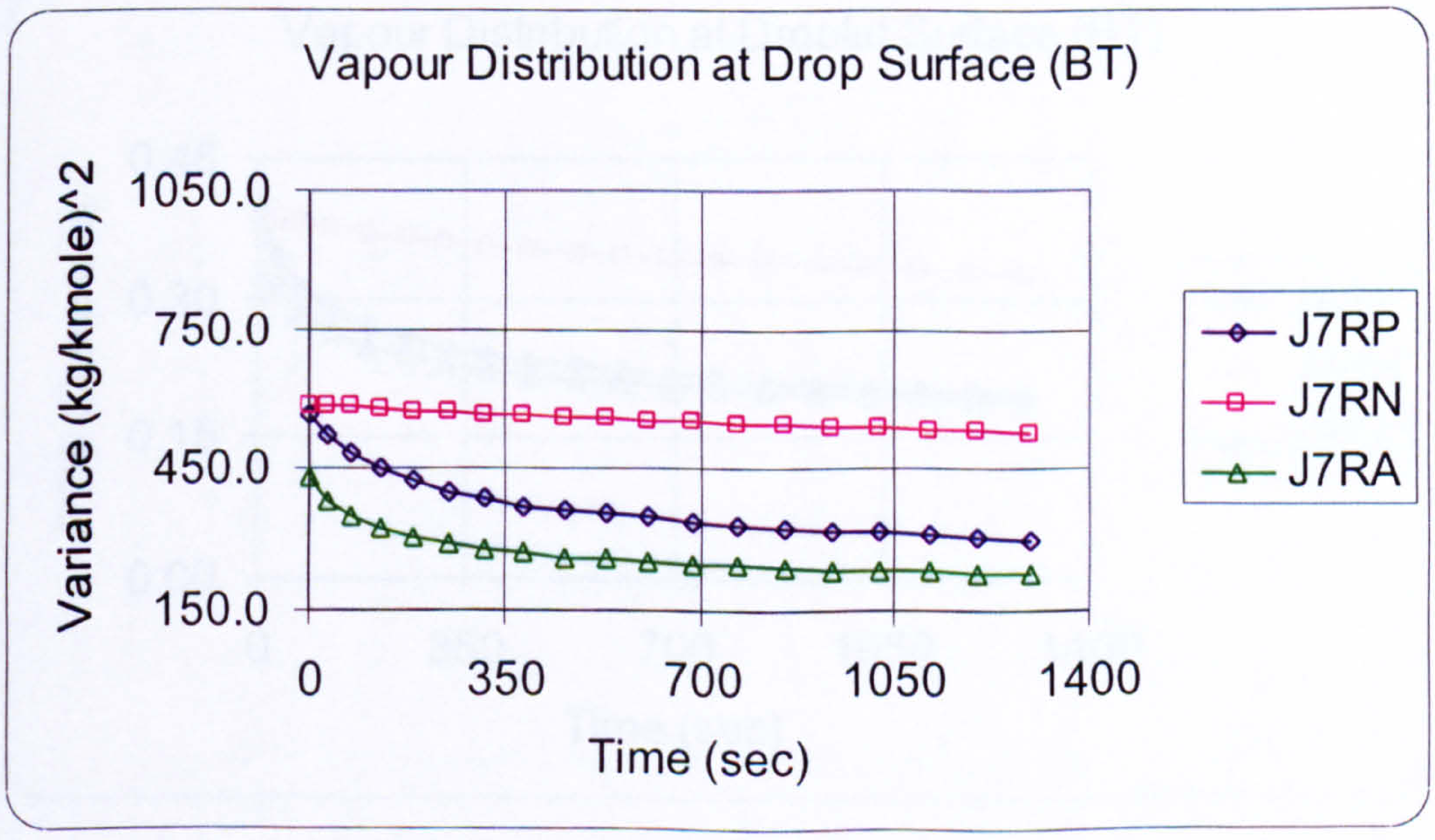

Figure-6.7 Vapour fuel mixture composition distribution variance at the droplet surface against evaporation time for model fuel J7 with homologues paraffin (J7RP-solid diamond with solid line), naphthene (J7RN-solid rectangle with solid line), and aromatic (J7RA-solid triangle with solid line)- : initial droplet diameter 639 μm, temperature $10\,^0c$, ambient convective velocity 3m/s at atmospheric conditions.

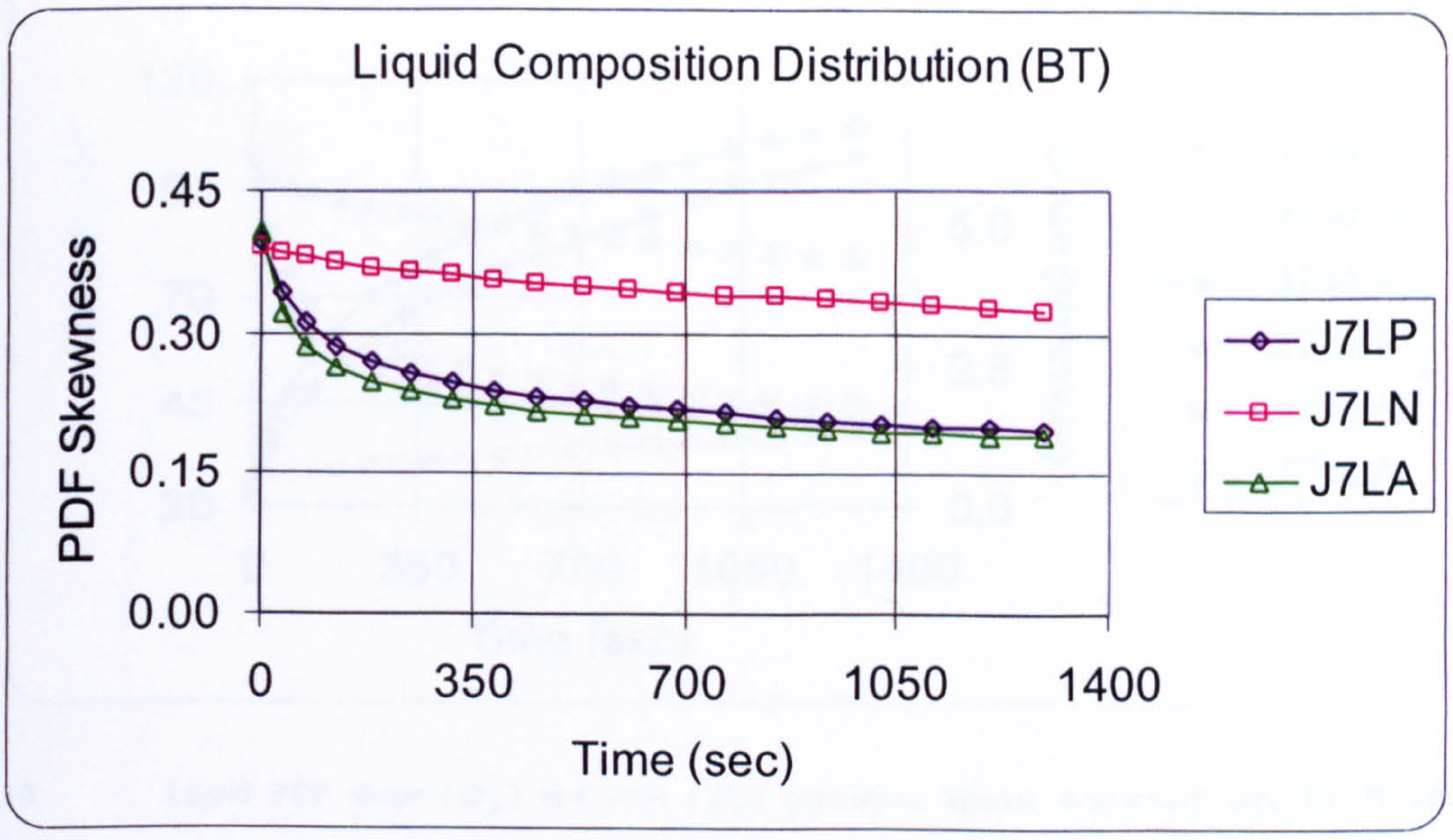

Figure-6.8 Liquid mixture composition distribution skewness against evaporation time for model fuel J7 with homologues paraffin (J7LP-open diamond with solid line), naphthene (J7LN-open rectangle with solid line), and aromatic (J7LA-open triangle with solid line)- initial droplet diameter 639 μm, temperature $10\,^0c$, ambient convective velocity 3m/s at atmospheric conditions.

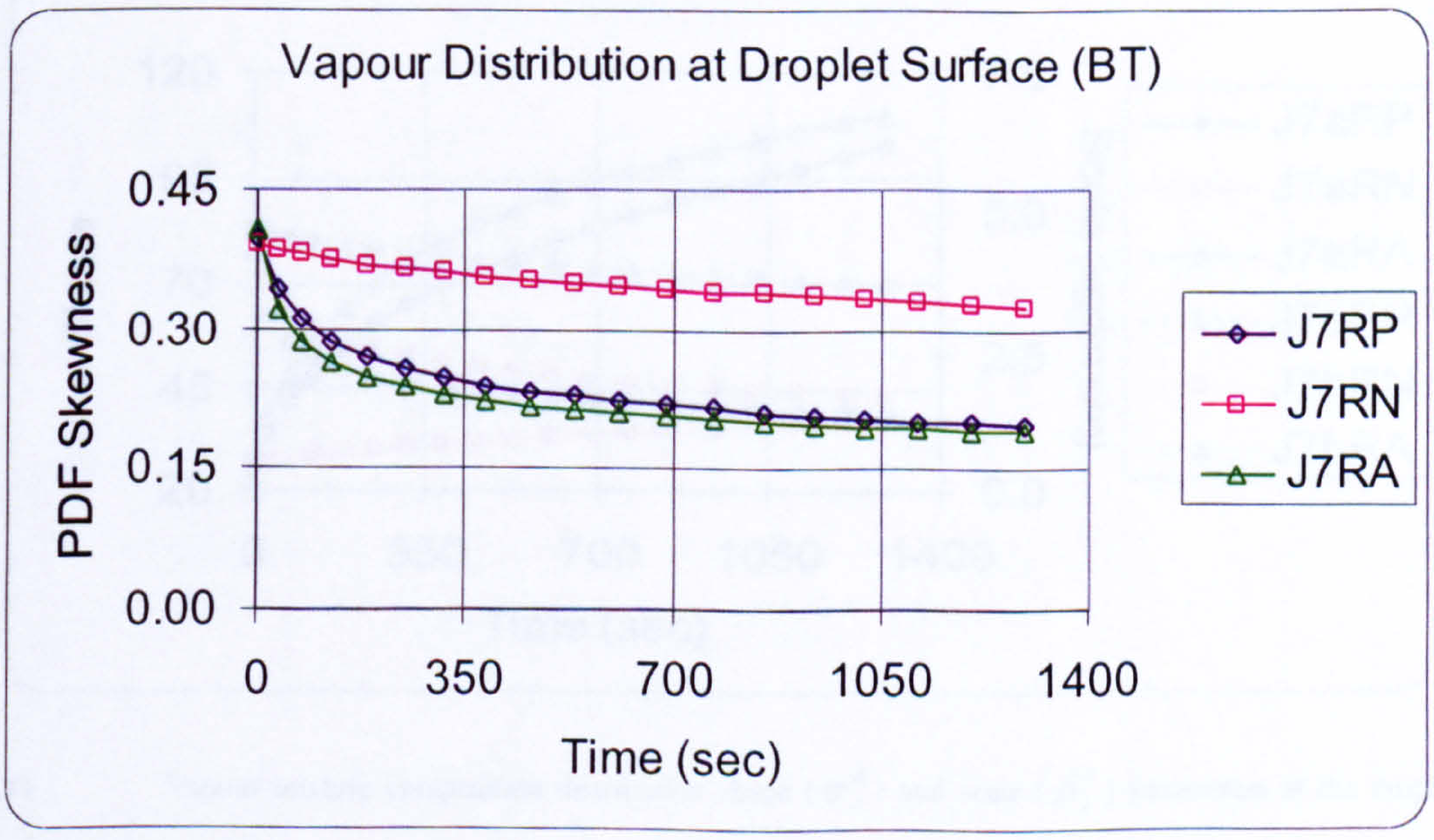

Figure-6.9 Vapour fuel mixture composition distribution skewness at the droplet surface against evaporation time for model fuel J7 with homologues paraffin (J7RP-open diamond with solid line), naphthene (J7RN-open rectangle with solid line), and aromatic (J7RA-open triangle with solid line)- : initial droplet diameter 639 μm, temperature $10\,^0c$, ambient convective velocity 3m/s at atmospheric conditions.

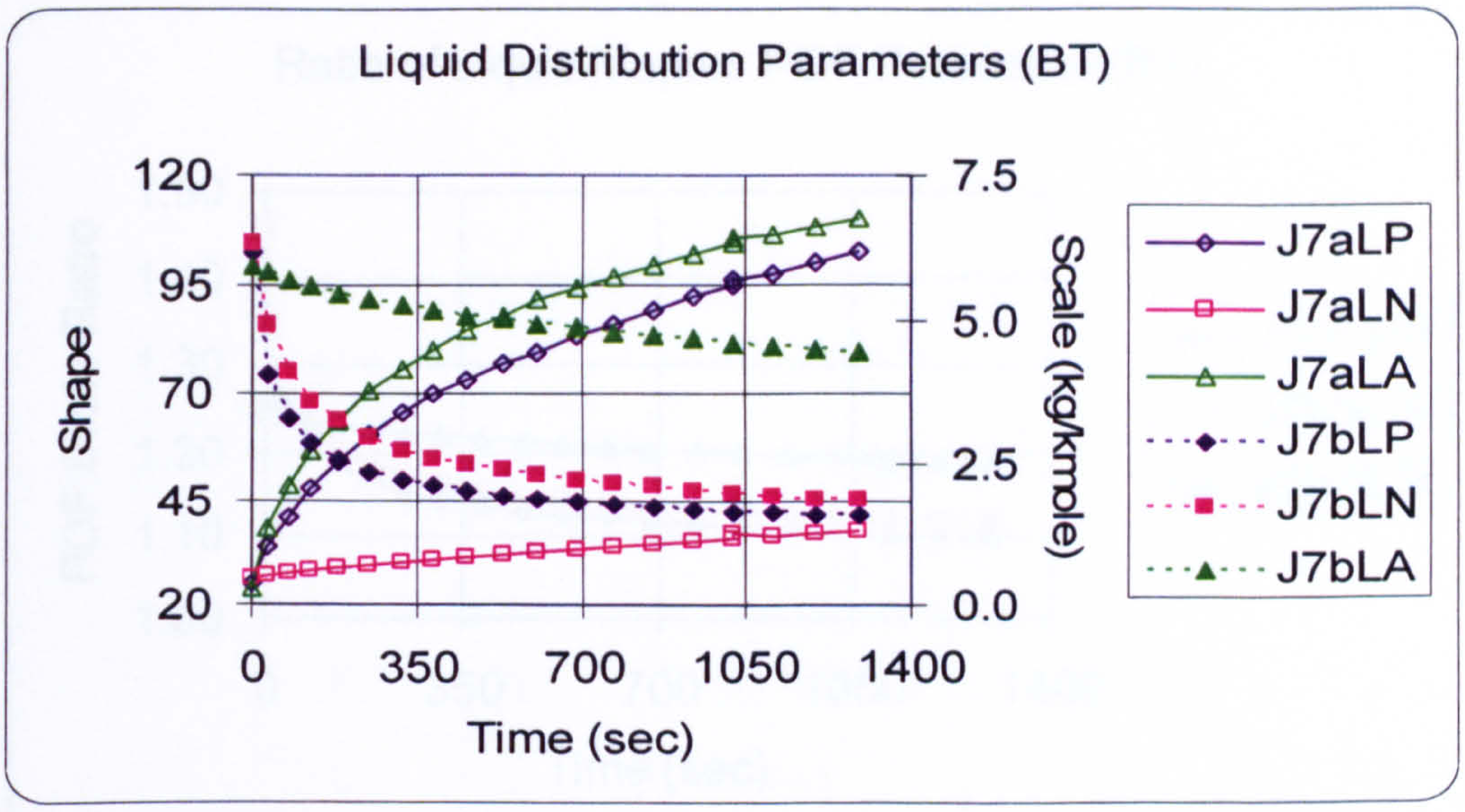

Figure-6.10 Liquid PDF shape (α_J^l) and scale (β_J^l) parameters against evaporation time for J7 with paraffin (α_1^l=J7aLP-open diamond with solid line; β_1^l=J7bLP-solid diamond with dashed lines), naphthene (α_2^l=J7aLN-open rectangle with solid line; β_2^l=J7bLN-solid rectangle with dashed lines), and aromatic (α_3^l=J7aLA-open triangle with solid line; β_3^l=J7bLA-solid diamond with dashed lines)- initial droplet diameter 639 μm, temperature 10 ^0c, ambient convective velocity 3m/s at atmospheric conditions.

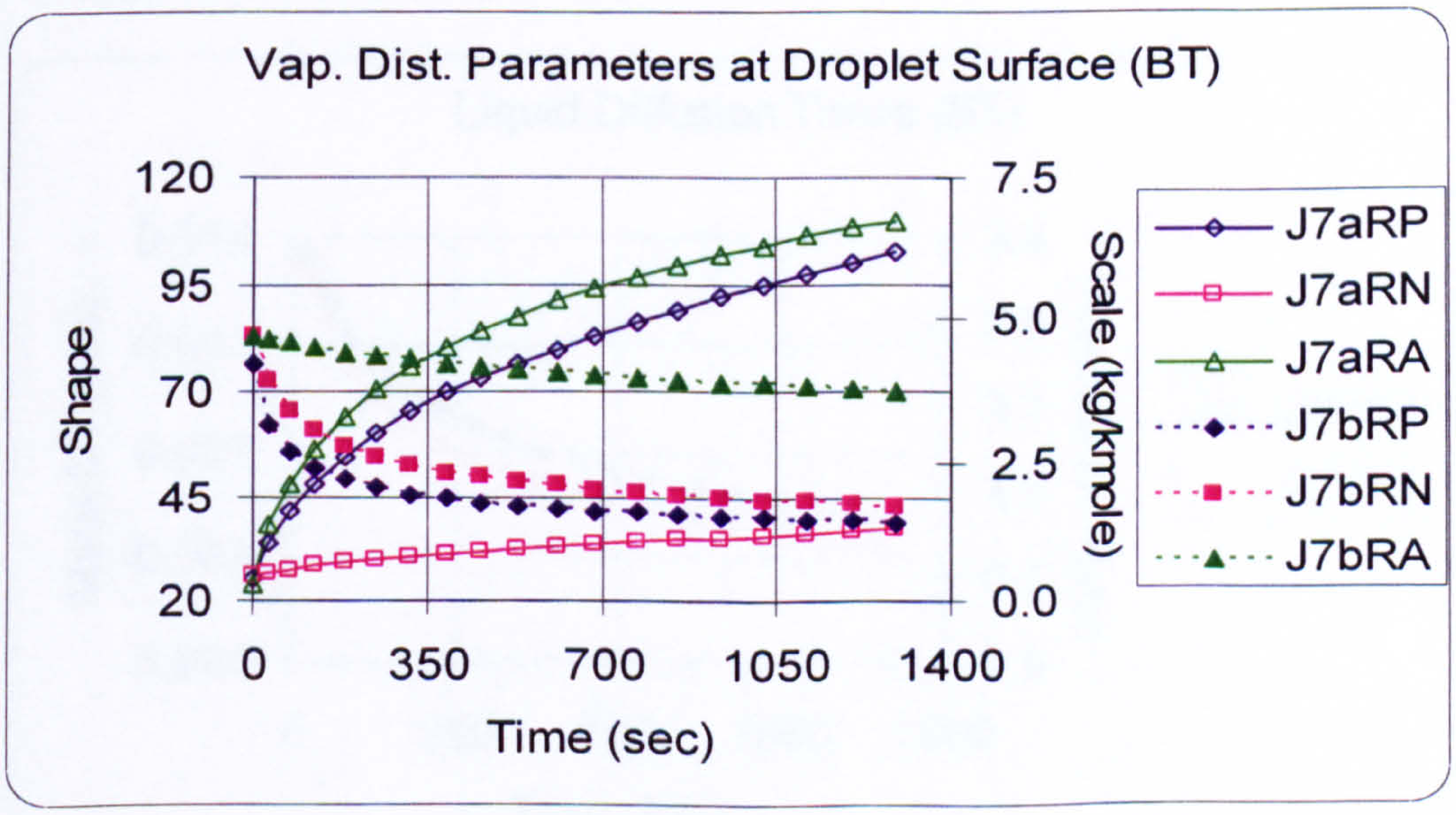

Figure-6.11 Vapour mixture composition distribution shape (α_J^R) and scale (β_J^R) parameters at the droplet surface against evaporation time for model fuel J7 with homologues paraffin (α_1^R=J7aRP-open diamond with solid line; β_1^R=J7bRP-solid diamond with dashed lines), naphthene (α_2^R=J7aRN-open rectangle with solid line; β_2^R=J7bLN-solid rectangle with dashed lines), and aromatic (α_3^l=J7aLA-open triangle with solid line; β_3^l=J7bLA-solid diamond with dashed lines)-initial droplet diameter 639 μm, temperature 10 ^0c, ambient convective velocity 3m/s at atmospheric conditions.

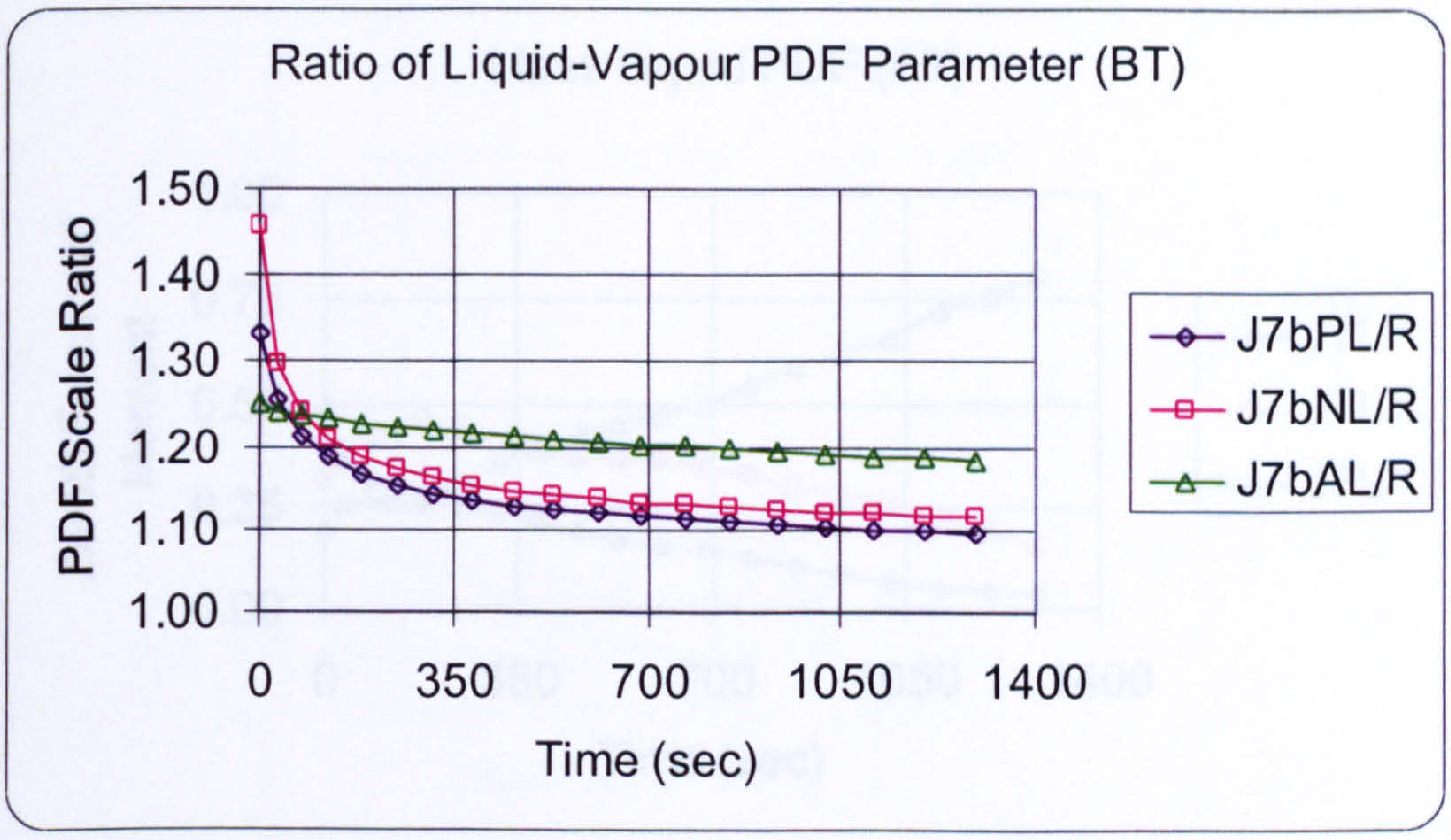

Figure-6.12 Ratios (β_J^l / β_J^R) of the liquid mixture PDF scale parameter and the vapour mixture PDF scale parameter at the droplet surface against evaporation time for model fuel J7 with homologues paraffin (β_1^l / β_1^R =J7bPL/R-open diamond with solid), naphthene (β_2^l / β_2^R =J7bNL/R-open rectangle with solid), and aromatic (β_3^l / β_3^R =J7bAL/R-open triangle with solid)-initial droplet diameter 639 μm, temperature 10 ^0c, ambient convective velocity 3m/s at atmospheric conditions.

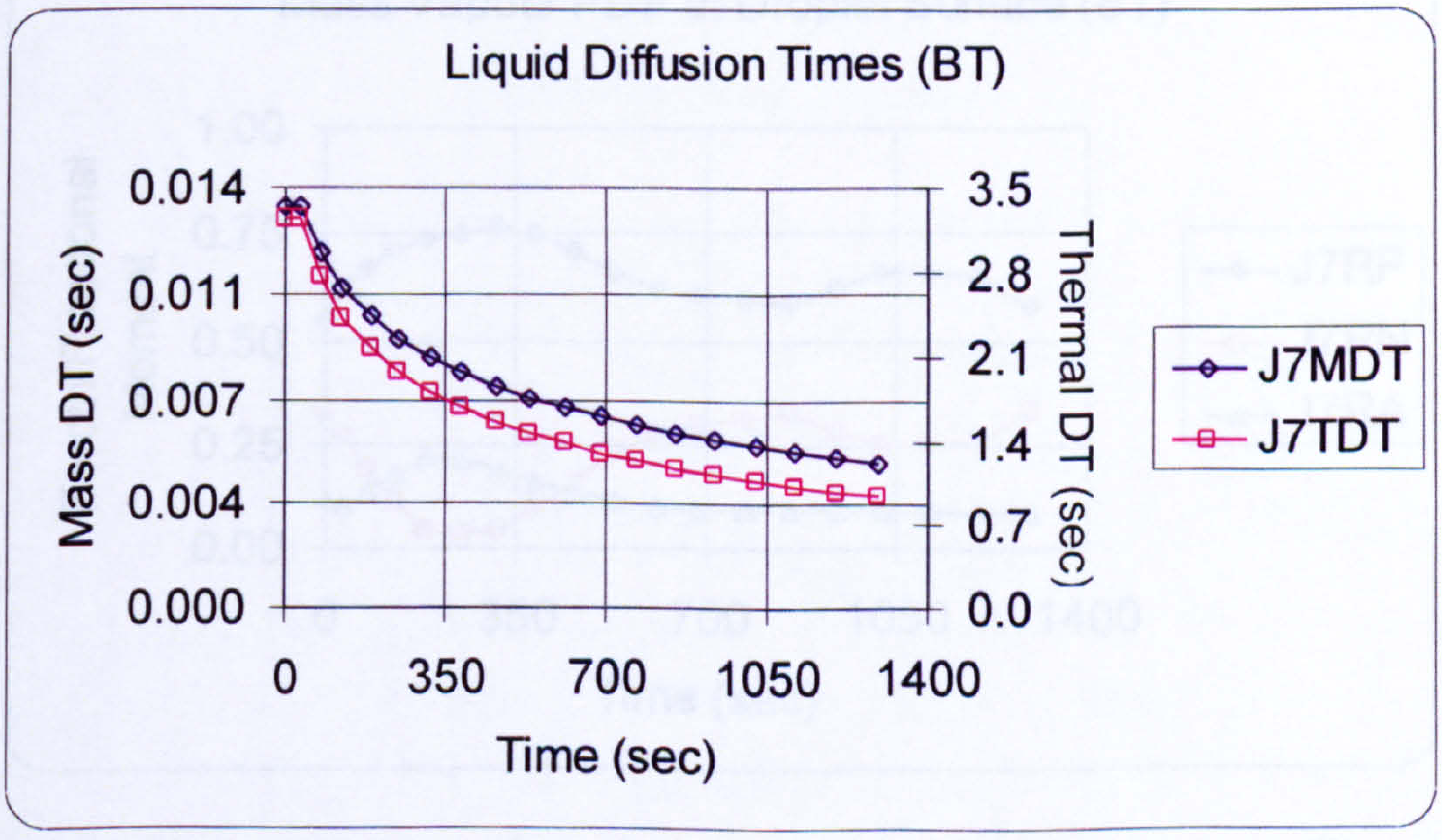

Figure-6.13 Liquid droplet mass diffusion time (J7MDT-open diamond with solid line) and thermal diffusion time (J7TDT-open rectangle with solid line) against evaporation time for model fuel J7: : initial droplet diameter 639 μm, temperature 10 ^0c, ambient convective velocity 3m/s at atmospheric conditions.

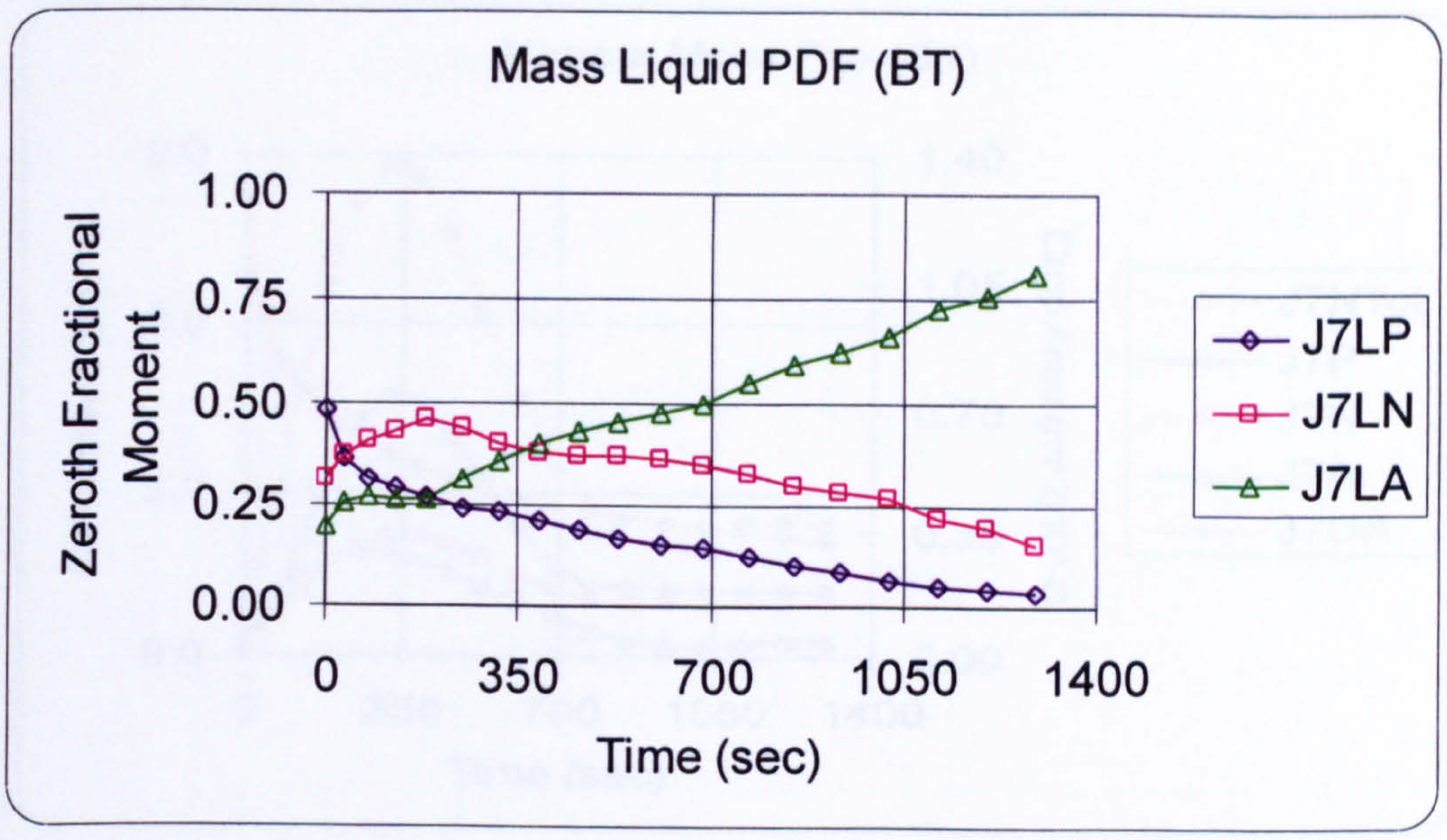

Figure-6.14 Liquid mixture 0th mass fractional composition distribution moment (Y_J^l) against evaporation time for model fuel J7 with homologues paraffin (Y_1^l =J7LP-open diamond with solid line), naphthene (Y_2^l =J7LN-open rectangle with solid line), and aromatic (Y_3^l =J7LA-open triangle with solid line)-initial droplet diameter 639 μm , temperature 10 ^0c , ambient convective velocity 3m/s at atmospheric conditions.

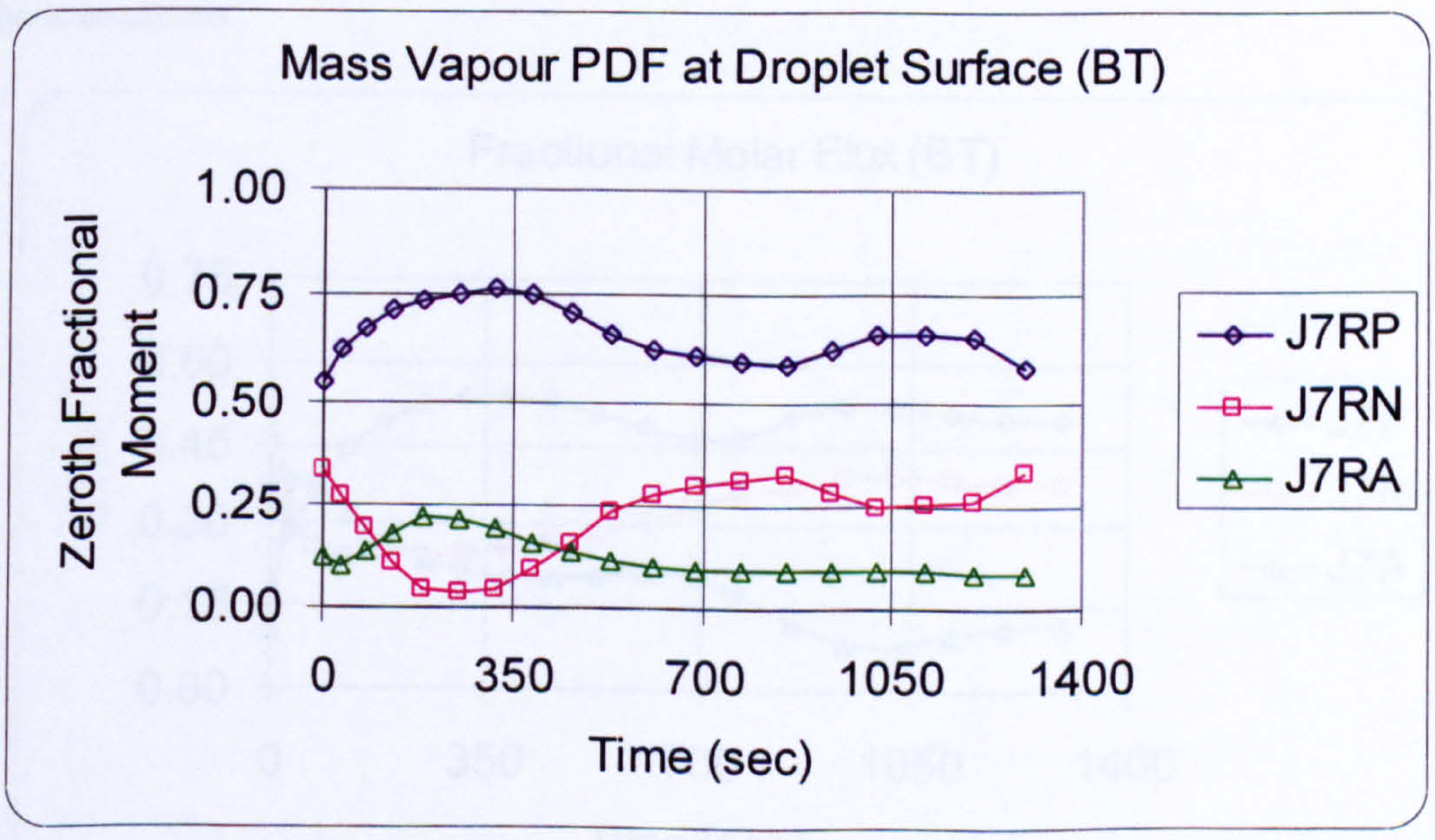

Figure-6.15 Vapour fuel mixture 0th mass fractional composition distribution moment (Y_J^l) at the droplet surface against evaporation time for model fuel J7 with homologues paraffin (Y_1^R =J7RP-open diamond with solid line), naphthene (Y_2^R =J7RN-open rectangle with solid line), and aromatic (Y_3^R =J7RA-open triangle with solid line)-initial droplet diameter 639 μm , temperature 10 ^0c , ambient convective velocity 3m/s at atmospheric conditions.

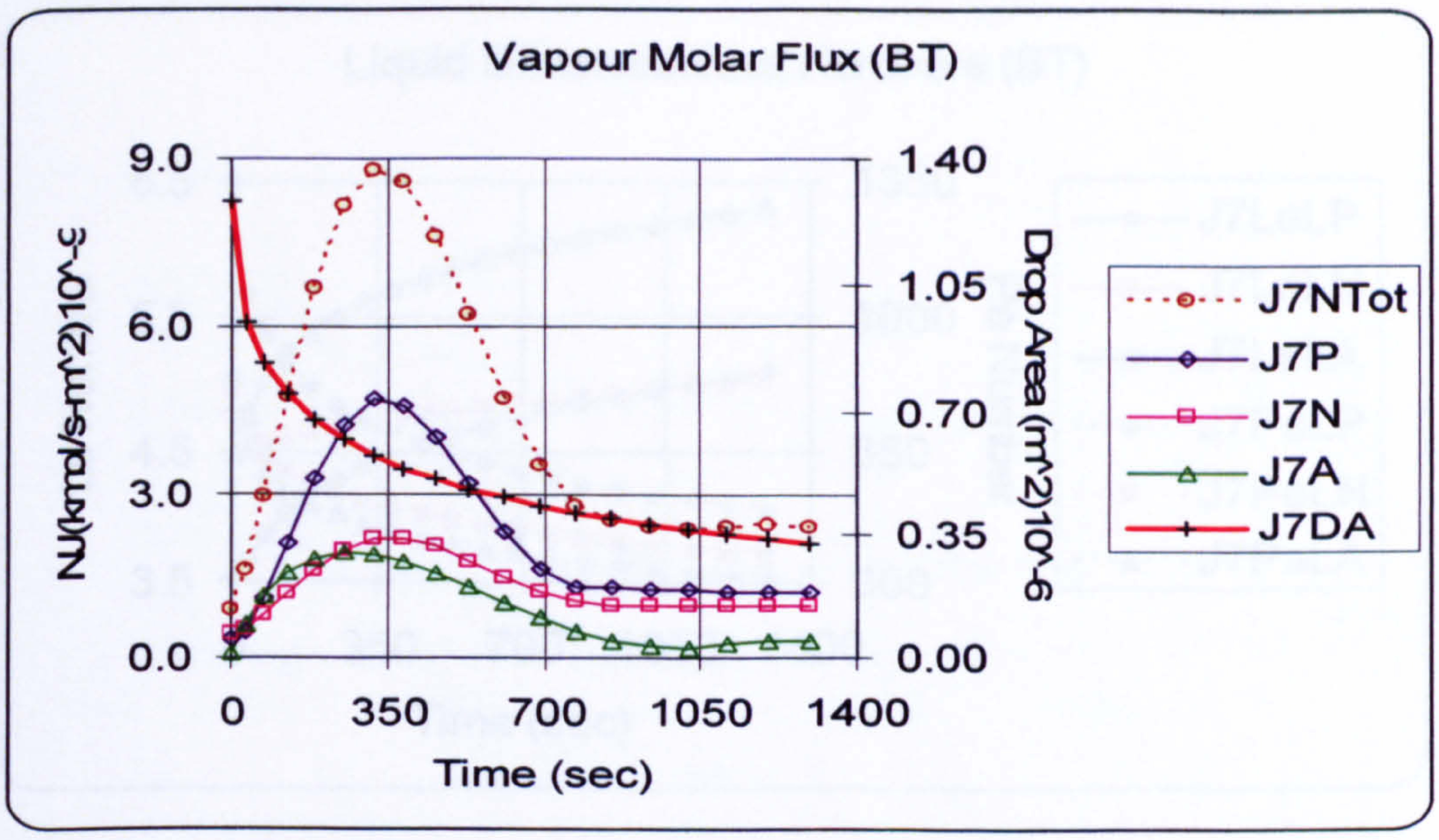

Figure-6.16 Total vapour molar flux ($N_{T(n)}$ =J7NTot-open circle with dashed lines) of model fuel J7 with homologues paraffin ($N_{1(n)}$ =J7P-open diamond with solid line), naphthene ($N_{2(n)}$ =J7N-open rectangle with solid line), aromatic ($N_{3(n)}$ =J7A-open triangle with solid line), and instantaneous droplet area (J7DA-+ with solid line) against evaporation time: initial droplet diameter 639 μm , temperature $10\,^0c$, ambient convective velocity 3m/s at atmospheric conditions.

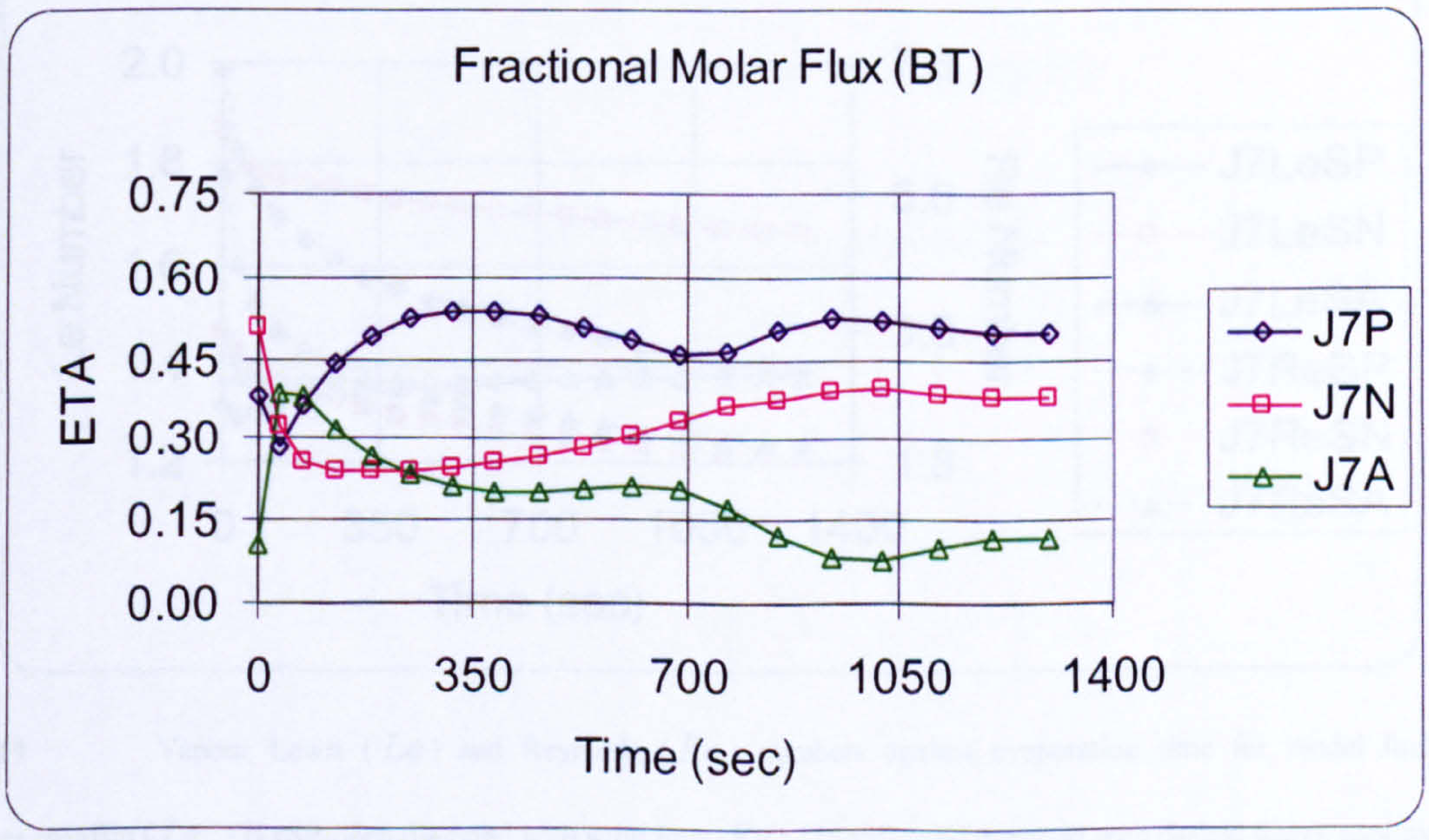

Figure-6.17 Fractional molar fluxes (η_J) against evaporation time for model fuel J7 with homologues paraffin (η_1 =J7P-open diamond with solid line), naphthene (η_2 =J7N-open rectangle with solid line) and aromatic (η_3 =J7A-open triangle with solid line)- : initial droplet diameter 639 μm , temperature $10\,^0c$, ambient convective velocity 3m/s at atmospheric conditions.

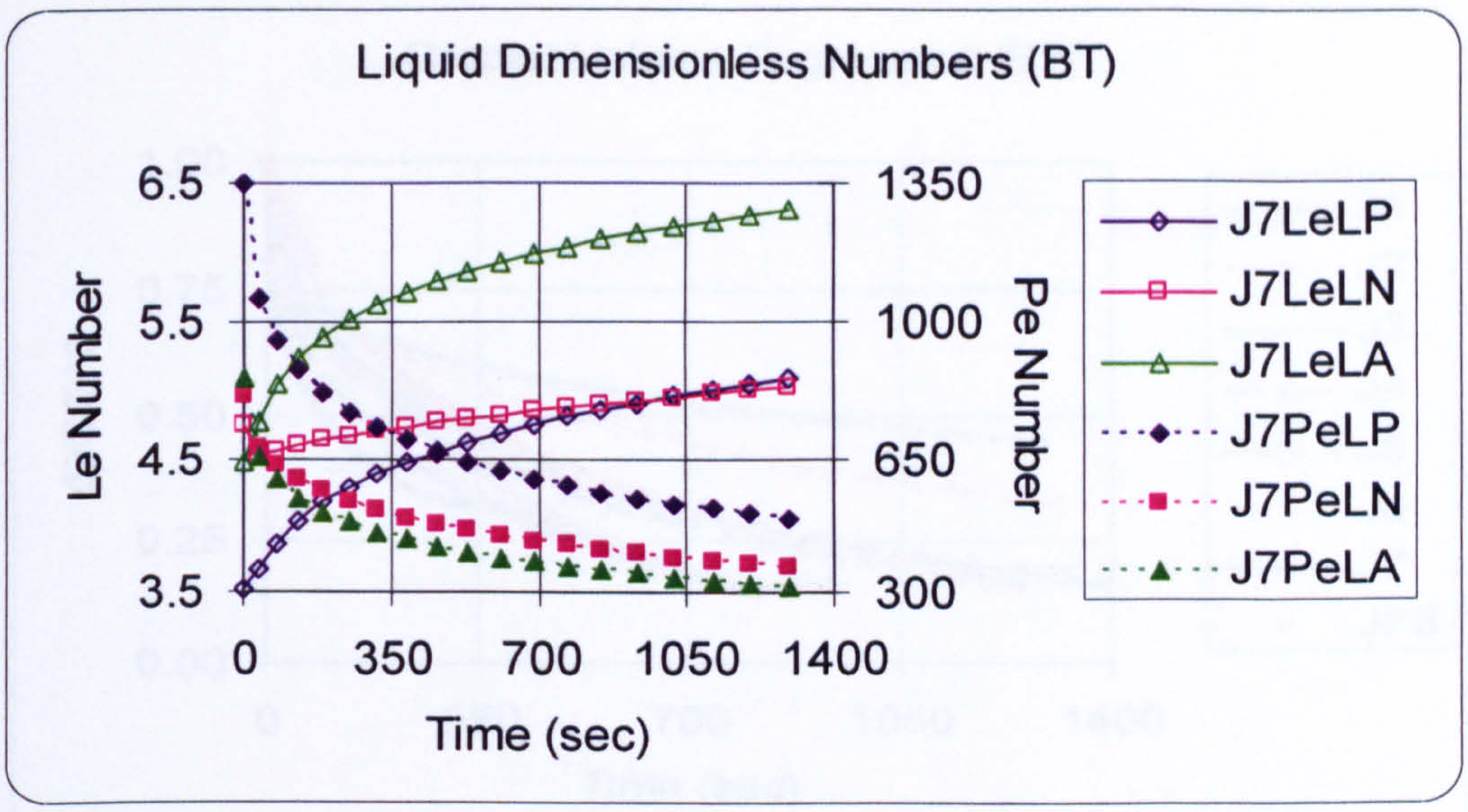

Figure-6.18 Liquid Lewis (Le) and Peclet (Pe) numbers against evaporation time for model fuel J7 with homologues paraffin (Le : J7LeLP-open diamond with solid line; Pe : J7PeLP-solid diamond with dashed lines), naphthene (Le : J7LeLN-open rectangle with solid line; Pe : J7PeLN-solid rectangle with dashed lines), and aromatic (Le : J7LeLA-open triangle with solid line; Pe : J7PeLA-solid triangle with dashed lines)- initial droplet diameter 639 μm , temperature 10 ^{0}c , ambient convective velocity 3m/s at atmospheric conditions.

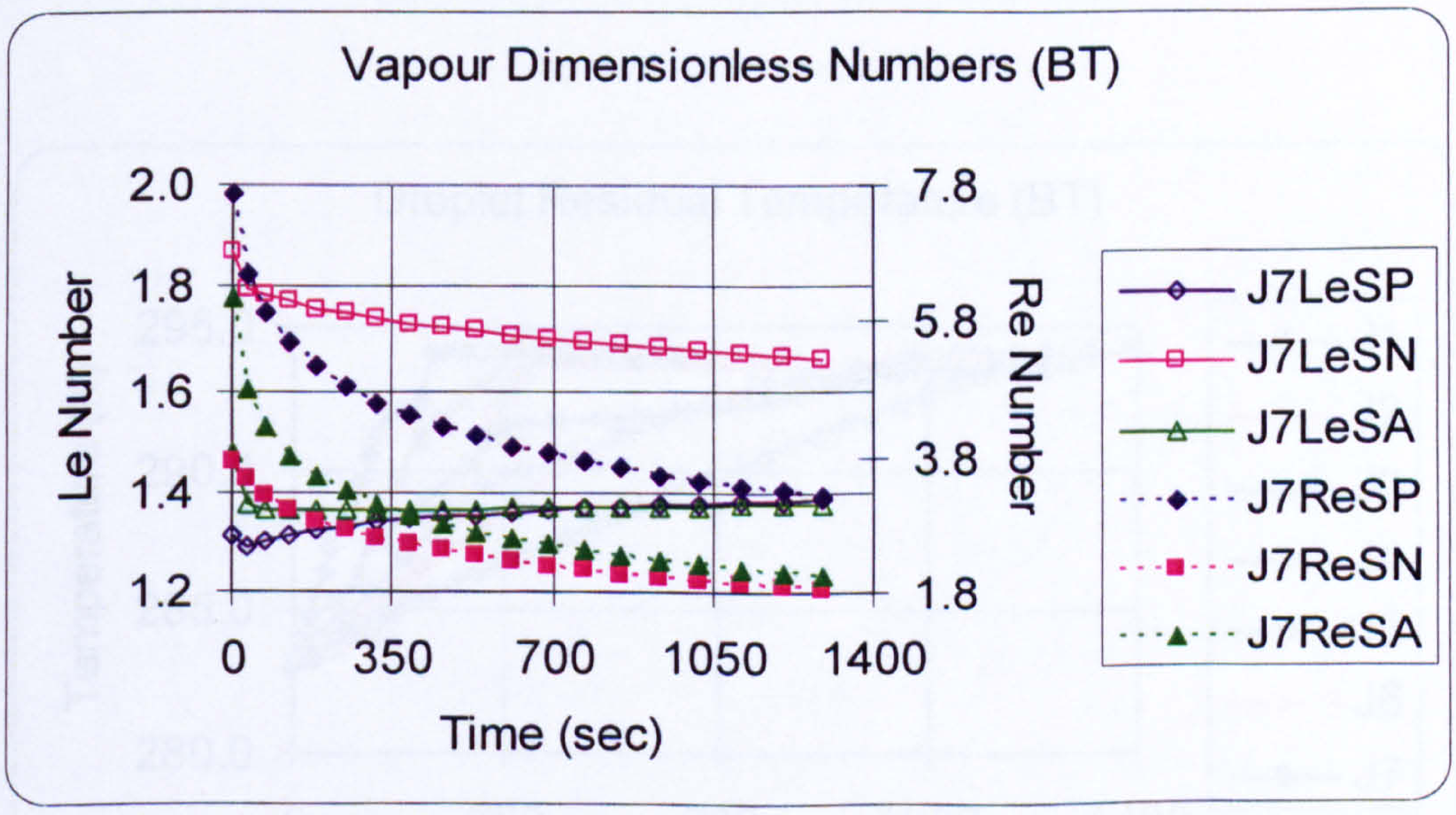

Figure-6.19 Vapour Lewis (Le) and Reynolds (Re) numbers against evaporation time for model fuel J7 with homologues paraffin (Le : J7LeSP-open diamond with solid line; Re : J7ReSP-solid diamond with dashed lines), naphthene (Le : J7LeSN-open rectangle with solid line; Re : J7ReSN-solid rectangle with dashed lines), and aromatic (Le : J7LeSA-open triangle with solid line; Re : J7ReSA-solid triangle with dashed lines)-initial droplet diameter 639 μm , temperature 10 ^{0}c , ambient convective velocity 3m/s at atmospheric conditions.

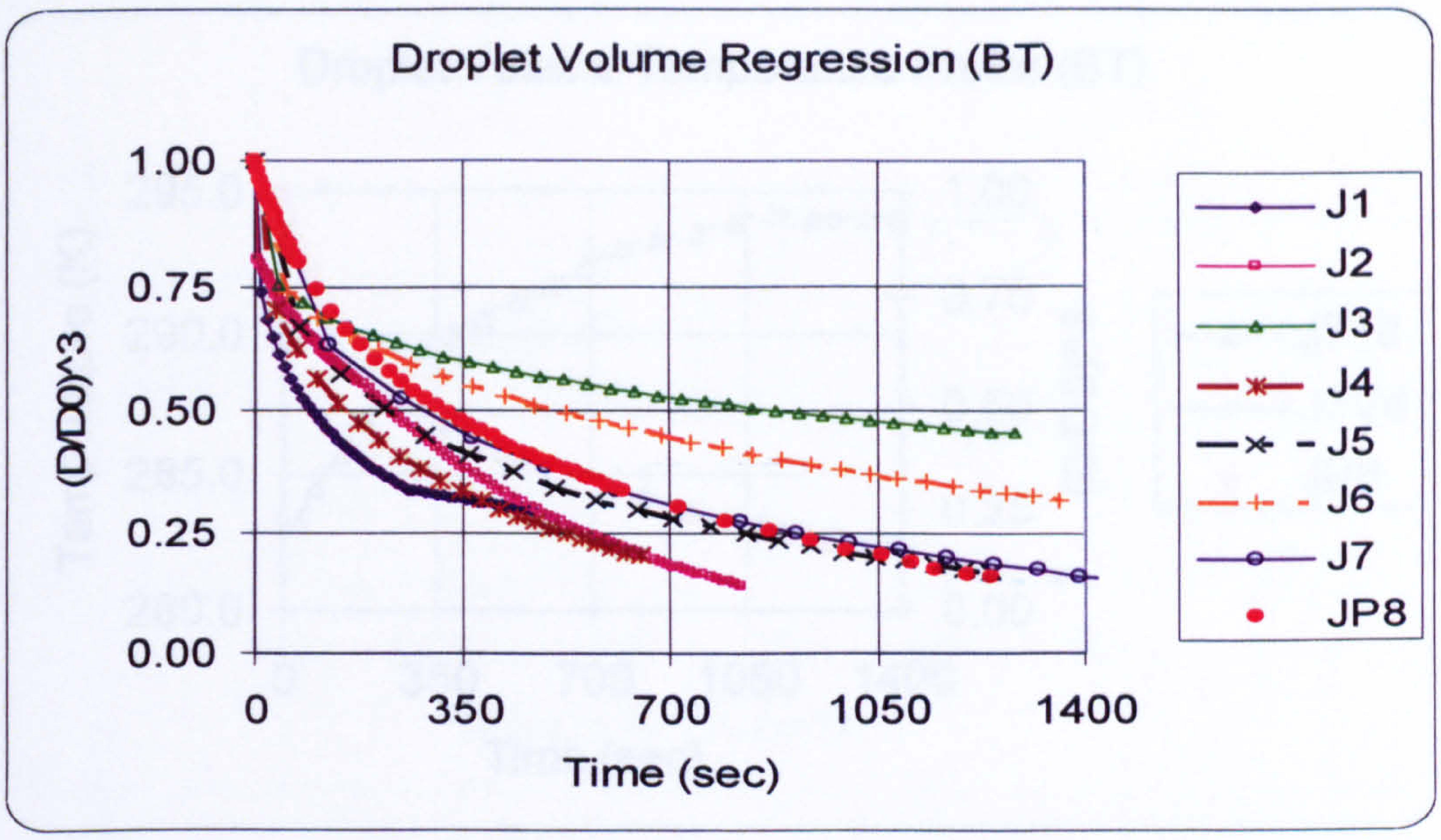

Figure-6.20 Liquid droplet relative volume (diameter) regression against evaporation time for model fuels J1 (open diamond with solid line), J2 (open rectangle with solid line), J3 (open triangle with solid line), J4 (asterisk with dashed lines), J5 (x with dashed lines), J6 (+ with dashed lines), J7 (open circle with solid lines) and the experimental data of Runge et al (1998) for fuel JP8 (solid circles)-initial droplet diameter 639 μm, temperature $10\,^0c$, ambient convective velocity 3m/s at atmospheric conditions.

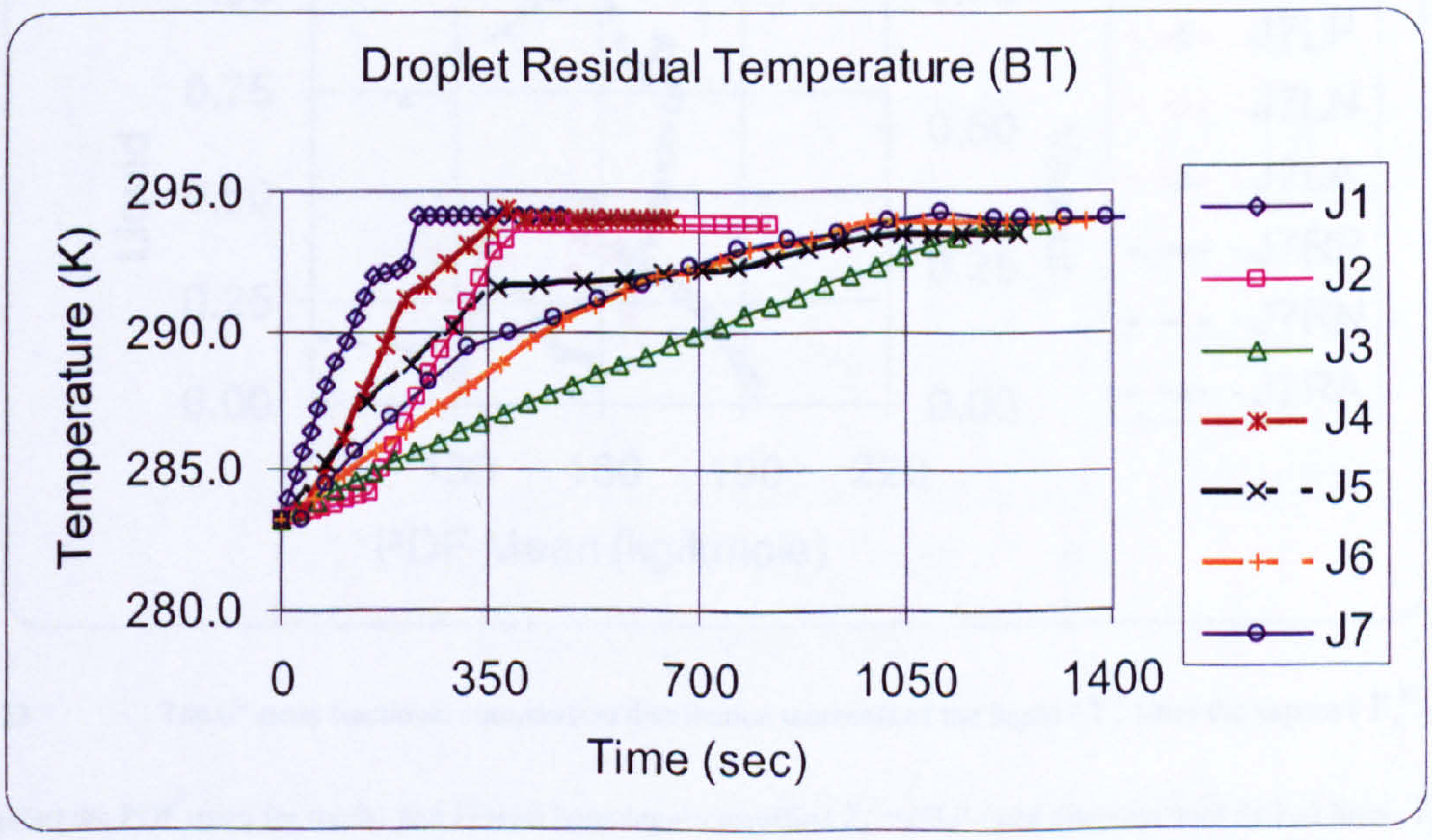

Figure-6.21 Liquid droplet residual temperature against evaporation time for model fuels J1 (open diamond with solid line), J2 (open rectangle with solid line), J3 (open triangle with solid line), J4 (asterisk with dashed lines), J5 (x with dashed lines), J6 (+ with dashed lines), and J7 (open circle with solid lines)-initial droplet diameter 639 μm, temperature $10\,^0c$, ambient convective velocity 3m/s at atmospheric conditions.

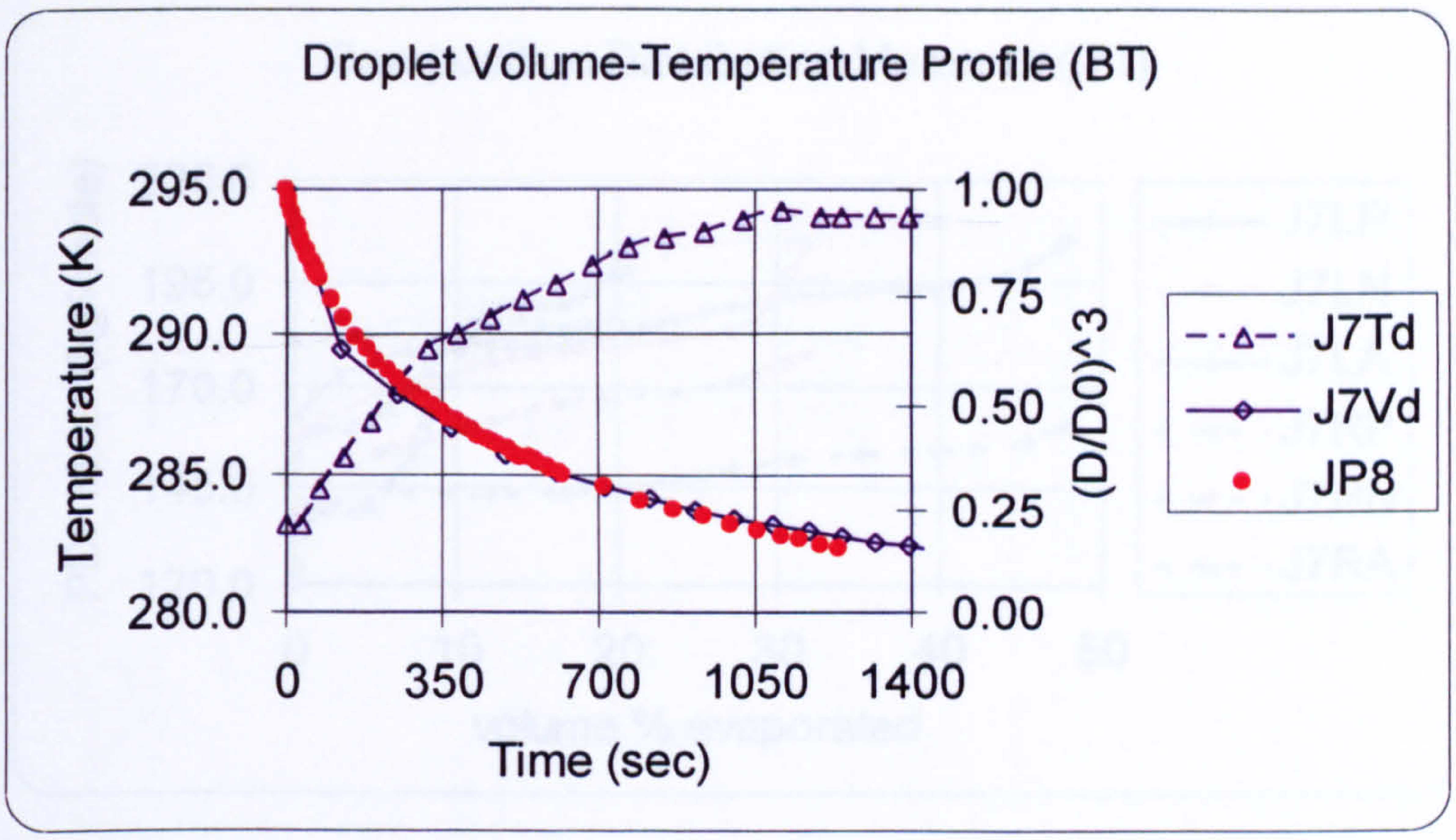

Figure-6.22 Profiles of the numerically simulated model fuel J7 liquid droplet residual temperature (J7Td-open triangle with dashed lines) and liquid droplet relative volume (diameter) regression (J7Vd-open circles with solid line) against evaporation time compared with the droplet relative volume regression experimental data of Runge et al (1998) for fuel JP8 (solid circles)-initial droplet diameter 639 μm , temperature $10\,^0 c$, ambient convective velocity 3m/s at atmospheric conditions.

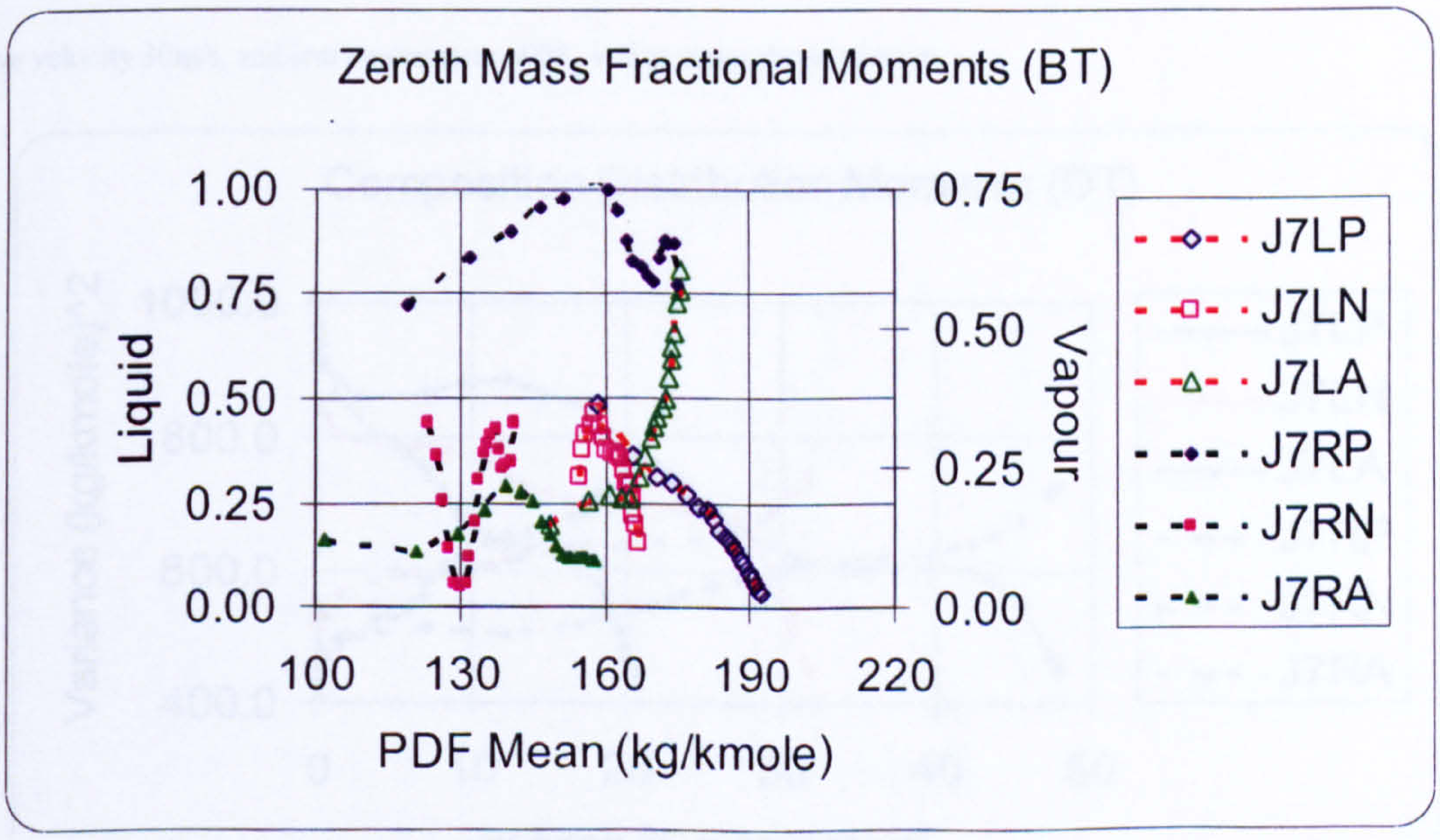

Figure-6.23 The 0th mass fractional composition distribution moments of the liquid (Y_J^l) and the vapour (Y_J^R) at droplet surface against the PDF mean for model fuel J7 with homologues paraffin (Y_1^l =J7LP-open diamond with dashed lines, Y_1^R =J7RP-solid diamond with dashed lines), naphthene (Y_2^l =J7LN-open rectangle with dashed lines; Y_2^R =J7RN-solid rectangle with dashed lines), and aromatic (Y_3^l =J7LA-open triangle with solid line; Y_3^R =J7RA-solid triangle with dashed lines)-initial droplet diameter 639 μm , temperature $10\,^0 c$, ambient convective velocity 3m/s at atmospheric conditions.

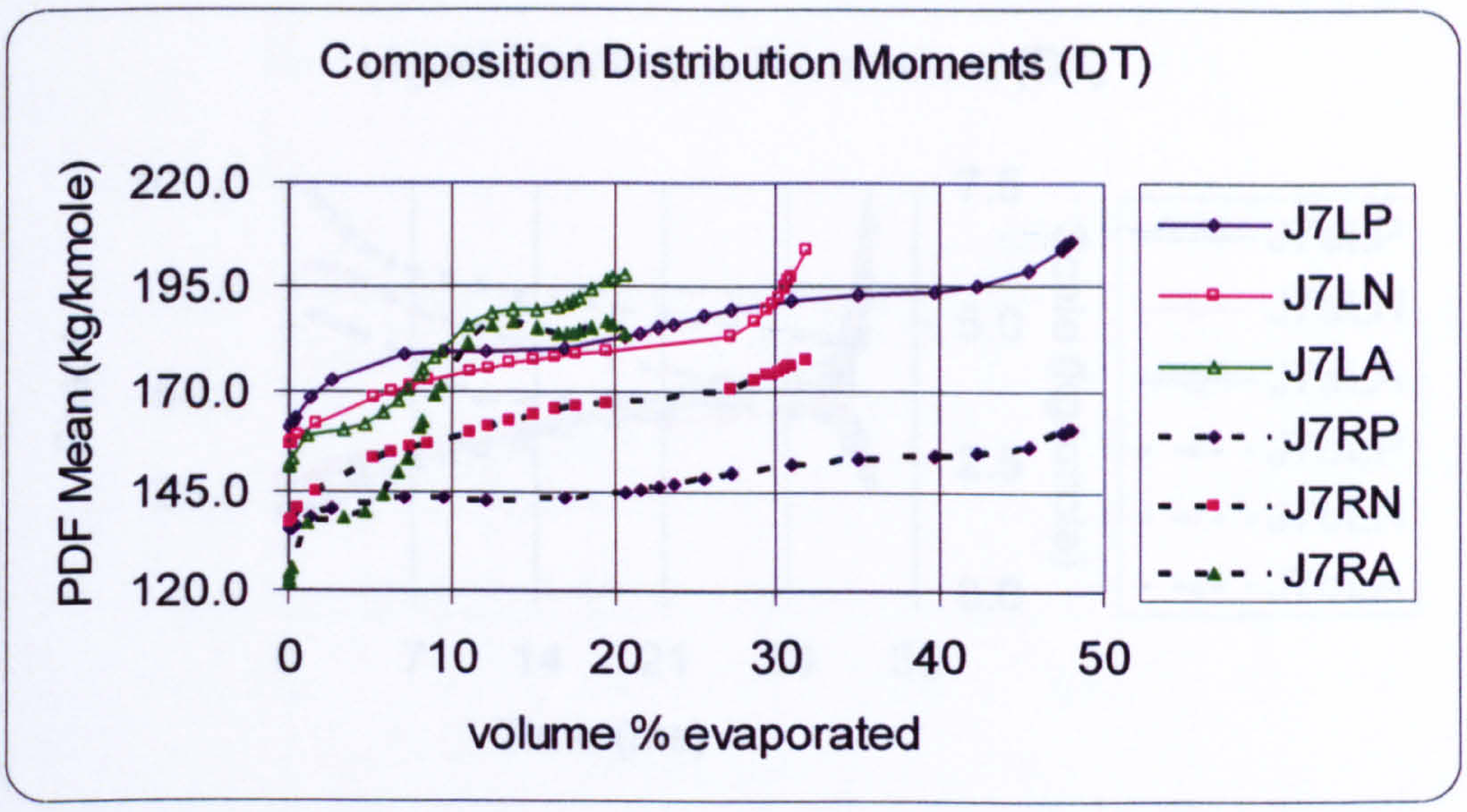

Figure-6.24 PDF mean of the liquid (θ_J^l) and the vapour (θ_J^R) at droplet surface against the volume % evaporated for model fuel J7 with homologues paraffin (θ_1^l =J7LP-open diamond with solid line, θ_1^R =J7RP-solid diamond with dashed lines), naphthene (θ_2^l =J7LN-open rectangle with solid line; θ_2^R =J7RN-solid rectangle with dashed lines), and aromatic (θ_3^l =J7LA-open triangle with solid line; θ_3^R =J7RA-solid triangle with dashed lines)-initial droplet diameter 639 μm , temperature 21 ^0c , ambient convective velocity 30m/s, ambient temperature 600K, and at atmospheric pressure.

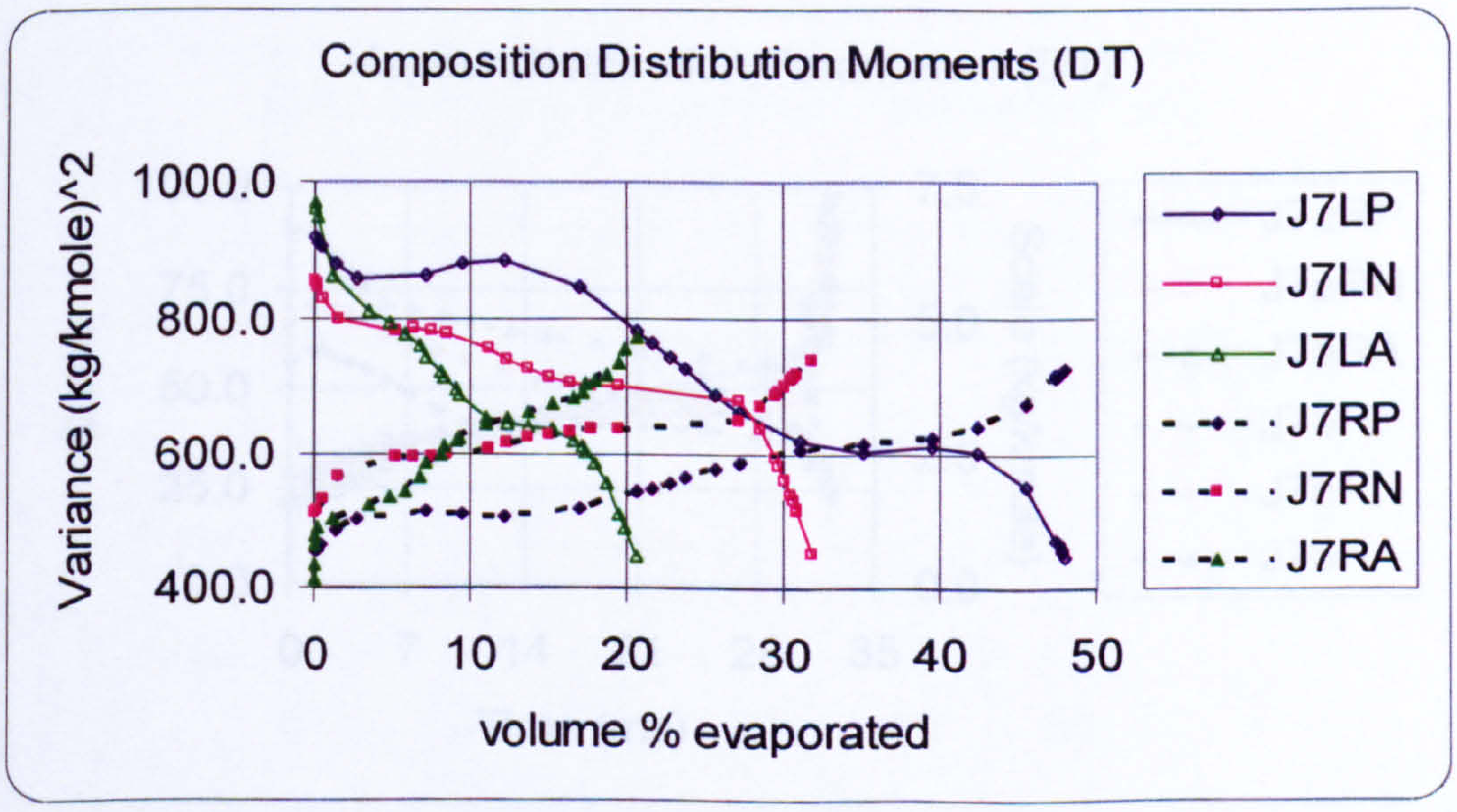

Figure-6.25 PDF variance of the liquid ($(\sigma^2)_J^l$) and the vapour ($(\sigma^2)_J^R$) at droplet surface against the volume % evaporated for model fuel J7 with homologues paraffin ($(\sigma^2)_1^l$ =J7LP-open diamond with solid line, $(\sigma^2)_1^R$ =J7RP-solid diamond with dashed lines), naphthene ($(\sigma^2)_2^l$ =J7LN-open rectangle with solid line; $(\sigma^2)_2^R$ =J7RN-solid rectangle with dashed lines), and aromatic ($(\sigma^2)_3^l$ =J7LA-open triangle with solid line; $(\sigma^2)_3^R$ =J7RA-solid triangle with dashed lines)- initial droplet diameter 639 μm , temperature 21 ^0c , ambient convective velocity 30m/s, ambient temperature 600K, and at atmospheric pressure.

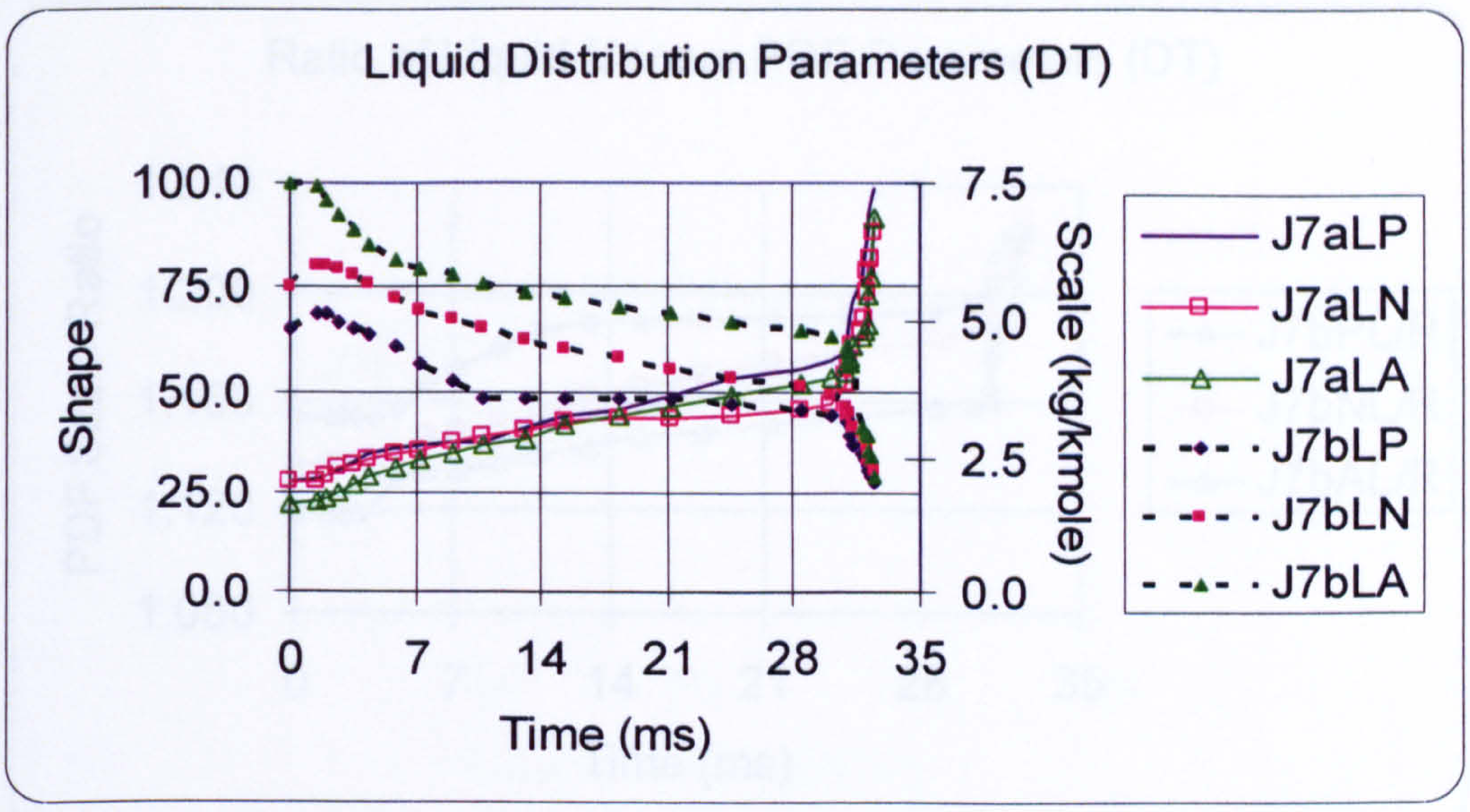

Figure-6.26 Liquid PDF shape (α^l_J) and scale (β^l_J) parameters against evaporation time for model fuel J7 with homologues paraffin (α^l_1=J7aLP-open diamond with solid line, β^l_1=J7bLP-solid diamond with dashed lines), naphthene (α^l_2=J7aLN-open rectangle with solid line; β^l_2=J7bLN-solid rectangle with dashed lines), and aromatic (α^l_3=J7aLA-open triangle with solid line; β^l_3=J7bLA-solid triangle with dashed lines)- initial droplet diameter 639 μm, temperature 21 ^0c, ambient convective velocity 30m/s, ambient temperature 600K, and at atmospheric pressure.

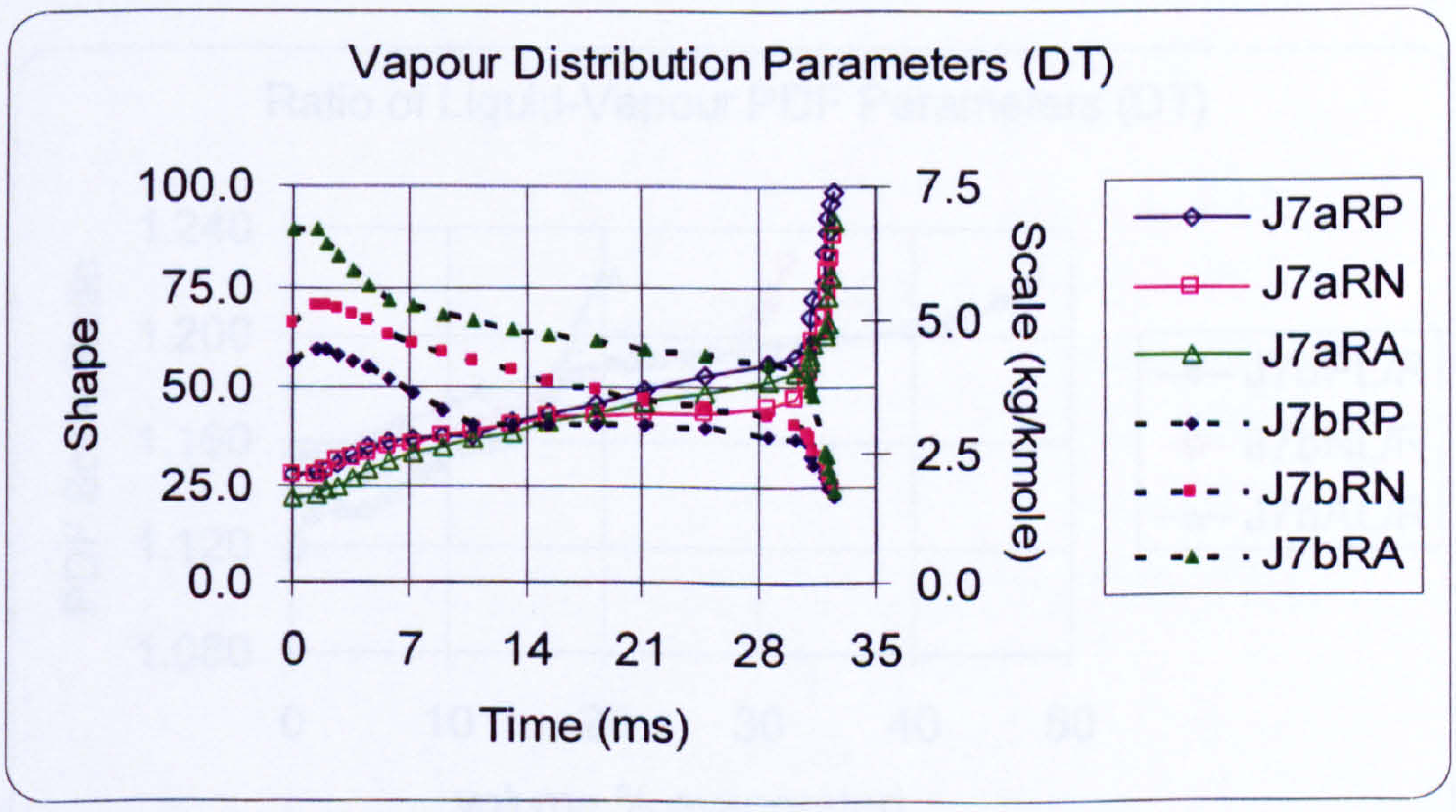

Figure-6.27 Vapour PDF shape (α^l_J) and scale (β^l_J) parameters at droplet surface against evaporation time for model fuel J7 with homologues paraffin (α^R_1=J7aRP-open diamond with solid line, β^R_1=J7bRP-solid diamond with dashed lines), naphthene (α^R_2=J7aRN-open rectangle with solid line; β^R_2=J7bRN-solid rectangle with dashed lines), and aromatic (α^R_3=J7aRA-open triangle with solid line; β^R_3=J7bRA-solid triangle with dashed lines)- initial droplet diameter 639 μm, temperature 21 ^0c, ambient convective velocity 30m/s, ambient temperature 600K, and at atmospheric pressure.

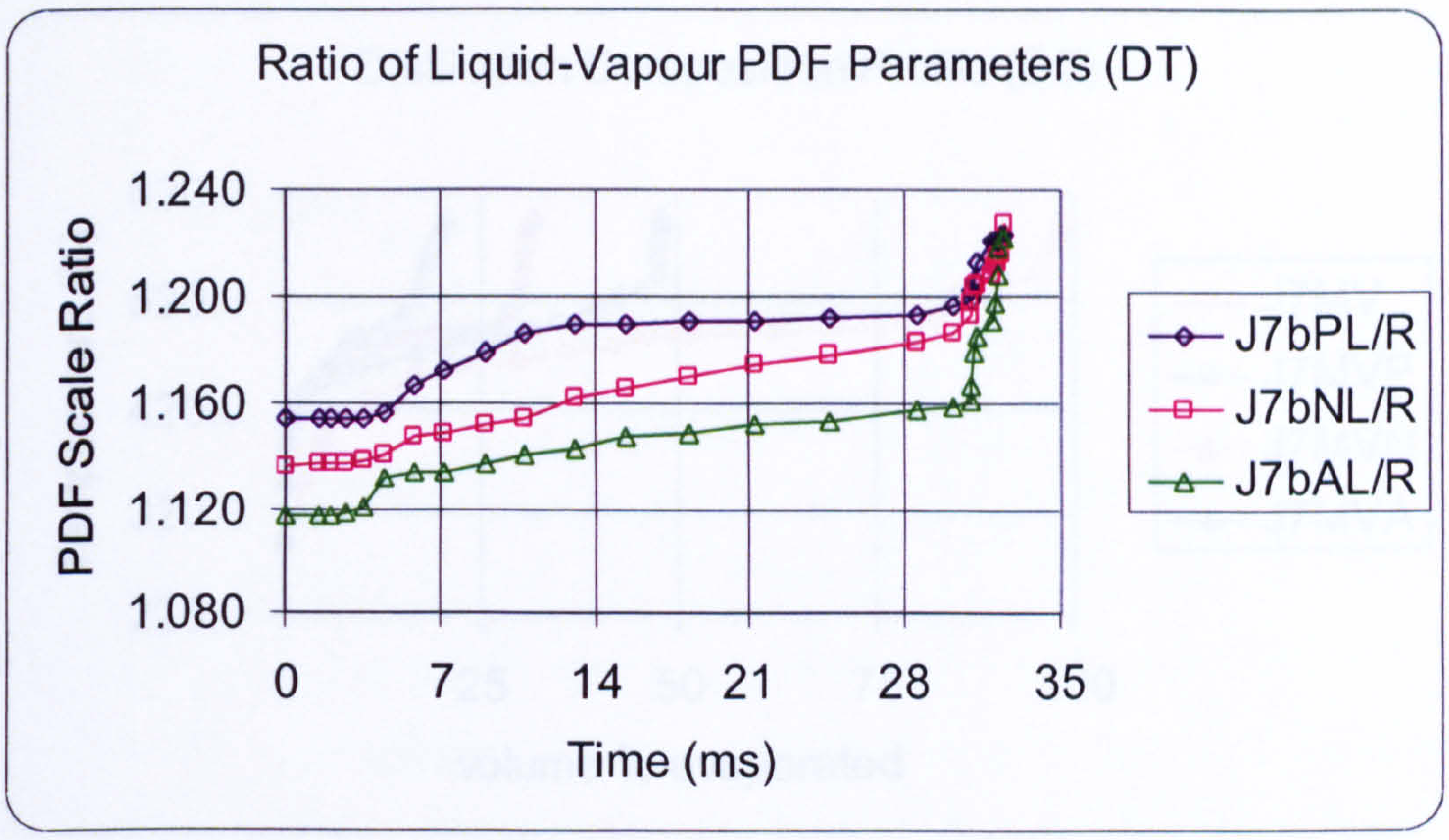

Figure-6.28 Ratios (β_J^l/β_J^R) of the liquid mixture PDF scale parameter and the vapour mixture PDF scale parameter at the droplet surface against evaporation time for model fuel J7 with homologues paraffin (β_1^l/β_1^R =J7bPL/R-open diamond with solid), naphthene (β_2^l/β_2^R =J7bNL/R-open rectangle with solid), and aromatic (β_3^l/β_3^R =J7bAL/R-open triangle with solid)- initial droplet diameter 639 μm , temperature 21 ^0c , ambient convective velocity 30m/s, ambient temperature 600K, and at atmospheric pressure.

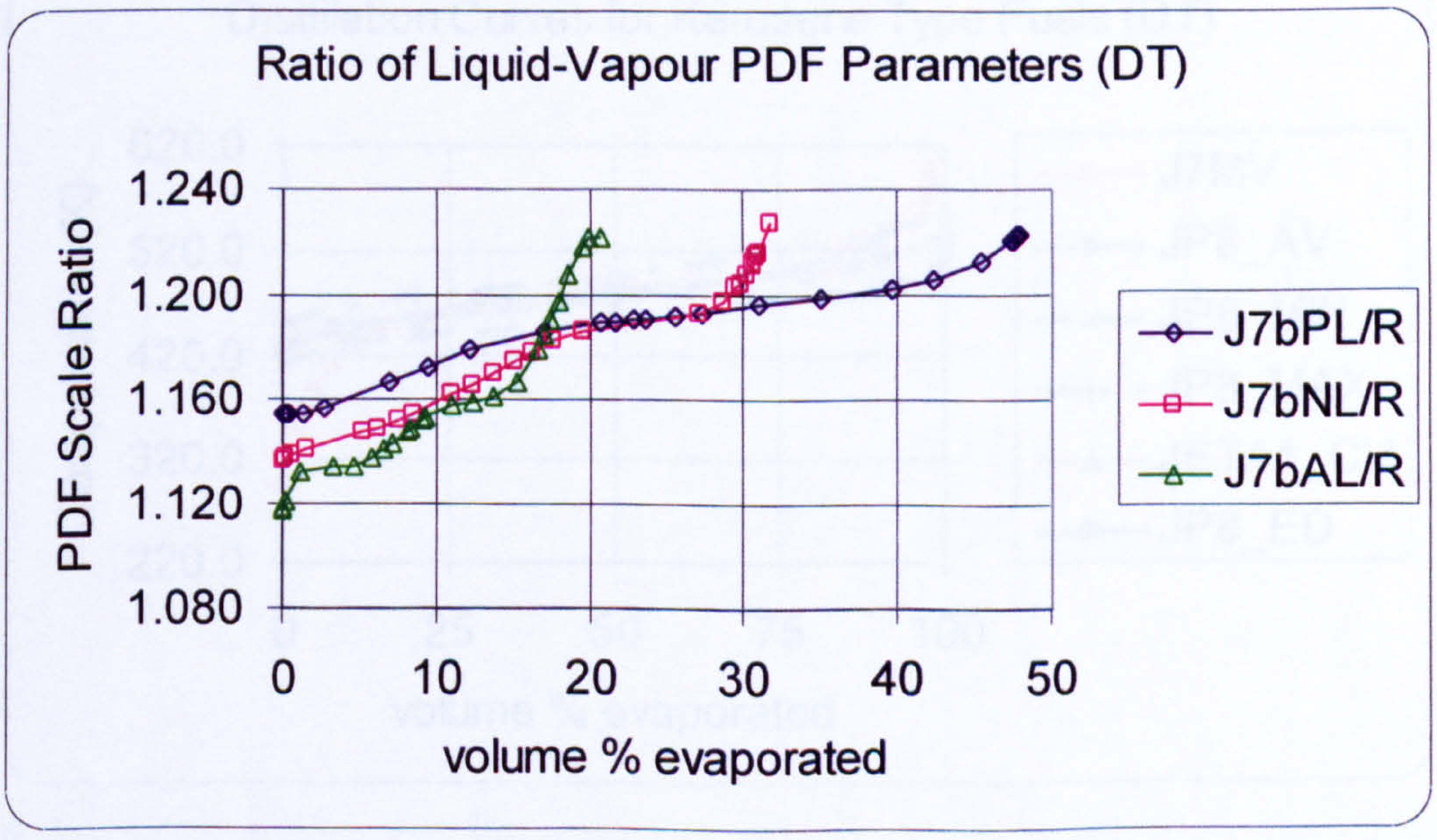

Figure-6.29 Ratios (β_J^l/β_J^R) of the liquid mixture PDF scale parameter and the vapour mixture PDF scale parameter at the droplet surface against volume % evaporated for model fuel J7 with homologues paraffin (β_1^l/β_1^R =J7bPL/R-open diamond with solid), naphthene (β_2^l/β_2^R =J7bNL/R-open rectangle with solid), and aromatic (β_3^l/β_3^R =J7bAL/R-open triangle with solid)- initial droplet diameter 639 μm , temperature 21 ^0c , ambient convective velocity 30m/s, ambient temperature 600K, and at atmospheric pressure.

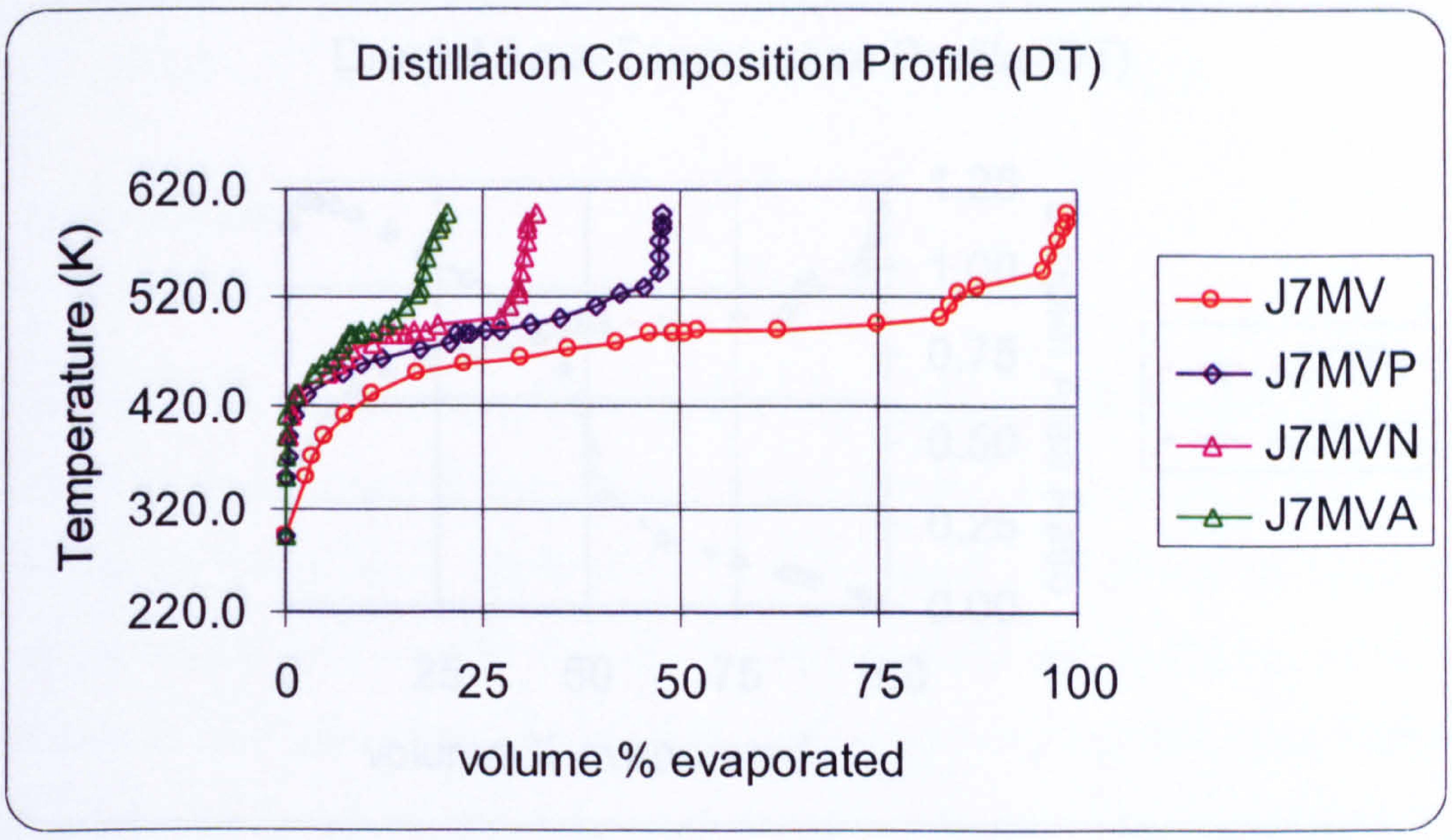

Figure-6.30 Residual Liquid Temperature against fractional and total volume % evaporated for model fuel J7 with homologues paraffin (J7MVP-open diamond with solid line), naphthene (J7MVN-open rectangle with solid line), aromatic (J7MVA-open triangle with solid line) and total distillation curve of J7 (J7MV-open circle with solid line)- initial droplet diameter 639 μm , temperature 21 ^0c , ambient convective velocity 30m/s, ambient temperature 600K, and at atmospheric pressure

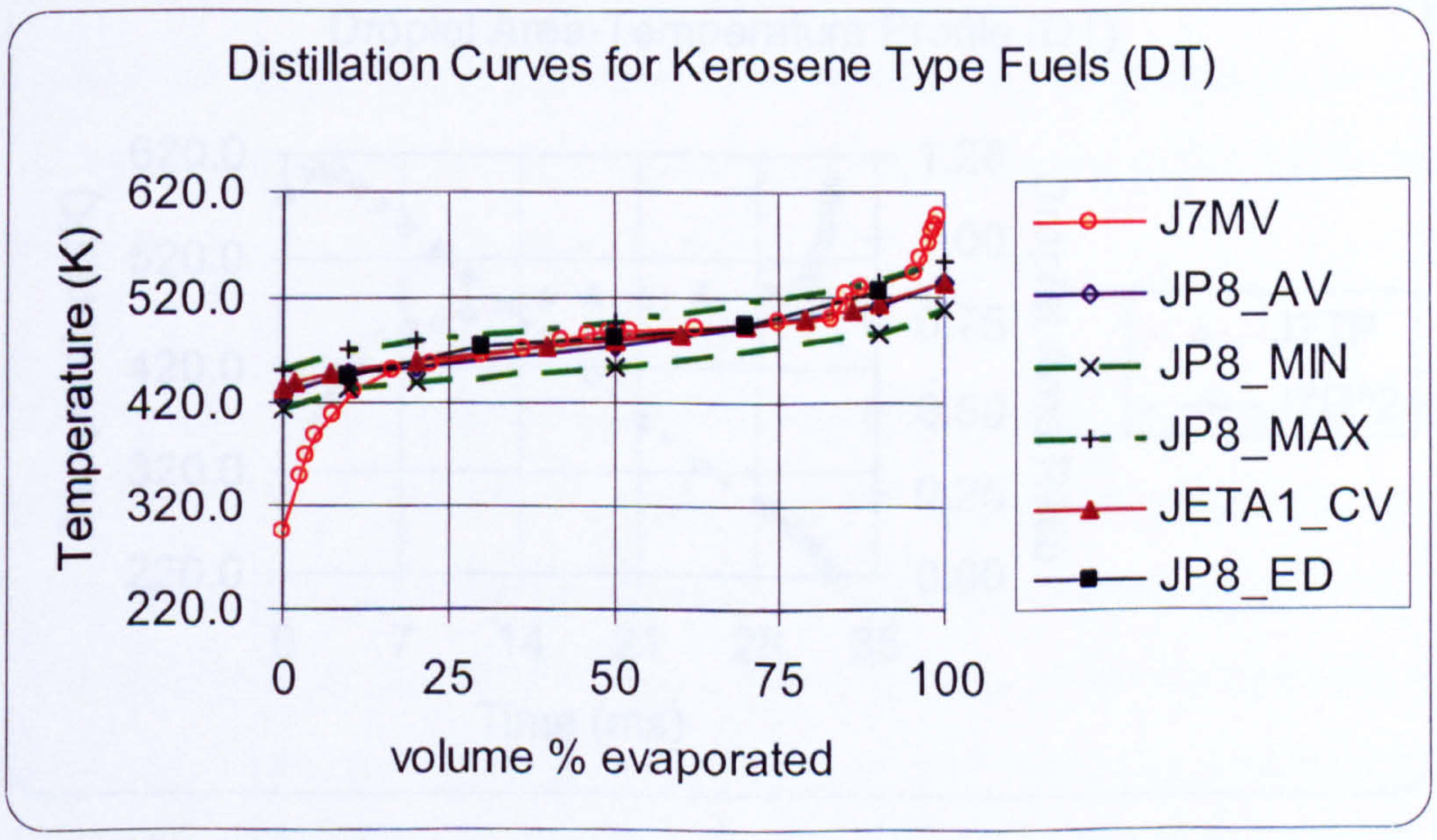

Figure-6.31 Distillation curves of various kerosene type fuels compared with the numerically simulated total distillation of J7 (J7MV-open circle with solid line), the most volatile JP8 variant (JP8_MIN- x with dashed lines); the least volatile JP8 variant (JP8_MAX- + with dashed lines), average JP8 variant (JP8_AV-open diamond with solid line), JP8 composition as analysed by Maurice et al (2001) (JP8_ED-solid rectangle with solid lines), and JET A1 as specified by Chevron (JETA1_CV-solild triangle with solid lines)-initial droplet diameter 639 μm , temperature 21 ^0c , ambient convective velocity 30m/s, ambient temperature 600K, and at atmospheric pressure

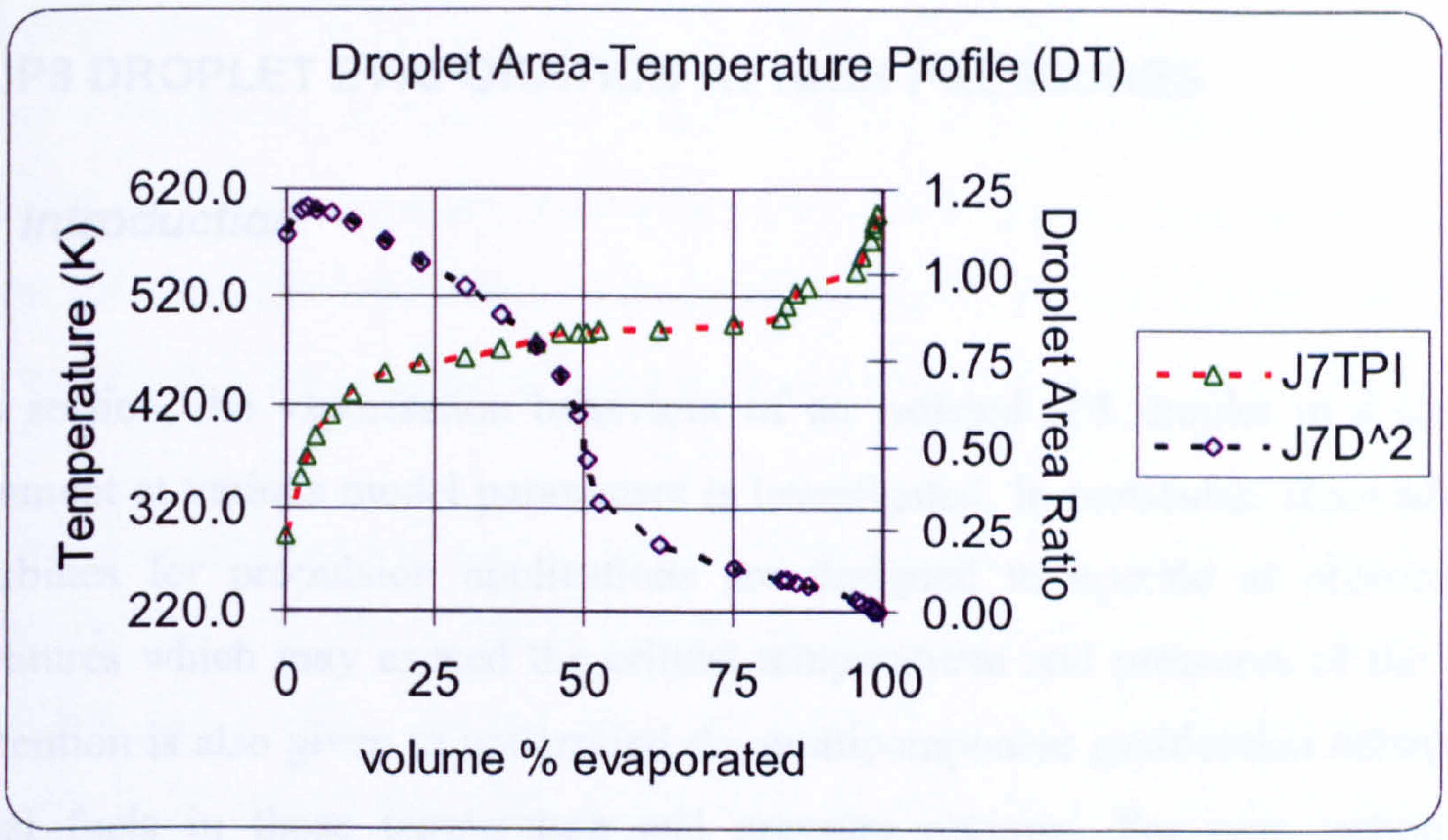

Figure-6.32 Droplet Residual Temperature (J7TPI-open triangle with dashed lines) and Droplet Instantaneous area normalised by its initial area (D^2/D_0^2 =J7D^2-open circle with dashed lines) against volume % evaporated- initial droplet diameter 639 μm, temperature 21 ^0c, ambient convective velocity 30m/s, ambient temperature 600K, and at atmospheric pressure

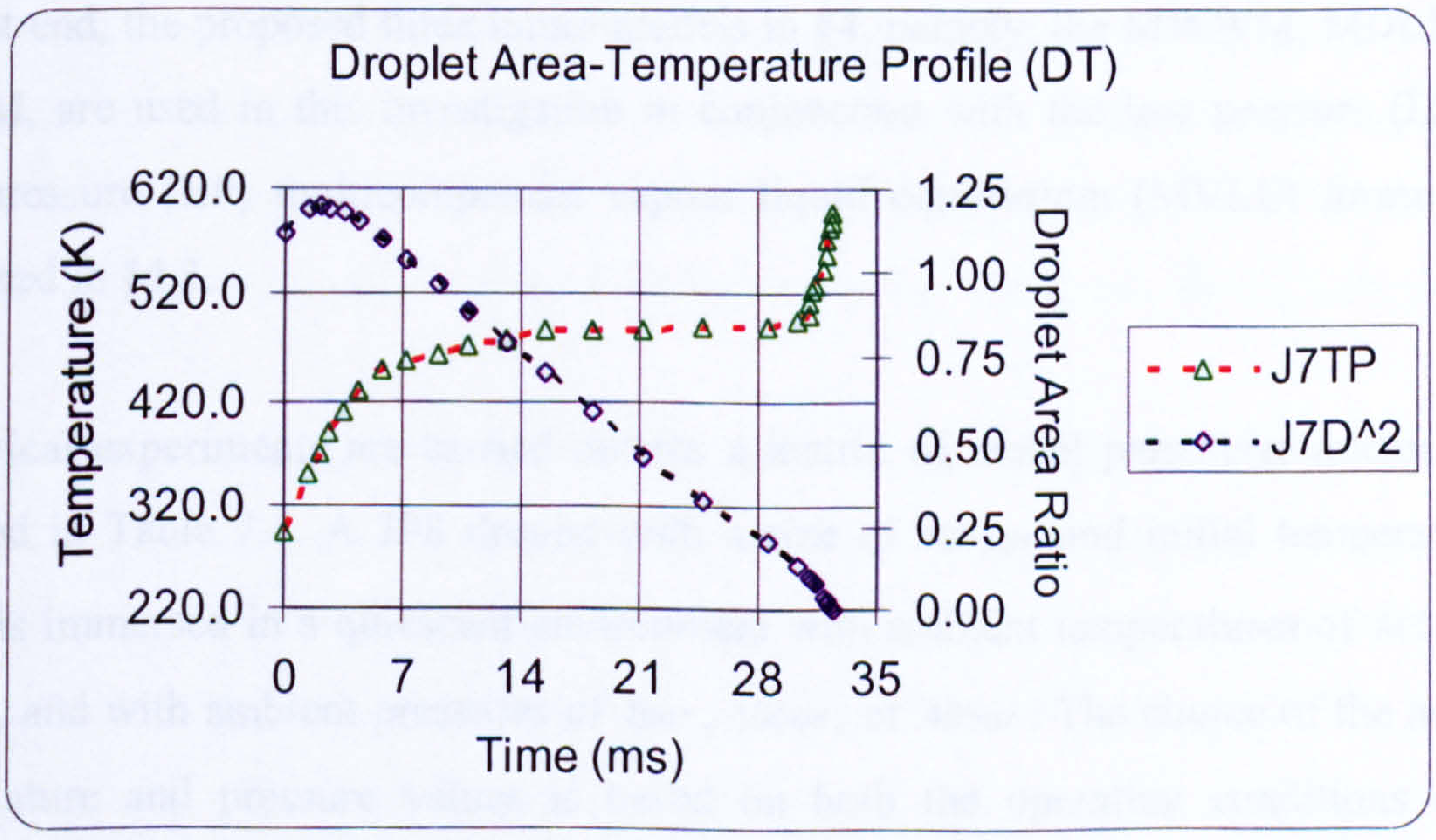

Figure-6.33 Droplet Residual Temperature (J7TP-open triangle with dashed lines) and Droplet Instantaneous area normalised by its initial area (D^2/D_0^2 =J7D^2-open circle with dashed lines) against droplet evaporation time- initial droplet diameter 639 μm, temperature 21 ^0c, ambient convective velocity 30m/s, ambient temperature 600K, and at atmospheric pressure.

7. JP8 DROPLET EVAPORATION AT HIGH PRESSURES

7.1 Introduction

In this section, the vaporisation behaviour of an isolated JP8 droplet in a quiescent environment at various model parameters is investigated. In particular, since advanced gas turbines for propulsion applications are designed to operate at pressures and temperatures which may exceed the critical temperatures and pressures of the fuel in use, attention is also given to understand the multicomponent gasification behaviour of practical fuels in those temperature and pressure regimes. For new technological concepts of aero engine gas turbines and direct injection diesel engines, the range of the ambient temperatures and pressures, respectively, could be in excess of 700-1500K and 10-50 bar, where the treatment of non-ideal and variable thermotransport properties both in the gas and liquid phases play a significant role (Kneer et al, 1993).

To that end, the proposed three liquid models in §4, namely, the MWWM, MDLM, and MEDM, are used in this investigation in conjunction with the low pressure (LP) and high pressure (HP) multicomponent vapour liquid equilibrium (MVLE) formulations discussed in §4.3.

Numerical experiments are carried out for a matrix of model parameter intensities as outlined in Table 7.1. A JP8 droplet with a size of $100\mu m$ and initial temperature of $300K$ is immersed in a quiescent environment with ambient temperatures of $800K$ and $1200K$, and with ambient pressures of $1bar$, $10bar$, or $40bar$. The choice of the ambient temperature and pressure values is based on both the operating conditions of gas turbines and the critical temperature and pressure values of the fuel components that constitute fuel JP8 itself so that it will allow parametric studies to asses the performance of the models and to understand the behaviour of multicomponent evaporation. The size of the droplet used in this investigation is higher than the size of droplets that are found in practical sprays (which is in the order of $5-40\mu m$), but it is thought to illustrate the effect of internal thermal distribution better. It must be pointed out that for a single component droplet evaporation, Miller et al (1998) have shown that when the evaporation rate is sufficiently large, the evaporation behaviour of droplets with diameter $\leq 50\mu m$ to be markedly different from those with larger diameters, where non-equilibrium effects are dominant. However, in this investigation, no direct investigation is conducted to establish the effect of droplet diameter on the vaporisation behaviour of multicomponent mixtures, although qualitative comparisons can be made in some cases.

The detailed descriptions of the numerical methods that are used to solve the liquid models using both the 0D-MWMM and the 1D-MDLM and MEDM are described in §5. For the 1D-models, 50-cells are used initially in the liquid phase. The grid distribution is in such a way that immediately adjacent to each of the left and right boundaries, 20-equally spaced fine grids are used, while the rest 10-coarse grids are assigned for the region in between. On the other hand, the 1D-gas phase transport equations are solved using 50-exponentially spaced grid points in ζ^v (the non-dimensionalised radius in the gas phase as described in §5), where the fine grids are localised close to the droplet surface, getting coarser exponentially with increasing ζ^v. After the start of the computation, however, the grid adaptation procedure controls the distribution of the grid depending on the flow conditions. In addition, as in §6, the mixture thermotransport properties with the correlation coefficients tabulated in Appendix A7 are used, and are allowed to vary spatially and temporally in both phases.

In the previous chapter, the performance of the LP formulation of the MWMM was validated against the experimental results of Runge et al (1998) and the distillation characteristics of various kerosene type fuels. However, the modelling of droplet evaporation at high pressure represents a scientifically challenging problem, and the conventional LP droplet evaporation models may not be valid at high pressure conditions (Yang, 2001). For example, the gas phase non-idealities and the solubility of gases in the liquid phase are negligible at low pressure while it is an essential consideration at high pressure conditions. In particular, at high pressures, the behaviour of mass transport in the liquid interior and the multicomponent nature of the fuel at the droplet surface are great points of interest to characterise the evaporation rates. The evaporation behaviours of multicomponent fuels at high parametric intensities, including values above the critical pressures of some of the components that constitute the fuel, are investigated in later sections. However, in the section to follow, an extensive investigation on the evaporation behaviour of multicomponent fuels and the performance of the three droplet evaporation models at various temperatures and pressures is presented. The aim is to identify the salient features of the CT based liquid models and to select the most accurate and efficient models in order to utilise them for further investigations, where the practical operating conditions of gas turbine combustors and diesel engines are the case in point. Note that all the significant observations will be further elucidated in §8.

7.2 Evaporation at low-elevated model parameter intensities

7.2.1 Predictions of droplet temperature and diameter time histories

The numerical investigation at low parameter intensity (at an ambient pressure and temperature of, respectively, 1bar and 800K) is associated with the need to validate the performance of the 1D-MDLM and MEDM low pressure (LP) and high pressure (HP) formulations against the 0D-MWMM LP case that was validated in §6. Once the vaporisation behaviour and the performance of the models at this ambient conditions is established, similar tests at elevated parameter intensities (ambient temperatures $T^{\infty} = 1200K$ and ambient pressures of $P^{\infty} = 10bar$) are carried out to further gauge the performance and sensitivity of the various liquid evaporation models against changes in the ambient condition as stipulated in Table 7.1. At this stage, the numerical tests at the ambient pressure of $P^{\infty} = 40bar$ are not considered for a reason which will be obvious in later sections and for presentation purposes too.

Since previous droplet evaporation model investigations (Aggarwal et al, 1994; Miller et al, 1998) employ mostly two quantities, namely, the evolution of the droplet surface temperature and the evolution of the normalised droplet diameter to describe the essential behaviours of the liquid gasification, the same approach is adopted here. Although these traditional methods rarely use the liquid and vapour composition evolutions to describe the time-wise behaviours of these two quantities, the vapour produced at the droplet surface (or equally the evaporation rate) is one of the main quantities that all models or experiments are expected to provide. The choice of the droplet surface temperature and the normalised droplet diameter as quantities to validate the accuracy of droplet evaporation models is mainly dictated by the availability of measured experimental data on the volume averaged droplet temperature and the droplet diameter regression, where the droplet surface temperature and the normalised droplet surface area can be extracted.

Liquid Model	Temperature (K)	VLE	Pressure (bar)		
			1	10	40
MWMM	800	LP	*w*1	*w*5	*w*9
		HP	*w*2	*w*6	*w*10
	1200	LP	*w*3	*w*7	*w*11
		HP	*w*4	*w*8	*w*12
MDLM	800	LP	*d*1	*d*5	*d*9
		HP	*d*2	*d*6	*d*10
	1200	LP	*d*3	*d*7	*d*11
		HP	*d*4	*d*8	*d*12
MEDM	800	LP	*e*1	*e*5	*e*9
		HP	*e*2	*e*6	*e*10
	1200	LP	*e*3	*e*7	*e*11
		HP	*e*4	*e*8	*e*12

Table 7.1 Liquid JP8 fuel droplet evaporation test conditions and test case numbers identifications for the liquid models MWWM (*w*1 - *w*12), MDLM (*d*1 - *d*12), and MEDM (*e*1 - *e*12).

However, the majority of droplet evaporation modelling relies on model-to-model comparison rather than on validating models against experimental data (Miller et al, 1998). Unlike the traditional models, however, this investigation extensively employs various quantities that describe the composition evolution to characterise the evaporation behaviour of the fuel under consideration. This is due to the fact that the composition evolution of both the liquid and vapour phases are readily available in the CT formulation as demonstrated in §6.

Figures 7.1-7.3 each depicts the time-wise predictions of (a) the droplet surface temperature and (b) the square of the normalised droplet diameter at low-elevated model parameter intensities using the proposed 0D-MWMM, 1D-MDLM and MEDM. In the MWMM, the composition of the droplet is assumed to be well-mixed, which allows it to maintain a spatially uniform but temporally varying composition and temperature. Thermal energy exchange with the gas phase raises the droplet temperature while forcing the migration of the mixture components as vapour fuel at the droplet surface. In the MDLM and MEDM, the 1D-transient diffusion equation for the composition and temperature are solved in the liquid phase. The two models differ mathematically in the manner by which the diffusivities are evaluated. The significance of the physical process is that the MEDM introduces diffusivity enhancement factor whose value falls in the range 1-2.72, while the enhancement factor for the MDLM is unity (Abramzon and Sirignano, 1989). In effect, the MEDM mass and thermal diffusions are enhanced by up to 2.72 as described by equation $(4-20)$ compared to the MDLM. The diffusivity enhancement factor in the MEDM takes into account the internal liquid circulation, which contributes by enhancing the liquid heating and the mass diffusion, respectively, at the beginning and later stages of the droplet vaporisation.

The predictions for the droplet surface temperatures time histories by the MWMM (Figure 7.1a) show that the results at low parameter intensities (corresponding to the numerical tests at $P^{\infty} = 1bar$ in Table 7.1) for the LP and HP formulations at the respective ambient temperatures of $T^{\infty} = 800K$ (plots w1 and w2) and $T^{\infty} = 1200K$ (plots w3 and w4) to be very similar. However, the effect of the high ambient temperature $T^{\infty} = 1200K$ provides faster rate of droplet heating (plots w3 and w4) compared to the lower ambient temperature $T^{\infty} = 800K$ case (plots w1 and w2). For both temperature values, the droplet heating (and simultaneous evaporation) is followed by an equilibrium (wet-bulb)[4] droplet temperature profile and a further heating (and

---

[4] In the literature, the wet-bulb or equilibrium temperature is associated to the droplet surface temperature where the net heat flux is zero, and hence no heat of vaporisation is required. In this investigation, however, it signifies the state of the droplet where its surface temperature is quasi-steady, with very small temperature gradient, and yet, non-zero heat flux and non-zero-enthalpy of vaporisation.

simultaneous evaporation) process. The behaviour of a droplet showing further heating after it attains its wet-bulb temperature is, as far as to this author's knowledge, a new observation compared to those predictions by other traditional evaporation models in the literature, which mainly employ single component fuels. Once this statement is made, further corroboration on this finding will be presented in later sections. However, at this stage, for presentation purposes, the focus of the investigation is to describe the effect of the LP and HP formulations (described in §4) on the performance of the models considered when there is variation in the ambient conditions.

In Figure 7.1b, the square of the normalised droplet diameter evolution (and hence the droplet vaporisation rate) shows a slight discrepancy between the results of the respective LP and HP formulations (plots w1 and w2; and plots w3 and w4). Although they are at the same test conditions, the LP formulations at both temperatures (plots w1 and w3) show a relatively faster evaporation during the predominant droplet heating period compared to the results for the HP formulations (plots w2 and w4). However, during the period where the droplet seems to attain a wet-bulb temperature, the rate of evaporation predicted by the LP formulations (plots w1 and w3) slows down, increasing the droplet life time slightly compared to the HP formulation predictions (plots w2 and w4). This is not a surprising result to observe from the MWMM, which assumes uniformity in composition and temperature distribution in the liquid.

In addition, the LP formulation is based on the Clausius-Clapeyron relations, which is derived by making three assumptions. First, it assumes the latent heat of vaporisation to be constant in the temperature range being considered. Second, it assumes an ideal gas phase, and third, vapour volume is assumed to be much larger than liquid volume. In particular, the first assumption implies that after the droplet reaches its wet-bulb temperature, the net heat penetrating the liquid phase becomes zero, and fails to prompt faster vaporisation.

The discrepancy between the LP and HP formulations prediction both for the temperature profiles and for the droplet surface regression rates further deteriorates at elevated pressure (Figure 7.1). Due to the increase in the ambient pressure the liquid mixture boiling temperatures are expected to rise. To that end, both the LP and HP formulation predictions show this effect (Figure 7.1a, LP plots w5, w7; and HP plots w6, w8). However, the LP prediction show a markedly different heating rate and a corresponding lower droplet equilibrium temperature (wet-bulb temperature) than that predicted by its HP counterpart.

In the LP case, the droplet maintains its equilibrium (wet-bulb) temperature for a much longer period (plots w5 and w7 in Figure 7.1a), prompting a slower evaporation rate and longer droplet life time (plots w5 and w7 in Figure 7.1b). On the other hand, the HP prediction responds to the changes in the ambient conditions in a different manner from its LP counterpart. As expected, the HP case reveals the effect of high heat supply resulting in faster evaporation rate (temperature and surface regression plots w6 and w8, respectively, in Figure 7.1a and 7.1b). Since the range of the boiling point temperature at normal atmospheric condition are (391-544 K for paraffin, 397-573 K for naphthene, and 412-578 K for aromatic) lower than that can be attained at $P^{\infty} = 10bar$, the temperature profile increases non-monotonically.

It is interesting to note that the HP predictions for the droplet surface regression rates (plots w2 and w4 in Figure 7.1b) at $P^{\infty} = 1bar$ are enveloped by their equivalents at $P^{\infty} = 10bar$ (plots w6 and w8), prompting a proposition - droplet life time increases with pressure, but decreases if the temperature is adjusted to increase. However, the LP predictions conform to the long held view that droplet life time increases with increasing pressure (Aggarwal et al, 1984). Figures 7.2 and 7.3, respectively, show numerical tests using the MDLM and MEDM with the same test condition as the MWMM presented earlier. The effect of the ambient pressure on the predictions of the MDLM and MEDM using the LP and HP formulations are, in general, similar to the predictions of the droplet temperature profile and droplet surface regression by the MWMM, with few minor exceptions. Although it is interesting to observe the departures in the predictions due to the LP and HP formulations, further information is required to establish the performance of each model against each other, and such investigation is described in the following section.

7.2.2 Model-to-Model Comparisons using the LP and HP formulations

Figures 7.4, 7.5, 7.6, and 7.7, respectively, depict the comparisons of predictions by the three models (MWMM, MDLM, MEDM) at ambient temperature $T^{\infty} = 800K$ employing LP formulation, at $T^{\infty} = 800K$ employing HP formulation, at $T^{\infty} = 1200K$ employing LP, and at $T^{\infty} = 1200K$ employing HP, whilst using an ambient pressure of either $P^{\infty} = 1bar$ or $P^{\infty} = 10bar$ in each test case.

At $T^{\infty} = 800K$, the LP formulation predictions for the droplet surface temperature and droplet surface regression rate, both at $P^{\infty} = 1bar$ or $P^{\infty} = 10bar$, show two interesting results (Figure 7.4). First, for both the ambient pressures, the slow rate of heating predicted by the MWMM (plots w1 or w5 in Figure 7.4a) never surpassed the wet-bulb temperature predicted by both the MDLM (plots d1 or d5) and the MEDM (plots e1 or e5). Although it has faster heating rate and the wet-bulb temperature is raised due to the elevated pressure (plots w5, d5, e5), the droplet lifetime is prolonged correspondingly. In addition, higher droplet surface temperature is predicted by the MWMM at the elevated pressure condition (plots w5, d5, and e5 in Figure 7.4a).

The second result is related to the model formulation itself, where the MEDM invokes heat and mass diffusivity enhancement factor to accelerate droplet heating to realise faster vaporisation at a later stage. The MEDM diffusivity enhancement factor, although it stays just over the unity limit, it never contributed in the rate of evaporation at the later stages of the droplet life time for the ambient temperature and pressure conditions considered so far. Indeed, the findings indicate the limitations of the semi-empirical diffusivity enhancement factor for the test cases at hand. This issue is further elucidated while investigating the droplet centre profiles below. In addition, it will be discussed in relation to the LP and HP formulations in comparison to experimental data in order to choose the best models to employ for further investigation (see §7.22).

Meanwhile, the reason for the first effect is that traditional methods assume an asymptotic limit for the droplet surface temperature, where droplet heating is followed by a wet-bulb temperature, beyond which, there is no net heat entering the droplet interior. However, in continuous mixtures or real aviation fuels like JP8, the heating is transient and there is always heating through out most of the droplet lifetime, until the droplet interior is heated up enough so that the heaviest component of the liquid fuel is forced to migrate towards the droplet surface as vapour fuel. Since the MWMM has a relatively slow rate of heating than the other two models (MDLM and MEDM), the droplet surface temperature increases slowly but continuously. Consistent predictions are observed for the droplet surface regression rates (Figure 7.4b), and further discussion is given in §8.

Figure 7.5 depicts the predictions of the HP formulation at $T^{\infty} = 800K$, and at $P^{\infty} = 1bar$ or $P^{\infty} = 10bar$. When $P^{\infty} = 1bar$, the predictions by the LP (Figure 7.4, plots w1, d1, e1) and HP(Figure 7.5, plots w2, d2, e2) are very similar. However, at $P^{\infty} = 10bar$, the predictions by the LP (Figure 7.4 plots w5, d5, e5) and the HP formulations (Figure 7.5, plots w6, d6, e6) show markedly different features. First, both the heating rate and the wet-bulb temperature are raised substantially, while the droplet life time is reduced by 14-17% from that predicted by the LP formulation. Second, the prediction by all the MWMM, MDLM and MEDM employing the HP formulation is much more similar than those predicted by using the LP formulations.

These results are plausible, and yet, the accuracy must be assessed against experimental data. It is obvious to observe the effect of the increase in the ambient pressure that resulted in raising the liquid boiling point and hence the wet-bulb temperature, which nonetheless has diminished the diffusivity due to its inverse dependence on pressure as stated by Fuller's method (Polling et al, 2000), although the ambient temperature is still high enough to motivate vaporisation. Similar tests using the LP and HP formulations, but at $T^{\infty} = 1200K$, respectively, are presented in Figures 7.6 and 7.7. The LP predictions (Figure 7.6) show an increase of 48-59% in the droplet life time due to the elevated pressure, while the HP predictions at elevated pressure show a reduction in the droplet life time of 39-27%. In estimating the percentage variation, it is assumed that the LP and HP predictions at $P^{\infty} = 1bar$ are indistinguishable.

To elucidate the droplet heating process further, the droplet centre temperatures for the 1D-models of the HP formulation are presented in Figure 7.7a. When $P^{\infty} = 1bar$, the heating rate and the corresponding prediction for the droplet surface temperature by the MDLM at the beginning of evaporation is faster than that predicted by the MEDM, although the MDLM only accounts for the heat transport that is conducted through the liquid, ignoring any convection heat transport that may arise due to internal liquid circulation. The MEDM, however, includes the later effect, by employing a diffusivity enhancement factor greater than unity. Although the MEDM shows a slightly faster rate of heating at the beginning, it is the MDLM that sets the pace afterwards.

This is contrary to results reported elsewhere (Abramzon and Sirignano, 1989; Sirignano, 1999), where the predictions for the single component variant of the MEDM is enveloped between those of the single component variant of the MWMM and MDLM. Of course, there is, in principle, an important difference between the model developed by Abramazon and Sirignano (1989) and the MEDM. In addition to the MEDM being a multicomponent droplet evaporation model, it also deals with evaporation in stagnant condition by employing a droplet surface velocity based on the droplet surface regression rate to compute the droplet Peclet number that is responsible for the heat and mass transfer enhancement. It must be pointed out that Abramzon and Sirignano (1989) generated a surface velocity to compute the droplet Peclet number in a quiescent environment by giving the droplet an initial velocity so that the relative velocity will be non-zero (see discussion in §4.2.2). Therefore, Abramzon and Sirignano (1989) did not really validate their model for stagnant conditions although it is claimed the model is applicable at any flow conditions. In addition, the range of the diffusivity enhancement factor is reported to vary between $1 \leq \chi_{(\alpha:D)} \leq 2.72$, which is based on a semi-empirical correlation of the Nusselt number asymptotics calculated by (Johns and Beckman, 1966), but for a solid sphere, where there is no internal circulation, and a very high liquid Peclet number, where convective transport dominates diffusion transport.

These author's, however did not provide the (limiting) ambient conditions where the diffusivity enhancement factor ($\chi_{(\alpha;D)}$) is more effective. In the test cases conducted so far, the diffusivity enhancement factor is in the range $1.097 \leq \chi_{(\alpha;D)} \leq 1.113$. Although it shows a faster heating rate than the MDLM, the heating effect never translated into the enhancement of mass diffusion at a later stage of the droplet lifetime. However, it is interesting to note that when the droplet enters the hot environment, only a small portion of the droplet volume near its surface will be heating up quickly while the core of the droplet remains "cold". Eventually, the temperature within the droplet will become nearly uniform before the end of its lifetime (Figure 7.7a, plots d4 and d8; e4 and e8).

When $P^{\infty} = 10bar$, the heat transfer is enhanced further with $1.103 \leq \chi_{(\alpha;D)} \leq 1.113$, and the droplet reaches the wet-bulb temperature faster, which is followed by a nearly uniform internal temperature profile. It must be pointed out at this stage that with increasing temperature and pressure, the prediction of all the there models employing the HP formulation becomes relatively similar (Figure 7.7a, plots d8, e8, d8c, e8c; and Figure 7.7b, plots w8, d8, e8). Although the previous presentations are logical and plausible in order to further elucidate the model predictions in Figures 7.1-7.7, the assessment on the performance of the models shall be determined based on comparisons with experimental data, and such exercises is presented in the following section.

7.2.2. Numerical test against the experiments of Hiroyasu et al (1976).

Hiroyasu et al (1976) conducted experimental studies on the evaporation of a single droplet for ambient pressure ranges of 0-50 bar and ambient temperature ranges of 373-773 K, where the time histories for droplet size and/or for droplet surface temperature of various fuels (n-heptane, iso-octane, n-hexadecane, ethanol, benzene, kerosene, light oil as well as water) are recorded. The objective of the investigation was to obtain information on liquid droplet evaporation at high pressures and temperatures corresponding to the supercritical state of the droplet in order to bridge a knowledge gap that is a necessary requirement for a more valid rocket combustion model in design and instability studies, and also to use it in the fundamental studies of soot and nitrogen oxide formation in combustion devices.

The experimental apparatus consists of a pressure vessel and a moving electric furnace, where the pressure in the vessel is increased by feeding gaseous nitrogen from a tank. A droplet hanging on a fine quartz thread of $400\mu m$ is subjected to a hot gas by the displacement of the electric furnace resulting in evaporation. The vessel has two windows of quartz glass to observe the evaporation process, while the gas temperature in the furnace is varied from room temperature up to 773 K using a volt slider. A droplet maker that consists of a plunger, hypodermic needle and a connecting tube to suspend the droplet at the tip of the quartz thread is used, while a copper-constantan thermocouple of diameter $50\mu m$ is attached to measure the droplet temperature. The hot junction of the thermocouple is placed near the tip of the quartz thread to measure the droplet surface temperature, with no mechanism put in place to rectify the surface temperature value while the droplet surface is in recession. It must be pointed out that the recorded data may not always coincide with the surface temperature of the droplet, although the difference is expected not to be so large. In order to record the evaporation process, the droplet is back-lighted by a reflector lamp through a ground glass plate at the window of the vessel, where a silhouetted droplet image is taken by a 16mm movie camera. The size of the droplet is then determined by assuming the silhouettes on the film to be ellipsoid and comparing it with the image of the quartz thread whose diameter is measured before hand (and whose thermal expansion is very low), while the film speed is calibrated by taking the picture of a watch. It is reported that the image quality was good enough to allow detailed observation, where the ellipsoid size was measured at right angles along the major and minor axis. As such, an effective diameter is calculated which has the same surface area as the ellipsoid.

At an ambient temperature of $T^{\infty} = 573K$ and ambient pressure of $P^{\infty} \sim 30bar$, the time histories of liquid water, n-hexadecane, light oil and kerosene droplets of initial diameter $1800\mu m$ are plotted (Hiroyasu et al, 1976), and the kerosene data is used to validate and assess the performance of the models proposed in this investigation.

To that end, Figure 7.8 depicts the numerical simulation of JP8 fuel in comparison with the kerosene fuel considered by Hiroyasu et al (1976). Although the droplet surface temperature evolution for kerosene fuel is not presented by Hiroyasu et al (1976), Figure 7.8a depicts the numerical predictions for the droplet surface temperature using all the three proposed models employing both the LP and HP formulations. However, the predictions for the droplet centre temperature predictions are conducted using the 1D-modles (MDLM and MEDM).

The droplet surface temperature predictions by the LP formulation (plots w20 for MWMM, d20 for MDLM, and e20 for MEDM) in general show slower heating rates, long period of equilibrium (wet-bulb temperature), and hence longer droplet life time and an abrupt increase in temperature close to the end of evaporation. Since the heating rate is slow, the droplet centre temperature profile predicted by the two models (plots d20c and e20c) looks very similar, except at the beginning and end of the evaporation. All the models that employ the LP formulation to predict the droplet surface regression (Figure 7.8b, plots w20, d20, and e20) are very poor in comparison with the experimental data of Hiroyasu et al (plot HIRO).

On the other hand, the HP formulation presents a different feature both for the temperature profile and the droplet surface regression. In fact, a closer observation also reveals interesting features of the models behaviour as well. First, the droplet surface temperature shows a fast heating rate, where the MWMM (plot w21) predicting the slowest and the MDLM (plot d21) predicting the fastest while the MEDM (plot e21) stays some how in between. The corresponding droplet centre temperature profiles show slow conduction heat transfer (MDLM plot d21c) compared to the one predicted by the MEDM (plot e21c) that takes into account liquid circulation, and hence convection heat transfer inside the liquid. Interestingly enough, the range of the diffusivity enhancement factor is now in the range of $1.447 \le \chi_{(\alpha;D)} \le 1.693$, much higher than observed for all the test cases conducted so far. This corresponds to an increase in pressure but a lower temperature than the test cases presented earlier. Indeed, the liquid circulation enhancement and its effect on improving the rate of convective heat transfer and liquid mass diffusion is evident. This effect is more pronounced once the droplet reaches the wet-bulb temperature. This is in accord with the theory (Abramzon and Sirignano, 1989), where the relative profiles of the MEDM should be enveloped by the MWMM and MDLM as indication for the mixing as an enhancement for the heat and mass transfer.

Although the mixing or heat or mass transfer enhancement phenomena was not observed in previous test cases where the ambient pressure was not significantly higher than the atmospheric, it is instructive to pose the question what instigates the process, and wether there is a cut-off point where the ambient conditions (temperature, pressure, and/or convection) must satisfy to initiate droplet internal circulation. However, before delving into the conditions that must be satisfied to initiate liquid core circulation as an enhancement to liquid heat and mass diffusion, the performances of the models while employing either the LP or HP formulations must be scrutinised further against the experiments of Hiroyasu et al (1976) so that the reminder of this investigation only employs the most accurate models.

The predictions of the droplet surface regression by all the models (MWMM, MDLM, and MEDM) show an abrupt increase in droplet heating and a correspondingly large swell in liquid volume. Questions could be asked about the extent of such a swelling, which is symptomatic with the behaviour of liquids that have the tendency to increase in volume corresponding to an increase in temperature. This type of change is characterised by the liquid coefficient of thermal expansion, which is a property used as a measure for the rate of volume increase with temperature. To that end, a typical value for a coefficient of expansion for a kerosene type jet fuel is $0.00099/{}^0C$. For a droplet diameter of $1800\mu m$ that undergoes a temperature rise of 300^0C, the fuel diameter could increase by $534.6\mu m$ to reach to a maximum swelling of 29.7% $(2334.6\mu m)$, which is in fact higher than the diameter recorded by Hiroyasu et al (1976). Similarly, the numerical results did not reach such maximum value (Figure 7.8b, plots w21 for MWMM, d21 for MDLM, and 321 for MEDM). In particular, the MWMM under-predicts the heating and the droplet volume expansion by a greater margin than the other two models, although the two models (MDLM and MDEM) in turn under-predict the heating and volume expansion compared to the experimental data. Since the temperature profile for this experiment is not provided by Hiroyasu et al, it is not possible to compare the heat flux going into the droplet and to establish the cause of the rapid and large thermal expansion with certainty. In addition, while the experiment indicates the fast vaporisation rate is due to an initially strong heating (which motivates internal liquid circulation and hence liquid mass diffusion), the numerical results rather predict a slow vaporisation rate. However, the numerical results are in accord with the experimental data at the end of the evaporation process, although the data falls close to the model which is expected to be less accurate, namely the MWMM.

The objective of the exercise in this section was to demonstrate the huge discrepancy that underlies in using the LP and HP formulations for various ambient pressures. Indeed, the comparison with the experimental data demonstrated that except for pressures close to atmospheric conditions, the LP formulations shall not be used to model droplet evaporation at elevated or high pressure regimes.

However, the slight discrepancy between the predictions of all the models using the HP formulation (plots w21, d21, e21) and the experimental data of Hiroyasu et al (plot HIRO) in Figure 7.8b can be attributed to three considerations. First, as described earlier, the experimental set up did not put a mechanism in place to account for the radiation heat transfer from the electric furnace walls and the conductive heat transfer through the quartz fiber into the droplet interior. This unaccounted heat will certainly increase the thermal expansion and the rate of liquid heating thereby causing enough temperature gradient to initiate liquid internal circulation to accelerate the rate of vaporisation. Second, the numerical test uses the thermotransport properties and composition of fuel JP8 while the experiment was carried out using commercial kerosene. Although JP8 is a kerosene-based multipurpose fuel, the variation of its precise composition from batch to batch could introduce noticeable differences. In particular, JP8 has lower vapour pressure and higher flash points than most kerosene fuels due to the presence of heavy components, which makes it less flammable and less likely to ignite accidentally as well as to have a slower evaporation rate. Therefore, the faster rate of vaporisation recorded in the experiment and the slower rate of vaporisation predicted by the models could be due to the slightly different thermotransport properties which might exist between the experimental and numerical fuels used. Third, the indirect method of the droplet size measurement, which is based on image comparison with the quartz thread, might have introduced further errors. This might add to the discrepancy observed on the numerical result.

In general, the comparison of the numerical predictions at high pressures with the experimental data of Hiroyasu et al (1976) in this section, and the inference made based on the comparisons between the LP and HP predictions close to atmospheric (§6 and plots w1-w4, d1-d4, and e1-e4) indicate the versatility of the HP formulation, except for its computational expense. Therefore, the HP formulation can be used for all ambient conditions while the LP is restricted to only to pressures close to the atmospheric.

7.4. Evolution of fractional composition distribution moments

In the previous sections, it is demonstrated that the models which employ the HP formulation to be the most accurate representation of an evaporating droplet and could provide the best result at all ambient pressures and temperatures. To further corroborate the numerical results and essential features of the CT based model, the composition time histories and the vaporisation behaviour in relation to the droplet temperature are presented. Therefore, in the section to follow, only the HP version of the MWMM, MDLM and MEDM are used, while the LP formulation, except at atmospheric pressure conditions, are deem to be redundant in the subsequent studies.

First, the MWMM model is used to describe the volume averaged liquid droplet profile and the equivalent progress at the droplet surface where vapour fuel is supplied. Since the discrepancy between the numerical predictions of the HP form of the MWMM, MDLM, and MEDM is very minor, the MWMM volume averaged liquid composition evolution in relation to the vapour at the droplet surface is considered to reveal the essential features of the model. These are depicted in Figures 7.9 and 7.10.

Figure 7.9a and 7.10a, respectively, are the time-wise description of the 0^{th}-fractional composition distribution moments of the liquid and the vapour for paraffin, naphthene and aromatic homologues. The liquid composition profile (Figure 7.9a) shows the preferential mass transport of the paraffin and naphthene over the aromatic. In reference to their initial composition profiles, this preferential diffusional process indicates a drop in the composition of the paraffin and naphthene while the aromatic composition rises. This is reflected on the corresponding vapour supplied at the droplet surface (Figure 7.10a), where a high proportion of vapour paraffin followed by naphthene is shown, while the proportion of the volatile aromatic supplied at the beginning of the evaporation could not keep the pace with the other two homologues, and hence decreasing continuously.

Two interesting observation can be made. The first one is the absence of a qualitative change irrespective of the value of the ambient temperature and pressure conditions. The second observation is on the preferential vaporisation, where, although the sequence in the rate of vaporisation – paraffin followed by naphthene and then aromatic (or the PNA-sequence that was also observed in §6) holds true, each homologue maintains its presence until the end of vaporisation. These observations are consistent with the droplet surface temperature and droplet surface regression profiles predicted using the HP formulation (Figures 7.1-7.7). The reason for the lack of qualitative changes could be directly related to the linearity of the thermotransport correlations for each homologue. On the other hand, the second observation shows its consistency with the central assumption of the MWMM, where uniformity in composition and temperature is invoked. Therefore, after each time step, the droplet composition and temperature distribution evolves uniformly, owing to the fact that the fractional composition distribution moments are relative description of each homologue, like mole or mass fraction.

Figures 7.9b and 7.10b, respectively, describe the time-wise predictions of the liquid PDF mean and the vapour PDF mean against the droplet surface temperature. Similarly, Figures 7.9c and 7.10c, respectively, describe the time-wise predictions of the liquid PDF variance and the vapour PDF variance against the droplet surface temperature.

The liquid PDF mean profile at $T^{\infty} = 800K$ (plots w2p for paraffin, w2n for naphthene, and w2a for aromatic) show a rapid rise in the primary heating period for paraffin with a relatively slower rate for naphthene. Once the most volatile components are vaporised however, the PDF means assume a quasi-steady profile corresponding to the droplet wet-bulb temperature (Figure 7.1a or 7.5b plot w2). However, the aromatic shows a different feature. After loosing a very small fraction of its volatile components (not noticeable) it starts to increase linearly, but at a faster rate than the naphthene until it reaches to its maximum point. The effect of the secondary heating, which is manifested by the rapid rise in droplet temperature after it finishes its period of waiting at the wet-bulb temperature, is also evident and it corresponds to the PDF mean of the heavy components. Unlike the 0th-fractional composition distribution moment, which is a relative description, the 1st-moment (PDF mean) provides a better (but not exact) insight on the identity of the fuel component evaporating, roughly corresponding to the molecular weight.

Interestingly enough, an increase in the ambient pressure to $P^{\infty} = 10bar$ (plots w6p, w6n, w6a), did not show significant change to the PDF mean initially. However, it diminishes its rate of evaporation and hence the PDF mean as if the components are becoming heavier, prolonging the droplet life time. On the other hand, an increase in ambient temperature of $T^{\infty} = 1200K$ (w4p, w4n, w4a) accelerates the rate of rise in the PDF mean and hence its rate of evaporation, shortening the droplet life time by 34-46 %. The case of higher pressures and temperatures ($P^{\infty} = 10bar$ and $T^{\infty} = 1200K$, plots w8p, w8n, w8a) again signifies a faster rate of rise in the PDF mean, further shortening the droplet life time by 42-56%.

The PDF variances also depict the behaviour of the evaporation process. In the first instance, there is a slight drop in the liquid PDF variance, suggesting a decrease in the distribution width or removal of the most volatile components, followed by a prolonged quasi-steady period, which corresponds to the equilibrium droplet temperature. This is followed by a further drop at the end of the evaporation process corresponding to the secondary heating period and simultaneous evaporation of the heavier components. The qualitative behaviour is similar when both ambient temperatures and pressures are increased, except for the aromatic (plots w6a, w8a).

The vapour PDF mean evolution is similar to the liquid PDF mean evolution, except, owing to the vapour PDF mean is building up at the droplet surface starting from the most volatile component up to the heaviest ones, its initial value is relatively low (123 kg/kmole for the vapour compared with the 153 kg/kmole for the liquid). However, the PDF variance (width) of the most volatile component is small, and the width of the PDF increases as more components are changed into vapour and increase the concentration. The vapour PDF mean and its variance are plotted against the droplet surface temperature to provide further insight. There are three regions of interest. The first one is during the droplet primary heating period, the second corresponds to the period for the droplet wet-bulb temperature while the third is during the secondary droplet heating. In the primary droplet heating process, the effect of pressure is relatively significant in the evolution of the aromatic homologue, where its mean does not change until the other homologues reach their wet-bulb condition for both ambient temperature ranges. Starting from around the mid-point of the wet-bulb temperature however, the heavier components of all the homologues evolve appreciably in a similar fashion. The PDF variances (Figure 7.10c) also confirm this behaviour.

On the other hand, Figures 7.11-13 depict the droplet internal temperature and composition profiles. However, Figure 7.11b is an exception and it shows the latent heat of vaporisation in relation to the liquid boiling and critical temperatures.

In the previous sections, it was shown that the differences between the predictions of the more detailed 1D-model (MEDM) and its simpler equivalent model (MDLM) are very minor, except during high model parameter intensities and for the huge computational expenses incurred while employing the MEDM. In addition, the nature of the droplet centre temperature and surface temperature profiles in Figure 7.7a and 7.8a, and the unremarkable effect of the heat and mass diffusivity enhancement factor in the MEDM suggest that better understanding on the evolution of the temperature and composition profile could be gained at the lower ambient temperature $T^{\infty} = 800K$. Since heating is faster at the higher ambient temperature, there could be an overlap of internal temperature profiles after the first phase of heating. Therefore, the MDLM at ambient temperature of $T^{\infty} = 800K$ and ambient pressure of $P^{\infty} = 1bar$ are used to study the internal profiles of the droplet.

The profiles are taken in four stages, based on the remaining percentage volume of the droplet in the order ~100%, 75%, 50%, and 25%. When the droplet is immersed into the ambient gas, the core temperature is very low in 90% of the droplet volume, while the rest 10% forms a thin boundary layer with high thermal gradient (Figure 7.11a, plot 1d2). The core temperature is continuously increasing in most of the remaining droplet volume with the exception of the small liquid surface thermal boundary layer. The temperature at the right boundary is consistent with the droplet surface temperature depicted in Figure 7.2a. The temperature profile decays towards the droplet centre. Although the core temperature isotherms are significantly lower than the temperatures near the droplet surface, the evidence for significant heating that can be differentiated based on the temporal variation in the isotherms is depicted by Figure 7.11a (right hand scale, plots 2d2, 3d2, 4d2). However, the gradient is not large enough to prompt internal circulation as there are no convex-minimum (unstable) points on the isotherms.

Figure 7.11b shows the boiling and critical temperatures of JP8 in conjunction with the latent heat of vaporisation against the droplet surface temperature. This is a very interesting result. During the primary heating period, the heat required to vaporise the more volatile components decreases continuously until it reaches the wet-bulb temperature where the effective enthalpy of vaporisation becomes minimum. In all the traditional models in the literature, the enthalpy of vaporisation is considered to be zero at the wet-bulb temperature, as there is no need for a net heat flux to further vaporise the liquid fuel. In particular it assumes a single boiling temperature or a point. However, in multicomponent fuels, the term in the enthalpy of vaporisation (described by equation $(A6-9)$ in Appendix A6), which is of the form $\left(T_{crJ} - T^{vR} / T_{crJ} - T_{bJ}\right)^{0.38}$ is dependent both on the droplet surface temperature and the boiling point temperature curve, which in turn is dependent on the composition PDF mean. When the ambient temperature is high, the droplet has shorter primary heating period and its surface temperature closely follows the boiling temperature curve, where the term $\left(T_{crJ} - T^{vR} / T_{crJ} - T_{bJ}\right)^{0.38}$ can be approximated close to unity. During primary droplet heating, for example –test case d2 in Table 7.1, the above term only varies between 0.9 and 1.26, decreasing as the droplet surface temperature is increasing. However, when the droplet surface temperature reaches its wet-bulb temperature at ~439 K, which nearly corresponds to a C_{10}-aromatic, a C_{11}-naphthene, C_{12}-paraffin, and which is a typical value for mid-point distillation curves of kerosene type fuels (refer to Figure 7.10b plots w2p, w2n, w2a for the same temperature range assuming MWMM and MDLM predict very close values), it shows more heat is required to vaporise the remaining components of JP8 fuel. This is marked by an abrupt rise in the boiling and/or critical temperatures of the aromatic homologue. For continuous vaporisation including secondary heating, the enthalpy of vaporisation is raised and starts to fall back again, and it never reached zero.

It is instructive to observe the ranges of the droplet boiling temperature and molecular weight depicted in Figure 6.1 in relation to the PDFs used for paraffin, naphthene, and aromatic. It is evident that the quasi-steady wet-bulb temperature always lies within the middle-band of the distribution, where there are components with the highest proportion of the mixture composition. The components that fall close to the left and right bands (legs) of the PDF correspond to the primary and secondary heating regimes, suggesting three regimes of evaporation. Before elaborating this three-regime vaporisation process, however, more information on the behaviour of the liquid interior is presented next.

Figures 7.12 and 7.13 describe the liquid composition evolution. It is interesting to observe that for the same class or homologue (paraffin, naphthene, or aromatic), the iso-mean (equal PDF mean) lines do not cross, indicating the preferential as well as continuous removal of the relatively light components during most of the droplet life time. At the beginning of the evaporation, the paraffin shows a higher PDF mean gradient close to the droplet surface (Figure 7.12, plot 1d2) compared to the naphthene and aromatics, indicating its high volatility and the corresponding volatile components localisation close to the thin boundary layer. But, the rate of growth is markedly different between the paraffin and naphthene on one hand and the aromatic on the other, consistent with the prediction of the MWMM depicted by Figure 7.9b (plots w2p, w2n, and w2a). Similar observation are found for the PDF variance and the 0^{th}-fractional composition distribution moment, respectively, depicted by Figures 7.13a and 7.13b.

The evolution of the liquid PDF variance (Figure 7.13a), which signifies the width or the amount of the component depleted within each homologue the relative departure from the mean. At the beginning of the evaporation process, all the PDF variances indicate homogeneous mixtures, designated by nearly straight lines (plots ld2p, ld2n, ld2a). But, preferential diffusion dictates that the most volatile components to be localised close to the thin boundary layers, where paraffin and naphthene components are the case in point while the aromatic stays almost unchanged. The progressive behaviour indicate the same behaviour, except when 25% volume remaining, the composition of the naphthene and aromatic was unchanged, or relatively growing.

The liquid 0^{th}-fractional composition distribution moments depicted by Figure 7.13c show similar behaviour that is consistent with the vapour 0^{th}-fractional composition distribution moment depicted by Figure 7.10a, but using the MWMM. These relative profiles indicate the preferential diffusion in the liquid too, where the paraffin and naphthene are progressively depleted compared to the aromatic. However, owing to the percentage composition of the fuel, neither homologue was depleted totally while 25% of the droplet volume was remaining.

7.2.4. Evaporation at LPP gas turbine operating conditions

The realistic representation of multicomponent gas turbine fuels evaporation (and combustion) is of great importance to understand the behaviour of the fuel vapour distribution, and hence the accurate prediction of ignition, flame stability, combustion characteristics, and the behaviour of pollutant formation/reduction. To that end, outstanding issues, including the detailed and/or reduced chemistry model of multicomponent hydrocarbon fuels, turbulent-chemistry interaction especially for predicting soot, and the gasification behaviour of an isolated multicomponent fuel droplet in stagnant and convective conditions attracted great interest in recent years

(Gupta, 1997). However, these studies are limited either to a single surrogate fuel or a binary component fuels, which exhibit differently from real aviation fuels.

To address the gasification behaviour of real aviation fuels at gas turbine operating temperature and pressure conditions, a range of condition that correspond to the operating condition of LPP gas turbine, but in a stagnant environment, are considered. The test cases correspond to both the LP and HP formulations at various ambient temperatures but only at the ambient pressure of $P^{\infty} = 40bar$ as outlined in Table 7.1. Although the LP formulations are shown to be unsuitable for high pressure conditions, the tests were carried out to understand the trends of droplet lifetime with increasing pressure. Therefore, only the high temperature test cases that employ the HP formulation are presented.

To that end, Figure 7.14 depicts the gasification behaviour of JP8 fuel in a quiescent ambient temperature $T^{\infty} = 1200K$ and ambient pressure $P^{\infty} = 10bar$. Considering that JP8 has critical temperatures in the range 635-848 K with a corresponding critical pressure in the range 36-16 bar, its is easy to see that the operation is in the transcritical-supercritical regime. Figure 7.14a depicts the droplet surface temperature and the droplet centre temperature. The MWMM (plot w12) slightly under-predicts the droplet heating compared to the MDLM (plot d12), which solves the heat conduction equation ignoring liquid circulation. Consistent with the theory, the MEDM (plot e12) predicts a situation in between the MWMM and MDLM. This implies, the MEDM takes longer time for droplet heating, and further evidence is depicted by the droplet centre temperature (plots d12c and e12c). However, after the droplet reaches its wet-bulb temperature, the MWMM attains the highest droplet surface temperature while the MDLM predicts the lowest as expected.

The droplet surface regression in Figure 7.14b also confirms the observations in Figure 7.14a. The MEDM prediction shows higher droplet thermal expansion than the MDLM, which in turn results in a lower vaporisation rate during its short heating period. The MWMM shows a relatively small thermal expansion, and yet slower rate of droplet heating and a correspondingly faster evaporation rate during its wet-bulb temperature range. Due to the presence of high thermal gradient, the MEDM predicts the contribution of vaporisation enhancement due to the liquid mass diffusion and internal circulation. The molar flux also confirms this observation. However, it is interesting to note that as far as the HP formulation is employed, both models predict a more or less similar droplet life time. This could be due to the increasing similarity in liquid and vapour phase thermotransport properties at transcritical-supercritical temperatures and pressures, where at the phase interface, the liquid and vapour are indistinguishable. The predictions at the LPP operating temperature and pressure conditions clearly show the consistency of the numerical results and the theoretically expected relative profiles of the models, where the MWWM over-predicts vaporisation rate (with smaller droplet lifetime) and the MDLM under-predicts the vaporisation rate (larger droplet lifetime). The MEDM, which is known to be the most accurate model fall between the MWMM and MDLM.

Figure 7.15 depicts the dependence of droplet lifetime on ambient temperature and pressure while employing the LP and HP formulations using all the liquid models proposed in §4. In Figure 7.15a, it is easy to observe that for the same ambient temperature and a varying ambient pressure, both models employing the LP and HP formulations show an increase in droplet lifetime with pressure. However, the LP distinctively over-predicts the droplet lifetime. An increase in the ambient temperature to $T^{\infty} = 1200K$, however, reveal a much more interesting result. While the LP formulation indicates a rapid rise in the droplet life time for ambient pressures in the range of $P^{\infty} = 1-16.7 bar$, the HP predictions show a slow decay of droplet lifetime for the same range of ambient pressures. As the pressure increases to $P^{\infty} = 40 bar$, there is very little change in the droplet lifetime for both the LP and HP formulation, although the LP formulation prediction is higher by 75%. The inflexion points at $P^{\infty} = 16.7 bar$ for both the LP and HP droplet lifetime-ambient pressure curves corresponds to the critical points of some of the components of JP8 fuels as described earlier. Due to the high ambient temperature and pressure, heating at critical state is feasible, prompting zero surface tension and causing rapid disruption and fast liquid mass diffusion due to the liquid and vapour phase being indistinguishable at supercritical state.

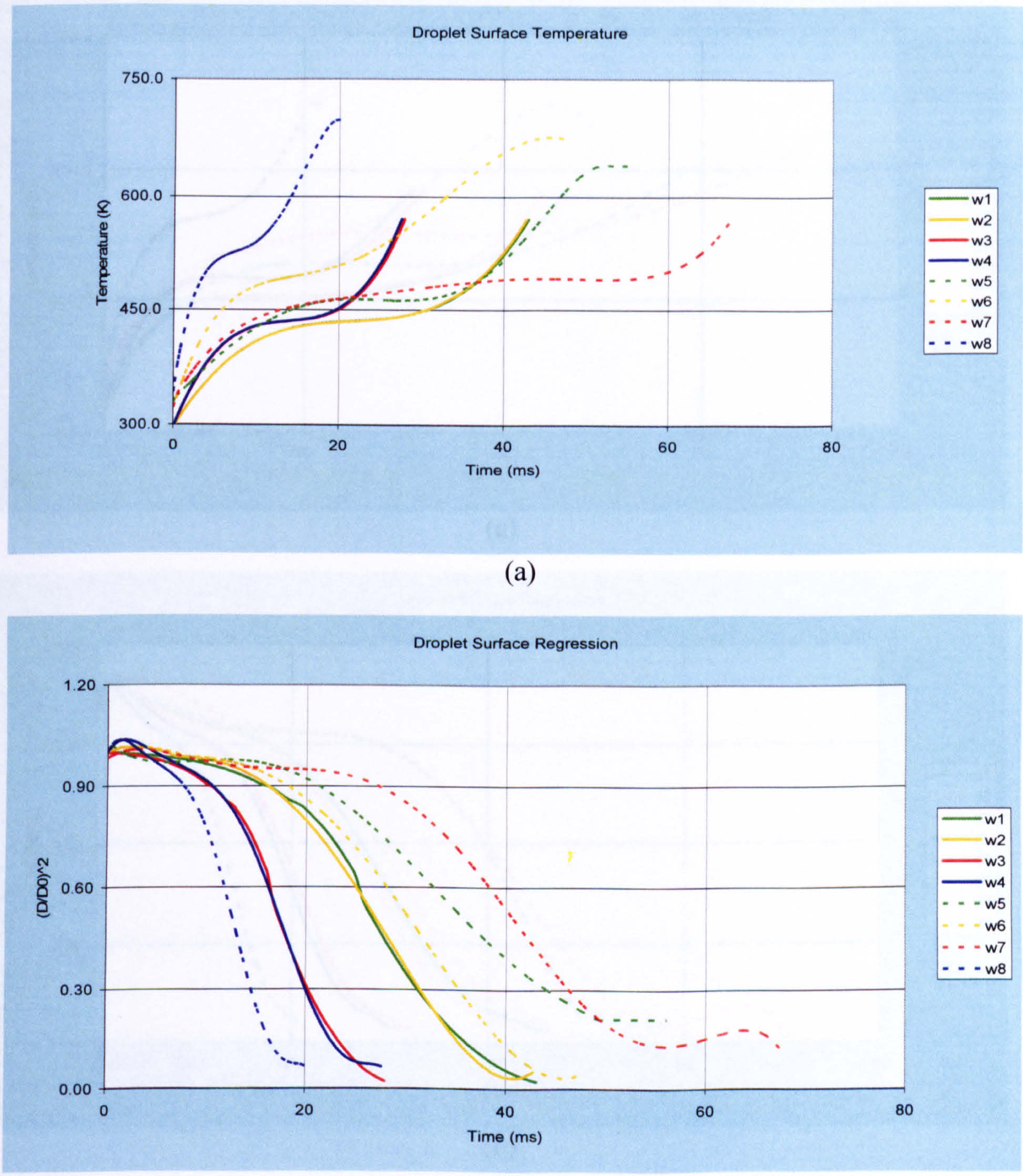

(a)

(b)

Figure 7.1 (a) Droplet surface temperature and (b) droplet normalised area predictions using MWMM low pressure (LP) and high pressure (HP) formulations for a droplet size of $100\mu m$ and temperature $300K$ in quiescent environment of various ambient temperatures and pressures: w1-(LP at $T^{\infty} = 800K$ and $P^{\infty} = 1bar$); w2-(HP at $T^{\infty} = 800K$ and $P^{\infty} = 1bar$); w3-(LP at $T^{\infty} = 1200K$ and $P^{\infty} = 1bar$); w4-(HP at $T^{\infty} = 1200K$ and $P^{\infty} = 1bar$); w5-(LP at $T^{\infty} = 800K$ and $P^{\infty} = 10bar$); w6-(HP at $T^{\infty} = 800K$ and $P^{\infty} = 10bar$); w7-(LP at $T^{\infty} = 1200K$ and $P^{\infty} = 10bar$); w8-(HP at $T^{\infty} = 1200K$ and $P^{\infty} = 10bar$) for fuel JP8 consisting 47.8% paraffin, 31.6% naphthene, and 20.6% aromatic by volume.

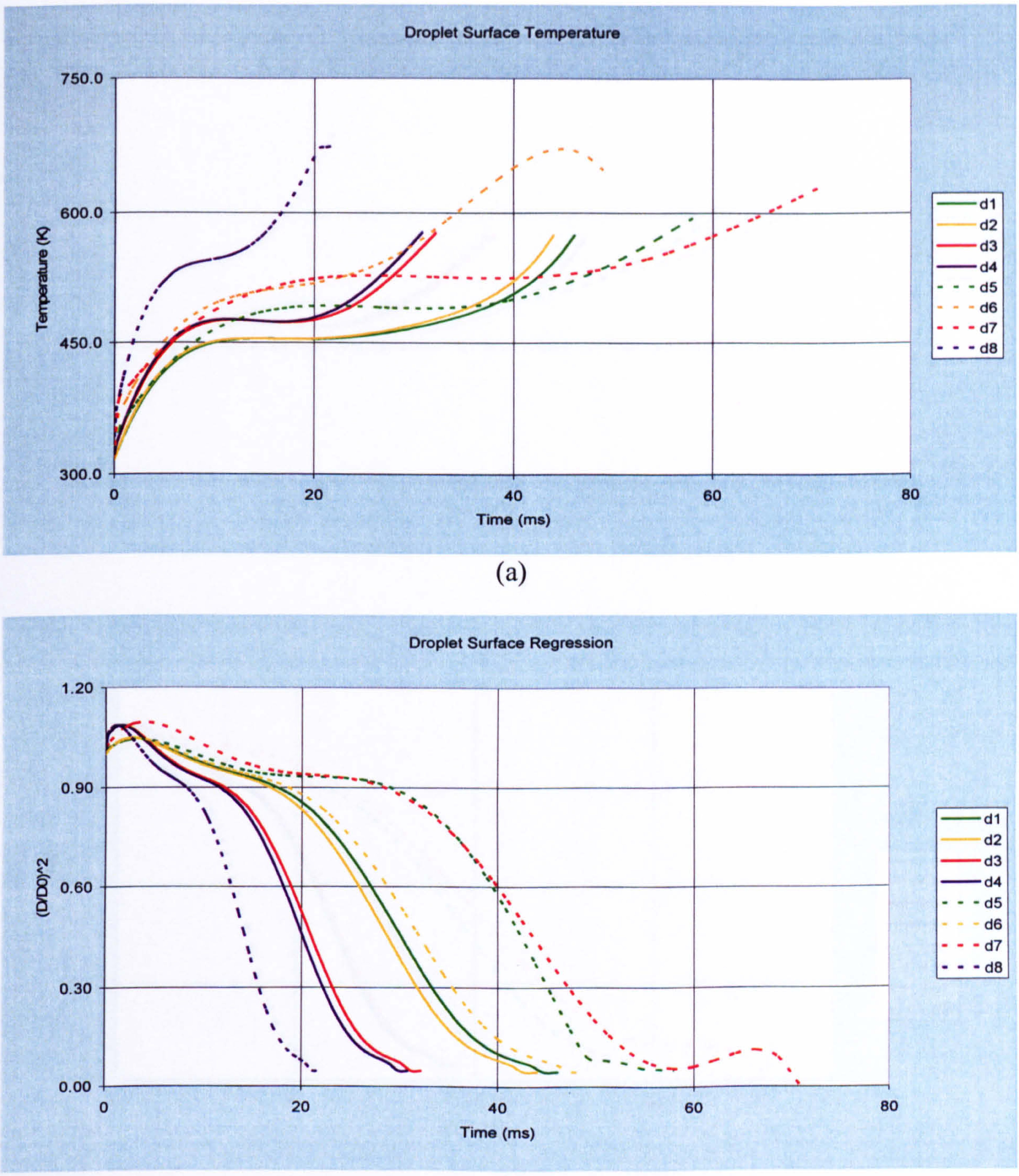

(a)

(b)

Figure 7.2 (a) Droplet surface temperature and (b) droplet normalised area predictions using MDLM low pressure (LP) and high pressure (HP) formulations for a droplet size of $100\mu m$ and temperature $300K$ in quiescent environment of various ambient temperatures and pressures: d1-(LP at $T^{\infty} = 800K$ and $P^{\infty} = 1bar$); d2-(HP at $T^{\infty} = 800K$ and $P^{\infty} = 1bar$); d3-(LP at $T^{\infty} = 1200K$ and $P^{\infty} = 1bar$); d4-(HP at $T^{\infty} = 1200K$ and $P^{\infty} = 1bar$); d5-(LP at $T^{\infty} = 800K$ and $P^{\infty} = 10bar$); d6-(HP at $T^{\infty} = 800K$ and $P^{\infty} = 10bar$); d7-(LP at $T^{\infty} = 1200K$ and $P^{\infty} = 10bar$); d8-(HP at $T^{\infty} = 1200K$ and $P^{\infty} = 10bar$) for fuel JP8 consisting 47.8% paraffin, 31.6% naphthene, and 20.6% aromatic by volume.

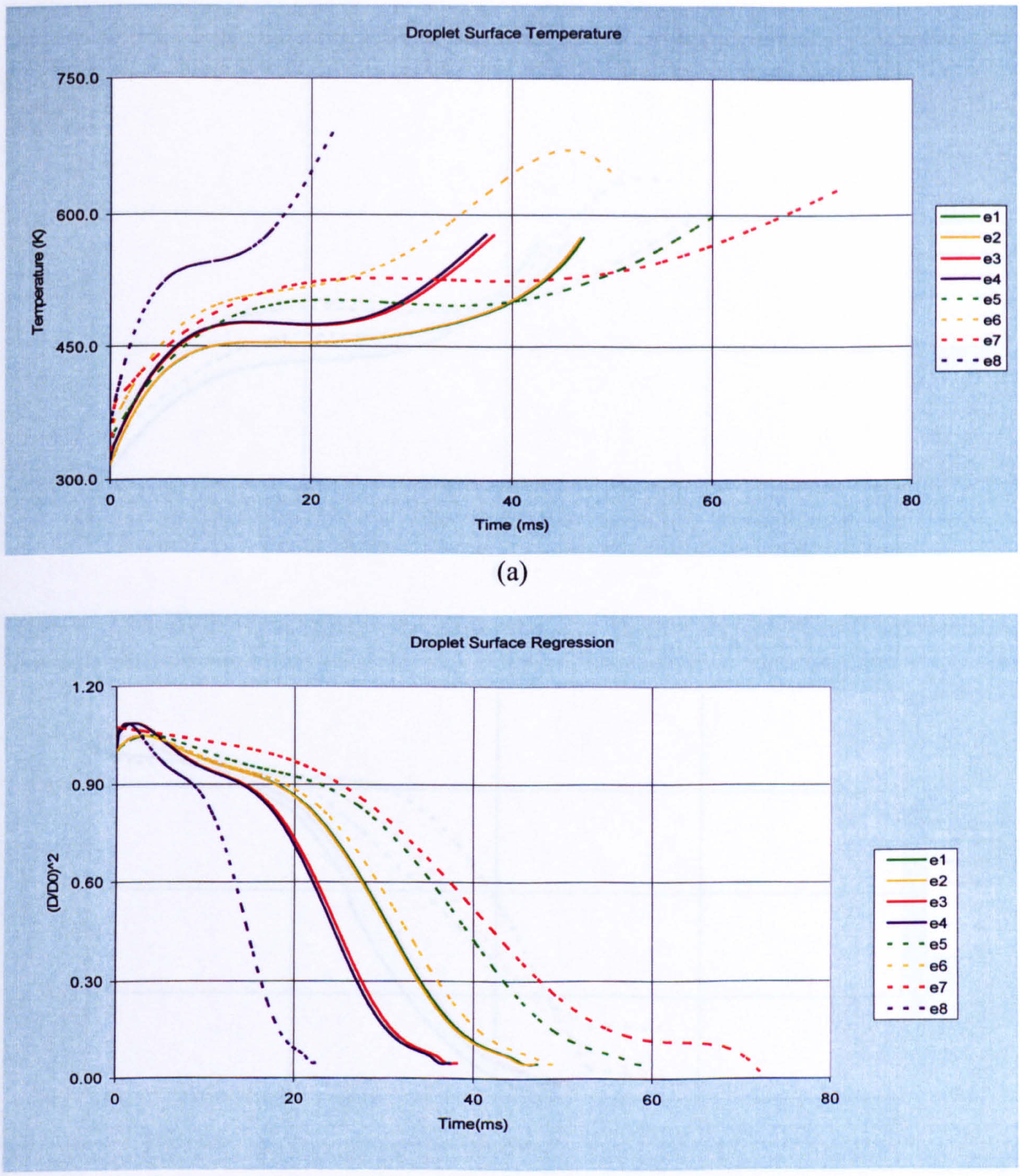

(a)

(b)

Figure 7.3 (a) Droplet surface temperature and (b) droplet normalised area predictions using MEDM low pressure (LP) and high pressure (HP) formulations for a droplet size of $100\mu m$ and temperature $300K$ in quiescent environment of various ambient temperatures and pressures: e1-(LP at $T^{\infty} = 800K$ and $P^{\infty} = 1bar$); e2-(HP at $T^{\infty} = 800K$ and $P^{\infty} = 1bar$); e3-(LP at $T^{\infty} = 1200K$ and $P^{\infty} = 1bar$); e4-(HP at $T^{\infty} = 1200K$ and $P^{\infty} = 1bar$); e5-(LP at $T^{\infty} = 800K$ and $P^{\infty} = 10bar$); e6-(HP at $T^{\infty} = 800K$ and $P^{\infty} = 10bar$); e7-(LP at $T^{\infty} = 1200K$ and $P^{\infty} = 10bar$); e8-(HP at $T^{\infty} = 1200K$ and $P^{\infty} = 10bar$) for fuel JP8 consisting 47.8% paraffin, 31.6% naphthene, and 20.6% aromatic by volume.

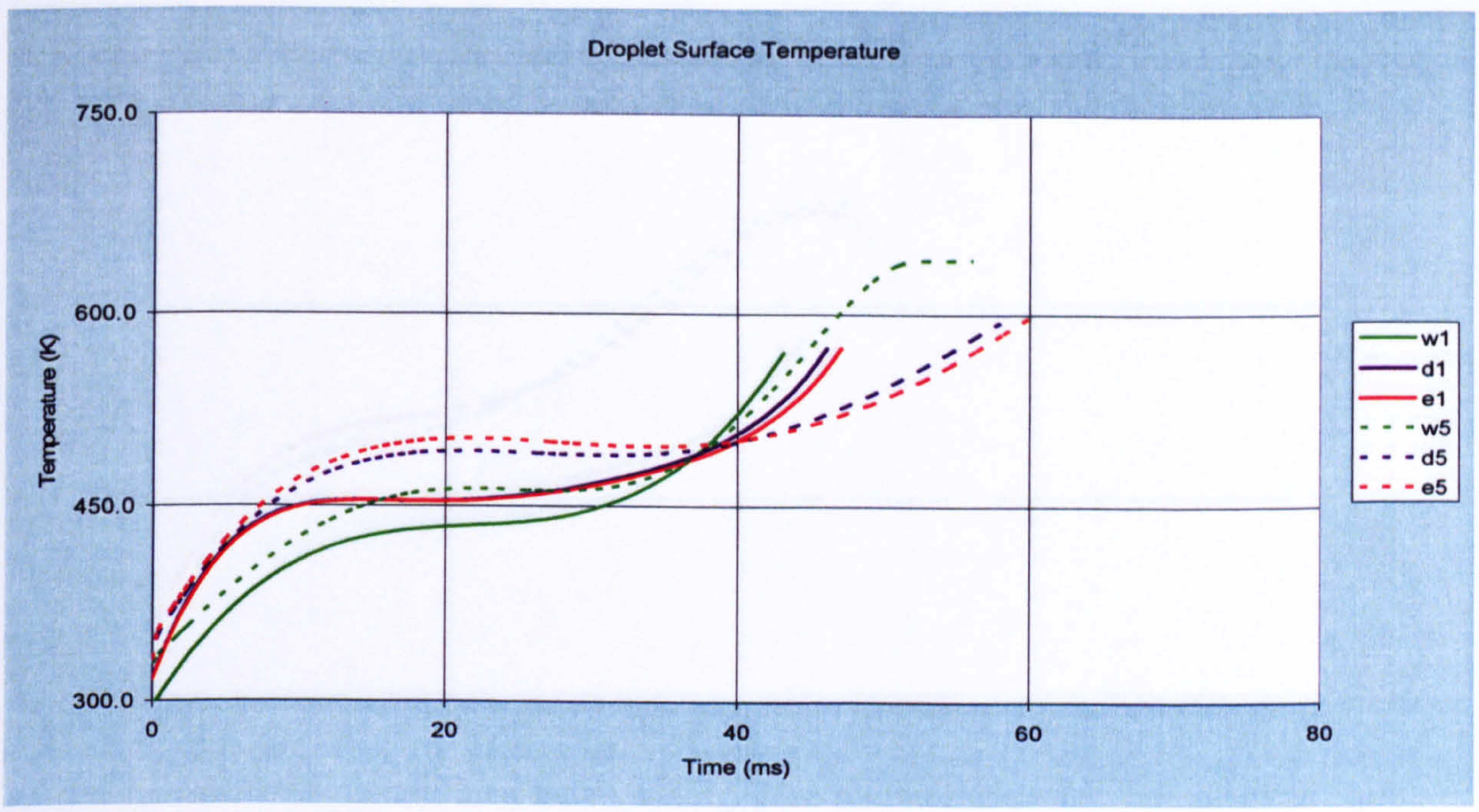

(a)

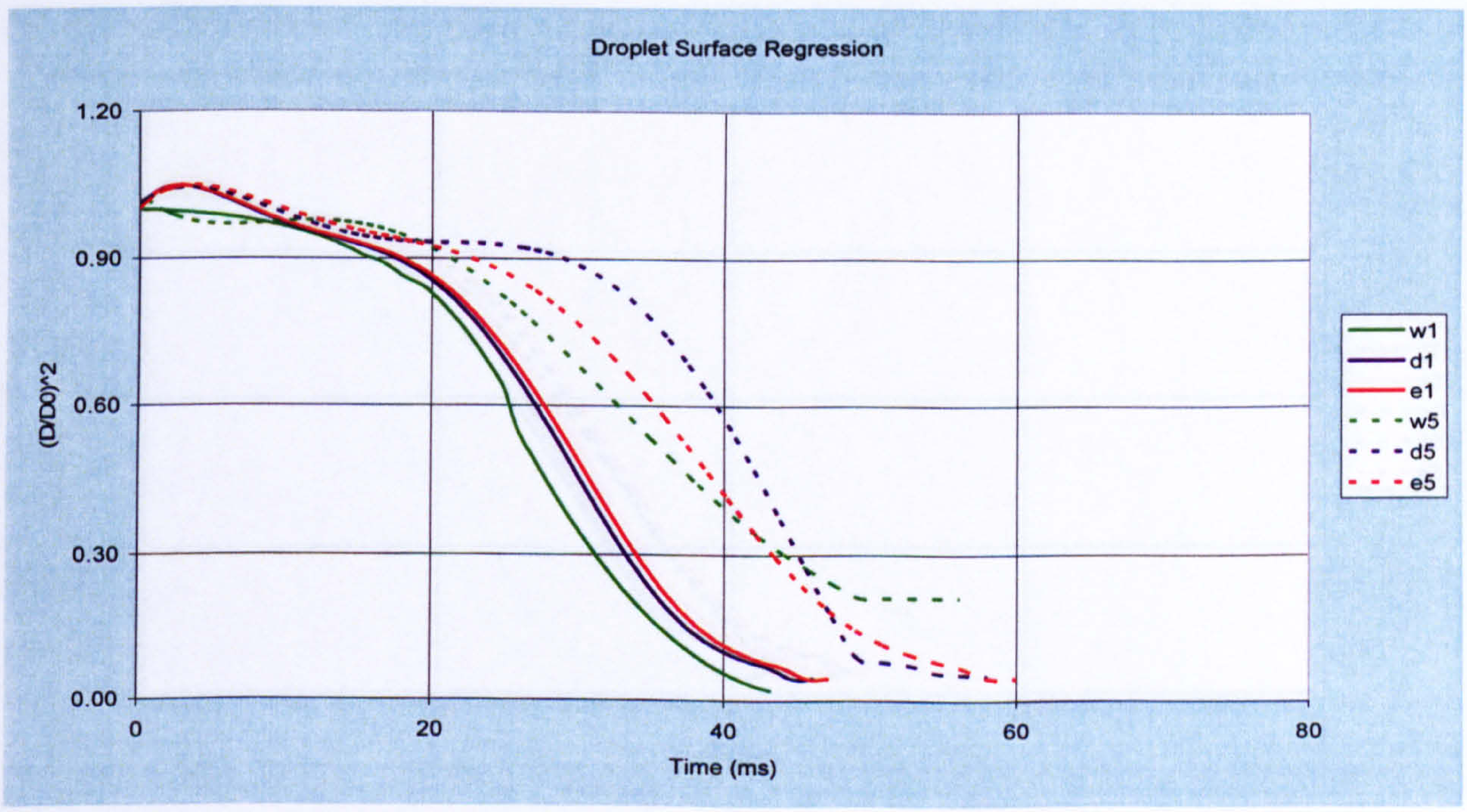

(b)

Figure 7.4 Comparison of model predictions for (a) Droplet surface temperature and (b) droplet normalised area predictions using the MWWM, MDLM, and MEDM low pressure (LP) formulations for a droplet size of $100\mu m$ and temperature $300K$ in quiescent environment at ambient temperatures of $T^{\infty} = 800K$ and various pressures: w1-(MWMM at $P^{\infty} = 1bar$); d1-(MDLM at $P^{\infty} = 1bar$); e1-(MEDM at $P^{\infty} = 1bar$); w5-(MWMM at $P^{\infty} = 10bar$); d5-(MDLM at $P^{\infty} = 10bar$); and e5-(MEDM at $P^{\infty} = 10bar$) for fuel JP8 consisting 47.8% paraffin, 31.6% naphthene, and 20.6% aromatic by volume.

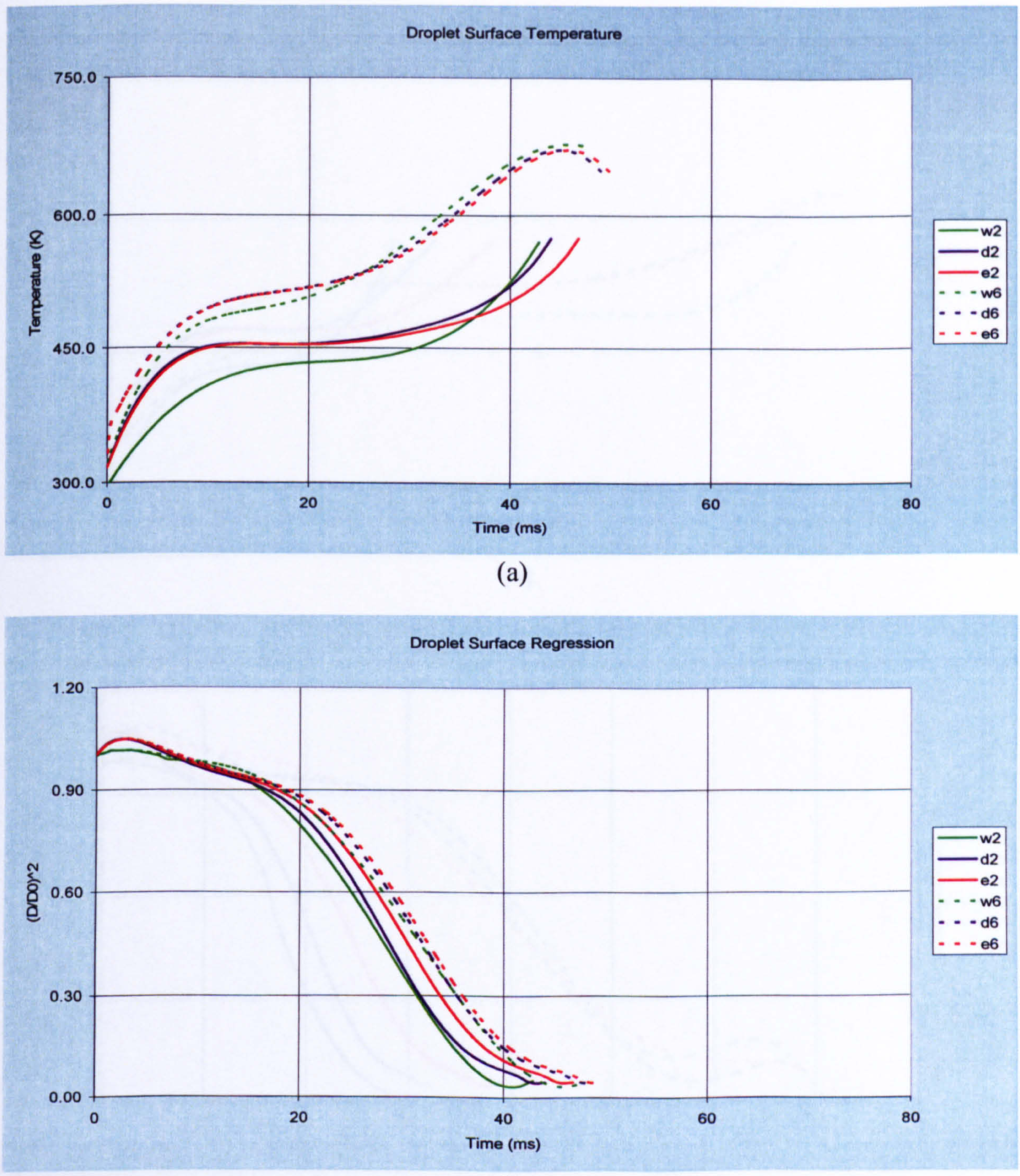

(a)

(b)

Figure 7.5 Comparison of model predictions for (a) Droplet surface temperature and (b) droplet normalised area predictions using the MWWM, MDLM, and MEDM high pressure (HP) formulations for a droplet size of $100\mu m$ and temperature $300K$ in quiescent environment at ambient temperatures of $T^{\infty} = 800K$ and various pressures: w2-(MWMM at $P^{\infty} = 1bar$); d2-(MDLM at $P^{\infty} = 1bar$); e2-(MEDM at $P^{\infty} = 1bar$); w6-(MWMM at $P^{\infty} = 10bar$); d6-(MDLM at $P^{\infty} = 10bar$); and e6-(MEDM at $P^{\infty} = 10bar$) for fuel JP8 consisting 47.8% paraffin, 31.6% naphthene, and 20.6% aromatic by volume.

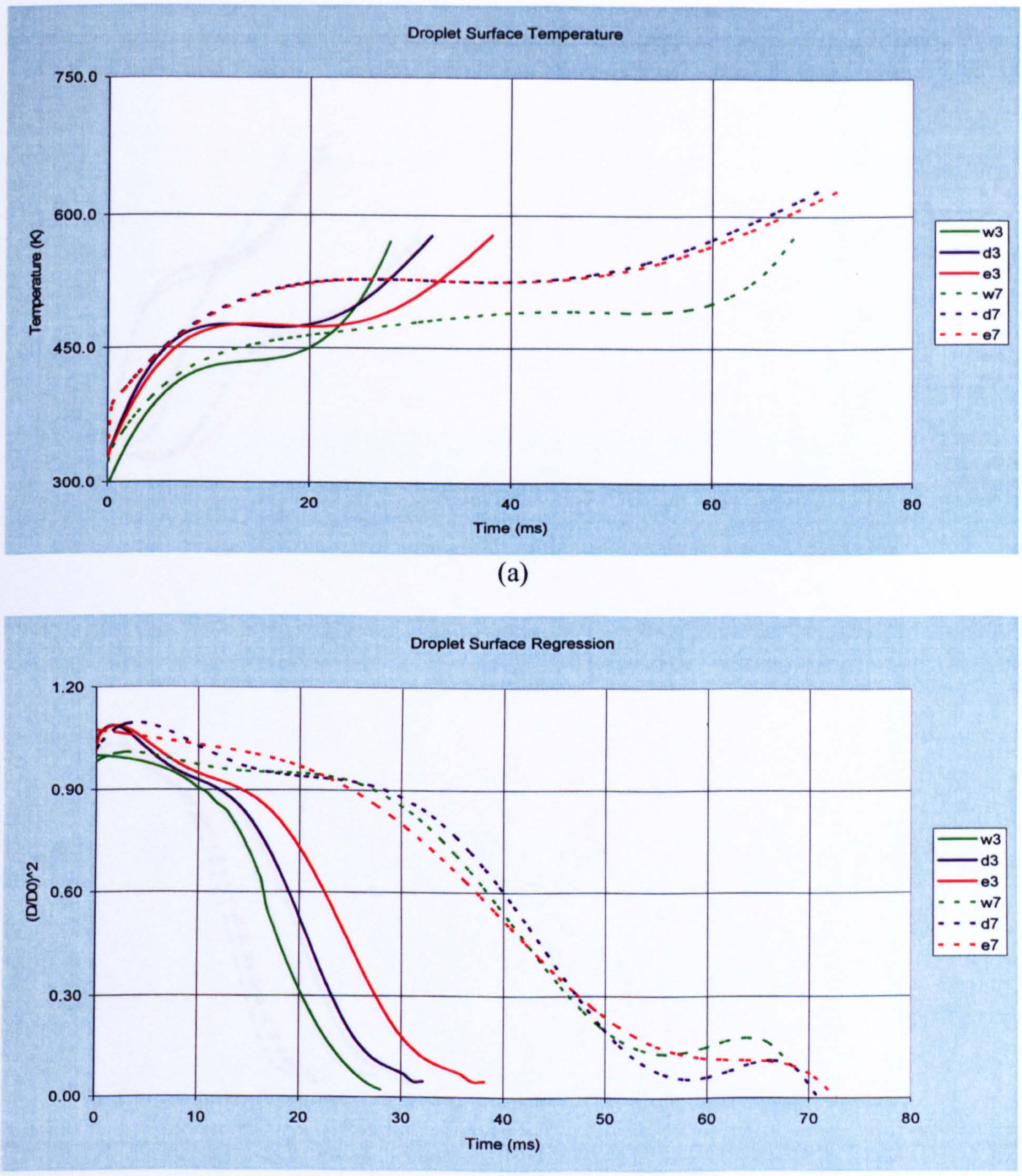

(a)

(b)

Figure 7.6 Comparison of model predictions for (a) Droplet surface temperature and (b) droplet normalised area predictions using the MWWM, MDLM, and MEDM low pressure (LP) formulations for a droplet size of $100\mu m$ and temperature $300K$ in quiescent environment at ambient temperatures of $T^{\infty} = 1200K$ and various pressures: w3-(MWMM at $P^{\infty} = 1bar$); d3-(MDLM at $P^{\infty} = 1bar$); e3-(MEDM at $P^{\infty} = 1bar$); w7-(MWMM at $P^{\infty} = 10bar$); d7-(MDLM at $P^{\infty} = 10bar$); and e7-(MEDM at $P^{\infty} = 10bar$) for fuel JP8 consisting 47.8% paraffin, 31.6% naphthene, and 20.6% aromatic by volume.

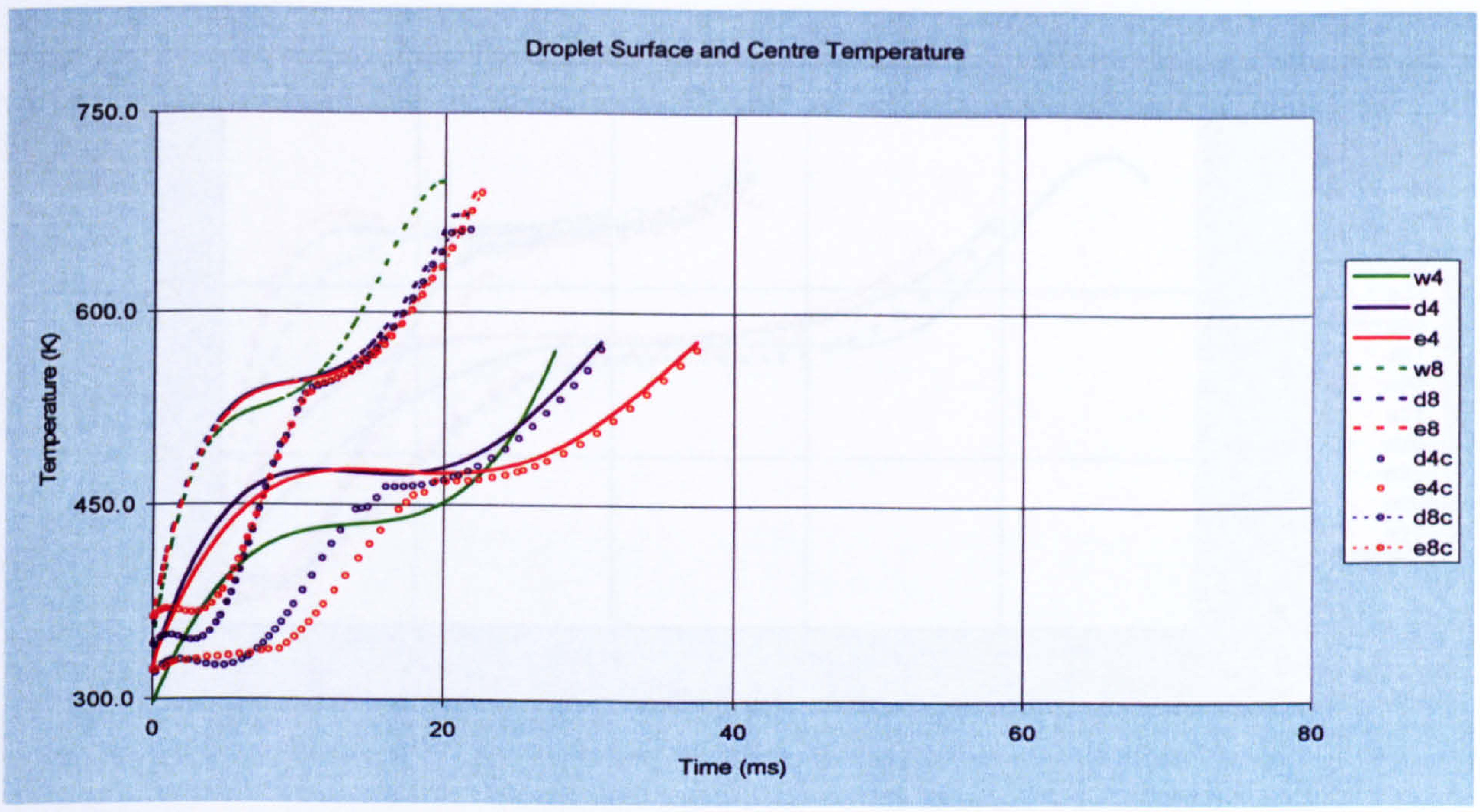

(a)

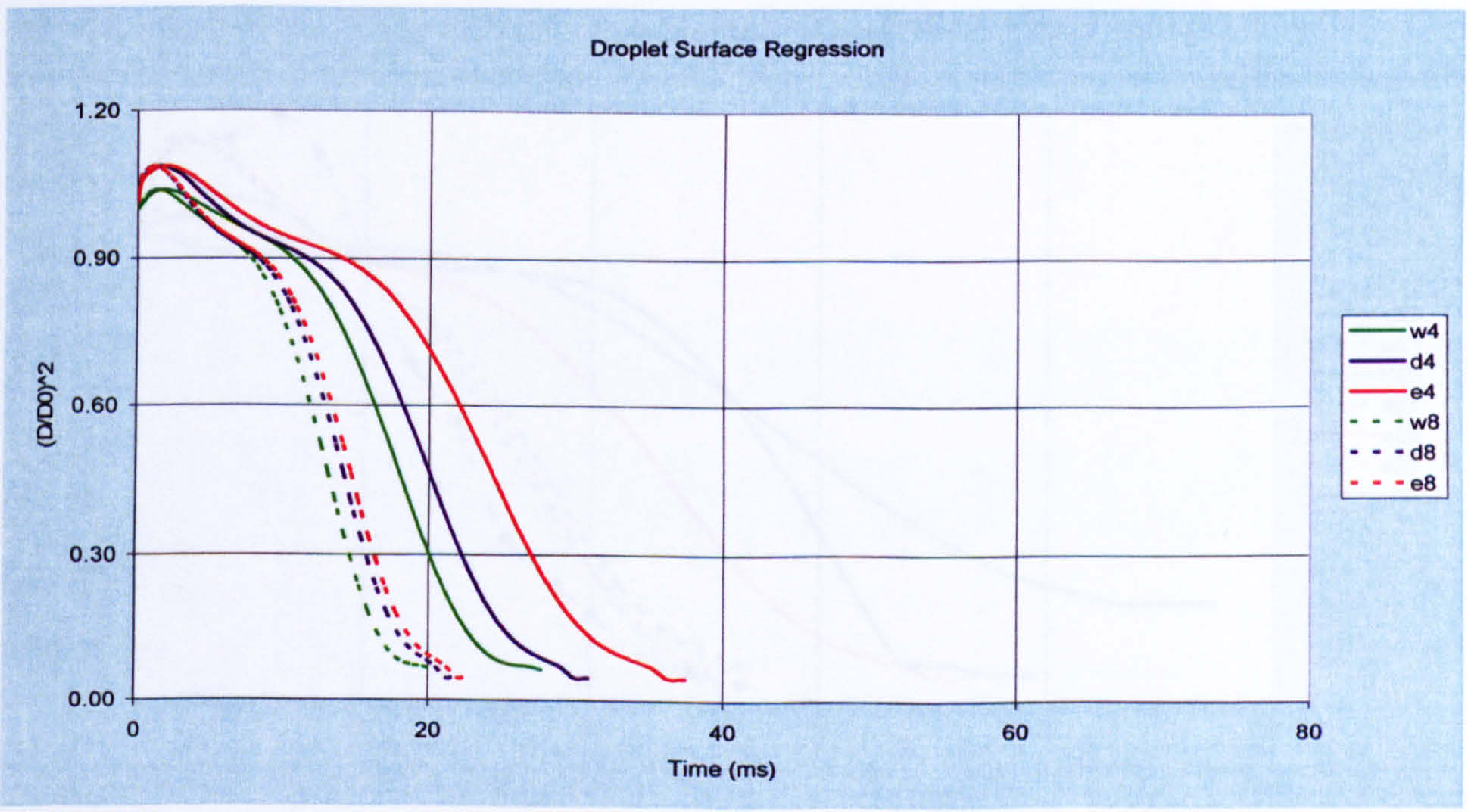

(b)

Figure 7.7 Comparison of model predictions for (a) Droplet surface temperature and (b) droplet normalised area predictions using the MWWM, MDLM, and MEDM high pressure (HP) formulations for a droplet size of $100\mu m$ and temperature $300K$ in quiescent environment at ambient temperatures of $T^{\infty} = 1200K$ and various pressures: w4-(MWMM at $P^{\infty} = 1bar$); d4-(MDLM at $P^{\infty} = 1bar$); e4-(MEDM at $P^{\infty} = 1bar$); w8-(MWMM at $P^{\infty} = 10bar$); d8-(MDLM at $P^{\infty} = 10bar$); e8-(MEDM at $P^{\infty} = 10bar$), and temperature at droplet centre d4c-(MDLM at $P^{\infty} = 1bar$); e4c-(MEDM at $P^{\infty} = 1bar$); d8c-(MDLM at $P^{\infty} = 10bar$); and e8c-(MEDM at $P^{\infty} = 10bar$) for fuel JP8 consisting 47.8% paraffin, 31.6% naphthene, and 20.6% aromatic by volume.

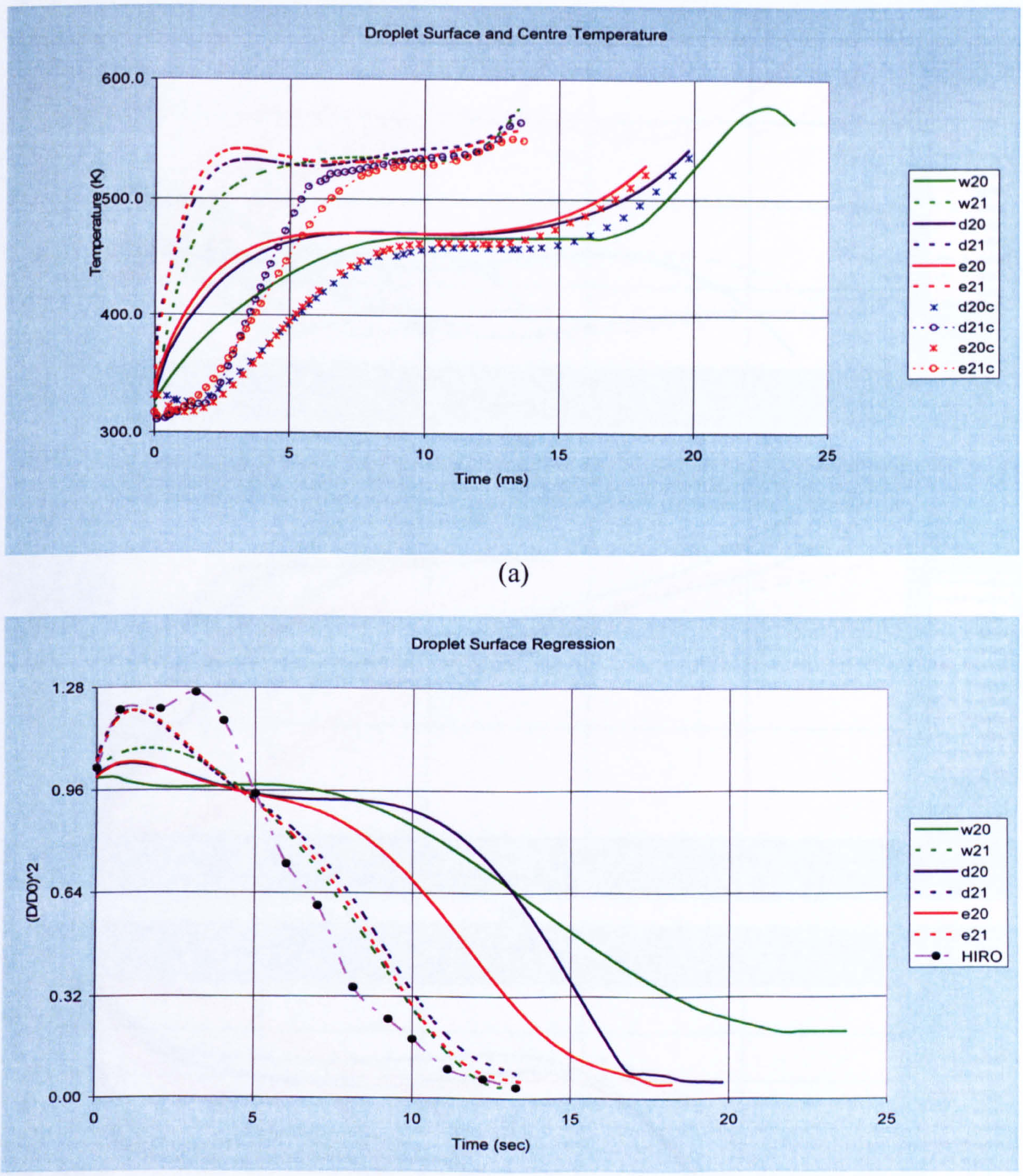

(a)

(b)

Figure 7.8 Comparison of model predictions for (a) Droplet surface temperature and (b) droplet normalised area using the MWWM, MDLM, and MEDM low pressure (LP) and high pressure (HP) formulations for a droplet size of $1800\mu m$ and temperature $300K$ in quiescent environment at ambient temperatures of $T^{\infty} = 573K$ and ambient pressure of $P^{\infty} = 30atm$: w20-(MWMM LP), w21-(MWMM HP), d20-(MDLM LP), d21-(MDLM HP), e20-(MEDM LP), e21-(MEDM HP), and predictions of temperature at the droplet centre: d20c-(MDLM LP), d21c-(MDLM HP), e20c-(MEDM LP), e21c-(MEDM HP) by employing fuel JP8 that consists 47.8% paraffin, 31.6% naphthene, and 20.6% aromatic by volume and compared with the kerosene experimental data HIRO-(of Hiroyasu et al (1976)).

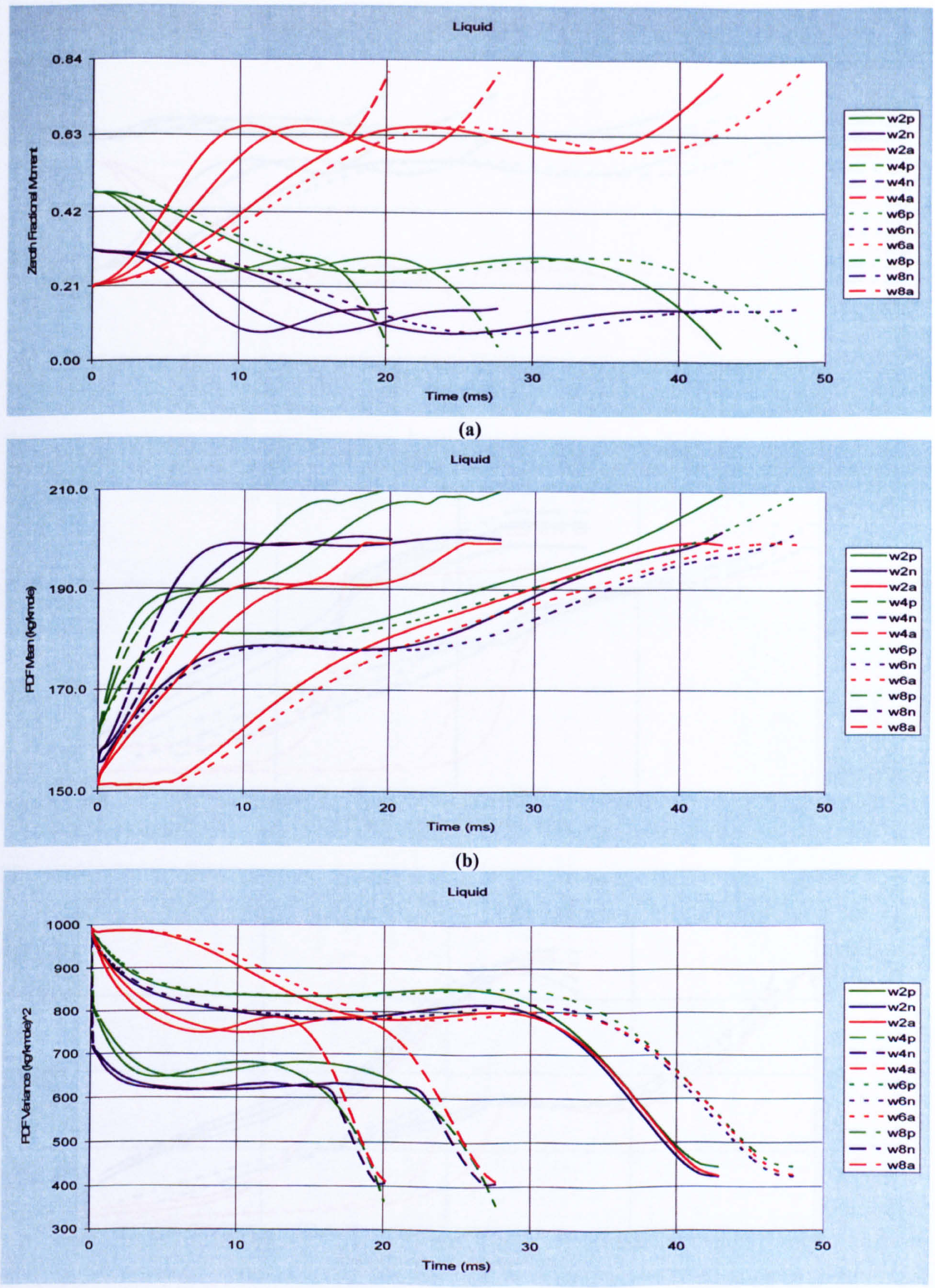

(a)

(b)

(c)

Figure 7.9 Liquid (a) 0^{th}-Fractional Moments (b) PDF Mean, and (c) PDF Variance predictions using MWMM HP formulation for paraffin (plots w2p, w4p, w6p, and w8p), naphthene (plots w2n, w4n, w6n, and w8n), and aromatic (plots w2a, w4a, w6a, and w8a) for a droplet size of $100\mu m$ and initial temperature $300K$ in quiescent environment: w2-($T^{\infty} = 800K$ and $P^{\infty} = 1bar$); w4-($T^{\infty} = 1200K$ and $P^{\infty} = 1bar$); w6-($T^{\infty} = 800K$ and $P^{\infty} = 10bar$); and w8-($T^{\infty} = 1200K$ and $P^{\infty} = 10bar$); for fuel JP8 consisting 47.8% paraffin, 31.6% naphthene, and 20.6% aromatic by volume.

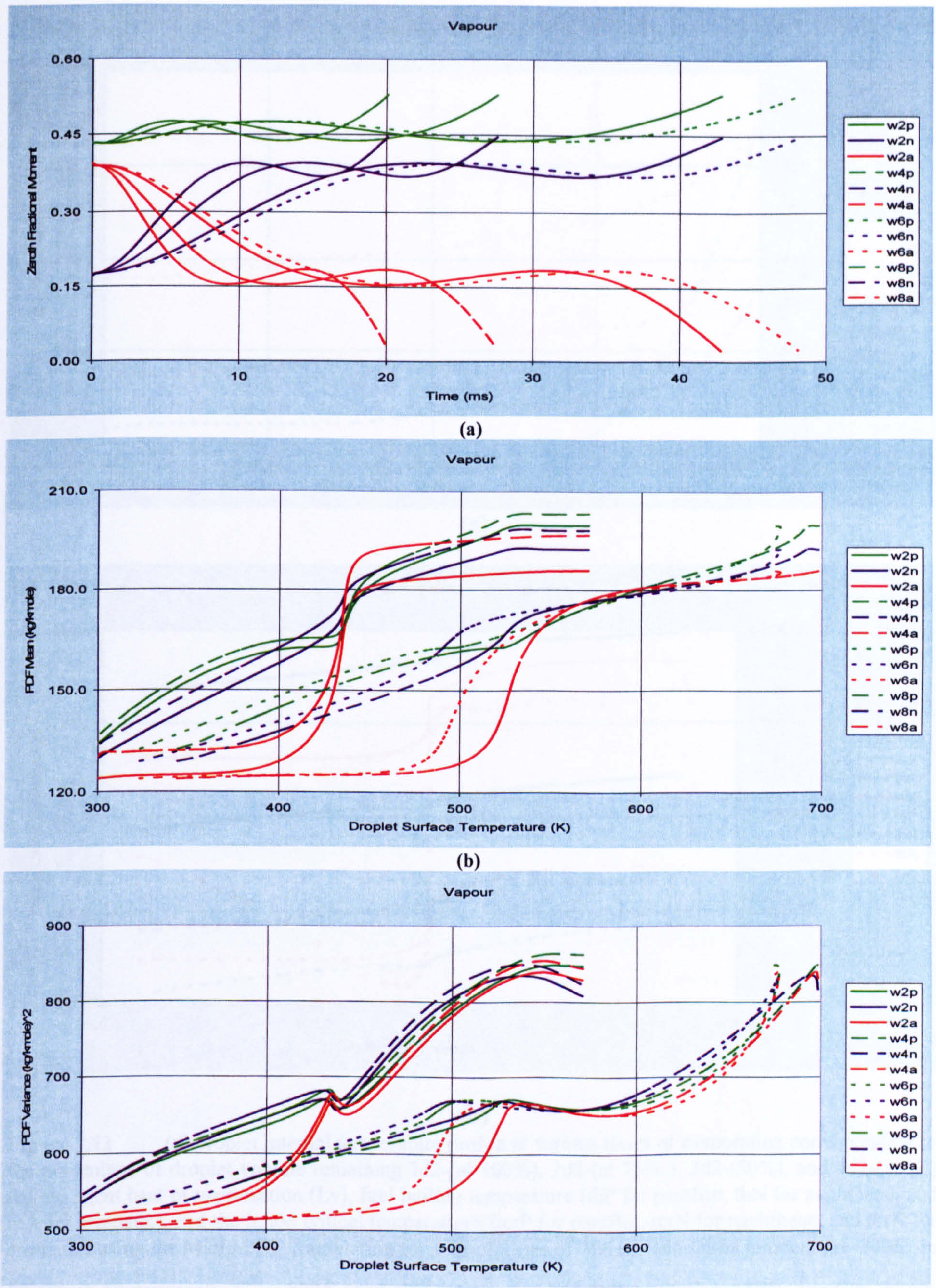

(a)

(b)

(c)

Figure 7.10 Vapour (a) 0^{th}-Fractional Moments (b) PDF Mean, and (c) PDF Variance predictions using MWMM HP formulation for paraffin (plots w2p, w4p, w6p, and w8p), naphthene (plots w2n, w4n, w6n, and w8n), and aromatic (plots w2a, w4a, w6a, and w8a) for a droplet size of $100\mu m$ and initial temperature $300K$ in quiescent environment: w2-($T^{\infty} = 800K$ and $P^{\infty} = 1bar$); w4-($T^{\infty} = 1200K$ and $P^{\infty} = 1bar$); w6-($T^{\infty} = 800K$ and $P^{\infty} = 10bar$); and w8-($T^{\infty} = 1200K$ and $P^{\infty} = 10bar$); for fuel JP8 consisting 47.8% paraffin, 31.6% naphthene, and 20.6% aromatic by volume.

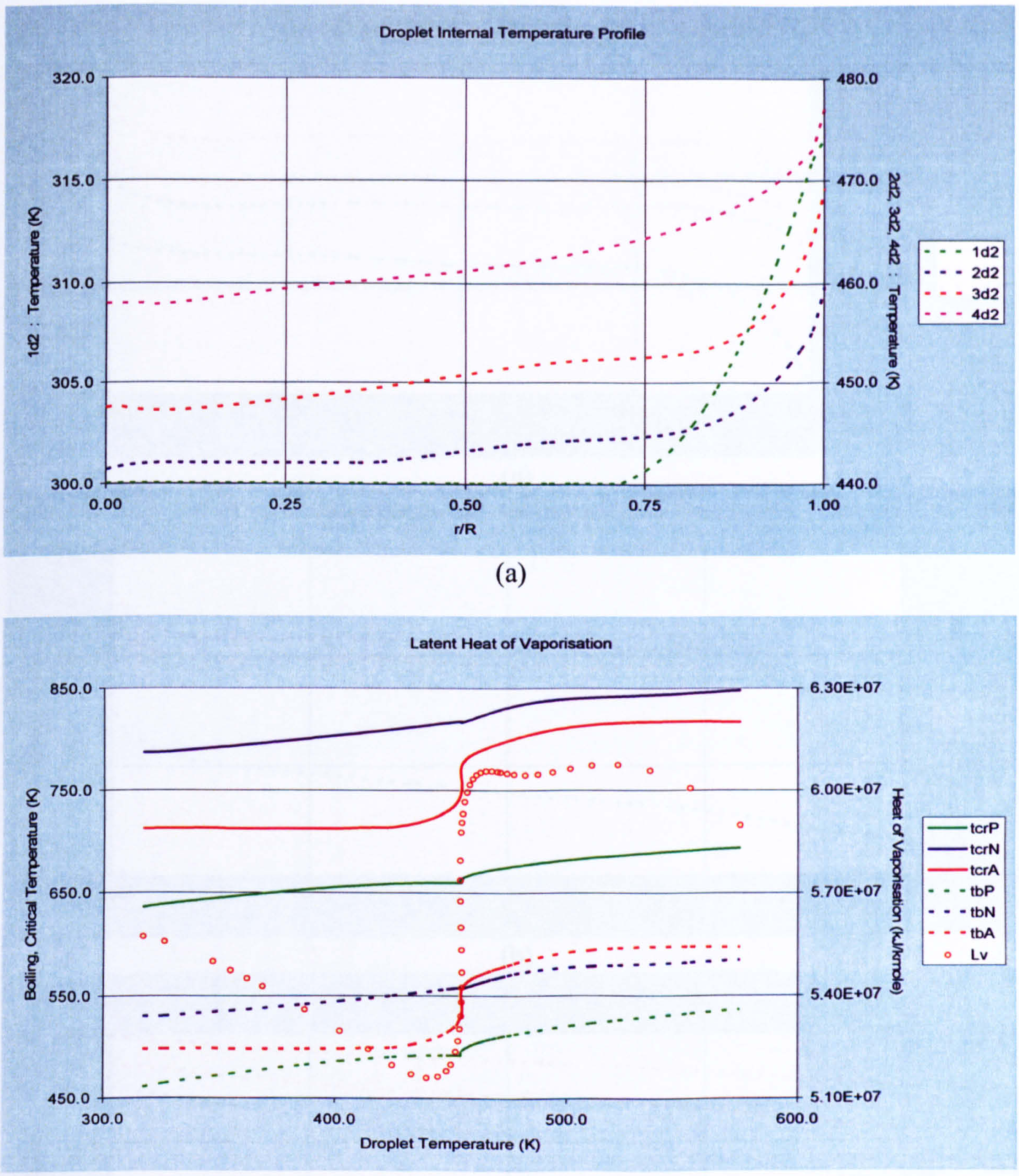

(a)

(b)

Figure 7.11 (a) droplet internal temperature profile at various times of evaporation corresponding to the percentage of droplet volume remaining 1d2-(at 100%), 2d2-(at 75%), 3d2-(50%), and 4d2-(25%) (b) the latent heat of vaporisation (Lv), fuel boiling temperature (tbP for paraffin, tbN for naphthene, and tbA for aromatic), and the liquid critical temperatures (tcrP for paraffin, tcrN for naphthene, and tcrA for aromatic) using the MDLM HP formulation for a droplet size of $100\mu m$ and initial temperature $300K$ in quiescent environment: $T^{\infty} = 800K$ and $P^{\infty} = 1bar$ for fuel JP8 consisting 47.8% paraffin, 31.6% naphthene, and 20.6% aromatic by volume.

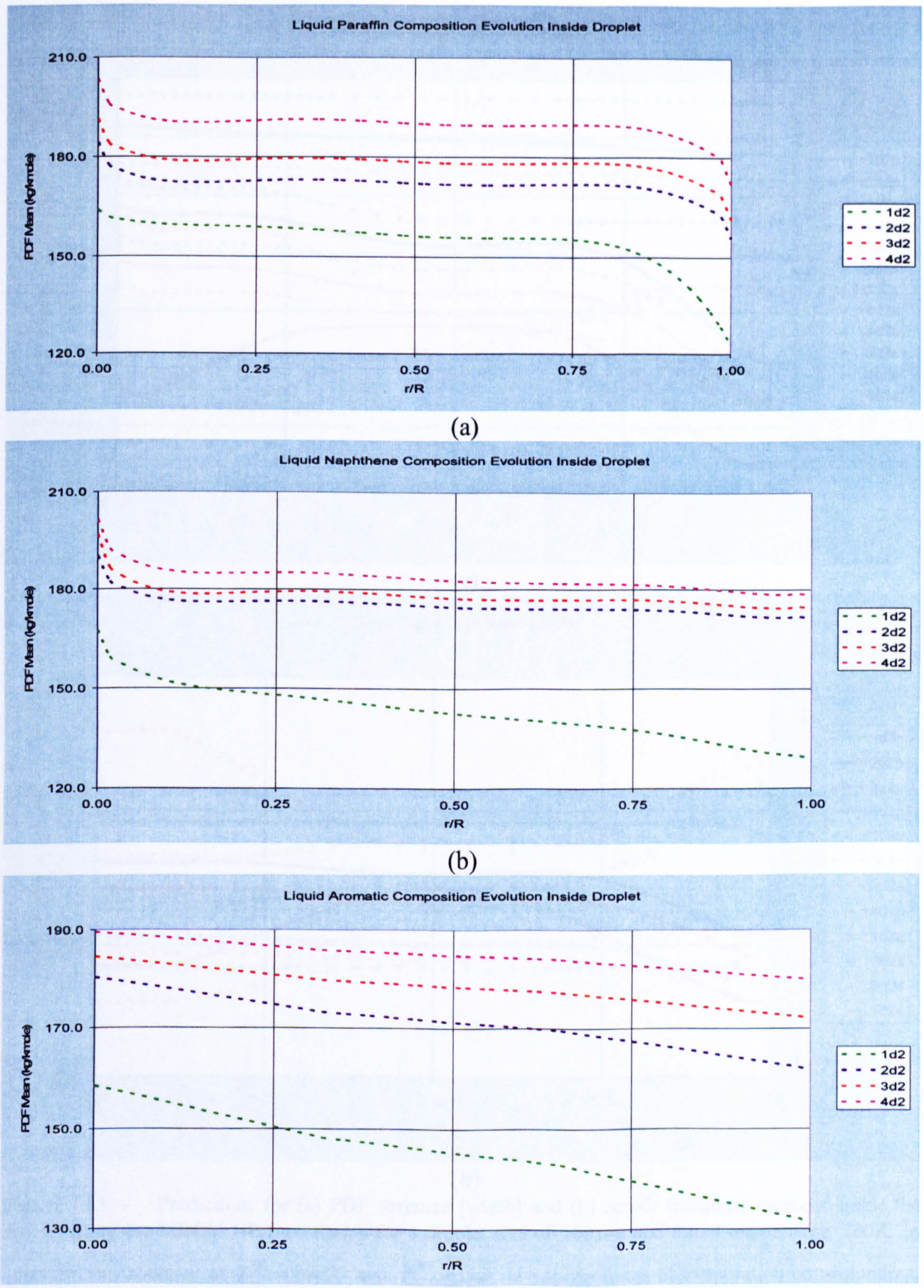

(a)

(b)

(c)

Figure 7.12 PDF Mean predictions inside the droplet for homologue (a) paraffin, (b) naphthene, and (c) aromatic using the MDLM HP formulations for a droplet size of $100\mu m$ and initial temperature $300K$ in quiescent environment of $T^{\infty} = 800K$ and $P^{\infty} = 1bar$ at various times of evaporation corresponding, respectively, to the percentage of droplet volume remaining and evaporation time 1d2-(at 100% and ~ 0ms), 2d2-(at 75% and ~14ms), 3d2-(50% and ~17ms), and 4d2-(25% and ~21ms) for fuel JP8 consisting 47.8% paraffin, 31.6% naphthene, and 20.6% aromatic by volume.

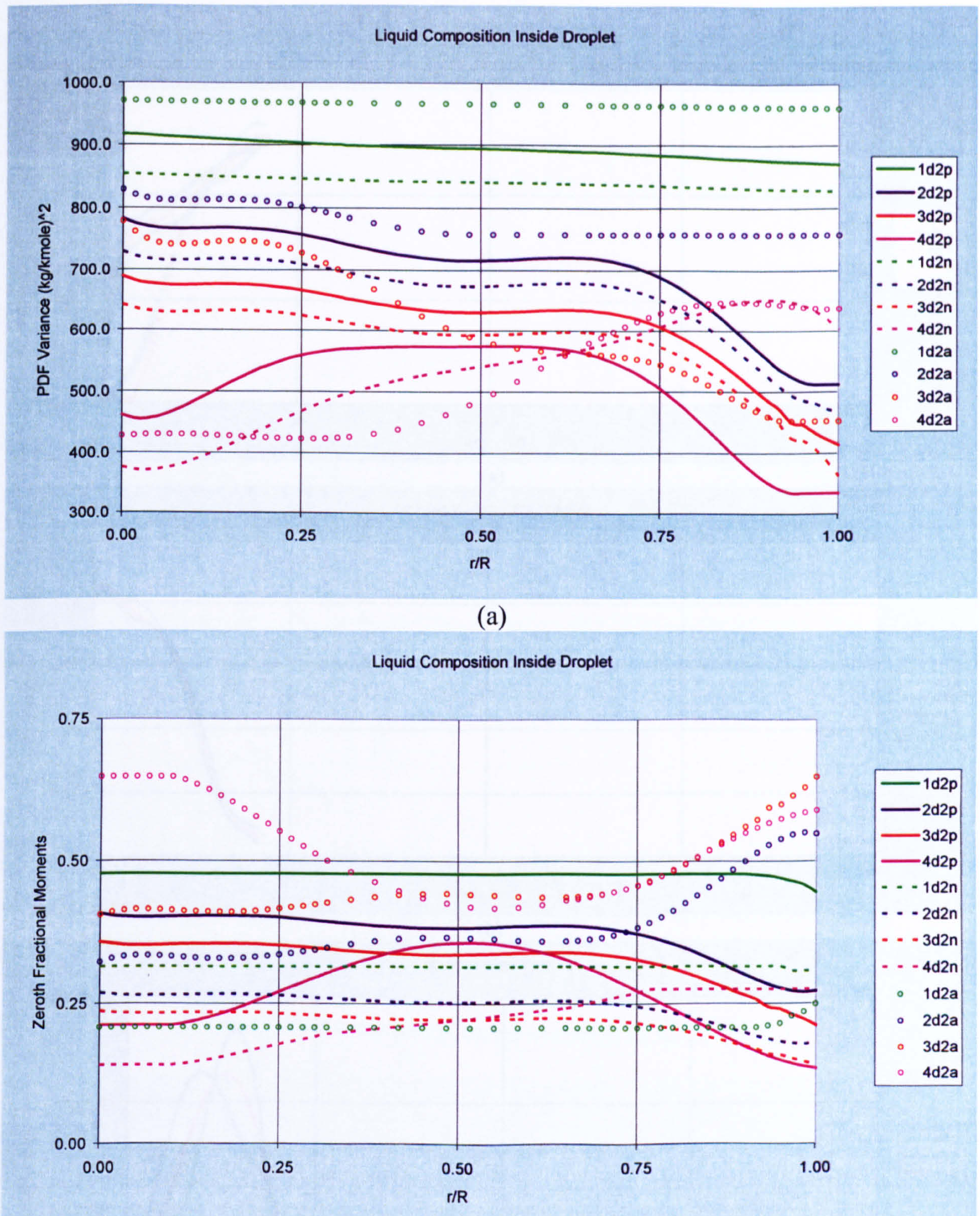

(a)

(b)

Figure 7.13 Predictions for (a) PDF variance (width) and (b) zeroth fractional moment inside the droplet using the MDLM HP formulation for a droplet size of $100\mu m$ and initial temperature $300K$ in quiescent environment of $T^{\infty} = 800K$ and $P^{\infty} = 1bar$ at various times of evaporation corresponding, respectively, to the percentage of droplet volume remaining and evaporation time 1d2p-(paraffin at 100% and ~ 0ms), 2d2p-(paraffin at 75% and ~14ms), 3d2p-(paraffin at 50% and ~17ms), and 4d2p-(paraffin at 25% and ~21ms); 1d2n-(naphthene at 100% and ~ 0ms), 2d2n-(naphthene at 75% and ~14ms), 3d2n-(naphthene at 50% and ~17ms), and 4d2n-(naphthene at 25% and ~21ms); 1d2a-(aromatic at 100% and ~ 0ms), 2d2a-(aromatic at 75% and ~14ms), 3d2a-(aromatic at 50% and ~17ms), and 4d2a-(aromatic at 25% and ~21ms); for fuel JP8 consisting 47.8% paraffin, 31.6% naphthene, and 20.6% aromatic by volume and having a droplet life time of ~44 ms..

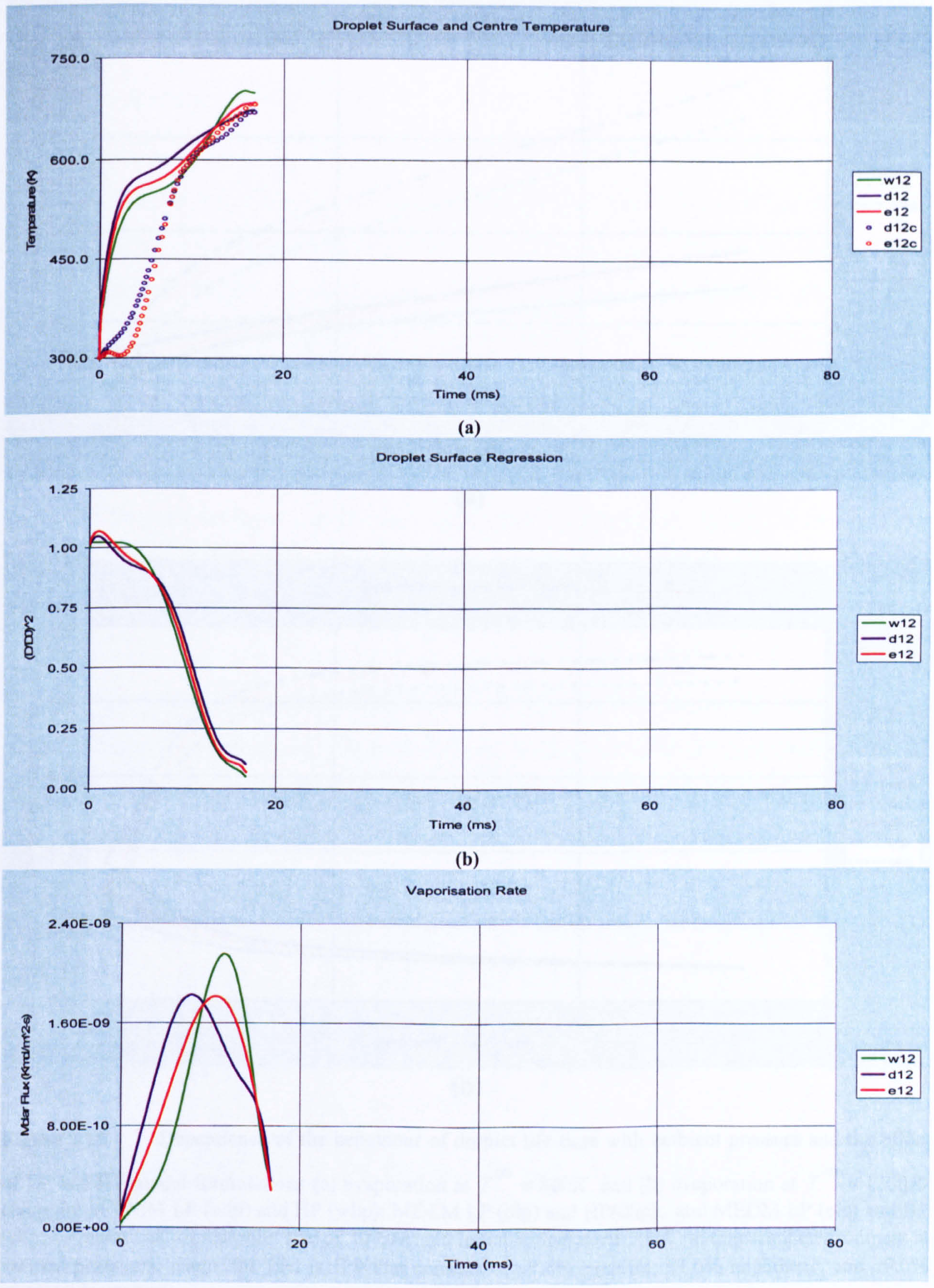

Figure 7.14 Predictions for the droplet (a) surface and centre temperature (b) normalised area and (c) vaporisation rate using the WMMM (w12), MDLM (d12), MEDM (e12) HP formulations for a droplet size of $100\mu m$ and initial temperature $300K$ in quiescent environment of $T^{\infty} = 1200K$ and $P^{\infty} = 40bar$ for fuel JP8 consisting 47.8% paraffin, 31.6% naphthene, and 20.6% aromatic by volume and having a droplet life time of ~44 ms..

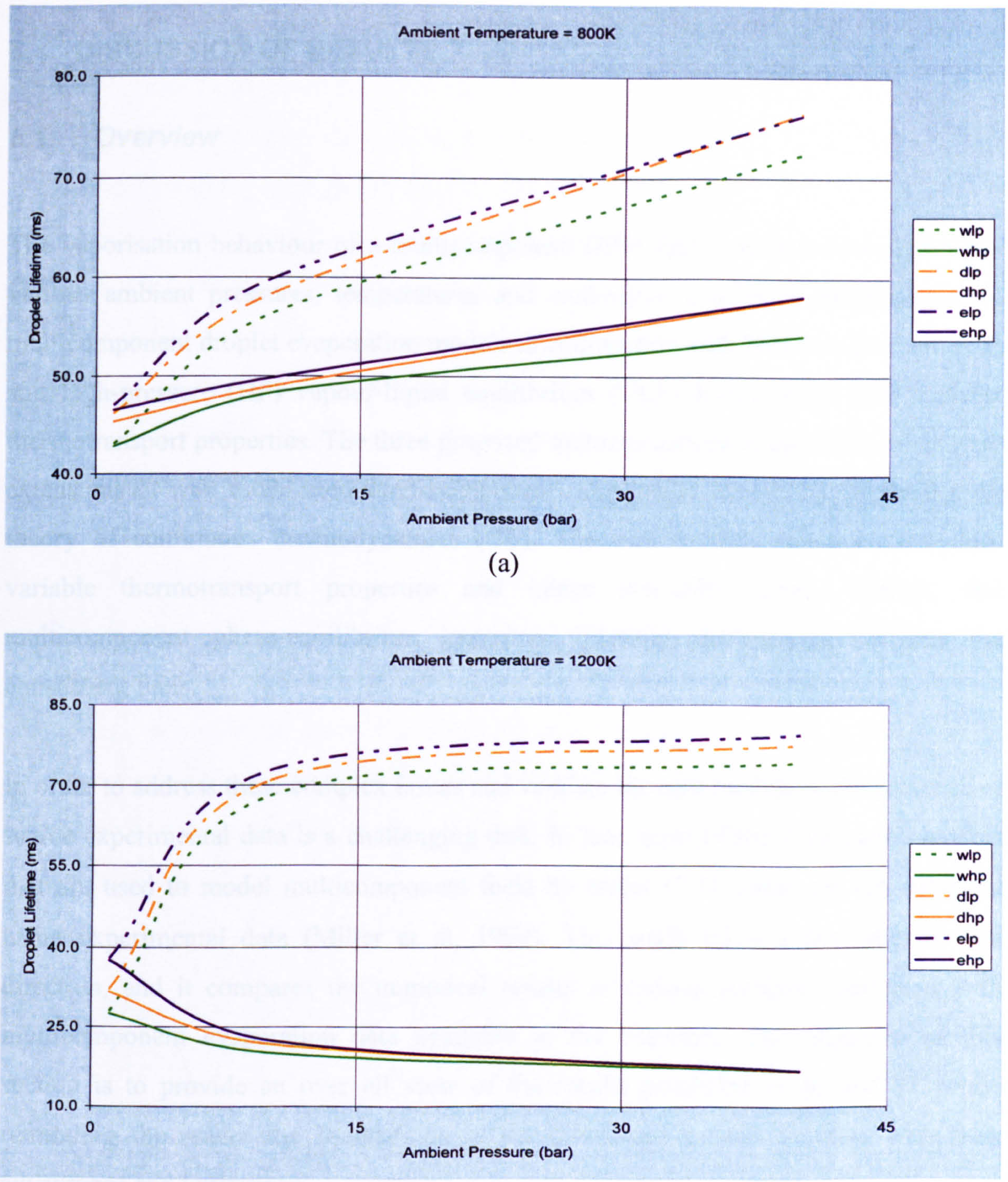

(a)

(b)

Figure 7.15 Dependence of the behaviour of droplet life time with ambient pressure and the effect of LP and HP model formulations (a) evaporation at $T^{\infty} = 800K$ and (b) evaporation at $T^{\infty} = 1200K$ using the MWMM LP (wlp) and HP (whp); MDLM LP (dlp) and HP(dhp); and MEDM LP (elp) and HP (ehp) formulations for a droplet size of $100\mu m$ and initial temperature $300K$ in quiescent environment at various pressures, where the fuel is JP8 that consists of 47.8% paraffin, 31.6% naphthene, and 20.6% aromatic by volume.

8. DISCUSSION OF RESULTS

8.1. *Overview*

The vaporisation behaviour of a multicomponent (JP8) fuel droplet is investigated for various ambient pressures, temperatures and convective conditions employing three multicomponent droplet evaporation models in conjunction with both low-pressure (LP) and high-pressure (HP) vapour-liquid equilibrium (VLE) formulations with variable thermotransport properties. The three proposed multicomponent evaporation models are extensions of well established singlecomponent evaporation models by employing the theory of continuous thermodynamics (CT). The new models, however, introduce variable thermotransport properties and hence non-unity Lewis number, and multicomponent phase-equilibrium including volatility differentials between the constituent fuels.

In order to address these complex issues and validate the new models in the presence of scarce experimental data is a challenging task. In fact, most of the evaporation models that are used to model multicomponent fuels by major CFD codes are not validated using experimental data (Miller et al, 1998). This study takes a first step in that direction, and it compares the numerical results at various ambient conditions with multicomponent evaporation data available in the literature. The objective of this section is to provide an over all view of the results presented in §6 and §7, while reminding the reader the foundations of the developed models together with their advantages and limitations.

The tests were carried out in two classes. The first class of tests are presented in §6 while the second is presented in §7. The first class is devoted to validate one of the suitable evaporation models against the experimental data of JP8 fuel jettisoning at low temperature and pressure as well as its distillation characteristics at moderate temperature and low pressure. The study of JP8 fuel evaporation at low pressure is used to understand the effect of fuel composition and the behaviour of composition evolutions with regard to the CT formulation by employing seven different types of fuels. The second class however, is conducted at low-high model parameter intensities. Although the evaporation of JP8 fuel was conducted at low pressure in §6, the investigation at the same pressure in §7 differs in the size of the droplet, the ambient temperature, and the ambient convective strength employed. Therefore, the objective of the second class is two fold. The first objective is to get a complete picture on the behaviour of the proposed multicomponent droplet evaporation models at various ambient conditions and to gauge if there is any similarity with the corresponding well established singlecomponent models in the literature. The second is on the practical aspects of the models implementation with regard to their use with either the LP or HP formulations, where the dependence of the droplet lifetime on ambient conditions is a point of interest.

Although the results and detail discussion is given both in §6 and §7, an elaborate and unified discussion of these results is presented in the remaining part of this section. However, in order to draw conclusions from the investigation by analysing the performance of the proposed models, this discussion of results first brings into frame the physical models and the ensuing mathematical or numerical models that are used in this investigation.

8.2. Effects of ambient conditions on the performance of models

The ambient conditions, among others, include the pressure, temperature, convective strength, and the far field composition or vapour concentration. But, not all of these ambient conditions are investigated exhaustively. The transport of heat and mass in the liquid is generally transient in nature, so is the gas when the ambient pressure is above the critical pressure. However, in all the models, the gas-phase is assumed to be quasi-steady, and no possibility is introduced to resolve full transients. It can be recalled from the development of the gas-phase approximate analysis in §3 that based on a quasi-steady assumption, correlations for the Nusselt and Sherwood numbers, which are generally time dependent, are developed.

However, the liquid phase transience is explored directly in the three models proposed, although after the results in §6 and §7, it can be argued that the other two models are in fact limiting cases for the third one. To shape the presentation of this section both from the view point of the numerical results as well as its future implication, a general perspective on the physical model considered is presented first. It is envisaged that such a presentation will provide a basis in furtherance the work and its implementation in multidimensional CFD codes.

For the liquid model, the most obvious transient that can be chosen is when an initially homogeneous droplet is immersed into a high ambient-temperature condition. In the absence of ambient convection, the theoretical assumptions confirmed by the numerical results in Figures 7.7a, 7.8a, and 7.11a is that immediately after the droplet is immersed into the hot gas, the core of the droplet maintains its low temperature. In such situations, the liquid Prandtl and Schmidt numbers are large and the time scale for momentum diffusion will be comparatively short. Depending on the values of the liquid Prandtl and Schmidt as well as the corresponding momentum diffusion time scale (which requires further investigation to establish), a spherical vortex is expected to be established quickly with short turn-around time. Since the turn-around times of the spherical vortex is short compared to the characteristics times of heat and mass diffusion, properties along the streamlines are assumed to be constant, which is usually called the Kronig-Brink limit (Johns and Beckmann, 1966). Therefore, the heat and mass diffusion become normal to the streamlines between the droplet core and the droplet surface. In this situation, the effect of the vortex is expected to reduce the core-surface length scale of diffusion by enhancing the heat and mass transfer rates.

Unfortunately, at this initial stage, the liquid boundary layers are thin and yet growing corresponding to the liquid Nusselt and Sherwood numbers that are large and yet decreasing, prompting penetration problem for heat and mass transfer. Eventually, however, the liquid boundary layer starts to feel the symmetry boundary condition at the core, where the temperature and concentration profiles become self-similar at a thermal diffusion time and mass diffusion time, respectively, in the order of $R^2 / Le^l_{J(n)} D^l_{J(n)}$ and $R^2 / D^l_{J(n)}$. For a droplet immersed in a hot ambient gas, although it is known (Johns and

Beckmann, 1966; Renksizbulut and Yuen, 1983) that the temperature profile to become self similar much faster than the concentration profile due to the large Lewis number corresponding to the low liquid core temperature, most droplet evaporation models assumed $Le^{l}_{J(n)} = 1$, prompting equal thermal diffusion and mass diffusion times.

In the presence of convection at the ambient (or when there is relative velocity between the droplet and the carrier gas), however, convective boundary layers, and separated near wakes can surround the droplet with non-zero shear stress and tangential velocity at the same point. Such boundary layers enhance the heat and mass transport rates over the values of the spherically symmetric droplet. In addition, the shear force on the liquid surface causes an internal circulation that enhances the heating of the liquid, which as a result increases the vaporisation rates with increasing Reynolds number. Nevertheless, a parametric study to establish the dependence of liquid circulation either due to shear forces due to an ambient convection or thermal gradient due to ambient temperature has not been established.

In general, the 0D and 1D-liquid evaporation models that are used in this investigation are simplified mathematical representations of the physical models described earlier. If the developed internal circulation is vigorous enough to completely mix the interior of the droplet homogeneously and instantly, a spatially uniform temperature and composition can be assumed, resulting in the MWMM. On the other hand, if the heat and mass transfer due to the internal liquid circulation is ignored and only conduction heat transfer and molecular diffusion is assumed, it results the MDLM. The introduction of a semi-empirical correlation for the effective heat and mass diffusivity to account for the internal liquid circulation results in the MEDM. As such, all models can be reduced to equation $(4-13)$ by considering suitable values for $\Gamma^{eff}_{\Phi^{l}_{J(n)}}$ in equation $(4-19)$.

During vaporisation, in particular, for the range of ambient conditions typical of recent propulsion devices, the models also include the unresolved and controversial topics of determining multicomponent phase equilibria at high and supercritical pressures with the corresponding choice of appropriate equation of state, the importance of liquid diffusion, and effect of variable thermotransport properties. Although the development of such highly varied and complex models is one aspect of this investigation, it also considered decoupled problems in order to isolate a limited set of issues. As such, the gasification behaviour of an isolated droplet in a quiescent environment is described in §7, while convective effects that may contribute to the internal circulation of the liquid droplet are ignored from the 1D-models. Only the effect of ambient temperature and pressure on liquid circulation is considered, while convection effects are investigated indirectly based on the results from the 0D-MWMM.

8.2.1. Effect of convective strength on rates of evaporation

The two test cases for the evaporation of JP8 fuel (BT: base test and DT: distillation test in §6) are conducted under ambient convective conditions. In this study, the term fuel droplet evaporation refers to the process when the droplet in the liquid phase gained sufficient energy to enter the vapour phase. Therefore, for evaporation to happen the kinetic energy attained by the fuel molecules due to thermal diffusion or mass diffusion must overcome the cohesive surface tension of the liquid at the surface, and must further prompt phase transition. From this point of view, the BT for the jettisoning JP8 fuel can not be categorised as evaporation, and yet, it is assumed to loosely satisfy the condition of evaporation only for descriptive purposes. The DT is essentially an evaporation test which was conducted in an ambient temperature well above the boiling points of all the constituents of JP8, but well below the critical temperature. On the other hand, the BT mass transport is solely due to convective weathering or aerodynamic shearing, since the ambient temperature was well below the boiling point of the most volatile component to prompt evaporation.

In the BT, it took nearly four hours to reduce the droplet diameter by 80% and the heavier components were found very resistant to convective weathering process. In most of the composition distribution moments that are used to characterise the evaporation process, however, the numerical results provided an accurate picture on the process. The composition PDF, its fractional moments and its mean depicted the composition evolution very well. In particular, the ratio of the liquid and vapour PDF scale parameter is used to determine the existence of thermodynamic phase transition. The liquid PDF variance depicted the depletion of the components due to convective weathering, whereas the vapour PDF variance, due to the relative strength of convective transport, did not describe the fuel accumulation very well.

The DT is conducted at ambient pressure using moderate temperature and moderate convective condition (Table 6.2). Although this test is carried out for a droplet diameter six times larger and an ambient temperature well below those used in §7, a qualitative comparison can be made to identify the effect of convective condition in genuine evaporation cases. From the droplet lifetime history, it is easy to observe that the DT predicted by the MWMM with a droplet lifetime of 34.2 ms is comparable to those quiescent tests at $T^{\infty} = 1200K$ of §7 as predicted by any of the models (MWMM, MDLM, MEDM). Note that since the DT is carried out for an ambient pressure of $P^{\infty} = 1bar$, no distinction is made wether the model predictions are based on LP or HP formulations, although the DT is based on only the LP formulation and operated at half the ambient temperature of the tests in §7. On the other hand, the DT prediction shows a higher evaporation rate and short droplet lifetime than that of the tests in §7 with $T^{\infty} = 800K$. This quantitative comparison can be used to establish the importance of convection in the vaporisation process.

It is easy to demonstrate that by inferring the direct proportionality between the molar flux $N_{T(n)}$ and the droplet lifetime τ_{life}, the effect of convection and droplet size on vaporisation can be established. First, observe the molar flux described by equation $(3-47)$ together with the convective corrections that embodies the Reynolds number as described by equation $(3-45)$. The use of the droplet Reynolds number, which is estimated based on the droplet radius as in equation $(2-4)$, into the convective correlation described by equation $(3-45)$ reveals that the droplet lifetime and radius to vary according to $\tau_{life} \sim R^2$ for very low Reynolds number, and $\tau_{life} \sim R^{3/2}$ for high Reynolds number. This indicates that the dependence of the droplet lifetime on droplet size decreasing with increasing Reynolds number. Therefore, disadvantage of large droplet size in DT is offset by the strong convective environment. If the ambient temperature is high enough to prompt vaporisation, the convective ambient condition enables to accelerate the vaporisation process further. Since the flow in motion has more energy than the slowly moving vapour at the droplet surface, the ambient convective flow increase the vaporisation by both reducing the concentration of vapour at the droplet surface as well as inducing shear forces that in turn cause liquid circulation to enhance the droplet heating process and hence faster vaporisation. Since the tests in §7 show a faster vaporisation rate for higher ambient temperature and pressure conditions, high convective ambient condition will contribute to further accelerate the evaporation process so that the droplet lifetime will be reduced dramatically.

8.2.2. Effect of ambient temperature and pressure on vaporisation

Although the effect of high ambient temperature on the rate of droplet evaporation is well established, modelling the combined effect of high ambient temperature and ambient pressure, in particular, passed the critical values of the fuel has been a challenging problem. The recognition of this complexity only allows the study of decoupled problems in order to isolate limited sets of issues. Consequently, the focus of this investigation was focused on one of the most essential aspects of the evaporation process, namely, the nature of percentage vapour composition production at the droplet surface by employing LP and HP vapour-liquid equilibriums. The vapour fuel at the droplet surface is believed to have a strong influence on the entire combustion process. Liquid fuels do not burn, but vapour fuels do, and the mode of vaporisation and mixing controls the stability and leanness of the combustion process.

The LP formulation described by equation $(4-32_a)$ is a limiting case of the well established combined vapour-liquid equilibrium (CVLE) method, which is a preferred option at low pressure conditions for its computational efficiency. Although the CVLE method is highly accurate and computationally expensive for conditions other than the low-pressure limiting conditions, it has not been applied in spray combustion related modelling. Therefore, further investigation is required to establish its validity in this case. From equation $(4-32_a)$, it is easy to observe that the introduction of the unity correction factor $\Im_j$ implies uniformity in the activity coefficients of all components of the mixture, which is valid only for ideal mixtures. Therefore, the method can not represent the partial vapour pressures correctly if the pressure is elevated. From that perspective, the LP formulation can not represent the true dependence of the fuel mixture on the ambient temperature and pressure, although the boiling temperature is related to the vapour pressure as in equation $(A4-7_a)$. The boiling temperature, it must be pointed out, is in turn dependent on the PDF mean, but not the 0th-fractional composition distribution moment. Therefore, it only shows a nearly linear relationship with both temperature and pressure, failing to take into consideration the compositional evolution and the changes in the thermotransport properties. Although temperature has the effect of accelerating vaporisation, the numerical results presented in §7 demonstrated that the ambient pressure to have a much greater effect on the vaporisation process, in particular, when a comparison between the LP and HP formulations are employed. Since the LP formulation is assumed redundant for pressures not close to atmospheric conditions, only the results from the HP formulations will be discussed here.

The HP formulation is based on a rigorous derivation, which employs a general cubic equation of state (CEOS) with various mixing and combining rules. It takes pressure, temperature, and composition into account. Clearly, for conditions above the critical point, the contribution of the ambient pressure and temperature in accelerating vaporisation is limited, although it has significant contribution for values below the critical point, and τ_{life} decays nearly exponentially with T^{∞} and P^{∞}. Therefore, for faster vaporisation, operation close to or within the range of the fuel critical points is expected to speed up vaporisation by reducing the droplet life time.

8.2.3. Effects of variable thermotransport properties on liquid models

The treatment of droplet evaporation and the transport of vapour mixture under the assumption of variable thermotransport properties will have a far reaching implication if the correlations of these thermotransport properties are conducted in a non-linear and accurate manner. In this study, the thermotransport properties, in the most part, are linearly correlated with composition, while it suitably maintains either linear or non-linear relationship with temperature and pressure. For example, the behaviour of vaporisation at low temperature (BT condition), is not as complex as when the temperature and pressure are raised. This is because the non-linear relationship between thermotransport properties with temperature, while it evolves linearly with composition. A complete assessment on the effect of variable thermotransport properties is beyond the scope of this work. However, the temperature, droplet surface regression and the composition evolution suggest a distinctive behaviour which is most likely due to the introduction of the thermotransport properties.

8.2.4. Effect of high pressure on Liquid Mass Diffusion

The numerical test results clearly affirm that the importance of casting multicomponent droplet evaporation under the HP formulation, where the determination of the droplet vaporisation rate and the droplet surface temperature must be carried out using an appropriate equation of state. In particular, when the pressure is so great and surpasses the critical pressure of the liquid, the sub-critical LP models are not applicable.

When a liquid droplet is immersed in a hot supercritical quiescent environment, due to conduction heating, the droplet diameter is expected to swell corresponding to an increase in temperature, which in turn reduces the liquid density. On the other hand, the opposite effect is induced on liquid density due to high ambient pressure, although liquid compressibility is insignificant compared to gasses. However, the non-uniformity of density inside the droplet must be taken into account and hence liquid convection must be considered. Most of this process contributed for the profiles observed both in Figures 7.8 and 7.14. In such situation, like the test in the regime of the LPP operating conditions, temperature rises until it reaches close to the critical temperature value, during which, the mixture composition on either side of the liquid-vapour interface is imposed by chemical equilibrium, where mass diffusion occurs in the droplet. In a competing environment of high temperature and high pressure situation, the droplet vaporisation is accelerated due to mixing with the ambient. If both the temperature and pressures are in transcritical-supercritical regimes, the surface tension will be reduced dramatically. However, in all the plots for the droplet surface temperature, although there is a trend for the wet-bulb temperature to rise towards the critical temperature of the liquid with increase in the ambient temperature and pressure, at no time it reaches the critical point, even during supercritical conditions.

8.3 Compositional Variations during Vaporisation

The investigations both at convective and stagnant conditions provided various profiles of the mixture composition that enable to characterise the vaporisation behaviour in detail. In particular, rather than following the time histories of relative (fractional) compositions alone, the CT formulation introduced the actual evolution of the fuel composition in groups of homologues.

In general, two major observation can be derived from the composition profile descriptions in §6 and §7. The first observation is in relation to the qualitative behaviour of the composition profile in the presence and absence of ambient convection. The second observation relates to the mode of composition depletion or accumulation with regard to the PDF shape.

In the presence of ambient convection, the qualitative behaviour of the composition profile is dependent on the convective strength. The liquid PDF mean for BT (Figure 6.4) and the liquid PDF for DT (Figure 6.24) evolve appreciably differently. Similarly, the vapour PDF mean for BT and DT evolve differently (Figures 6.5 and 6.24), so do the liquid and vapour PDF variances (Figures 6.6, 6.7 and 6.25). In particular, the time histories for the BT 0th-fractional composition moments of the liquid phase (Figure 6.14) and the vapour phase (Figure 6.15) show a remarkable difference with those of the DT (Figure 6.30). In fact, this is not a surprising result when one looks on the theoretical details of the proposed models. In particular, the rate of vaporisation and the Sherwood number correction for the spherically symmetric assumption of the model through Clift et al (1978) correlation (equations $(3-21)$ and $(3-45)$) are directly dependent on the Reynolds number, and hence with the convective strength. What is worth mentioning is the behaviour of the mixing that would result in practical application. When turbulence dominates mixing, it will be interesting to establish the intimate link that will arise between the composition PDF profiles and the convective strength. In the absence of ambient convection, the 0^{th}-fractional composition distribution moments and to a lesser extent the PDF mean and variances both for the liquid and vapour phase show a remarkably similar qualitative behaviour (Figures 7.9 and 7.10).

However, irrespective of the ambient conditions, all the composition profiles portray three distinct vaporisation behaviours. These are the vaporisation cases of (a) minor components with relatively lower boiling point temperatures that occupy the left end of the distribution, (b) major components with relatively moderate boiling point temperatures that occupy the majority of the middle of the distribution, and (c) minor components with relatively high boiling temperatures that occupy the right end of the distribution. In all classes of the numerical tests carried out in this investigation (BT and DT in §6 and the model comparisons in §7), the predictions reveal that the volatile minor components (case a) vaporise first followed by the major fuels (case b), while the minor heavy components (case c) vaporise last, except for the BT where the ambient condition was not high enough to deplete these components. In fact, the profiles of both the droplet surface temperature and the droplet surface regression follow the same behaviour, where the primary and secondary heating periods (with simultaneous evaporation) coinciding with the minor components while the major components coincide with the period of the droplet equilibrium temperature.

The distinctive vaporisation behaviour of each homologue confirms that complex mixtures like fuel JP8 require multiple PDF representation. In addition, it will be interesting to see how the distinctive vaporisation behaviour of these homologues will affect practical spray evaporation and combustion simulation, and its ability to predict conditions for ignition and flame propagation.

CONCLUSIONS AND FUTURE WORKS

A new approach for modelling the evaporation of multicomponent complex mixtures is developed with the aim of applying it in practical spray combustion simulations of advanced gas turbine combustors. The model employs the theory of continuous thermodynamics to represent the mixture composition using multiple probability density functions. This enables one to more accurately capture the entire range of compositions that constitute commercial fuels, which includes hundreds and thousands of discrete components.

The theoretical analysis and the numerical investigations for an isolated droplet at various ambient temperature, pressure, and convective conditions reveal the versatility and richness of the new approach in providing accurate representation of the fuel evaporation behaviour.

The investigation considered three liquid models in conjunction with the simple LP phase equilibrium formulation and the more detailed HP phase equilibrium formulation that employs a general cubic equation of state. Based on the extensive literature survey, the mathematical and numerical model development, and the model validation carried out in this investigation, the following observations and conclusions are made.

- For ambient pressures close to the atmospheric and with ambient temperature ranging from low-high, but high enough to vaporise the fuel, the low-pressure (LP) and high-pressure (HP) vapour liquid equilibrium (VLE) formulations in conjunction with all the three models performed nearly equally. However, for slower rate of evaporation, the MWMM with its LP variant is a preferred option both for its accuracy and computational efficiency.
- At elevated-high ambient pressures with a corresponding ambient temperature high enough to vaporise the fuel, the LP formulation predictions using all the three models deteriorated with increasing pressure due to the gas-phase non-idealities, while the predictions with the HP variant employing either of the three

models at all pressures gave very good to excellent agreements with available experimental data in the literature. In addition, the LP formulation predicted the droplet lifetime incorrectly.

- Droplet lifetime increases with pressures when the ambient temperature is low-moderate, while it shows the opposite effect for high temperatures. This is due to the fact that in the final stages of evaporation the factor determining the phase equilibrium is switched from the ambient pressure to the droplet's temperature and the latent heat of vaporisation is reduced by an increase in the droplet's temperature, where the effect is more amplified at high temperature.
- The theoretically expected relative prediction behaviours of the three models is poor for low-elevated ambient temperature and pressure condition, but excellent relative profiles and agreements with experimental data is observed at high ambient temperatures and pressures. This is in particular a case in point for the MEDM, where the diffusivity enhancement factor is very low and its contribution insignificant when the ambient conditions are not very high and the droplet is in a quiescent environment.
- The accuracy of the predictions is highly dependent more on the phase equilibrium (LP or HP) and the thermotransport properties employed than on the liquid models used, although further investigation is required, for example - in practical spray simulation, to establish its dependence on other factors.
- The distinctive vaporisation behaviour of each homologue suggests that multicomponent fuels can not be represented using single or binary fuels. In particular, the vaporisation behaviour is highly dependent both on the volatility differential of the fuel that can be only represented by a boiling temperature curve rather than a single boiling point as well as a latent heat of vaporisation curve that determines the vaporisation histories while the droplet is at its quasi-steady (wet-bulb) temperature.

Although this investigation developed models that could be used to represent practical multicomponent fuels, and it also identified various important issues that must be considered in this type of modelling exercises, the following points are believed to be key in furtherance the work.

- Detail experimental data for real commercial fuels incorporating the measurement of not only the usual droplet temperature and droplet surface regression, but more importantly, the vapour composition and the liquid internal temperature must be carried out. Since measuring the composition of commercial fuels with hundreds and thousands of components is a likely impossible task, the homologue based model developed here could be used as a guide to device measurement techniques on homologue basis. The liquid internal temperature profile measurement will be an important step to understand the distinction, if there is any, between the various liquid models proposed in the literature and the salient processes that affect the vaporisation process. If possible, such experiments would be most useful if conducted in more than one of the three regimes: (a) quiescent conditions without natural convection (e.g. microgravity condition) and with natural convection (e.g. drop hanging on a quartz fibber), (b) forced convection both as single droplet and practical sprays at various pressures and temperatures, in particular, close to the operating conditions of practical combustion devices.
- In the presence of comprehensive experimental data, the developed models can further be investigated for their accuracy and efficiency and must be extended for practical applications and implemented into multidimensional codes. It is suggested, however, models that account for the liquid (spray) flow and transport, including spray jet break-up, atomisation, droplet-break, droplet coalescence, droplet dispersion, and droplet vaporisation must be developed as a separate module from the main gas-phase solver using a generic framework as intended in AMOLBSC. This will enable for the spray code to be easily portable and could be interfaced and tested with various gas-phase codes.
- Finally, since the CT formulation developed in this investigation is also applicable both for continuous and semi-continuous mixtures of hydrocarbons, polymers, and functional materials, it will be interesting to investigate its applicability in that area, for example – using a Lagrangian volume averaged technique to model sprays with better computational efficiency.

REFERENCES

Abramovitz, M., and I. A., Stegun (1972). Handbook of Mathematical Functions, Dover Publications, New York.

Abramzon, B., and W. A. Sirignano (1989). Droplet vaporisation model for spray combustion calculations. Intl. J. heat-Mass Trans. 32 (9) : 1605-1618.

Acrovis, A., and T. D. Taylor, (1962). Heat and Mass Transfer from Single Spheres in Stokes Flow, Phys. Fluids 5: 387-394

Adjerid, S. and J. E. Flaherty (1986). A moving-mesh finite element method with local refinement for parabolic partial differential equations, Comp. Methods Appl. Mech. Engrg. 55 : 3-26.

Adjerid, S., J.E. Flaherty, P.K. Moore and Y. Wang (1992). High-order adaptive methods for parabolic systems, Phys.D 60 : 94-111.

Aggarwal, S. K. (1987). Modelling of a Dilute Vaporising Multicomponent Fuel Spray. Int. J. Heat & Mass Trans. 30 : 1949-1961.

Aggarwal, S. K., and F. Peng (1995). A review of droplet dynamics and vaporisation modelling for engineering calculations. J. Eng. Gas Turb. Power, 117 : 453-461.

Aggarwal, S. K., A. Y. Tong, and W. A. Sirignano (1984). A Comparison of Vaporisation Models in Spray Calculations. AIAA J. 22 (10) : 1448-1457.

Arcoumanis, C., M. Gavaises, and B. French (1997). Effect of Fuel Injection Processes on the Structure of Diesel Sprays, SAE Technical Paper 970799.

Aris, R., and G. R. Gavalas (1966). On the Theory of Reactions in Continuous Mixtures. Phil. Trans. Roy. Soc. A. 260 : 351-393.

Ascher, U., and R. D. Russell (1981). Reformulation of boundary value problems into "standard " form, SIAM Review , 23:238 –254.

Ascher, U., R.M.M Mattheij, and R.D.Russell (1995), Numerical Solution of Boundary Value Problems for Ordinary Differential Equations, SIAM, Philadephia.

Balakrishnan, N., and J. Wang (2000). Simple efficient estimation for the three parameter gamma distribution, J. Statistical Planning & Inference 85: 115-126.

Balakrishnan, N. (2001). Personal Communication.

Bardon, M. F., J. E. D. Gauthier, and V. K. Rao (1990). Flame Propagation through Sprays of Multicomponent Fuel.; J. Inst. Energy, 63 : 53-60.

Bellan, J., and K. Harstad (1987a). Analysis of the Convective Evaporation of Nondilute Clusters of Drops. Int. J. Heat & Mass Trans. 30(1) : 125-136.

Bellan, J., and K. Harstad (1987b). The Details of the Convective Evaporation of Dense and Dilute Clusters of Drops. Int. J. Heat & Mass Trans. 30(6): 1083-1093.

Bellan, J., and M. Sommerfeld (1978). Theoretical Examination of Assumptions commonly used for the Gas Phase Surrounding a Burning Droplet. Comb. Flame. 33: 107-122.

Berlemont, A., M. S. Grancher, and G. Gouesbet (1995). Heat and Mass Transfer Coupling between Vaporising Droplets and Turbulence using a Lagrangian Approach. Int. J. Heat & Mass Transfer, 38 (16) : 3023-3034.

Berzins, M., P. J. Capon, and P. K. Jimack (1998). On spatial adaptivity and interpolation when using the method of lines, Appl. Num. Math. 26: 117-133.

Bieterman, M., and I. Babuska, (1986). An adaptive method of lines with error control for parabolic equations of the reaction-diffusion type. J. Comp. Phys. 63: 33-66.

Bird, R. B., W. E. Stewart, and E. N. Lightfoot (1960). Transport Phenomena. Wiley, New York.

Botella, O., (2002) On a collocation B-spline method for the solution of the Navier–Stokes equations. Comput. Fluids 31 (2002), pp. 397–420.

Bowman, K.O., L. R. Shenton (1988). Properties of Estimators for the Gamma Distribution. Marcel Dekker, New York.

Chang, K-C., and J-C. Yang (1999). Unsteady Drag Consideration in Stochastic Eulerian-Lagrangian Formulation of Two-Phase Flow. AIAA J. 37(4) : 435-442.

Chiang, C. H., M. S. Raju, and W. A. Sirignano (1992). Numerical Analysis of Convecting, Vaporising Fuel Droplets with Variable Properties. Int. J. Heat & Mass Trans., 35 (5) : 1307 – 1324.

Chen, G., S. K. Aggarwal, T. A. Jackson, and G. L. Switzer (1997). Experimental study of pure and multicomponent fuel droplet evaporation in a heated-air flow. Atom. Sprays. 7 : 317-337.

Chen, C. S., and M. M. El-Wakil (1969). Experimental and Theoretical Studies of Burning Drops of Hydrocarbon Mixtures. Proc. Instn. Mech. Engrs. 184 (3J) : 95-108.

Chou, G. F., and J. M. Prausnitz (1986). Adiabatic Flash calculations for Continuous or Semi-Continuous Mixtures using an Equation of State. Fluid Phase Equilb. 30 : 75-82.

Clewell, H. J., (1980). Evaporation and Ground-Fall of JP-4 Jet Fuel from USAF Aircraft-III. ESL-TR-80-56, Air Force Engineering Services Centre, AFB, FL.

Clewell, H. J., (1983). Ground Contamination by Fuel Jettisoned from Aircraft. J Aircraft, 20 : 382-384.

Clift, R., J. R. Grace, and M. E. Weber (1978). Bubbles, Drops, and Particles. New-York, Academic Press.

Cohen, A. C., and N. J. Norgaard (1977). Progressively censored sampling in the three-parameter gamma distribution. Technometrics 19:333–340.

Cohen, A.C., B. J. Whitten (1982). Modified moment and maximum likelihood estimators for parameters of the three-parameter gamma distribution. Commun. Stat. Simulation Comput. 11: 197-216.

Cohen, A.C., B. J., Whitten (1986). Modified moment estimation for the three-parameter gamma distribution. J. Quality Tech. 18: 53-62.

Cotterman, R. L., R. Bender, and J. M. Prausnitz (1985). Phase Equilibria for Mixtures Containing Very Many Components : Development and Application of Continuous Thermodynamics for Chemical Process Design. Ind. Engng. Chem. Process Design. 24 : 194-203.

Cotterman, R. L., and J. M. Prausnitz (1985). Flash Calculations for Continuous or Semicontinuous Mixtures Using an Equation of State. Ind. Eng. Chem. Process Des. Dev., 24 : 434-443.

Crocco, L., and S. I. Cheng (1956). Theory of Combustion Instability in Liquid Propellant Rocket Motors, Sci. Tech. 1: 9-18.

Crowe, C. T., T. R. Troutt, and J. N. Chung (1996). Numerical Models for Two-Phase Turbulent Flows, Ann. Rev. Fluid Mech., 28 : 11-43.

Crowe, C. T., M. Sommerfeld, and Y. Tsuji (1998). Multiphase Flows with Droplets and Particles, CRC Press, Boca Raton, FL.

Delplanque, J. P., and W. A. Sirignano (1995). Transcritical Vaporisation and Combustion of LOX Droplet Arrays in a Convective Environment, Comb. Sci. Tech. 105 : 327-344.

Diaz, J. C., G. Fairweather, and P. Keast (1983). FORTRAN packages for solving certain almost block diagonal linear systems by modified alternate row and column elimination, ACM Trans. Maths. Softw. 17: 153-166.

Dwyer, H. A., P. Stapf, and R. Maly (2000). Unsteady Vaporisation and Ignition of a Three-Dimensional Droplet Array, Comb. and Flame, 121 : 181-194.

Elghobashi, S., and G. C. Truesdell (1993). Direct Simulation of Particle Dispersion in a Decaying Isotropic Turbulence, J. Fluid Mech. 242 : 655-700.

El Wakil, M. M., R. J. Priem, H. J. Brikowski, P. S. Myers, and O. A. Uyehara. (1956). NACA TN 3490.

Faeth, G. M. (1977). Current Status of Droplet and Liquid Combustion. Prog. Energy Comb. Sci. 3: 191-224.

Faeth, G. M. (1983). Evaporation and Combustion of sprays. Prog. Energy Comb. Sci. 9 : 1-76.

Faeth, G. M. (1987). Mixing, Transport and Combustion in Sprays. Prog. Energy Comb. Sci. 13 : 293-345.

Faeth, G. M., L. P. Hsiang, and P. K. Wu (1995). Structure and Breakup Properties of Sprays, Int. J. Multiphase Flow, 21:99-127.

Fairweather, G., (1973). Finite Element Galerkin Methods for Differential Equations, Marcel Dekker, Inc., New York,1973.

Fairweather G, Meade D. A survey of spline collocation methods for the numerical solution of differential equations. In: Diaz JC, editor. Mathematics for large scale computing. Lecture notes in pure and applied mathematics, vol. 120. New York: Marcel Dekker; 1989.

Frank-Kamenetskii, D. A. (1969). Diffusion and Heat Transfer in Chemical Kinetics, (2nd Edn) Plenum Press, New York.

Frossling, N., (1938). Evaporation of Falling Drops, Gerl. Beitr. Geophysics 52 : 170.

Ganesh, M., and I. H. Sloan (1999). Optimal order spline methods for nonlinear differential and integro-differential equations, Appl Num Math 29: 445 –78.

Gal-Or, B. (2005). Borderless, Multidisciplinary Thermodynamics, Editorial Review: Continuous Thermodynamics Series, Int. J. of Turbo & Jet Eng. (in press).

Gal-Or, B., H. T. Cullinan, and R. Galli (1975). New Thermodynamic Transport Theory for Systems with Continuous Component Density Distributions. Chem. Engng. Sci. 30 : 1085-1092.

Givler, S. D., and J. Abraham (1996). Supercritical Droplet Vaporisation and Combustion Studies, Prog. Energy. Comb. Sci. 22 : 1-28.

Godsave, G. A. E. (1953). Burning of Fuel Droplets. Fourth Symposium (International) on Combustion, 818-830.

Gouesbet, G., and A. Berlmont (1999). Eulerian and Lagrangian Approaches for Predicting the Behaviour of Discrete Particles in Turbulent Flows. Prog. Energy Comb. Sci. 25 : 133-159.

Gupta, A. K., (1997). Gas Turbine Combustion: prospects and Challenges. Energy Convers. Mgmnt., 38(10-13) : 1311-1318.

Hallett, W. L. H. (2000). A Simple Model for the Vaporisation of Droplets with Large Numbers of Components. Comb. Flame, 121 : 334-344.

Hallett, W. L. H., and M. A. Ricard (1992). Calculations of the Auto-Ignition of Liquid Hydrocarbon Mixtures as Single Droplets. Fuel 71: 225-229.

Hansen, J. P., and I. R. McDonald (1976). Theory of Simple Liquids, Academic Press, New York.

Harstad, K. G., Le Clercq, P. C., and Bellan, J., (2003). Statistical Model of Multicomponent-Fuel Drop Evaporation for Many-Drop Flow Simulations. AIAA J. 41 (10): 1858-1874 (October).

Haywood, R. J., M. Renksizbulut, and G. D. Raithby (1994). Transient deformation and evaporation of droplets at intermediate Reynolds numbers, Int. J. Heat Mass Transfer, 37 (9): 1401-1409.

Hindmarsh, A. C. (1976). Preliminary documentation of GEARIB: Solution of mplicit systems of ordinary differential equations with banded Jacobian, Technical Report UCID-30130, Lawrence Livermore National Laboratory.

Hindsmarsh, A. C. (1983). ODEPACK,: a systematized collection of ODE solvers. In Sci. Computing, (R. Stepleman, et al. Eds.), IMACS/North-Holland Pub. Co.

Hirose, H., (1995). Maximum likelihood parameter estimation in the three parameter gamma distribution, Comp. Stat & Data Analy. 20 : 343-354.

Holderbaum, T., and J. Gmehling (1991). PSRK: A Group Contribution Equation of State Based on UNIFAC, Fluid Phase Equilibria, 70 : 251-265.

Hu, Y., X. Ying, D. T. Wu, and J. M. Prausnitz (1995). Continuous Thermodynamics for Polydisperse Polymer Solutions. Fluid Phase Equilibria. 104 : 229-252.

Hubbard, G. L., V. E. Denny, and A. F. Mills (1975). Droplet Evaporation: Effects of Transients and Variable properties. Intl. J. Heat-Mass Transfer. 18 : 1003-1008.

Johns, L. E. and R. B. Beckman (1966). Mechanism of Dispersed-Phase Mass Transfer in Viscous, Single-Drop Extraction System. AIChE J, 12 : 10-16.

Johnson, N. J., and S. Kotz, (1970).Continuous Univariate Distribution–I.Wiley, New York.

Kehlen, H., M. T. Ratzsch, and J. Bergmann (1985). Continuous Thermodynamics of Multicomponent Systems, AIChE. J., 31: 1136-1148.

Kneer, R., M. Schneider, B. Noll, and S. Wittig (1993). Diffusion Controlled Evaporation of a Multicomponent Droplet: Theoretical Studies on the Importance of Variable Liquid Properties. Int. J. Heat & Mass Trans. 36(9) : 2403-2415.

Kumagai, S., and H. Isoda (1957).Combustion of Fuel Droplets in a Falling Chamber. Sixth Symposium (International) on Combustion, 726.

Kumagai, S., T. Sakai, and S. Okajima (1971). Combustion of Free Fuel Droplets in a Freely Falling Chamber. Thirteen Symposium (International) on Combustion, 779.

Kuo, K. K. (1986). Principles of Combustion. John Wiley, New York.

Lara-Urbaneja, P., and W. A. Sirignano (1981). Theory of Transient Multicomponent Droplet Vaporisation in a Convective Field, Proc. Combust. Inst. 18 : 1365-1374.

Law, C. K. (1976a). Unsteady Droplet Combustion with Droplet Heating. Comb. Flame, 26 : 17-22

Law, C. K. (1976b). Multicomponent Droplet Combustion with Rapid Internal Mixing. Comb. Flame, 26 : 219-233.

Law, C. K., (1977). A Model for the combustion of Oil/Water Emulsion Droplets, Comb. Sci. Techn. 17: 29-38.

Law, C. K., and H. K. Law (1977). Theory of Quasi-Steady One-Dimensional Diffusional Combustion with Variable Properties Including Distinct Binary Diffusion Coefficients. Comb. Flame, 29 : 269-275.

Law, C. K. (1982). Recent Advances in Droplet Vaporisation and Combustion. Prog. Energy Comb. Sci. 8 : 171-201.

Law, C.K., Prakash, S., and W. A. Sirignano (1977).Theory of Convective, Transient, Multicomponent Droplet Vaporisation, Proc. Combust. Inst. 16 : 605-617.

Law, C. K., and W. A. Sirignano (1977). Unsteady Droplet Combustion with droplet Heating II: Conduction Limit. Comb. Flame, 28 : 175-186.

Leimkuhler, B., L. Petzold, and C. W. Gear (1991). Approximation methods for the consistent initialisation of differential-algebraic equations, SIAM, J. Numer. Analy., 28: 205-226.

Libby, P. A., and F. A. Williams (1994). Turbulent Reacting Flows. Academic Press.

Loth, E., (2000) Numerical approaches for motion of dispersed particles, droplets and bubbles. Prog. Energy. Comb. Sci. 26, 161-223.

Maru, W-A., and J. B. Moss (2003). Modelling Multicomponent Fuel Spray Evaporation Using Multiple PDFs, Proc. European Comb. Meeting, Orleans, France.

Maurice, L. Q., H. Lander, T. Edwards, and W. E. Harrison III (2001). Advanced Aviation Fuels: a look ahead via a historical perspective, Fuel, 80: 747-756.

Maxey, M. R., and J. J. Riley (1983). Equation of Motion of a Small Rigid Sphere in Non-Uniform Flow. Phys. Fluids. 26 : 883-889.

Miller, K., (1981). Moving Finite Elements – II, SIAM J. Num. Analy. 18: 1033-1057.

Miller, R. S., K. Harstad, and J. Bellan (1998). Evaluation of Equilibrium and Non-Equilibrium Evaporation Models for Many-Droplet Gas-Liquid Flow Simulation. Int. J. Multiphase Flow, 24 : 1025 – 1055.

Mitchell, A. R., (1980). The Finite Difference Method in Partial Differential Equations , Wiley, New York.

Moore, P. K., (1995). Comparison of adaptive methods for one dimensional parabolic systems, Appl. Numer.Math.16 : 471–488.

Moore, P. K., (2001). Interpolation error-based a posteriori error estimation for two-point boundary value problems and parabolic equations in one space dimension, Numer. Math, 90 : 149–177.

Muhlbaur, A. L., and J. D. Raal (1995). Computation and thermodynamic interpretation of high-pressure vapour-liquid equilibrium – a review, The Chem. Eng. J., 60 :1-29.

Newbold, F. R., and N. R. Amundson (1973). A model for Evaporation of a Multicomponent Droplet. AIChE J. 19 : 22-30.

Nowak, U., J., Frauhammer, and U. Nieken, (1996). A fully adaptive algorithm for parabolic differential equations in one space dimension. Computers in Chemical Engineering, 20 : 547-561.

Okajima, S., and S. Kumagai (1974). Further Investigation of Combustion of Free Droplets in a Freely Falling Chamber Including Moving Droplets. Fifteen Symposium (International) on Combustion.

Orbey, H., and S. I. Sandler (1995). AIChE J., 41(3) : 683

Pang, W-K., S-H., Hou, B-W. T., Yu, and K-W. K., Li (2004). A simulation based approach to the parameter estimation of the three-parameter gamma distribution, Euro. J. Operation. Research, 155 : 675-682.

Petzold, L. R., (1982). A description of DASSL: A differential/algebraic system solver, Technical Report, Sandia Labs, Livermore, CA.

Polling , B. E., J. M. Prausnitz, and J. P. O'Connell (2000). The Properties of Gases and Liquids, 5th Edn, McGraw-Hill, New York.

Prakash, S., and W. A. Sirignano (1975). Preliminary analysis of a fuel droplet in a convective field, Central and Western State Section Meeting/Combustion Institute, San Antonio (preprint).

Prakash, S., and W. A. Sirignano (1978). Liquid Fuel Droplet Heating with Internal Circulation. Int. J. Heat & Mass Trans. 23(3) : 253-268.

Prakash, S., and W. A. Sirignano (1980). Theory of Convective Droplet Vaporisation with Unsteady heat Transfer in the Circulating Liquid Phase. Int. J. Heat & Mass Trans. 21 : 885-895.

Prommersberger, K., G. Maier, and S. Wittig (1998). Validation and Application of a Droplet Evaporation Model for Real Aviation Fuel, Proceedings of NATO-RTO Meeting on Gas Turbine Engine Combustion, Emissions and Alternative Fuels, Lisbon, Portugal, 12-16 October.

Rah, S-C., A. F. Sarofim, and J. M. Beer (1986). Ignition and Combustion of Liquid Fuel Droplets. Part II-Ignition Studies. Comb. Sci. Tech. 49 : 169-184.

Raju, M. S., and W. A. Sirignano (1989). Spray Computations in a Centerbody Combustor, J. Eng. Gas Turbines Power 1 : 710-718.

Raju, M. S., and W. A. Sirignano (1990). Multicomponent Spray Computations in a Modified Centerbody Combustor, J. Eng. Gas Turbines Power 6 :97-105.

Rangel, R. H., and W. A. Sirignano (1988). Unsteady Flame Propagation in a Spray with Transient Droplet Vaporisation, Proc. Comb. Inst. 22 : 1931-1939.

Ranz, W. E., and W. R. Marshall (1952). Evaporation from Drops. Chem. Engng. Prog. 48 : 141-173.

Ratzsch, M. T., and H. Kehlen (1983). Continuous Thermodynamics of Complex Mixtures. Fluid Phase Equilibria, 14 : 225-234.

Renksizbulut, M., and R. J. Haywood (1988). Transient droplet evaporation with variable properties and internal circulation at intermediate Reynolds numbers. Intl. J. Multiphase Flow. 14(2) : 189-202.

Renksizbulut, M., and M. C. Yuen (1983). Experimental Study of Droplet Evaporation with Variable Properties and Internal Circulation at Intermediate Reynolds Numbers. Int. J. Multiphase Flow, 14 : 189.

Runge, T., M. Teske, C. E. Polymeropoulos (1998). Low-Temperature Vaporisation of JP-4 and JP-8 Fuel Droplets, Atomisation and Sprays, 8 : 25-44.

Saad, M. A., and G. J. Antonides (1975). Temperature distribution in a vaporizing droplet with internal heat generation, Comb. and Flame, 25: 79-84.

Salacuse, J. J., and G. J. Stell (1982). J. Chem. Phys, 77 : 3714.

Schlichting, H., (1979). Boundary Layer Theory, 7th Edn, McGraw-Hill, New York.

Schmehl, R., H. Rosskamp, M. Willmann, and S. Wittig (1999). CFD analysis of spray propagation and evaporation including wall film formation and spray/film interactions. Int. J. of Heat and Fluid Flow, 20 : 520-529.

Madsen, N., K., and R. F. Sincovec (1979). Software for nonlinear partial differential equations, ACM Trans. Math. Software, 1: 232-263.

Sirignano, W. A. (1978). Theory of Multicomponent Fuel Droplet Vaporisation. Archives of Thermodynamics and Combustion. 9 : 231-247.

Sirignano, W. A. (1983). Fuel Droplet Vaporisation and Spray Combustion. Prog. Energy Comb. Sci. 9 : 291-322.

Sirignano, W. A. (1985) Linear Model of Convective Heat Transfer in a spray. Recent Advances in Aerospace Science, C. Casici (Edr.), Plenum, New York.

Sirignano, W. A. (1993). Fluid Dynamics of Sprays – 1992 Freeman Scholar Lecture, J. Fluids Eng. 115 : 345-378.

Sirignano, W. A. (1999). Fluid Dynamics and Transport of Droplets and Sprays. Cambridge University Press.

Sirignano (2003) Personal communication.

Spalding, D. B. (1953). The Combustion of Liquid Fuels. Fourth Symposium (International) on Combustion. 847-864.

Sparrow, E. M., and J. L. Gregg (1957). The Variable Fluid Property Problem in Free Convection, Trans. ASME, paper No. 57-A-46 : 879-886.

Tamim, J., and W. L. H. Hallett (1995). A Continuous Thermodynamics Model For Multicomponent Droplet Vaporisation. Chem. Eng. Sc., 50(18) : 2933-2942.

Toikka, A. M., and J. D. Jenkins (2002). Conditions of thermodynamic equilibrium and stability as a basis for the practical calculation of vapour–liquid equilibria, Chem. Eng. J. 89(1-3): 1-27.

Tolpadi, A. K., S. K. Aggarwal, and H. C. Mongia (2000). An advanced spray model for applications to the prediction of gas turbine combustor flow fields, Numerical Heat Transfer A: 38, 325-340.

Tong, A. Y., and W. A. Sirignano (1982a). Transient Thermal Boundary Layer in Heating of Droplet with Internal Circulation: Evaluation of Assumptions. Comb. Sci. Tech. 11 : 87-94.

Tong, A. Y., and W. A. Sirignano (1982b). Analytical Solutions for Diffusion and Circulation in a Vaporising Droplet. Nineteenth Symposium (International) on Combustion. 1007-1020.

Tong, A. Y., and W. A. Sirignano (1983). Analysis of Vaporising Droplet with Slip, International Circulation and Unsteady Liquid Phase and Quasi-Steady Heat Transfer. ASME-JSME Thermal Joint Engineering Conference.

Tong, A. Y., and W. A. Sirignano (1986a). Multicomponent Droplet Vaporisation in a High Temperature Gas. Comb. Flame. 66 : 221-235.

Tong, A. Y., and W. A. Sirignano (1986b). Multicomponent Transient Droplet Vaporisation with Internal Circulation: Integral Equation Formulation and Approximation Solution. Num. Heat Trans. 10 : 253-278.

Torres, D. J., P. J. O'Rourke, and A. A. Amsden (2003). Efficient multicomponent fuel algorithm, Comb. Theory and Modelling 7 : 67-86.

Vande Wouwer, A., Ph. Saucez, and W. E. Schiesser (2001). Adaptive Method of Lines, Chapman & Hall / CRC.

Vargaftik, N. B., (1975). Tables on the Thermophysical properties of Liquids and Gases, Hemisphere Publishing Corp.

Waldman, C. H. (1974). Fifteen Symposium (International) on Combustion.

Wang, R. (1999). High Order Adaptive Method of Lines for 1D Parabolic Equations, M.Sc. Thesis, Dalhousie University, Halifax, Canada.

Wang, K-Y., D. E. Shallcross, P. Hadjinicolaou, and C. Giannakopoulos (2002). An efficient Chemical System Modelling Approach, Env. Modelling & Software, 17 : 731-745.

White, A. B., (1979). On the selection of equidistributing meshes for two-point boundary value problem, SIAM J. Num. Analy. 16 : 472-502.

White, F. M. (1991). Viscous Fluid Flow, McGraw-Hill, New York.

William, B., and A. S. Teja (1988). Characteristic Viscosity as a third parameter in corresponding states calculations of transport properties: Part II-Undefined Mixtures, The Chem. Eng. J. 37 : 71-78.

Williams, F. A., (1965). Combustion Theory, Addison-Wesley Publishing Co.

Williams, F. A., (1973). Combustion of Droplets of Liquid Fuels: A Review. Comb. Flame. 21 : 1-31.

Williams, F. A., (1976). Fundamentals of Oil Combustion. Prog. Energy. Comb Sci. 2 : 167-179.

Williams, F. A., (1985). Combustion Theory, 2nd Edn., The Benjamin/Cummings Publishing Co.

Wolpert, D. H., and W.G. Macready (1997). The no free lunch theorem. IEEE Trans. Evolutionary Computing. 1(1) : 67–82.

Yang, V., (2001). Liquid Propellants Droplet Combustion and Cluster behaviour at supercritical Conditions, AFOSR-F49620-98-10034 (preprint).

Yuen, M. C., and L. W. Chen (1976). On Drag of Evaporating Droplets. Comb. Sci. Technol. 14 : 147-154.

Zhu, G-S., and S. K. Aggarwal, (2000). Transient supercritical droplet evaporation with emphasis on the effects of equation of state, Int. J. Heat and Mass Transfer, 43 (7): 1157-1171.

Zhu, G-S., R. D. Reitz, and S. K. Aggarwal (2001). Gas-phase unsteadiness and its influence on droplet vaporization in sub- and super-critical environments, Int. J. Heat and Mass Tran. 44(16):3081-3093.

PART III: APPENDICES

A1. Derivation of Distribution Moments in Mass and Molar Terms

In continuous thermodynamics, the distribution function customarily represents the molar distribution of the mixture to calculate the vapour-liquid equilibrium. But, this is by no means an absolute restriction. In this study, the zeroth fractional composition distribution moment X_J^p is taken to represent the average mole fractions of all species contained in a bin of a single homologue. Therefore, the (mass) Y_J^p and (molar) X_J^p fractional composition distribution moments, respectively, of a homologue can be defined as:

$$Y_J^p = \frac{\rho_{J(n)}^p}{\rho_{J(n)}^p} \qquad (A1-1)$$

$$X_J^p = \frac{c_{J(n)}^p}{c_{J(n)}^p} \qquad (A1-2)$$

In equation $(A1-1)$, the mass density for a vapour mixture is determined under the assumption that the mixture obeys the ideal equation of state, while the saturation liquid density is determined using the Rackett equation with an appropriate mixing rule (Polling et al, 2000). However, equations $(A1-1)$ and $(A1-2)$ are related if the molecular weight (which is the independent variable in the CT formulation) is used as:

$$Y_J^p = \frac{\rho_{J(n)}^p}{\rho_{J(n)}^p} = \frac{c_{J(n)}^p \theta_J^p}{c_{J(n)}^p \sum_J X_J^p \theta_J^p} = \frac{c_{J(n)}^p \int_M W_J^p(M)MdM}{\left(c_{J(n)}^p / X_J^p\right)\theta_J^p} = \frac{X_J^p \theta_J^p}{\theta_J^p} \qquad (A1-3)$$

Note that the mean of the molar distribution is defined by the distribution give by equation $(3-4)$ as $\theta_J^p = \int_M W_J^p(M)MdM$ and the molar average of the distribution mean is given as $\theta_J^p = \sum_J X_J^p \theta_J^p$. Using the distribution function given by equation

$(3-1)$, and noting that $Y_J^p = \int_M Y_J^p W_J^p(M)dM$ due to the normalisation condition of the PDF and the independence of Y_J^p on the PDF, equation $(A1-3)$ can be written as:

$$\int_M Y_J^p W_J^p(M)M^0 dM = \frac{X_J^p}{\theta_J^p}\int_M W_J^p(M)M^1 dM \qquad (A1-4_a)$$

The two distributions in equation $(A1-4_a)$ necessarily take different distribution parameters when used in conjunction with the mass and molar fractional composition distribution moments. Equation $(A1-4_a)$ can be weighed $n-$times to yield the $n^{th}-$moment of the *mass* fractional composition distribution and the $(n+1)^{th}-$moment of the *molar* fractional composition distribution as:

$\Phi_{J(n)}^v = 1$

$$\left(Y_J^p \Pi_{J(n)}^p = \Phi_{J(n)}^p\right)_{mass} = \left(\frac{X_J^p \Pi_{J(n+1)}^p}{\theta_J^p} = \frac{\Phi_{J(n+1)}^p}{\theta_J^p}\right)_{molar} \qquad (A1-4_b)$$

Noting from $(A1-3)$ that $1/\theta_J^p = X_J^p/\theta_J^p Y_J^p$, equation $(A1-4_b)$ can be further reduced to show an important transformation from mass-space to molar-space as:

$$\left(\Pi_{J(n)}^p\right)_{mass} = \left(\frac{\Pi_{J(n+1)}^p}{\theta_J^p}\right)_{molar} \qquad (A1-5)$$

It is interesting to observe from equation $(A1-5)$, like in the molar distribution, the zeroth-moment of the mass distribution reduces to unity as:

$$\left(\Pi_{J(n=0)}^p\right)_{mass} = \left(\frac{\Pi_{J(1)}^p}{\theta_J^p}\right)_{molar} = \left(\frac{\theta_J^p}{\theta_J^p}\right)_{molar} = 1 \qquad (A1-6)$$

A2. Vapour Mixture FCDM Transport Equation using CT

The general conservation equations for the *molar* form of discrete species multicomponent reacting flows can be written as in equation $(3-11)$ as (Kuo, 1986):

$$\frac{\partial}{\partial t}(c\,y_i) + \nabla.(c\,v\,y_i) = \nabla.\,(c\,D_{im}\,\nabla\,y_i) + (\dot{c}\,y_i)^S + (\dot{c}\,y_i)^C \qquad (A2-1)$$

In equation $(A2-1)$, y_i is the species mole fraction of the vapour/gas-phase mixture, c is the average molar mixture density that is determined from the equation of state assuming an ideal mixture, v is the average molar velocity, and D_{im} is the binary diffusion coefficient between the fuel species and the ambient gas. The source terms in $(A2-1)$ represent effects due to spray evaporation $(\dot{c}\,y_i)^S$ and combustion $(\dot{c}\,y_i)^C$.

In continuous thermodynamics, the dependent variables y_i representing the mole fractions of each species in the homologue are replaced by a PDF (Ratzsch and Kehlen, 1983), Cotterman and Prausnitz, 1985) of the form:

$$y_i = \int_M X_J^p G^p(M)dM\,. \qquad (A2-2)$$

In equation $(A2-2)$, X_J^p is the zeroth-fractional composition distribution moment (which can be taken to resemble a homologue mole fraction), while $G^p(M)$ is the composition PDF for semi-continuous mixtures as decribed by equation $(3-1)$.

By replacing equation $(A2-2)$ into equation $(A2-1)$, the governing equations for multicomponent reactive flows in the framework of continuous thermodynamics can be derived after the following simplifications. First, it is easy to observe that with the exception of the diffusion term $\nabla.\,(c\,D_{im}\,\nabla\,y_i)$, the simplifications of all other terms in equation $(A2-1)$ are trivial. Therefore, the transport of materials by diffusion will be given special attention, and is treated as follows. First the inner part of the diffusion term is expanded using vector identity as $\nabla(cD_{im}y_i) = c\,D_{im}\,\nabla y_i + y_i\nabla(cD_{im})$, which in conjunction with the PDF in equation $(A2-2)$ takes the form:

$$c\,D_{im}\,\nabla y_i = \nabla(cD_{im}y_i) - y_i\nabla(cD_{im}) =$$

$$\nabla\left(c^p_{J(n)} \int_0^\infty \underbrace{\left(D^p_{Jm}(M)G^p(M)dM\right)}_{\overline{D}^p_{Jm(n)}} X^p_J \right) - X^p_J \int_0^\infty G^p(M)\left[\nabla\left(c^p_{J(n)}D^p_{Jm}(M)\right)dM\right] \quad (A2-3_a)$$

Now, attention will be given for the two integral terms on the RHS of equation $(A2-3_a)$. Expanding the first integral equation on the RHS $(A2-3_a)$, which takes the form $\nabla\left(c^p_{J(n)}\overline{D}^p_{Jm(n)}X^p_J\right) = \nabla\left(c^p_{J(n)}\overline{D}^p_{Jm(n)}\right)X^p_J + c^p_{J(n)}\overline{D}^p_{Jm(n)}\nabla X^p_J$, the diffusion part of the governing equation $(A2-1)$ can be rewritten as:

$$\nabla.\left(c\,D_{im}\,\nabla y_i\right) =$$

$$\nabla.\left\{\nabla\left(c^p_{J(n)}\overline{D}^p_{Jm(n)}\right)X^p_J + c^p_{J(n)}\overline{D}^p_{Jm(n)}\nabla X^p_J - X^p_J\int_0^\infty G^p(M)\left[\nabla\left(c^p_{J(n)}\overline{D}^p_{Jm(n)}(M)\right)dM\right]\right\} \quad (A2-3_b)$$

Note that in equation $(A2-3_a)$ and $(A2-3_b)$, an average diffusion coefficient of the mixture over the distribution $\overline{D}^p_{Jm(n)} = \int_M \left(D^p_{Jm}(M)G^p(M)dM\right)$ is defined for clarity. However, the expanded form $\nabla\left(c^p_{J(n)}\overline{D}^p_{Jm(n)}X^p_J\right) = \nabla\left(c^p_{J(n)}\overline{D}^p_{Jm(n)}\right)X^p_J + c^p_{J(n)}\overline{D}^p_{Jm(n)}\nabla X^p_J$ will be retained to complete the modelling. With the above discussions, and noting that X^p_J is independent of the integral where the integral is over all the entire molecular weight and with a normalisation condition as $\int_0^\infty G^p(M)dM = \int_M G^p(M)dM = 1$, the transport equations take the form:

$$\begin{aligned}&\frac{\partial}{\partial t}\left(c_J^p\int_M X_J^p G^p(M)dM\right)+\nabla.\left(vc_J^p\int_M X_J^p G^p(M)dM\right)=\\&\nabla.\left[c_J^p\left(\int_M D_{Jm}^p(M)G^p(M)dM\right)\nabla X_J^p\right]+\\&\nabla.\left[\nabla\left(c_J^p\int_M D_{Jm}^p(M)G^p(M)dM\right)X_J^p-X_J^p\int_M G^p(M)\nabla\left(c_J^p D_{Jm}(M_J)\right)dM\right]\\&+\left(\dot{c}_J^p\int_M X_J^p G^p(M)dM\right)^C+\left(\dot{c}_J^p\int_M X_J^p G^p(M)dM\right)^S\end{aligned}\qquad (A2-4)$$

Equation $(A2-4)$ is weighted $n-$times to compute the higher moments of the composition distribution. However, in this study, only four-moments $n=0,1,2,3$ are considered to describe the evolution of the mixture. The condition for $n=0$ is described by equation $(A2-4)$. In addition, the numerical approximation of the difference terms on the RHS of equation $(A2-4)$ is close to zero for all the moments as $\nabla\left(c_{J(n)}^p\int_M D_{Jm}^p(M)G^p(M)dM\right)X_J^p-X_J^p\int_M G^p(M)\nabla\left(c_J^p D_{Jm}(M_J)\right)dM=0$. The simplified form of $(A2-4)$ for the 0^{th} – fractional composition distribution moment is $\frac{\partial}{\partial t}\left(c_{J(n)}^p X_J^p\right)+\nabla.\left(vc_{J(n)}^p X_J^p\right)=\nabla.\left(c_{J(n)}^p\overline{D}_{Jm(n)}^p\nabla X_J^p\right)+\left(\dot{c}_{J(n)}^p X_J^p\right)^C+\left(\dot{c}_{J(n)}^p X_J^p\right)^S$, which can be weighted by $M^{n=1}$, $M^{n=2}$, and $M^{n=3}$ corresponding to $n=1,2,3$ to yield, respectively, the 1^{st}, 2^{nd}, and 3^{rd}-fractional composition distribution moments as:

$$\frac{\partial}{\partial t}\left(c_{J(n)}^p\Phi_{J(n)}^p\right)+\nabla.\left(vc_{J(n)}^p\Phi_{J(n)}^p\right)=\nabla.\left(c_{J(n)}^p\overline{D}_{Jm(n)}^p\nabla\Phi_{J(n)}^p\right)+\left(\dot{c}_{J(n)}^p\Phi_{J(n)}^p\right)^C+\left(\dot{c}_{J(n)}^p\Phi_{J(n)_J}^{p\ \ p}\right)^S\qquad (A2-5)$$

In equation $(A2-5)$, $\Phi_{J(n)}^p=X_J^p\Pi_{J(n)}^p$ and the diffusion coefficients corresponding to higher moments take the form: $\overline{D}_{Jm(n)}^p\Pi_{J(n)}^p=\int_0^\infty D_{Jm}^p(M)M^n G^p(M)dM$. However, the numerical values of the diffusivity coefficients corresponding to $n=1,2,3$ are found to be very similar, and only the value of diffusivity coefficient $\overline{D}_{Jm(n)}^p$ is used. In order to use the molar fractional composition distribution moments in equation $(A2-5)$ for multidimensional codes like SOFIE, where composition is described in mass terms, the relation $c^{p}_{J(n)}=\rho^{p}_{J(n)}/\theta^{p}_{J}$ and equation $(A1-4_{b})$ are employed. Multiplying both sides of equation $(A1-4_{b})$ by $c^{p}_{J(n)}=\rho^{p}_{J(n)}/\theta^{p}_{J}$ a relation of the form $\left(\rho^{p}_{J(n)}Y^{p}_{J}\Pi^{p}_{J(n)}/\theta^{p}_{J}\right)_{mass}=\left(c^{p}_{J(n)}X^{p}_{J}\Pi^{p}_{J(n+1)}/\theta^{p}_{J}\right)_{molar}$ can be established, where up on cancelling θ^{p}_{J} yields $\left(\rho^{p}_{J(n)}Y^{p}_{J}\Pi^{p}_{J(n)}\right)_{mass}=\left(c^{p}_{J(n)}X^{p}_{J}\Pi^{p}_{J(n+1)}\right)_{molar}$. Note that the degree of moments n-in the $\Pi^{p}_{J(n;n+1)}$ term must be treated with great care to avoid confusion in the transformation process. As stated by equation $(A1-6)$, the transformation starts with a mass-space $n=0$. To that end, the terms on the LHS of equation $(A2-5)$ can be easily transformed, where the molar averaged velocity is converted to mass averaged velocity with out introducing any dimensional discrepancy. However, the terms on the RHS of equation $(A2-5)$ must be treated separately. The expanded forms of the diffusion and evaporation source terms are:

$$\begin{aligned}\nabla\cdot\left(c^{p}_{J(n)}\overline{D}^{p}_{Jm(n)}\nabla\Phi^{p}_{J(n)}\right)&=\nabla\cdot\left(\left(\rho^{p}_{J(n)}/\theta^{p}_{J}\right)\overline{D}^{p}_{Jm(n)}\nabla\left(\theta^{p}_{J}Y^{p}_{J}\Pi^{p}_{J(n)}\right)\right)\\&=\nabla\cdot\left(\rho^{p}_{J(n)}\overline{D}^{p}_{Jm(n)}\nabla\left(Y^{p}_{J}\Pi^{p}_{J(n)}\right)\right)+\nabla\cdot\left(\left(\rho^{p}_{J(n)}Y^{p}_{J}\Pi^{p}_{J(n)}/\theta^{p}_{J}\right)\overline{D}^{p}_{Jm(n)}\nabla\theta^{p}_{J}\right)\end{aligned}\qquad(A2-6)$$

$$\begin{aligned}\left(\dot{c}^{p}_{J(n)}\Phi^{p}_{J(n)}\right)^{C}&=\left(\left(\rho^{p}_{J(n)}/\theta^{p}_{J}\right)^{\prime}\left(\theta^{p}_{J}Y^{p}_{J}\Pi^{p}_{J(n)}\right)\right)^{C}\\&=\left(\dot{\rho}^{p}_{J(n)}Y^{p}_{J}\Pi^{p}_{J(n)}-\frac{\rho^{p}_{J(n)}}{\theta^{p}_{J}}\dot{\theta}^{p}_{J}Y^{p}_{J}\Pi^{p}_{J(n)}\right)^{C}=\left(-\dot{\rho}^{p}_{J(n)}Y^{p}_{J}\Pi^{p}_{J(n)}(E-1)\right)^{C}=S^{ch}_{\Phi^{p}_{J(n)}}\end{aligned}\qquad(A2-7)$$

In equation $(A2-7)$, $E=\left(\rho^{p}_{J(n)}/\dot{\rho}^{p}_{J(n)}\right)\left(\dot{\theta}^{p}_{J}/\theta^{p}_{J}\right)$, and the source term for combustion takes similar form as $(A2-7)$. Although the variation in $\nabla\left(Y^{p}_{J}\Pi^{p}_{J(n)}\right)$ is significant, the term $\nabla\theta^{p}_{J}\rightarrow 0$ leading for the second term on the RHS of $(A2-6)$ to vanish. Therefore, the mass fractional composition distribution moments take the form:

$$\left(\rho^{p}_{J(n)}\Phi^{p}_{J(n)}\right)_{t}+div\left(\rho^{p}_{J(n)}v^{v}\Phi^{p}_{J(n)}\right)=div\left(\Gamma^{p}_{\Phi^{p}_{J(n)}}\,grad\,\Phi^{p}_{J(n)}\right)+S^{ch}_{\Phi^{p}_{J(n)}}+S^{vap}_{\Phi^{p}_{J(n)}}\qquad(A2-8)$$

A3. Vapour Mixture Energy Transport Equation using CT

There are various forms of equations that govern the transport of energy in multicomponent mixtures. One form of the energy equation for discrete multicomponent mixtures, but neglecting viscous dissipation, work done by pressure and body forces, Dufour and Soret effects, and internal heat generation (Bird et al, 1960; Kuo, 1986) takes the form:

$$\rho\frac{Dh}{Dt}+\nabla\cdot\sum_{i}h_i\vec{j}_i=\nabla\cdot\left(\lambda\nabla T\right)\qquad\left(A3-1_a\right)$$

In equation $\left(A3-1_a\right)$, $\vec{j}_i=\rho D_{im}\nabla y_i$ is the component diffusivity flux, ρ is the mass density, y_i is the species mass fraction, and λ is the thermal conductivity. A more convenient form of the energy equation that is derived based on the same assumptions as equation $\left(A3-1_a\right)$ is (Libby and Williams, 1994):

$$\rho c_p\frac{DT}{Dt}+\sum_{i}\vec{j}_i\cdot\nabla h_i=\nabla\cdot\left(\lambda\nabla T\right)-\nabla\cdot\sum_{i}h_i\dot{\omega}_i\qquad\left(A3-1_b\right)$$

In equation $\left(A3-1_b\right)$, T is the temperature, c_o is the mixture specific heat, and $\dot{\omega}$ is the mass production rate of the species due to chemical reaction. When the enthalpy depends on temperature alone, $\nabla h_i=c_{pi}\nabla T$, the expanded form of $\left(A3-1_b\right)$ becomes:

$$\rho c_p\frac{\partial T}{\partial t}+\left(\rho c_p v+\sum_{i}c_{pi}\vec{j}_i\right)\nabla T=\nabla\cdot\left(\lambda\nabla T\right)-\nabla\cdot\sum_{i}h_i\dot{\omega}_i\qquad\left(A3-1_c\right)$$

In most heat and mass transfer analysis, the energy equations described by $\left(A3-1_{a-c}\right)$ neglect the energy transport by mass diffusion (or interdiffusion term $\sum_{i}\vec{j}_i\cdot\nabla h_i$). While adopting the above equations in the framework of continuous thermodynamics, however, there appears to be a fundamental discrepancy which term representing energy transport by mass diffusion to neglect and in what form. In particular, since one of the prime objectives of this research is the development of droplet evaporation models that can be used to simulate the evaporation duct of an advanced gas turbine combustor (before combustion), knowledge of the the energy transport by diffusion is thought to be essential. Although establishing the importance of the contribution of the energy transport by mass diffusion in vapour-gas mixtures requires further investigation, the main focus here is in understanding what the neglected term entails in the first place.

It is well known that the form of equation $(A3-1_a)$ is not easy to implement in CFD codes due to the definition of the total enthalpy h in terms of the reference enthalpy $\Delta h_{f,i}^0$ (Ponsoit and Veynante, 2001) as:

$$h=\sum_i h_i y_i = \sum_i \left(h_{si} + \Delta h_{f,i}^0\right) y_i \qquad (A3-2)$$

In general, the component enthalpy is replaced as $h_i = h_{si} + \Delta h_{f,i}^0$, so that the sensible enthalpy $h_{si} = \int_T Cp_i dT$ is zero at $T = T^0$ for all substances, even though the reference enthalpy at $T = T^0$, namely, $\Delta h_{f,i}^0$, is not and it may be a constant. It is easy to observe that the genral form of the energy equation $(A3-1_a)$ contains terms – for example, $\rho Dh/Dt$ and $\nabla \cdot \sum_i h_i \vec{j}_i$, whose values change if different constants are added to the enthalpies of the individual components. This is also true for terms $\sum_i \vec{j}_i \cdot \nabla h_i$ and $\nabla \cdot \sum_i h_i \dot{\omega}_i$ in equations $(A3-1_b)$ and $(A3-1_c)$. If the temperature datum at which the enthalpies of the species are assigned to be zero is changed, then in general $\rho Dh/Dt$ and $\nabla \cdot \sum_i h_i \vec{j}_i$ would take different values. It is at this juncture that the choice of either a single constant for all components or different constants corresponding to each component becomes a point of interest. To that end, although the form of equation $(A3-1_b)$ is the most suitable form of the energy equation widely used in droplet evaporation modelling and the form adopted in this study, equation $(A3-1_a)$

will be used primarily to establish the effect of the datum state enthalpies instead. The choice of equation $(A3-1_a)$ is evident due to the fact that one of the main issues to establish is the dependence of the enthalpy on datum states, where the transported scalar in equation $(A3-1_a)$ is the case in point.

In the CT framework, the idea is always to formulate a single representative value for an ensemble of large components. In this case, a single value of a reference enthalpy is the preferred form so that the relationship between enthalpy and the composition distribution can be established. To that end, the same constant $\hbar$ is used for all of the components present in the mixture so that the variation of the two terms in equation $(A3-1_a)$ can be described as:

$$\rho\frac{Dh}{Dt}=\rho\sum_i y_i\frac{Dh_i}{Dt}+\rho\sum_i h_i\frac{Dy_i}{Dt}=\rho\sum_i y_i\frac{D(h_i+\hbar)}{Dt}+\rho\sum_i(h_i+\hbar)\frac{Dy_i}{Dt}=\rho\frac{Dh}{Dt} \qquad (A3-3_a)$$

$$\nabla\cdot\sum_i h_i\vec{j}_i=\sum_i h_i\nabla\cdot\vec{j}_i+\sum_i\vec{j}_i\cdot\nabla h_i=\sum_i(h_i+\hbar)\nabla\cdot\vec{j}_i+\sum_i\vec{j}_i\cdot\nabla(h_i+\hbar)=\nabla\cdot\sum_i h_i\vec{j}_i \qquad (A3-3_b)$$

In equations $(A3-3)$, the normalisation condition $\sum_i y_i=1$ and the material derivative identity $D/Dt\sum_i y_i=0$ and $\sum_i\nabla\cdot\vec{j}_i=\nabla\cdot\sum_i\vec{j}_i=0$ due to continuity are used. These two equations demonstrate that the energy equation is independent of the reference enthalpy if the same reference enthalpy is used, contrary to common thermodynamics theory, which requires the component enthalpy at a reference temperature to constitute the sensible and reference enthalpy for each species (Ponsoit and Veynante, 2001). The independence of the enthalpy on a single reference enthalpy, if a common enthalpy is used, paves the way for using the CT framework to model the energy equation.

However, before formulating the energy equation in the CT framework, it is vital to understand the dependence of the energy equation using a datum state for each species in the discrete frmweork. In order establish this fact, consider the two terms $\rho Dh/Dt$ and $\nabla\cdot\sum_i h_i\vec{j}_i$ in equation $(A3-1_a)$, where the enthalpy depends on datum states of the species (say $\hbar_i$ and not the single constant $\hbar$ used in the earlier argument). The constant datum state enthalpies for each species $\hbar_i$ can be used instead of the single datum state enthalpy in equation $(A3-3_a)$ so that the following relationship can be established:

$$\rho\sum_i y_i\frac{D(h_i+\hbar_i)}{Dt}+\rho\sum_i(h_i+\hbar_i)\frac{Dy_i}{Dt}=\underbrace{\rho\sum_i y_i\frac{Dh_i}{Dt}+\rho\sum_i h_i\frac{Dy_i}{Dt}}_{\rho Dh/Dt}+\rho\sum_i\hbar_i\frac{Dy_i}{Dt} \qquad (A3-4_a)$$

In equation $(A3-4_a)$, it is interesting to observe the extra term $\rho\sum_i\hbar_i Dy_i/Dt$, which represents the energy transport due to species mass accumulation and convection, due to the simple transformation from a datum state independent enthalpy to datum state dependent state enthalpy formulation.

Similarly, expanding the second term over datum state enthalpies of equation $(A3-3_b)$,

$$\nabla\cdot\sum_i(h_i+\hbar_i)\vec{j}_i=\nabla\cdot\sum_i h_i\vec{j}_i+\sum_i\hbar_i\nabla\cdot\vec{j}_i \qquad (A3-4_b)$$

Note that the two terms $(A3-4_a)$ and $(A3-4_b)$ are nothing but the expressions on the LHS of the general energy equation $(A3-1_a)$. Therefore, the sum of the terms in equations $(A3-4_a)$ and $(A3-4_b)$ yields the following relation:

$$\begin{aligned}&\rho\sum_i y_i\frac{D(h_i+\hbar_i)}{Dt}+\rho\sum_i(h_i+\hbar_i)\frac{Dy_i}{Dt}+\nabla\cdot\sum_i(h_i+\hbar_i)\vec{j}_i\\&=\rho\frac{Dh_i}{Dt}+\nabla\cdot\sum_i h_i\vec{j}_i+\sum_i\hbar_i\rho\frac{Dy_i}{Dt}+\sum_i\hbar_i\nabla\cdot\vec{j}_i\end{aligned} \qquad (A3-4_c)$$

The last two terms on the RHS of equation $(A3-4_c)$ can be grouped as:

$$\begin{aligned}&\rho\sum_i y_i\frac{D(h_i+\hbar_i)}{Dt}+\rho\sum_i(h_i+\hbar_i)\frac{Dy_i}{Dt}+\nabla\cdot\sum_i(h_i+\hbar_i)\vec{j}_i\\&\quad=\rho\frac{Dh_i}{Dt}+\nabla\cdot\sum_i h_i\vec{j}_i+\sum_i\hbar_i\left(\rho\frac{Dy_i}{Dt}+\nabla\cdot\vec{j}\right)\end{aligned}\qquad(A3-4_d)$$

Note that, in the absence of chemical reaction, the term $\rho\, Dy_i/Dt+\nabla\cdot\vec{j}=\dot{\omega}=0$. If the conductive heat transfer term $\nabla\cdot(\lambda\nabla T)$ is included in the material derivative term $\rho\, Dh/Dt$, expanded in equation $(A3-3_a)$, and the divergence of the energy flux $\nabla\cdot\sum_i h_i\vec{j}_i$, expanded in equation $(A3-3_b)$, the final form of the datum state dependent energy equation exapanded in $(A3-4_d)$ and the governing equation $(A3-1)$ can be equated as:

$$\rho\frac{Dh}{Dt}+\nabla\cdot\sum_i h_i\vec{j}_i-\nabla\cdot(\lambda\nabla T)=\rho\frac{Dh_i}{Dt}+\nabla\cdot\sum_i h_i\vec{j}_i-\nabla\cdot(\lambda\nabla T)+\sum_i\hbar_i\left(\rho\frac{Dy_i}{Dt}+\nabla\cdot\vec{j}\right)\qquad(A3-5)$$

The simple conclusion that can be drawn from equation $(A3-5)$ is that in the absence of chemical reaction, the enthalpies of the species and the datum-states are arbitrary, and the sums of the first two terms on the RHS of equation $(A3-5)$ are independent of the datum states. Therefore, droplet evaporation modelling in the CT framework can proceed without worrying about the manner by which the datum state enthalpies are expressed.

A more fundamental issue that needs resolution is, however, the implication of the relation in equation $(A3-5)$ in conjunction with the extra term $\rho\sum_i\hbar_i\, Dy_i/Dt$ in equation $(A3-4_a)$, where as it is always done, the divergence of the energy flux $\nabla\cdot\sum_i h_i\vec{j}_i$ is neglected. In such situation, the extra term $\sum_i\hbar_i\nabla\cdot\vec{j}_i$ in equation

$(A3-4_b)$ or equation $(A3-5)$ is non-extistent as the term $\nabla\cdot\sum_i h_i\vec{j}_i$ is neglected in the first place. Therefore, if the divergence of the energy flux caused by the species interdiffusion is neglected, but the energy transport due to species mass accumulation and convection $\rho\sum_i \hbar_i\, Dy_i/Dt$ is included, then the energy transport equation would be erroneous as it depends on the enthalpy datum states, and hence forcing the results of the equation to depend incorrectly on the datum states. The energy equation must include a term that takes away the effect of the term $\rho\sum_i \hbar_i\, Dy_i/Dt$ which is as a result of the operation in equation $(A3-4_a)$ without any reference to the interdiffusion.

The above treatment shows that in the absence of chemical reaction, the energy equation is independent of the type of reference enthalpy chosen, be it constant or that ssociated with each species. When the flow and transport involves chemical reaction, only a single datum state is possible, which will be the case in the CT framework. In addition, the above treatment shows inaccuracy and the manner by which the interdiffusion of multicomponent mixture transport is neglected by many authors, with out due consideration on the energy lost due to species mass accumulation and convection. Therefore, in this investigation, the governing equation for energy transport in the framework of CT is formulated including the interdiffusion.

For flow and transport involving an evaporating droplet, the energy equation for mixtures composed of discrete species, the molar form of equation $(A3-1_b)$ can be expanded as:

$$c_p \frac{\partial}{\partial}(cT)+c_p\nabla(cvT)=\nabla\cdot(\lambda\nabla T)-\sum_i \vec{j}_i\cdot\nabla h_i \qquad (A3-6)$$

In equation $(A3-6)$ c, c_p, and λ are, respectively, the mixture molar density, the average mixture specific heat and the mixture conductivity, while T is the termperature. For a gas-vapour mixture, the average mixture specific heat, which is a strong function of the the mixture composition and temperature can be cast in continuous thermodynamics as:

$$Cp^{p}_{J(n)} = \sum_{J} \int_{M} X^{p}_{J} Cp^{p}_{J}(M) W^{v}_{J}(M) dM + \left(1 - \sum_{J} X^{p}_{J}\right) Cp_{A} \qquad (A3-7_{a})$$

In equation $(A3-7_{a})$, the homologue specific heat is assumed to vary linearly with the molecular weight as $Cp^{p}_{J}(M) = a_{cpJ} + b_{cpJ}M$, and the correlation coefficients are determined according the methods described in §4 and Appendix A7. Thus the gas-vapour mixture specific heat is of the form:

$$Cp^{p}_{J(n)} = Cp_{A} + \sum_{J} X^{p}_{J} \left\{ a_{cpJ} - Cp_{A} + b_{cpJ} \theta^{p}_{J} \right\} \qquad (A3-7_{b})$$

Note that in equation equation $(A3-7)$, the specific heat of the vapour fuel is assumed to evolve appreciably differently from that of the ambient gas. The mass transported due to energy gradient is $\vec{j}_{i} = -(\rho D_{im} \nabla y_{i}) = -\nabla(\rho D_{im} y_{i}) + y_{i} \nabla(\rho D_{im})$, which as shown by equations $(A2-3_{a})$, $(A2-3_{b})$ and the final result in equation $(A2-4)$ represents the diffusion accounted for the term $-\nabla.\left[c^{p}_{J} \overline{D}^{p}_{Jm(n)} \nabla X^{p}_{J}\right]$, where the diffusion coefficient for the fractional composition distribution moment $\overline{D}^{p}_{Jm(n)} = \int_{M} \left(D^{p}_{Jm}(M) G^{p}(M) dM\right)$ is used. Therefore, with the CT form of the interdiffusion term given by equation $(A3-8)$, the energy transport equation in molar terms with $\lambda^{p}_{J(n)} / Cp^{p}_{J(n)} = \Gamma^{p}_{T}$ is:

$$-\sum_{i} \vec{j}_{i} \cdot \nabla h = \sum_{J} \nabla.\left[c^{p}_{J} \overline{D}^{p}_{Jm(n)} \nabla X^{p}_{J}\right] \cdot \left[Cp_{A} + \sum_{J} X^{p}_{J} \left\{ a_{cpJ} - Cp_{A} + b_{cpJ} \theta^{p}_{J} \right\} \right] \nabla T \qquad (A3-8)$$

$$\left(c^{p}_{J(n)} T\right)_{t} + div\left(c^{p}_{J(n)} v^{p} T\right) = div\left(\Gamma^{p}_{T}\, grad\, T\right) + \left[\left\{ a_{cpJ} - Cp_{A} + b_{cpJ} \theta^{p}_{J} \right\} c^{p}_{J} \overline{D}^{p}_{Jm(n)} \nabla X^{p}_{J} \right] \nabla T \qquad (A3-9)$$

Equation $(A3-9)$ can be expressed in the general form of equation $(3-13)$.

A4. (Material) Phase Equilibrium using CT

A4.1. Introduction

Phase equilibria are establisehed in the framework of classical thermodynamics by matching the pressure, temperature, and chemical potential (fugacity) of each species in each phase. The fugacity is derived from the more fundamental term chemical potential, which is defined as the variation in the thermodynamic potential[5] of a region with respect to a change in the amount of a particular species of matter[6], while no other extensive properties altered. This is stated mathematically as:

$$\bar{\mu}_s^p\left(T,P,X_s^p\right)=\underset{\mathbf{A}}{\left(\frac{\partial G_s^{I,E}}{\partial n_s}\right)_{T,P,n_{k\neq s}}}=\underset{\mathbf{B}}{\left(\frac{\partial A}{\partial n_s}\right)_{T,V,n_{k\neq s}}}=\underset{\mathbf{C}}{\left(\frac{\partial U}{\partial n_s}\right)_{S,V,n_{k\neq s}}}=\underset{\mathbf{D}}{\left(\frac{\partial H}{\partial n_s}\right)_{S,P,n_{k\neq s}}} \qquad (A4-1)$$

The difficulty in using any forms of equation $(A4-1)$ lies in finding an expression for the chemical potential in terms of measured quantities: pressure, temperature, and composition. To that end, the Gibbs free energy and the Helmholtz free enrgy formulation gained popularity in fluid phase and chemical equilibra applications. However, in the framework of continuous thermodynamics, explicit expressions of individual discrete species are abandoned in fevour of (lumped) homologues. Therefore, the form of equation $(A4-1)$ and other well established relationships for discrete species will be modified to accommodate this new formulation. For example – the mole number of a discrete species in a mixture, n_i, can be related to the total mole number of the mixture, n, through its mole fraction as $n_i = n\,x_i$. Similarly, for a single homologue, Coterman et al (1985) have shown that by defining an extensive (mass

---

[5] The thermodynamic potentials are in the form of either the Gibbs free energy (G=U+PV-TS=H-TS), the Helmholtz free energy (A=U-TS), the free internal energy (U), or the free enthalpy (H), where S is the entropy and T is the temperature.

[6] The amount of matter could mean different things in different applications. For example, in the original definition, Gibbs used the mass of the specific species, while it is usually used as the number of moles in phas equilibrium or chemical (reaction) equilibrium applications, while it is used to represent the number of particles in solid state physics.

dependent) distribution $g^p(M)$, the total homologue mole numbers n_T^p can be related to the intensive distribution of the fractional composition $G^p(M)$ as:

$$g^p(M)=n_T^p G^p(M)=n_T^p\sum_{s=1}^{q}X_s^p\delta(M-M_s)+n_T^p\sum_{J=1}^{I}X_J^p W_J^p(M) \qquad (A4-2)$$

Note that equation $(A4-2)$ is designed for both mathematical clarity and consistency of the equilibrium condition. It is possible to slice the extensive distribution function in equation $(A4-2)$ into a series of equal width division of ΔM, where each slice has height $g^p(M)$. The $M's$ are the value of a range of molecular weight in one homologues series at the midpoint of the J^{th} homologue interval, where the continuous function $n_T G^p(M)$ is now replaced by a series of bars. The area of each bar represents a single homologue mole number, n_J. The approximation becomes exact when $\Delta M \to 0$, and $\frac{1}{n_T}\int_M g^p(M)dM=\frac{1}{n_J}\int_M X_J^p g^p(M)dM=\int_M G^p(M)dM=1$. Therefore, the relationship between the chemical potential and the Helmholtz free energy for semi-continuous mixture takes the form:

$$\bar{\mu}_J^p(M)=\left[\frac{\delta A^p}{\delta g^p(M)}\right]_{T,V,M_J=M} \qquad (A4-3)$$

Equation $(A4-3)$ is a functional derivative, and following the expression of Salacuse and Stell (1982) for the Helmholtz free energy δA^p, equation $(A4-3)$ takes the form:

$$\bar{\mu}_J^p(M)=\int_V^{\infty}\left\{\left[\frac{\delta P}{\delta g^p(M)}\right]_{T,V,M_J=M}-\frac{RT}{V}\right\}dV-RT\ln\left(\frac{P^0 V}{\delta g^p(M)RT}\right)+RT+\bar{\mu}^0(T,M)$$

$$(A4-4)$$

In equation $(A4-4)$, the chemical potential is derived as a functional derivative of the Helmholtz free energy (Hansen and McDonald, 1976). Therefore, equation $(4-23)$ can be rewritten as:

$$\ell n\left(\frac{f_s^p(T,P,M_J)}{X_s^p P}\right)=\ell n\Theta_s^p(T,P,M_J)=\frac{\overline{\mu}_s^p(T,P,M_J)-\overline{\mu}_s^{p0}(T,P)}{RT} \qquad (A4-5_a)$$

Using equation $(A4-4)$ into equation $(A4-5_a)$ yields:

$$RT\,\ell n\Theta_s^p(T,P,M_J)=\int_V^{\infty}\left\{\left[\frac{\delta P}{\delta g^p(M)}\right]_{T,V,M_J=M}-\frac{RT}{V}\right\}dV-RT\ell nZ \qquad (A4-5_b)$$

Equation $(A4-5_b)$ describes the fugacity coefficient as a function of temperature, pressure and composition, where up on using a suitable equation of state (EOS) and suitable mixing and combining rules gives the phase equilibria of both the vapour and liquid phases.

A4.2. Low Pressure Formulation

At low pressure, the correction factor $\Im_J$, and the activity coefficient ϖ_J^v, in equation $(4-32)$ tend to unity (Polling et al, 2000). Therefore, for the semi-continuous mixture considered in this study, it results in Rault's law, which can be stated as:

$$X_J^v G^v(M)P=X_J^l G^l(M)P_J^{sat}(M,T) \qquad (A4-6)$$

Note that equation $(A4-6)$ describes the (material) phase equilibrium of a single homologue (Cotterman et al, 1986) in the CT framework, and its departure from the discrete formulation (Sirignano, 1983, 1993) can be easily observed due to the lumping of the large number of discrete species into a single homologue. The extension of the single homologue formulation in equation $(A4-6)$ to multiple homologues is straightforward.

In equation $(A4-6)$, the vapour pressure is estimated using the Clausius-Clapeyron equation $P_J^{sat}(M,T)=P_{atm}\ Exp\left[\frac{S_{fg}}{R_u}\left(1-\frac{T_b}{T}\right)\right]$, where the boling temperature is correlated linearly with the molecular weight as $T_{bJ}=a_{bJ}+b_{bJ}M$ as described in §4 and Appendix A7, and S_{fg} is the entropy of vaporisation for the mixture. Replacing the correlation for the boiling temperature, the Clausius-Clapeyron relation becomes:

$$\begin{aligned} P_J^{sat}(M,T) &= P_{atm}\ Exp\left[\frac{S_{fg}}{R_u}\left(1-\frac{a_{bJ}}{T}\right)\left(1-\frac{b_{bJ}}{T-a_{bJ}}M\right)\right] \\ &= P_{atm}\ Exp\left[A_J\left(1-B_J M\right)\right] \end{aligned} \qquad (A4-7_a)$$

In equation $(A4-7_a)$, the substitution $A_J=\frac{S_{fg}}{R_u}\left(1-\frac{a_{bJ}}{T}\right)$ and $B_J=\frac{b_{bJ}}{T-a_{bJ}}$ are used, which can be simplified to:

$$\begin{aligned} P_J^{sat}(M,T) &= P_{atm} Exp\left[A_J\left(1-B_J M\right)\right] \\ &= P_{atm} Exp\left[A_J\left(1-\gamma_J^l B_J\right)\right] Exp\left[-A_J B_J \beta_J^l\left(M-\gamma_J^l/\beta_J^l\right)\right] \end{aligned} \qquad (A4-7_b)$$

Using the distribution function in equation $(3-4)$ and the Rault's law for a single homologue given by equation $(A4-6)$, the fractional composition distribution moments at the droplet surface takes the form:

$$\int_M X_J^v W_J^v(M)dM=\int_M X_J^l\frac{P_{atm}}{P}\frac{e^{\left[A_J\left(1-B_J M\right)\right]}}{\beta_J^l\Gamma\left(\alpha_J^l\right)}\left(\frac{M-\gamma_J^l}{\beta_J^l}\right)^{\alpha_J^l-1}e^{\left[-\left(1+A_J B_J \beta_J^l\right)\left(M-\gamma_J^l/\beta_J^l\right)\right]}dM \qquad (A4-8)$$

Using Euler's definition for the gamma function, which is of the form $\Gamma(\alpha)=\delta^\alpha\int_0^\infty \xi^{\alpha-1}e^{-\xi\delta}d\delta$, and integrating equation $(A4-8)$ by parts, the final form of the surface mole fraction yields:

$$X_J^{vR} = X_J^l \frac{P_{atm}}{P}\left(\frac{e^{[A_J(1-B_J M)]}}{\left(1+A_J B_J \beta_J^l\right)^{\alpha_J^l}}\right) \tag{A4-9}$$

Weighting equation $(A4-8)$ by M and M^2, the first and second moments of the distribution at the droplet surface take the form:

$$\theta_J^{vR} = \alpha_J^l\left(\frac{\beta_J^l}{1+A_J B_J \beta_J^l}\right)+\gamma_J^l = \frac{\theta_J^l-\gamma_J^l}{(1+\dfrac{A_J B_J (\sigma_J^l)^2}{\theta_J^l-\gamma_J^l})}+\gamma_J^l \tag{A4-10$_a$}$$

$$\psi_J^{vR} = \alpha_J^l(\alpha_J^l+1)\left(\frac{\beta_J^l}{1+A_J B_J \beta_J^l}\right)^2 + 2\alpha_J^l\left(\frac{\beta_J^l}{1+A_J B_J \beta_J^l}\right)\gamma_J^l + (\gamma_J^l)^2 \tag{A4-11$_b$}$$

A close observation in the forms of equations $(A4-10_a)$ and $(A4-11_b)$ in comparison to the definition of the mean and second moments of the distribution described by equation $(3-7)$ and $(3-8)$ gives an expression of the form:

$$\theta_J^{vR} = \alpha_J^l \beta_J^{l*} + \gamma_J^l \tag{A4-10$_b$}$$

$$\psi_J^{vR} = \alpha_J^l(\alpha_J^l+1)\beta_J^{l*2} + 2\alpha_J^l \beta_J^{l*}\gamma_J^l + (\gamma_J^l)^2 \tag{A4-11$_b$}$$

In equation $(A4-10)$ and $(A4-11)$, the relation $\beta_J^{l*} = \beta_J^l / \left(1+A_J B_J \beta_J^l\right)$ is used. If equations $(A4-10)$ and $(A4-11)$ are used to verify the relation $\psi - \theta^2 = \sigma^2$, an identity of the form ca be recovered as:

$$\alpha_J^l\left(\frac{\beta_J^l}{1+A_J B_J \beta_J^l}\right)^2 = \alpha_J^{vR}\left(\beta_J^{vR}\right)^2 = \alpha_J^{vR}\left(\frac{\theta_J^{vR}-\gamma_J^{vR}}{\alpha_J^{vR}}\right)^2 \tag{A4-12$_a$}$$

The numerator of the last term in equation $(A4-12_a)$ can be expanded using equations $(3-7)$ and $(A4-10)$ as $(\theta_J^{vR}-\gamma_J^{vR})^2=(\alpha_J^l\beta_J^{l*})^2+2\alpha_J^l\beta_J^{l*}(\gamma_J^l-\gamma_J^{vR})+(\gamma_J^l-\gamma_J^{vR})^2$. For equilibrium evaporation, the origin of the distribution function in both phases is the same. Therefore, the term $(\gamma_J^l-\gamma_J^{vR})=0$. Hence equation $(A4-12_a)$ reduces to $\alpha_J^{vR}\alpha_J^l(\beta_J^{l*})^2=(\alpha_J^l\beta_J^{l*})^2$. This implies that the final form of the relationship between the liquid composition distribution shape parameters and the vapour composition distribution shape parameters are of the form:

$$\alpha_J^l=\alpha_J^{vR} \tag{$A4-12_b$}$$

The finding in equation $(A4-12_b)$ is significant in that the composition distribution shape is unaffected because of the phase transition from liquid to vapour. However, it is interesting to see that using the definition for the first moment $\theta_J^{vR}=\alpha_J^{vR}\beta_J^{vR}+\gamma_J^{vR}$, and equating it to the expression in equation $(A4-10)$, the composition distribution scale parameters are related as $\beta_J^{vR}=\beta_J^{l*}$. This can be rewritten in its final form as:

$$\beta_J^{vR}=\frac{\beta_J^l}{1+A_JB_J\beta_J^l}=\frac{\beta_J^l}{K_\beta} \tag{$A4-12_c$}$$

The implications of the relationship between the three distribution parameters during phase equilibrium will have a significant effect on the modelling process. But, from the results of equation $(A4-12)$, the phase transition is characterised by a change in the scale parameter alone, by a factor K_β, which is in turn a function of the saturation temperature, the entropy of vaporisation, and scale parameter of the liquid distribution.

A4.3. High Pressure Formulation

High pressure phase equilibrium is achieved by applying equation $(4-29)$ both for the continuous and discrete species, in both the liquid and vapour phases. The form of equation $(4-29)$ for discrete species can be found elsewhere (Zhu and Aggarwal, 2000). For the continuous mixture, however, the treatment of the functional in equation $(A4-6)$ needs further elucidation so that the EOS in equation $(4-36)$ can be used. The functional with the extensive distribution is:

$$\delta P/\delta g^{p}(M) \rightarrow \left[\frac{\delta P}{\delta g^{p}(M)}\right]_{T,V,M_J=M} \qquad (A4-13)$$

From equation $(A4-13)$, it is easy to see that the volume and temperature are held constant, while the pressure is a function of the form $P=P(n,nb,n^2a)$, being a functional with respect to $g^{p}(M)$, where $\int_M g^{p}(M)dM = n_T^p \int_M G^{p}(M)dM = n_T^p = n$ from equation $(A4-2)$.Therefore, the general cubic equation of state described by equation $(4-36)$ can be rewritten as:

$$P=\frac{nR_uT}{V-(nb)}-\frac{(n^2a)}{[V+\varepsilon_1(nb)][V+\varepsilon_2(nb)]} \qquad (A4-14)$$

In equation $(A4-13)$, V is the extensive volume. Taking the functional variation of pressure with respect to the newly defined extensive distribution $g^{p}(M)$ in equation $(A4-2)$, equation $(A4-13)$takes the form:

$$\begin{aligned}\frac{\delta P}{\delta g^{p}(M)} &= \frac{\partial P}{\partial n}\frac{\partial n}{\partial g^{p}(M)}+\frac{\partial P}{\partial(nb)}\frac{\partial(nb)}{\partial g^{p}(M)}+\frac{\partial P}{\partial(n^2a)}\frac{\partial(n^2a)}{\partial g^{p}(M)}\\ &= \frac{\partial P}{\partial n}+\frac{\partial P}{\partial(nb)}\bar{b}(M)+\frac{\partial P}{\partial(n^2a)}n\bar{a}(M)\end{aligned} \qquad (A4-15_a)$$

In equation $(A4-15_a)$, the substitutions $\bar{a}(M)=\frac{1}{n}\frac{\partial(n^2a)}{\partial g^{p}(M)}$, $\bar{b}(M)=\frac{\partial(nb)}{\partial g^{p}(M)}$, and the identity $\frac{\partial n}{\partial g^{p}(M)}=1$, which are dependent on the mole number or concentration of the ensemble considered, are used. Isolating and expanding each of the terms in equation $\left(A4-15_a\right)$, the variation of pressure with composition takes the form:

$$\frac{\partial P}{\partial n}=\frac{R_u T}{\left[V-(nb)\right]} \qquad \left(A4-15_b\right)$$

$$\frac{\partial P}{\partial (nb)}=\frac{nR_u T}{\left[V-(nb)\right]^2}+n^2 a\left\{\frac{\varepsilon_1}{\left[V+\varepsilon_1(nb)\right]^2\left[V+\varepsilon_2(nb)\right]}+\frac{\varepsilon_2}{\left[V+\varepsilon_1(nb)\right]\left[V+\varepsilon_2(nb)\right]^2}\right\} \qquad \left(A4-15_c\right)$$

$$\frac{\partial P}{\partial (n^2 a)}=-\frac{1}{\left[V+\varepsilon_1(nb)\right]\left[V+\varepsilon_2(nb)\right]} \qquad \left(A4-15_d\right)$$

Using equations $\left(A4-15\right)$ for the pressure functional differentiation in equation $\left(4-29\right)$ yields:

$$\begin{aligned} &R_u T \ell n \Theta_J(M) \\ &= \bar{b}(M)\left[\int_V^{\infty}\left\{\frac{nR_u T}{\left[V-(nb)\right]^2}+\frac{n^2 a\varepsilon_1}{\left[V+\varepsilon_1(nb)\right]^2\left[V+\varepsilon_2(nb)\right]}+\frac{n^2 a\varepsilon_2}{\left[V+\varepsilon_1(nb)\right]\left[V+\varepsilon_2(nb)\right]^2}\right\}dV'\right] \\ &- \bar{a}(M)\left[\int_V^{\infty}\frac{n}{\left[V+\varepsilon_1(nb)\right]\left[V+\varepsilon_2(nb)\right]}dV'\right]+\int_V^{\infty}\frac{R_u T}{\left[V-(nb)\right]}dV'-\int_V^{\infty}\frac{R_u T}{V}dV'-R_u T\ln Z \end{aligned} \qquad \left(A4-16_a\right)$$

Equation $\left(A4-16_a\right)$ can be simplified to

$$\begin{aligned} &R_u T \ell n \Theta_J(M) \\ &= \bar{b}(M)\left[\int_V^{\infty}\left\{\frac{nR_u T}{\left[V-(nb)\right]^2}+n^2 a\varepsilon_1\Omega_{ik}+n^2 a\varepsilon_2\Omega_{ik}\right\}dV'\right]-\bar{a}(M)\left[\int_V^{\infty}n\Omega_{ik}dV'\right] \\ &+\int_V^{\infty}\frac{R_u T}{\left[V-(nb)\right]}dV'-\int_V^{\infty}\frac{R_u T}{V}dV'-R_u T\ln Z \end{aligned} \qquad \left(A4-16_b\right)$$

where $\Omega_{ik} = \dfrac{1}{[V+\varepsilon_1(nb)]^i\,[V+\varepsilon_2(nb)]^k}$, which after evaluating the integral yields:

$$\Omega_{11} = \frac{1}{n(\varepsilon_2 - \varepsilon_1)b}\left[ln\left(\frac{V_m + \varepsilon_2 b}{V_m + \varepsilon_1 b}\right)\right] \qquad (A4-17_a)$$

$$\Omega_{21} = \frac{1}{n^2(\varepsilon_2 - \varepsilon_1)b}\left[\frac{1}{V_m + \varepsilon_1 b} - \frac{1}{(\varepsilon_2 - \varepsilon_1)b}ln\left(\frac{V_m + \varepsilon_2 b}{V_m + \varepsilon_1 b}\right)\right] \qquad (A4-17_b)$$

$$\Omega_{12} = \frac{-1}{n^2(\varepsilon_2 - \varepsilon_1)b}\left[\frac{1}{V_m + \varepsilon_2 b} - \frac{1}{(\varepsilon_2 - \varepsilon_1)b}ln\left(\frac{V_m + \varepsilon_2 b}{V_m + \varepsilon_1 b}\right)\right] \qquad (A4-17_c)$$

Integrating equation $(A4-16_a)$ gives the fugacity coefficient of a single homologue as:

$$\begin{aligned} &R_u T\ell n\Theta_J(M) \\ &= \bar{b}(M)\left[\frac{R_u T}{V_m - b} - \frac{a}{b}\frac{V_m}{(V_m + \varepsilon_1 b)(V_m + \varepsilon_2 b)} - \frac{a}{b^2}\frac{1}{(\varepsilon_2 - \varepsilon_1)}ln\left(\frac{V_m + \varepsilon_1 b}{V_m + \varepsilon_2 b}\right)\right] \qquad (A4-18) \\ &+ \bar{a}(M)\left[\frac{1}{b(\varepsilon_2 - \varepsilon_1)}ln\left(\frac{V_m + \varepsilon_1 b}{V_m + \varepsilon_2 b}\right)\right] + R_u T\,ln\left(\frac{V_m}{V_m - b}\right) - R_u T\,ln Z \end{aligned}$$

The form of equation $(A4-18)$ requires the roots of the general cubic equation of state described by equation $(4-41)$. Therefore, the final form of the fugacity coefficient that can conveniently be used into the phase equilibrium calculations takes the form:

$$\begin{aligned} \ell n\Theta_J(M) = &\left[\frac{\bar{a}(M)}{a} - \frac{\bar{b}(M)}{b}\right]\frac{A^*}{B^*(\varepsilon_2 - \varepsilon_1)}ln\left(\frac{Z + \varepsilon_1 B^*}{Z + \varepsilon_2 B^*}\right) - ln(Z - B^*) \\ &+ \frac{\bar{b}(M)}{b}\left[\frac{B^*}{(Z - B^*)} - \frac{ZA^*)}{(Z + \varepsilon_1 B^*)(Z + \varepsilon_2 B^*)}\right] \end{aligned} \qquad (A4-19)$$

In equation $(A4-19)$, the substitution $A^* = aP/R^2T^2$, $B^* = bP/RT$, and $Z = V_m P/RT$ are used. Equation $(A4-19)$ is then rewritten as equation $(4-42)$ in §4.

To complete the high pressure VLE calculation, the expressions $\bar{a}(M)=\frac{1}{n}\frac{\partial(n^2a)}{\partial g^P(M)}$ and $\bar{b}(M)=\frac{\partial(nb)}{\partial g^P(M)}$ must be determined first using the relations described by equations $(4-37)$ and $(4-38)$. Using the chain rule for functional differentiation, and noting that the identity for the intensive distribution $\frac{\partial n}{\partial g^P(M)}=1$ holds for the semi-continuous mixtures, the simplified form of the expression $\bar{a}(M)$ becomes:

$$\begin{aligned}\bar{a}(M)=\frac{1}{n}\frac{\partial(n^2a)}{\partial g^P(M)}&=2a+2\sum_{s=1}^{q}\sum_{J=1}^{K}X_s^P\int_M X_J^P a_{Js}^P W_J^P(M)dM\\&+\sum_{J^+=1}^{K'}\sum_{J=1}^{K}\int_{M^+} X_J^P X_{J^+}^P a_J^P W_{J^+}^P(M^+)dM^+ + \sum_{J^+=1}^{K'}\sum_{J=1}^{K}\int_M X_J^P X_{J^+}^P a_J^P W_{J^+}^P(M)dM\end{aligned}\qquad (A4-20)$$

Following similar procedure as in equation $(A4-20)$, the expression $\bar{b}(M)$ becomes:

$$\bar{b}(M)=\frac{\partial(nb)}{\partial g^P(M)}=b+n\frac{\partial b}{\partial g^P(M)}=b+\sum_{J=1}^{K}\int_M X_J^P b_J^P W_J^P(M)dM \qquad (A4-21)$$

Equations $(A4-20)$ and $(A4-21)$ are numerically integrated due to the presence of the square root term in the a_J^P's and b_J^P's, as opposed to the usual analytical integration with exact distribution moments.

A5. Adaptive MOL using Basis Spline Collocation

A5.1. Introduction

The development of numerical methods based on B-Spline methodology is motivated by the substantial computational burden in spray combustion due to the large numbers of droplets and the associated grid to resolve the liquid phase and the gas phase flow and transport situations. From a numerical modelling perspective, an active area of research in spray combustion is devoted to reducing this computational burden through the development of highly accurate and efficient numerical methods, where adptivity and spline collocation methods are the case in point.In particular, the use of B-Splines is motivated by the development of robust and non-dissipative schemes on arbitrary meshes, where the resolution power of B-Splines with maximum continuity allows the representation and computation in a broad range of mass diffusion and thermal diffusion time scales which arises in droplet evaporation.

The Adaptive Method Of Lines using Basis Spline Collocation (AMOLBSC) package takes its root from the popular general purpose MOL based software package PDECOL (Madsen and Sincovec, 1979) that is used in solving systems of ODEs or PDEs. Such systems of equations are described by equation $(A5-1_a)$ with $0 \le \zeta \le 1$; $\tau \ge \tau_0$; having initial condition described by equation $(A5-1_b)$ with $0 \le \zeta \le 1$; $\tau = \tau_0 = 0$; and a (modified) separated left (droplet centre) and right (droplet surface) boundary conditions, respectively, described by equations $(A5-1_c)$ and $(A5-1_d)$ with $\zeta = \zeta_C$; $\tau \ge \tau_0$ and $\zeta = \zeta_R$; $\tau \ge \tau_0$ as:

$$\Phi_\tau(\tau,\zeta) = \mathrm{f}\left(\tau,\zeta,\Phi(\tau,\zeta),\Phi_\zeta(\tau,\zeta),\Phi_{\zeta\zeta}(\tau,\zeta)\right) \qquad (A5-1_a)$$

$$\Phi(\tau_0,\zeta) = \Phi_0(0,\zeta) \qquad (A5-1_b)$$

$$\mathrm{B_C}\left(\tau,\zeta_C,\Phi(\tau,\zeta_C),\Phi_\zeta(\tau,\zeta_C)\right) = 0 \qquad (A5-1_c)$$

$$\mathrm{B_R}\left(\tau,\zeta_R,\Phi(\tau,\zeta_R),\Phi_\zeta(\tau,\zeta_R)\right) = 0 \qquad (A5-1_d)$$

In equations $(A5-1)$, the vector valued functions $\mathbf{\Phi}(\tau,\zeta)$ of the scalar quantities (τ,ζ) consists of $\mathrm{N}_{\mathrm{PDE}}$ number of variables corresponding to the partial differential equations (PDEs) represented by $(A5-1_a)$, and the subscripts τ (normalised time scale) and ζ (normalised length scale) in $\mathbf{\Phi}_\tau$, $\mathbf{\Phi}_\zeta$, $\mathbf{\Phi}_{\zeta\zeta}$, designate its partial derivatives with respect to those scalar variables. The boundary conditions $\mathbf{B}_\mathrm{C}$ and $\mathbf{B}_\mathrm{R}$, respectively, represents the values at the droplet centre and the droplet surface. Therefore, according to equation $(5-1_a)$ in §5, the governing equations in $(A5-1)$ are designed for the liquid-space alone. The governing equations for the vapour-space must be treated by applying suitable initial and boundary conditions and by employing the quasi-staedy gas assumption to recover the governing equations derived in §3. Since there is no explicit requirement for $\mathbf{f}$ to actually depend on either $\mathbf{\Phi}$, $\mathbf{\Phi}_\zeta$ and/or $\mathbf{\Phi}_{\zeta\zeta}$, the form of the equation in $(A5-1)$ could be ODEs, first order PDEs, or second order PDEs. It is interesting to see that all of the liquid phase equations derived in §4 and §5, which take the form of ODEs or PDEs belong to the class of equations described by $(A5-1_a)$. In particular, equation $(5-9)$ with conditions in equations $(5-3)$, $(5-4)$, and $(5-5)$ are, respectively, of the same form as equation $(A5-1_a)$ with conditions in equations $(A5-1_b)$, $(A5-1_c)$, and $(A5-1_d)$. Traditionally, these equations are solved using finite difference and finite volume type methods, despite their known deficiency both in their computational accuracy and efficiency.

Computation with B-splines in geometrical modelling and mesh generation is a very popular and well established research (deBoor, 1978), although it features less prominently in solving flow and transport problems. The basic idea in the collocation method using B-splines is to seek a solution for the unknown vector valued functions $\mathbf{\Phi}$ as an approximate piecwisewise polynomials, $\tilde{\boldsymbol{\Phi}}$, which are in turn projected on their B-spline basis so that it coincides with the function at interpolation points and fulfil the differential equations in $(A5-1)$. To that end, a large volume of research papers and widely used (standard MOL) codes has been produced over the years, among which PDECOL (Madsen and Sincovec, 1979) is an example.

These standard MOL codes have three main components. First, a spatial discretisation of the RHS of equation $(A5-1_a)$ is carried out, usually based on the Galerkian method, using B-splines as the piecewise polynomial basis. The resulting equations of continuous differential in time and linear algebraic (or discrete algebraic in space) take the form of ODEs (or differential algebraic equations-DAEs). Second, a suitable ODE solver, usually that employ adaptive time integration, i.e., with variable time step sizes and possibly capable of varying the order of integration formula is selected to solve the resulting systems of ODEs. Third, a linear algebraic package is required to handle the DAEs that arise due to boundary conditions in the ODE equations and the ODE solver in the PDE equation.

However, there are many obvious limitations in PDECOL. First, the equations governing droplet evaporation and/or combustion, in most situations, are stiff ODEs or PDEs due to the different mass diffusion, thermal diffusion, flow and chemical kinetics time scales. Second, due to the non-linear terms evaluation in the Galerkin approximation employed by PDECOL, the technique is burdened by high computational cost. Third, the restrictions on the form of the boundary conditions and the fact that the boundary conditions must be consistent with the initial conditions excludes certain systems of PDEs, in particular, those which are advection dominated or have sharp phase interfaces (hyperbolic-prabolic type equations). Fourth, although the time integrator changes the time step size automatically and operates in an adaptive manner, the space descritisation is generally a static (non-adaptive) grid system, which limits the computational efficieny of the package, in particular, when dealing with clases of problems decribed by equation $(5-9)$. Therefore, this section is devoted to circumvent the previous four limitations of PDECOL so that a generic code based on a fully Adaptive Method Of Lines using B-Splines Collocation (AMOLBSC) can be established. The practice of developing improved generic codes based on well tested and popular packages with known shortcomings is not new. For example, Keast and Muir (1991), after a careful analysis and observation of the banded matrix used in PDECOL, they found out that the resultiing matrices are in fact almost block diagonal (ABD) matrices. The authors implemented the ABD matrix solver in PDECOL and called it EPDCOL, which provided up to 70% computational advantage over PDECOL both in storage and execution time. To that end, the improvement gained through EPDCOL is adopted in this work. In the following sections, the improvements made to make the transition from PDECOL/EPDCOL to AMOLBSC, particularly the spatial discretisation using B-Spline collocation of maximum continuity, the fully (temporal and spatial) adaptive technique development, and the simplified form developed in the treatment of the boundary conditions due to the application of special property of B-Splines are explored and implemented.

A5.2. Philosophy and Description of AMOLBSC

AMOLBSC is a framework to develop a purpose built package with the aim of incorporating all the liquid phase model equations governing the spray dynamics, evaporation, and combustion of multicomponent fuels in practical combustion devices, which all fall under the class of equations described by $(A5-1)$. The philosophy behind AMOLBSC is first and for most its modularity, where it is expected to be interfaced easily with any gas-phase flow and transport equation solver. To that end, AMOLBSC is designed to perform as time-adaptive ODE solver in the event that the governing equations to be solved are ODEs or IVPs. If the governing equations are PDEs or IVBPs, AMOLBSC performs as a fully adaptive (time and space) MOL sover for the resulting DAEs. The description of ODE solvers can be found elsewhere (Petzold, 1982). Therefore, more attention will be given in the organisation and structure of AMOLBSC as a general purpose package to solve PDEs that arise in science and engineering by using the Adaptive Mesh Refinement (AMR) technology. As such, the development in this section is primarily an attempt to present a general ODE and/or PDE solver that can be easily adopted for the problem discussed in §5.

A5.2.1 Spatial Descritisation

Since the starting point for the spatial descritisation of AMOLBSC is closely related to PDECOL (Madsen and Sincovec, 1979), the reader is advised to consult the literature about the background of that package. In this study, however, a novel B-Spline collocation method of maximum continuity with attractive properties of yielding high-resolution power is presented in the framework of the method of lines (MOL).

A5.2.1.1 Construction of Basis Splines of Maximum Continuity

Let $[\zeta_j]_{j=0}^{N}$ be a discretisation of an increasing sequence or a mesh defined on the interval $A = [0,1]$ (or on the interval $[\zeta_C, \zeta_R]$ in the liqud-phase space). Associated with the mesh, there is a spline function or a piecewise polynomial of order p (degree $p-1$ at most) belonging to the space $C^m(A)$ with maxiumum continuity or (m time differentiable) and whose high order derivatives posses jump discontinuities at their $m-1$ derivatives at each breakpoint $\zeta_j \in A$. Therefore, an approximation to the vector valued function $\Phi(\tau,\zeta)$, can be described by the spline function $\tilde{\Phi}(\tau,\zeta)$, which is commonly described by its B-representation (de Boor, 1978) as:

$$\tilde{\Phi}(\tau,\zeta) = \sum_{j=0}^{N} \tilde{\sigma}_j(\tau)\tilde{B}_j^p(\zeta) \qquad (A5-2)$$

In equation $(A5-2)$, the special basis spline (B-Spline) function of order p, $\tilde{B}_j^p(\zeta)$, is a piecewise polynomial of degree at most $p-1$, and are locally linear independent, which due to its locality, only p basis functions contribute to the summation in equation $(A5-2)$. Note that equation $(A5-2)$ decouples the approximate function $\tilde{\Phi}(\tau,\zeta)$ into a time dependent coefficient $\tilde{\sigma}_j(\tau)$ and a space dependent basis spline $\tilde{B}_j^p(\zeta)$. A well conditioned basis of the B-splines can be obtained with the recurrence formula (de Boor, 1978) as:

$$\tilde{B}_j^p(\zeta) = \frac{\zeta - \kappa_j}{\kappa_{j+p-1} - \kappa_j}\tilde{B}_j^{p-1}(\zeta) + \frac{\kappa_{j+p} - \zeta}{\kappa_{j+p} - \kappa_{j+1}}\tilde{B}_{j+1}^{p-1}(\zeta) \qquad (A5-3)$$

In equation $(A5-3)$, the non-decreasing sequence $\left[\kappa_j\right]_{j=0}^{N+p}$ are the extended knots at which the vector valued function approximations $\widetilde{\Phi}(\tau,\zeta)$, are tied together with the mesh as $\left[\zeta_j = \kappa_{j+p-1}\right]_{j=1}^{N-1} \in \Lambda$, by the maximum continuity condition $C^m(\Lambda)$ on their derivatives (Botella, 1999). Using the B-Spline of order $p=1$ as step functions defined by $\widetilde{B}_j^1(\zeta) = 1$ for $\zeta \in \lfloor \kappa_j, \kappa_{j+1} \rfloor$ and $\widetilde{B}_j^1(\zeta) = 0$ otherwise, equation $(A5-3)$ enforces the regularity of the B-splines, where the knots coincide with the breakpoints in the interior domain. The construction of the basis described above leaves freedom in the first p and last p of the knots. In many situations where extrapolation beyond ζ_C and ζ_R is not anticipated, it is common practice to set $\zeta_C = \kappa_1 = \ldots = \kappa_p = 0$ and $0 = \kappa_{N+1} = \ldots = \kappa_{N+p} = \zeta_R$, where it can be exploited to treat boundary value problems.

A5.2.1.2 Collocation at Gaussian Points

Although collocation methods are relatively simpler and are proved efficient numerical methods that can be applied directly to the original differential equation describing the physics of the problem, they feature less prominently in fluid flow and transport applications. Botella (1999) has recently applied the B-Spline collocation method for the solution of the unsteady Navier-Stokes equation with considerable success. Collocation is considered to be more efficient than methods that require integration of the differential equation. Fairweather and Meade (1989) provided an extensive survey of spline collocation methods in four categories as nodal, orthogonal, extrapolated (modified), and collocation (Galerkin), where the types of the collocation schemes are related to the location of the collocation points.

The orthogonal collocation method is widely used and is shown to yield optimal order accuracy for the error (de Boor, 1978). Orthogonal collocation points are the same as Gaussian integration points that are located at points on an interval where an associated Legendre polynomial, which is orthogonal itself, is zero. To that end, de Boor (1978) showed how an p^{th} order ODE governing a boundary value problem can be solved using a B-Spline curve that has C^{m-1} continuity using orthogonal collocation method. The number of collocation points needed depends on the degree and continuity of the B-Spline curve, where for a spline of order p (degree $p-1$ at most) and continuity m, the number of knot collocation points needed per knot interval is $p-1+m$. The author proved that, when collocating at Gaussian points for boundary value problems, the error at mesh points is particularly small compared to the error at other locations, achieving superconvergence. In addition, Ganesh and Sloan (1999) employed a Petrov-Galerkin method to solve an m^{th} order ODE using spline curves that have C^{m} continuity and discovered that by using spline curves that have C^{m} continuity, only far fewer data values, even as few as half the number for C^{m-1}, are needed to define the spline, although the authors still used collocation at Gauss points. To this author's knowledge, there are no similar results for transient problems involving C^{m} continuity of $m \geq 2$. To that end, this investigation deals with problems described by equations $(A5-1)$, where a mesh of an increasing sequence $[\zeta_i]_{i=0}^{N}$ associated with increasing sequence of canonical Gaussian points $\left[C_j\right]_{j+0}^{p-1}$ having a non-uniform mesh step size of the form $[\Delta\zeta_i = \zeta_i - \zeta_{i-1}]_{i=1}^{N}$ at the collocation points $[g_l]_{l=1}^{N_C}$ defined by (de Boor, 1978):

$$\left.\begin{array}{ll} g_1 & = 0 \\ g_l & = \zeta_{i-1} + \Delta\zeta_i C_j \\ g_{N_C} & = 1 \end{array}\right\} \left[\begin{array}{l} l = 1+(i-1)(p-1)+j \\ i = 1, \ldots, N \\ j = 1, \ldots, p-1 \end{array}\right. \qquad (A5-4)$$

In equation $(A5-4)$, the collocation point sequence $[g_l]_{l=1}^{N_C}$ includes the internal Gauss-Legendre points and points at each boundaries, where $N_C = N(p-m+1)+m$. Note that for $m=2$, the number of the collocation points in the whole computational domain become $N_C = N(p-1)+2$. Thefore, the approximate solution in equation $(A5-2)$ must satisfy the PDEs in $(A5-1)$ except at the two boundary points as:

$$\tilde{\Phi}_\tau(g_l,\tau) = \tilde{\mathbf{f}}\left(\tau, g_l, \tilde{\Phi}(g_l,\tau), \tilde{\Phi}_\zeta(g_l,\tau), \tilde{\Phi}_{\zeta\zeta}(g_l,\tau)\right);\ l = 2,\ldots,N_c-1 \qquad (A5-5)$$

Since $\tilde{\Phi}(\tau,\zeta)$ is a vector valued function consisting N_{PDE} scalar variables (12-fractional composition distribution moments and a temperature field), all N_{PDE} equations in $(A5-5)$ must be satisfied at all the $N_C = N(p-1)$ collocation points. Applying the approximate solutions interms of the B-Spline representation of equation $(A5-2)$ and noting that at each collocation point there are at most $p+1$ non-zero B-Spline basis functions (de Boor, 1978), the B-representation at each collocation point $g_l \; = \zeta_{i-1} + \Delta\zeta_i C_j$ of the j^{th}-Gaussian point of the i^{th}-interval takes the form:

$$\tilde{\Phi}(g_l,\tau) = \sum_{s=(i-1)(p-1)+1}^{N_C=i(p-1)+2} \tilde{\sigma}_s(\tau)\tilde{B}_s^p(g_l) \qquad (A5-6)$$

Equation $(A5-6)$ is substituted into equation $(A5-5)$ to generate:

$$\sum_s^{N_C} \dot{\tilde{\sigma}}_s(\tau)\tilde{B}_s^p(g_l) = \tilde{\mathbf{f}}\left(\tau, g_l, \tilde{\Phi}(g_l,\tau), \tilde{\Phi}_\zeta(g_l,\tau), \tilde{\Phi}_{\zeta\zeta}(g_l,\tau)\right) \qquad (A5-7)$$

In equation $(A5-7)$, $\dot{\tilde{\sigma}} = d\tilde{\sigma}/\mathrm{d}\tau$ and $\tilde{\mathbf{f}}$ is dependent on the vector valued function $\tilde{\Phi}(\tau,\zeta)$ and its derivatives, and when expressed in the form $(A5-6)$, the spatial $\tilde{B}_s^p(g_l)$ and temporal $\tilde{\sigma}_s(\tau)$ dependencies decouple for the collocation points in the range $l = 2, \ldots N_C - 1$. To determine the equations corresponding to $l = 1$ and $l = N_C$ however, extra equations that depend on the type of boundary conditions must be imposed. These boundary conditions (which will be determined later) combined with equation $(A5-7)$ then yield the required semidiscrete system of time dependent ODEs, which can be written, here after in a general form (Keast and Muir, 1991) as:

$$\tilde{F}(\tau,\tilde{\sigma})\,\dot{\tilde{\sigma}}(\tau) = \tilde{H}(\tau,\tilde{\sigma}) \qquad (A5-8)$$

The details and the strategies employed to integrate equation $(A5-8)$ are discussed later. However, since the boundary condition in this study is treated in a different manner from both PDECOL (Madsen and Sincovec, 1979) and EPDCOL (Keast and Muir, 1991), attention is given to this special treatment of the boundary conditions.

A5.2.2 Special Treatment of Boundary Conditons

In the original PDECOL code, non-homogeneous and non-separated boundary conditions of the form $\mathbf{B}\left(\tau, \boldsymbol{\Phi}(\zeta_C,\tau), \boldsymbol{\Phi}_\zeta(\zeta_C,\tau), \boldsymbol{\Phi}(\zeta_R,\tau), \boldsymbol{\Phi}_\zeta(\zeta_R,\tau)\right) = \dot{\mathbf{z}}$ corresponding to the homogeneous and separated boundary condition described by equations $(A5-1_c)$ and $(A5-1_d)$ were used, where the $\dot{\mathbf{z}} = \mathbf{dz/d}\tau$ term is an arbitrary time-dependent vector valued function. In short, PDECOL prescribes its boundary conditions in an ODE form so that it is consistent with the governing PDEs, although it in turn requires the initial condition to be consistent too. Such conditioning is known to create hinderance by increasing its complexity. Therefore, the boundaries in this study are treated in their original form. Using special properties of B-Splines of C^m continuity (de Boor, 1978), a general mixed boundary conditions at the droplet centre and at the droplet surface can be expressed by equations $(A5-9)$ as:

$$\begin{aligned}\widetilde{\boldsymbol{\Phi}}(0,\tau) &= \widetilde{B}_1^p(0)\widetilde{\boldsymbol{\sigma}}_1(\tau)\\ \widetilde{\boldsymbol{\Phi}}_\zeta(0,\tau) &= \left(\widetilde{B}_1^p(0)\right)_\zeta \widetilde{\boldsymbol{\sigma}}_1(\tau) + \left(\widetilde{B}_2^p(0)\right)_\zeta \widetilde{\boldsymbol{\sigma}}_2(\tau)\end{aligned} \qquad (A5-9_a)$$

$$\begin{aligned}\widetilde{\boldsymbol{\Phi}}(1,\tau) &= \widetilde{B}_{N_C}^p(1)\widetilde{\boldsymbol{\sigma}}_{N_C}(\tau)\\ \widetilde{\boldsymbol{\Phi}}_\zeta(1,\tau) &= \left(\widetilde{B}_{N_C}^p(1)\right)_\zeta \widetilde{\boldsymbol{\sigma}}_{N_C}(\tau) + \left(\widetilde{B}_{N_C-1}^p(1)\right)_\zeta \widetilde{\boldsymbol{\sigma}}_{N_C-1}(\tau)\end{aligned} \qquad (A5-9_b)$$

From equations $(A5-9)$, it is easy to observe that only two B-Spline basis and one from each of their derivatives appear at those Gaussian collocation points associated with the left and right boundaries. Therefore, equation $(A5-7)$ along with equations $(A5-9)$ form the required equation in $(A5-8)$, with $N_C = N(p-1)+2$ equations corresponding to each component of the vector valued function $\widetilde{\boldsymbol{\Phi}}(\tau,\zeta)$. To that end, the governing equation $(5-9)$ in §5 along with the boundary conditions at the droplet centre (left) and at the droplet surface (right) described, respectively, by equations $(5-4)$ and $(5-5)$ can be rewritten in a form similar to equation $(A5-8)$. However, before focusing into the specific details and before stating the final form of the numerical method in equation $(A5-8)$ along with the boundary conditions in equations $(A5-9)$ corresponding to the problem in §5, the AMOLBSC formulation is treated in a general manner. Therefore, some general issues of practical interest in relation to the resulting equations and, in particular, the time integration procedure are discussed. However, those issues in conjunction with a major computational effort associated with the linear systems that arise in the calculation performed by an ODE or DAE solvers will be discussed only briefly as the detail of such linear algebraic packages is vast and can be found elsewhere (Petzold, 1982).

A5.2.3 Time Integration

In general, the solution method employed to solve the systems of equations described by equation $(A5-8)$ is crucial to the success of the general purpose spray dynamics, evaporation, and combustion code (AMOLBSC) that is developed as a framework for further development. For equations of the form described by $(A5-8)$, where the coefficient matrix $\tilde{F}(\tau,\tilde{\sigma})$ is non-singular and the right hand side vector $\tilde{H}(\tau,\tilde{\sigma})$ doesn't totally contain zero entries, it can be rearraneged in a general differential algebraic equations (DAEs) of the form:

$$\tilde{P}(\tau,\tilde{\sigma},\dot{\tilde{\sigma}})=\tilde{F}(\tau,\tilde{\sigma})\;\dot{\tilde{\sigma}}(\tau)\;-\;\tilde{H}(\tau,\tilde{\sigma})=0 \qquad (A5-10)$$

DAEs of the form described by equation $(A5-10)$ are usually solved by employing linear multistep methods called backward differential formulas (BDF) (Petzold, 1982). The simplest BDF is the implicit Euler method, where it replaces the time derivative in $(A5-10)$ by a backward difference of the form $\tilde{P}(\tau_{n+1},\tilde{\sigma}_{n+1},\frac{\tilde{\sigma}_{n+1}-\tilde{\sigma}_{n}}{\tau_{n+1}-\tau_{n}})=0$, where n is the time step level and $\Delta\tau_{n+1}=\tau_{n+1}-\tau_{n}$ is the time step size. While solving the resulting nonlinear algebraic system of equations in $\tilde{\boldsymbol{\sigma}}_{n+1}$ by numerical iterations, both constant time step size $\Delta\tau_{n+1} = \Delta\tau$, or variable time step sizes $\Delta\tau_{n+1}$can be used, although the variable time step sizes that are adaptive show great advantage in their computational efficiency.

There are three standard implementations of BDF methods that allow for time adaptivity or variable time stepsizes. These are the *fixed coefficient* method of Hindmarsh (1983), the *variable coefficient* method of Hindmarsh (1976) and the *fixed leading coefficient* methods of Petzold (1982). The fixed coefficient method is efficient for smooth problems, but possibly unstable for systems that require frequent time step size adjustments. The variable coefficient method is the most stable, but it is computationally expensive as it requires more Jacobian evaluation. The fixed leading coefficient, however, is a compromise between the other two methods, being less stable and requiring fewer Jacobian evaluations than the variable coefficient method. The fixed leading coefficient implementation is adopted in this study, where a stable $q < 7$-step BDF method of the form $\tilde{P}(\tau_{n+1}, \tilde{\boldsymbol{\sigma}}_{n+1}, \frac{\tilde{\boldsymbol{\alpha}}}{\Delta\tau_{n+1}} \tilde{\boldsymbol{\sigma}}_{n+1} + \tilde{\boldsymbol{\beta}}) = 0$, with known $\tilde{\boldsymbol{\alpha}}$ and $\tilde{\boldsymbol{\beta}}$, is used to iterate the unknown solution $\tilde{\boldsymbol{\sigma}}_{n+1}$ using Newton's method (Petzold, 1982). The $(j+1)^{th}$ Newton approximation of $\tilde{\boldsymbol{\sigma}}_{n+1}$ is given by:

$$\tilde{\boldsymbol{\sigma}}_{n+1}^{j+1} = \tilde{\boldsymbol{\sigma}}_{n+1}^{j} - \left(\underbrace{\frac{\tilde{\boldsymbol{\alpha}}}{\Delta\tau_{n+1}} \frac{\partial \tilde{P}}{\partial \dot{\tilde{\boldsymbol{\sigma}}}} + \frac{\partial \tilde{P}}{\partial \tilde{\boldsymbol{\sigma}}}}_{\tilde{M}} \right)^{l} \tilde{P}(\tau_{n+1}, \tilde{\boldsymbol{\sigma}}_{n+1}^{j}, \frac{\tilde{\boldsymbol{\alpha}}}{\Delta\tau_{n+1}} \tilde{\boldsymbol{\sigma}}_{n+1}^{j} + \tilde{\boldsymbol{\beta}}) \qquad (A5-11)$$

From equation $(A5-11)$, it is easy to observe that the nonsingular inverse iteration matrix $\tilde{M}$ depends on $\partial\tilde{P}/\partial\dot{\tilde{\boldsymbol{\sigma}}}$, $\partial\tilde{P}/\partial\tilde{\boldsymbol{\sigma}}$, $\tilde{\boldsymbol{\alpha}}$ as well as the time step size. The specific form of the general structure of the iteration matrix will be given in later sections when the formulation under development is complete and equations $(A5-8)$-$(A5-11)$ are applied directly to solve the droplet evaporaton problem.

A5.2.4 Spatial Adaptivity

Although temporal adaptivity in the method of lines (MOL) is widely practiced, there are very few codes that are fully adaptive and are able to automatically adjust both the temporal and spatial step sizes (Vande Wouwer et al, 2001). The aim in this section is to design a fully adaptive code by incorporating an adaptive mesh refinement (AMR) technology in the base code PDECOL.

There are three most common mesh adaptation strategies for the spatial discretisation of PDEs in nonstatonary grids. However, there are also other special classes of mesh adaptation strategies for resolving sharp fronts / shock waves on a fixed mesh for hyperbolic PDEs (Boden, 1997), which are not a point of interest in this investigation. The three mesh adaptation strategies; mesh motion (r-refinement), spatial mesh refinement or mesh coarsening (h-refinement), and mesh order variation (p-refinement), could be used independently or as a combination to generate more sophisticated techniques (Vande Wouwer et al, 2001). Based on the manner the grid is adapted, all the strategies fall under two main categories. In the first category, the method of defining node movements or grid adaptation is based on the equidistribution principle (EP)[7], while in the second category the grid adaptation is based on minimisation of a functional (MF)[8] (Vande Wouwer et al, 2001). In this study, the h-refinement of Adjerid et al (1992) based on EP is adopted. However, instead of the piecewise polynomial of degree p for the approximate solution $\tilde{\Phi}(\tau,\zeta)$ using Galerikin method with $C^{m=0}$ continuity at mesh points, a B-Spline collocation of maximum C^{m} continuity is used to determine a posteriori error and derive the h-refinement algorithm.

---

[7] The equidistribution principle (EP) attempts to position the mesh points such that some measure of the spatial error is equally distributed over the subintervals, and there are two common approaches to apply EP. In the first, the EP is applied in an integral form (employed in most h or hp-refinements), where the arclength function is chosen to represent an error distribution so that the new mesh points satify the the integral of the monitor function. In the second approach, the EP is applied in a differential form (employed in r-refinement), where each mesh point is considered to be functions of time with fixed number of mesh points. Assuming an arclength monitor function, the error in each sub-interval and their average so that mesh movement is determined based on the error values (White, 1979)

[8] For example, the functional could be an error indicator of the discretisation or the residual of the PDEs to be solved. In most cases, a measure of error is carried out on the resulting ODEs/DAEs for the solution and the nodal position by minimising the integral of the error measure with respect to the time derivative of the nodal positions and amplitudes (Miller, 1981).

A5.2.5 Spatial Error Estimation

In most of the posterior spatial error estimate techniques for the solutions of PDEs, the the error estimates are computed using piecewise polynomials of higher degree than that used to represent the solutions (Bieterman and Babuska, 1986). In this study, the approximation solution $\tilde{\boldsymbol{\Phi}}(\tau,\zeta)$ is computed in a piecewise polynomial subspace of degree p, while a second piecewise solution $\overline{\tilde{\boldsymbol{\Phi}}}(\tau,\zeta)$ is computed in a similar subspace but with degree $p+1$. In the following, it is assumed that all the expressions used in equations $(A5-1)$-$(A5-11)$ will be identified with a bar to denote its association with the approximate solution $\overline{\tilde{\boldsymbol{\Phi}}}(\tau,\zeta)$ of degree $p+1$. After the spatial discretisation or after the application of the collocation scheme on the general differential algebraic equations (DAEs) described by equation $(A5-10)$ along with the boundary condition described by equation $(A5-9)$, the approximate solutions $\tilde{\boldsymbol{\Phi}}(\tau,\zeta)$ and $\overline{\tilde{\boldsymbol{\Phi}}}(\tau,\zeta)$, respectively, take the form of equation $(A5-12)$ and equation $(A5-13)$:

$$\dot{\mathbf{B}}_{\mathrm{C}}\left(\tau,\, 0, \tilde{\boldsymbol{\Phi}}(0,\tau), \tilde{\boldsymbol{\Phi}}_{\zeta}(0,\tau)\right) = 0 \qquad (A5-12_a)$$

$$\sum_{s=(i-1)(p-1)+1}^{N_C=N(p-1)+2} \dot{\tilde{\boldsymbol{\sigma}}}_s(\tau)\tilde{B}_s^p(g_l) - \tilde{\mathbf{f}}\left(\tau, g_l, \tilde{\boldsymbol{\Phi}}(g_l,\tau), \tilde{\boldsymbol{\Phi}}_{\zeta}(g_l,\tau), \tilde{\boldsymbol{\Phi}}_{\zeta\zeta}(g_l,\tau)\right) = 0 \qquad (A5-12_b)$$

$$\dot{\mathbf{B}}_{\mathrm{R}}\left(\tau,\, 1, \tilde{\boldsymbol{\Phi}}(1,\tau), \tilde{\boldsymbol{\Phi}}_{\zeta}(1,\tau)\right) = 0 \qquad (A5-12_c)$$

$$\mathbf{B}_{\mathrm{C}}\left(\tau,\, 0, \overline{\tilde{\boldsymbol{\Phi}}}(0,\tau), \overline{\tilde{\boldsymbol{\Phi}}}_{\zeta}(0,\tau)\right) = 0 \qquad (A5-13_a)$$

$$\sum_{s=p(i-1)+1}^{Np+2} \dot{\overline{\tilde{\boldsymbol{\sigma}}}}_s(\tau)\overline{\tilde{B}}_s^p(\bar{g}_l) - \overline{\tilde{\mathbf{f}}}\left(\tau, \bar{g}_l, \overline{\tilde{\boldsymbol{\Phi}}}(\bar{g}_l,\tau), \overline{\tilde{\boldsymbol{\Phi}}}_{\zeta}(\bar{g}_l,\tau), \overline{\tilde{\boldsymbol{\Phi}}}_{\zeta\zeta}(\bar{g}_l,\tau)\right) = 0 \qquad (A5-13_b)$$

$$\mathbf{B}_{\mathrm{R}}\left(\tau,\, 1, \overline{\tilde{\boldsymbol{\Phi}}}(1,\tau), \overline{\tilde{\boldsymbol{\Phi}}}_{\zeta}(1,\tau)\right) = 0 \qquad (A5-13_c)$$

In equations $(A5-12)$, g_l is one of the $p-1$ Gauss-Legendre collocation points in the i^{th} sub-interval, while $\bar{g}_l$ in equation $(A5-13)$ belongs to the p Gauss-Legendre collocation points, $[i]_{i=1}^{N}$. Following similar steps, equations $(A5-12)$ and $(A5-13)$ can be rewritten in a similar form as equation $(A5-11)$ as:

$$\tilde{\boldsymbol{\sigma}}_{n+1}^{j+1} = \tilde{\boldsymbol{\sigma}}_{n+1}^{j} - \tilde{M}\tilde{P}(\tau_{n+1}, \tilde{\boldsymbol{\sigma}}_{n+1}^{j}, \frac{\tilde{\boldsymbol{\alpha}}}{\Delta\tau_{n+1}}\tilde{\boldsymbol{\sigma}}_{n+1}^{j} + \tilde{\boldsymbol{\beta}}) \qquad (A5-14)$$

$$\overline{\tilde{\boldsymbol{\sigma}}}_{n+1}^{j+1} = \overline{\tilde{\boldsymbol{\sigma}}}_{n+1}^{j} - \overline{\tilde{M}}\,\overline{\tilde{P}}(\tau_{n+1}, \overline{\tilde{\boldsymbol{\sigma}}}_{n+1}^{j}, \frac{\overline{\tilde{\boldsymbol{\alpha}}}}{\Delta\tau_{n+1}}\overline{\tilde{\boldsymbol{\sigma}}}_{n+1}^{j} + \overline{\tilde{\boldsymbol{\beta}}}) \qquad (A5-15)$$

Although it seems logical to treat equations $(A5-14)$ and $(A5-15)$ as separate DAEs, such a scheme will be computationally expensive and possibly unstable due to the large number of equations and interpolations that must be applied on the new mesh. In particular, the integration could be hampered seriously after remeshing due to the fact that the values of the two solutions at the previous steps would have to be interpolated from two different sources. Therefore, equations $(A5-14)$ and $(A5-15)$ are treated as a single DAE system. As such, no interpolation in time is required. Rather, after a remeshing, both solutions at the previous steps on the new mesh can be interpolated using the piecewise solution of degree $p+1$ using the recurrence formulas of (Newton's) divided differences, where for the j^{th} Newton approximation at time level n can be stated (Petzold, 1982) as:

$$\left[\tilde{\boldsymbol{\sigma}}_{n}^{j}\right] = \tilde{\boldsymbol{\sigma}}_{n}^{j} \qquad (A5-16_a)$$

$$\left[\tilde{\boldsymbol{\sigma}}_{n}^{j}, \tilde{\boldsymbol{\sigma}}_{n-1}^{j}, \ldots, \tilde{\boldsymbol{\sigma}}_{n-k}^{j}\right] = \frac{\left[\tilde{\boldsymbol{\sigma}}_{n}^{j}, \tilde{\boldsymbol{\sigma}}_{n-1}^{j}, \ldots, \tilde{\boldsymbol{\sigma}}_{n-k+1}^{j}\right] - \left[\tilde{\boldsymbol{\sigma}}_{n-1}^{j}, \tilde{\boldsymbol{\sigma}}_{n-2}^{j}, \ldots, \tilde{\boldsymbol{\sigma}}_{n-k}^{j}\right]}{\tau_{n} - \tau_{n-k}} \qquad (A5-16_b)$$

Similar recurrence formulas are applied for the B-spline coefficient $\overline{\tilde{\boldsymbol{\sigma}}}_{n}^{j}$ that belongs to the p Gauss-Legendre collocation points, and a suitable k^{th} order BDF scheme is employed. Now, the approximate solution of degree $p+1$ and p for the new mesh, respectively, are denoted by $\tilde{\boldsymbol{\Phi}}^{*}(g_{l}^{*}, \tau_{n-i})$ and $\overline{\tilde{\boldsymbol{\Phi}}}^{*}(\overline{g}_{l}^{*}, \tau_{n-i})$, the number of collocation points by N_{C}^{*} and $\overline{N}_{C}^{*}$, and the collocation points by g_{l}^{*} and $\overline{g}_{l}^{*}$. Note that

N_C^* is not necessarily the same as $\overline{N}_C^*$. Expressions without "$*$" describe the approximate solutions in the old mesh. The approximate solutions at the new mesh $\tilde{\boldsymbol{\Phi}}^*(g_l^*, \tau_{n-i})$ and $\overline{\tilde{\boldsymbol{\Phi}}}^*(\overline{g}_l^*, \tau_{n-i})$ can be determined by requiring it to interpolate the values of $\tilde{\boldsymbol{\Phi}}(g_l^*, \tau_{n-i})$ and $\overline{\tilde{\boldsymbol{\Phi}}}(\overline{g}_l^*, \tau_{n-i})$ at the new collocation points as:

$$\tilde{\boldsymbol{\Phi}}^*(g_l^*, \tau_{n-i}) = \overline{\tilde{\boldsymbol{\Phi}}}(g_l^*, \tau_{n-i}) \quad ; \quad l = 1, \dots, N_C^* \qquad (A5-17_a)$$

$$\overline{\tilde{\boldsymbol{\Phi}}}^*(\overline{g}_l^*, \tau_{n-i}) = \overline{\tilde{\boldsymbol{\Phi}}}(\overline{g}_l^*, \tau_{n-i}) \quad ; \quad l = 1, \dots, \overline{N}_C^* \qquad (A5-17_b)$$

Therefore, after determining the B-spline coefficients in equations $(A5-14)$ and $(A5-15)$ or the approximate solutions in equations $(A5-12)$ and $(A5-13)$ at the previous time level, a posteriori spatial error estimate can be obtained by comparing the two solutions globally and locally as:

$$\|e\| \cdot \|e\| = \int_0^1 \left\{ \left(\tilde{\boldsymbol{\Phi}} - \overline{\tilde{\boldsymbol{\Phi}}} \right) \Big/ \left(\in_A + \in_R \left| \tilde{\boldsymbol{\Phi}} \right| \right) \right\}^2 d\zeta \qquad (A5-18_a)$$

$$\|e_i\| \cdot \|e_i\| = \sum_{d=1}^{N_{PDE}} \int_{\zeta_{i-1}}^{\zeta_i} \left\{ \left(\tilde{\boldsymbol{\Phi}} - \overline{\tilde{\boldsymbol{\Phi}}} \right) \Big/ \left(\in_A + \in_R \left| \tilde{\boldsymbol{\Phi}} \right| \right) \right\}^2 d\zeta \quad ; \quad i = 1, \dots, N \qquad (A5-18_b)$$

In equation $(A5-18)$, the vector valued function $\|e\|$ represents the normalised error estimate for each PDE over the whole domain of the problem $\Lambda \in [0,1]$. On the other hand, $\|e_i\|$ represents the normalised error estimate of all the PDEs for the interval $\zeta \in [\zeta_{i-1}, \zeta_i]$, while $\in_A$ and $\in_R$ are vector valued parameters corresponding to the absolute and relative tolerances for each PDE. Based on the approximate errors described by equations $(A5-18)$, a remeshing strategy is developed in §5.

A6. Thermotransport Properties Correlation

In general, the thermotransport properties are assumed to vary with temperature, pressure, and composition. To understand the variability and to design empirical correlations with the distribution parameters or moments, an investigation was carried out on selected multicomponent paraffin, naphthene, and aromatic homologues that are known to constitute fuel JP8.

Considering the complexity of the PDF used to represent the fuel, a linear variation of thermotransport properties with molecular weight is used as in Tamim and Hallett (1995), who developed correlation coefficients for component-paraffin fuels excluding the components of the naphthene and aromatic group. In this investigation, a multivariate regression analysis is developed to compute the correlation coefficients both for the components of the paraffin, naphthene, and aromatic homologues, where some corrections are also proposed to the works of Tamim and Hallett (1995). To ascertain its validity, the coefficients are used to compute component properties and are compared with the experimental data of Vargaftik (1975), which shows good to excellent agreements. The correlations coefficients are provided in Appendix A7. However, thermotransport properties at constant temperatures and pressures will not be sufficient to understand the complex processes in droplet dynamics and evaporation. Therefore, extra corrections in temperature and pressure are done following well established property correlations and mixing rules (Polling et al, 2000). To that end, mixture properties of both the vapour and liquid phases are generated by integrating component property with the distribution moments.

In general, the diffusivities are computed so that it satisfies the general form of the transport equations $(3-13)$ or that of equation $(A2-8)$ derived in Appendix-A2. However, the homologue diffusivities must be modelled to satisfy the distribution function. The vapour diffusion coefficients are assumed to vary linearly with the molecular weight as:

$$D_J^v(M) = \left(a_{D_J} + b_{D_J} M\right)\varphi_{D_J} \qquad (A6-1)$$

In equation $(A6-1)$, the factor φ_D describing the temperature variation with diffusion can be fit with a Sutherland's type equation $\varphi_{D_J} = T^{5/2}/\left(b_{\varphi_J} + T\right)$. Application of equation $(A6-1)$ into the general transport equation $(3-13)$ yields diffusion coefficients corresponding to the distribution moments as:

$$D_{J(n=1)}^v = \left(a_{D_J} + b_{D_J}\theta_J^v\right)\varphi_{D_J} \qquad (A6-2_a)$$

$$D_{J(n=2)}^v = \left(a_{D_J} + b_{D_J}\frac{\psi_J^v}{\theta_J^v}\right)\varphi_{D_J} \qquad (A6-2_b)$$

$$D_{J(n=3)}^v = \left(a_{D_J} + \left[\frac{2}{\sqrt{\alpha_J^v}}\sigma_J^{(v)3} + 3\sigma_J^{(v)2}\,\theta_J^{(v)} + \theta_J^{(v)3}\right]\frac{b_{D_J}}{\psi_J^v}\right)\varphi_{D_J} \qquad (A6-2_c)$$

The diffusion coefficients corresponding to the different moments of paraffin have been shown to have very close numerical values (Tamim and Hallett, 1995), and only the first moment diffusivity is used. The same approach is adopted here for the other homologues too.

On the other hand, the liquid diffusion coefficients are determined based on the Wilke-Chang correlation (Polling et al, 2000), which is of the form:

$$D_J^l(M) = 7.4\cdot 10^{-2}\,\frac{\sqrt{\vartheta M}}{\mu_J^l\,V_m^{0.6}}T \qquad (A6-3)$$

In equation $(A6-3)$, the term ϑM is the sum of the mixture component molecular masses weighted by the association factor ϑ. For hydrocarbon and other non-polar molecules $\vartheta = 1$. Hence, when integrated with the distribution function, the term ϑM is simply the homologue mean molecular weight. $V_m = 1/c_J^l = M_J/\rho_J^l$ is the molar volume and μ_J^l is the mixture viscosity, which will be presented later. Using the distribution function in equation $(3-1)$, equation $(A6-3)$ is integrated numerically when the origin of the distribution function $\gamma_J^l \neq 0$. For the case $\gamma_J^l = 0$, however, analytical integration yields:

$$D_{J(n)}^l = 7.4\times10^{-12} \frac{\sqrt{\theta_J^l}}{\mu_{J(n)}^l} T\rho_{\bar{J}(n)}^{0.6(l)} \frac{\Gamma\left(\alpha_J^l + n - 0.6\right)}{\Gamma\left(\alpha_J^l\right)} \beta_J^{(n-0.6)l} \qquad (A6-4)$$

The thermal conductivity, both for the liquid and the vapour phases, is correlated as a linear function of the molecular weight, where the coefficients of correlation in turn vary linearly with temperature as:

$$\lambda_J^p(M) = a_{\lambda J}(T) + b_{\lambda J}(T)M \qquad (A6-5_a)$$

$$\begin{aligned} a_{\lambda J}(T) &= a_{kTJ} + b_{kTJ}T \\ b_{\lambda J}(T) &= a_{kCJ} + b_{kCJ}T \end{aligned} \qquad (A6-5_b)$$

The variation of the specific heat capacity, although dependent on composition and hence on the distribution moments, the dependence of the vapour and liquid phase specific heat capacity on temperature was found distinctively different. For the vapour phase, the correlations of Chou and Prausnitz (1986) are used. The correlation employs linear variation of specific heat capacity with molecular weight, while the correlation coefficients vary as cubic functions of temperature as (Appendix A6, Table A6.2):

$$Cp_J^v(T,M) = a_{cp_J}^v(T) + b_{cp_J}^v(T)M \qquad (A6-6_a)$$

$$a_{cp_J}^v(T) = A_{0J} + A_{1J}T + A_{2J}T^2 + A_{3J}T^3 \qquad (A6-6_b)$$

$$b_{cp_J}^v(T) = B_{0J} + B_{1J}T + B_{2J}T^2 + B_{3J}T^3 \qquad (A6-6_c)$$

On the other hand, the liquid specific heat capacity per mass is nearly independent of the molecular weight, and it is approximated as a quadratic function of temperature as:

$$Cp_J^l = \theta_J^l \left(a_{cp_J}^l + b_{cp_J}^l\, T + c_{cp_J}^l\, T^2\right) \qquad (A6-7)$$

The effective enthalpy of vaporisation for the liquid phase is taken as the sum of the enthalpy of all homologues in the mixture weighted by their fluxes, not by its mass fractions. At normal boiling point, the enthalpy of vaporisation of a mixture is nearly constant among homologous groups, and hence the homologue enthalpy of vaporisation can be written as:

$$h_{fg_J} = \left(a_{HJ} + b_{HJ}\, M\right)\varphi_{HJ} \qquad (A6-8)$$

In equation $(A6-8)$, φ_{HJ} accounts for the temperature correction factor based on the Watson equation (Polling et al, 2000), which relates the effective enthalpy of vaporisation of the mixture at its critical and boiling temperature. Hence, the effective enthalpy of vaporisation of the mixture takes the form:

$$L = \sum_J L_J = \sum_J \eta_J (a_{HJ} + b_{HJ}\theta_J^l) \left(\frac{T_{crJ} - T^{vR}}{T_{crJ} - T_{bJ}}\right)^{0.38} \qquad (A6-9)$$

The boiling point, the critical temperature, the critical molar volume, and the critical pressure are correlated as linear variations of molecular weight, respectively, as:

$$T_{bJ} = a_{bJ} + b_{bJ} M \qquad (A6-10)$$

$$T_{crJ} = a_{TcrJ} + b_{TcrJ} M \qquad (A6-11)$$

$$V_{mcrJ} = a_{mcrJ} + b_{mcrJ} M \qquad (A6-12)$$

$$P_{crJ} = a_{pcrJ} + b_{pcrJ} M \qquad (A6-13)$$

The vapour mixture viscosity is determined following the methods of William and Teja (1988) as:

$$\ell n(\mu_J^v) = a_{\mu J} + b_{\mu J} T_{bJ} + \frac{c_{\mu J}}{T_{bJ}} + \frac{d_{\mu J}}{T_{bJ}} \qquad (A6-14)$$

However, the liquid mixture viscosity is calculated using the mixing rules of Grunberg and Nissan (Polling et al, 2000) as:

$$\ell n(\mu_J^l) = \sum_{J=1} X_J^l \ell n \, \mu_J^{l*} + \sum_{J'} \sum_{J} X_{J'}^l X_J^l G_{J'J} \qquad (A6-15)$$

The binary interaction parameter $G_{J'J}$ is small for homologues of similar molecular weight, and in a mixture with many components the individual species mole fractions could be very small. Therefore, the second term can be neglected. The component viscosities in the first term of equation $(A6-15)$ are estimated using the Orrick and Erbar correlation (Polling et al, 2000) as:

$$\ell n \, \mu_J^{l*} = \ell n(\rho_J^l M) + A_{\mu J} + B_{\mu J} / T^l \qquad (A6-16)$$

The coefficients $A_{\mu J}$ and $B_{\mu J}$ are determined using linear group contributions in molecular weight as:

$$A_{\mu J} = C_{A1J} + C_{A2J} M \quad ; \quad B_{\mu J} = C_{B1J} + C_{B2J} M \qquad (A6-17)$$

Therefore, the mixture viscosity can be integrated from the component viscosity using equation $(A6-16)$ as:

$$\ell n(\mu_J^l) = \int_0^\infty X_J^l G^l(M) \ell n \, \mu_J^{l*}(M) dM \qquad (A6-18)$$

$$\ell n(\mu_J^l) = \ell n \rho_J^l + C_{A1J} + \frac{C_{B1J}}{T^l} + \left(C_{A2J} + \frac{C_{B2J}}{T^l} \right) \theta_J^l + \int_0^\infty G^l(M) \ell n(M) dM \qquad (A6-19)$$

For $\gamma_J^l = 0$, the integral in equation $(A6-19)$ reduces to a form:

$$\ell n(\mu_J^l) = \ell n\left(\rho_J^l \beta_J^l\right) + C_{A1J} + \frac{C_{B1J}}{T^l} + \left(C_{A2J} + \frac{C_{B2J}}{T^l}\right)\theta_J^l + \overline{\psi}(\alpha_J^l) \qquad (A6-20)$$

In equation $(A6-20)$, $\overline{\psi}(\alpha_J^l)$ is the digamma function (Abramovitz and Stegun, 1970). However, for $\gamma_J^l \neq 0$, equation $(A6-19)$ is integrated numerically. The correlations coefficients for equations $(A6-1)$-$(A6-20)$ are determined using multivariate regression analysis, and are given in Appendix A7.

A7. Tables of Correlation Coefficients

	$a\left(bar\ cm^6/mol^2\right)$						$b\left(cm^3/mol\right)$	
	a_{00}	a_{01}	a_{02}	a_{10}	a_{11}	a_{12}	b_0	b_1
Paraffin	-3.59×10^{2}	7.67×10^{1}	-1.61×10^{-4}	9.39×10^{1}	-7.80×10^{-2}	1.63×10^{-5}	-3.17×10^{1}	1.80×10^{0}
Naphthene	1.84×10^{2}	-1.86×10^{0}	5.56×10^{-3}	1.01×10^{2}	-0.12×10^{0}	3.81×10^{-5}	-1.31×10^{1}	1.57×10^{0}
Aromatic	-9.33×10^{1}	2.74×10^{1}	7.78×10^{-3}	5.42×10^{1}	-1.63×10^{-1}	8.71×10^{-4}	-9.62×10^{0}	1.73×10^{0}

Table A7.1 Constants for the SRK-EOS parameters (temperature range of 273.15K – 1711K)

Coefficients	**Paraffin**	**Naphthene**	**Aromatic**
A_{0cp}	2.465×10^{0}	-6.985×10^{0}	-4.282×10^{0}
A_{1cp}	-1.144×10^{-2}	-1.106×10^{-2}	-2.669×10^{-3}
A_{2cp}	1.759×10^{-5}	-4.485×10^{-6}	-5.492×10^{-6}
A_{3cp}	-5.972×10^{-9}	3.811×10^{-9}	3.242×10^{-9}
B_{0cp}	-3.561×10^{-2}	-2.794×10^{-3}	-6.189×10^{-3}
B_{1cp}	9.367×10^{-4}	8.497×10^{-4}	8.126×10^{-4}
B_{2cp}	-6.030×10^{-7}	-5.333×10^{-7}	-4.703×10^{-7}
B_{3cp}	1.324×10^{-10}	1.342×10^{-10}	1.058×10^{-10}

Table A7.2 Coefficients for the vapour mixture specific heat capacity (Chou and Prausnitz, 1986))

Coefficients	**Paraffin**	**Naphthene**	**Aromatic**
a_D	2.890×10^{-9}	2.708×10^{-9}	3.551×10^{-9}
b_D	-6.600×10^{-12}	-2.912×10^{-12}	-8.620×10^{-12}
b_φ	2.500×10^{2}	2.505×10^{2}	2.470×10^{2}
a_{kT}	1.090×10^{-4}	6.137×10^{-5}	1.086×10^{-4}
b_{kT}	-1.910×10^{-7}	1.521×10^{-7}	-1.109×10^{-7}
a_{kC}	-2.370×10^{-2}	-1.412×10^{-2}	-2.375×10^{-2}
b_{kC}	3.470×10^{-5}	-3.377×10^{-5}	2.220×10^{-5}
a_{cp}	2.260×10^{0}	4.700×10^{-1}	1.080×10^{0}
b_{cp}	-2.940×10^{-3}	4.500×10^{-3}	1.510×10^{-3}
c_{cp}	9.460×10^{-6}	-2.500×10^{-6}	2.750×10^{-6}
a_H	2.070×10^{7}	4.733×10^{7}	8.286×10^{6}
b_H	1.350×10^{5}	-1.690×10^{4}	2.606×10^{5}
a_b	2.085×10^{2}	3.485×10^{2}	1.904×10^{2}
b_b	1.567×10^{0}	1.170×10^{0}	2.040×10^{0}
a_{Tcr}	4.408×10^{2}	5.800×10^{2}	3.847×10^{2}
b_{Tcr}	1.210×10^{0}	1.329×10^{0}	2.170×10^{0}
a_{mcr}	1.590×10^{1}	8.790×10^{0}	1.310×10^{1}
b_{mcr}	4.103×10^{0}	8.227×10^{-1}	9.783×10^{-1}
a_{pcr}	6.070×10^{1}	6.800×10^{1}	6.230×10^{1}
b_{pcr}	-1.778×10^{-1}	-2.370×10^{-1}	-2.36×10^{-1}

Table A7.3 Thermotransport correlation coefficients

Coefficients	**Paraffin**	**Naphthene**	**Aromatic**
a_μ	-5.226×10^0	7.733×10^0	5.886×10^0
b_μ	1.763×10^{-3}	2.043×10^{-3}	1.772×10^{-3}
c_μ	-3.648×10^0	-1.145×10^1	-7.190×10^0
d_μ	-2.695×10^0	-7.117×10^0	-2.710×10^0
C_{A1}	-6.920×10^0	-7.881×10^0	-5.731×10^0
C_{A2}	-1.500×10^{-2}	-2.349×10^{-2}	-9.731×10^{-3}
C_{B1}	2.609×10^2	4.332×10^2	1.270×10^2
C_{B2}	7.070×10^0	1.131×10^1	4.754×10^0
a_ω	8.5172×10^{-2}	6.8174×10^{-2}	9.034×10^{-1}
b_ω	2.8346×10^{-3}	1.767×10^{-3}	7.555×10^{-2}

Table A7.4 Thermotransport correlation coefficients